UNIVERSITY OF TRENTO

DOCTORAL THESIS

Intermodal four wave mixing for heralded single photon sources in silicon

Author:
Stefano SIGNORINI

Supervisor:
prof. Lorenzo PAVESI

A thesis submitted in fulfillment of the requirements for the degree of Doctor of Philosophy

in the

Nanoscience Laboratory
Department of Physics

10 June 2019

Stefano Signorini
Intermodal four wave mixing for heralded single photon sources in silicon
10 June 2019
Supervisor: Lorenzo Pavesi
Reviewers: Dr. Roberto Osellame and Prof. Christian Pedersen

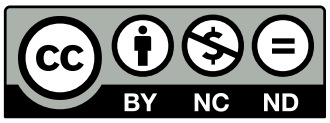

University of Trento
Nanoscience Laboratory
Department of Physics
Via Sommarive, 14
38123, Trento

Declaration of Authorship

I, Stefano SIGNORINI, declare that this thesis titled, "Intermodal four wave mixing for heralded single photon sources in silicon" and the work presented in it are my own. I confirm that:

- This work was done wholly or mainly while in candidature for a research degree at this University.
- Where any part of this thesis has previously been submitted for a degree or any other qualification at this University or any other institution, this has been clearly stated.
- Where I have consulted the published work of others, this is always clearly attributed.
- Where I have quoted from the work of others, the source is always given. With the exception of such quotations, this thesis is entirely my own work.
- I have acknowledged all main sources of help.
- Where the thesis is based on work done by myself jointly with others, I have made clear exactly what was done by others and what I have contributed myself.

Signed:

Date:

UNIVERSITY OF TRENTO

Abstract

Department of Physics

Doctor of Philosophy

Intermodal four wave mixing for heralded single photon sources in silicon

by Stefano SIGNORINI

High order waveguide modes are nowadays of great interest for the development of new functionalities in photonics. Because of this, efficient mode couplers are required. In this thesis a new strategy for mode coupling is investigated, based on the interference arising from two coherent tilted beams superimposed in a star-coupler. Handling the high order modes allows to explore new processes within the photonics platform, as the intermodal four wave mixing. Intermodal four wave mixing is a new nonlinear optical process in waveguide, and it is here demonstrated on a silicon chip. Via intermodal four wave mixing it is possible to achieve a large and tunable frequency conversion, with the generation of photons spanning from the near to the mid infrared. The broadband operation of this process is of interest for the field of quantum photonics. Single photon sources are the main building block of quantum applications, and they need to be pure and efficient. Via intermodal four wave mixing, it is here demonstrated the generation of single photons above 2 μm heralded by the idler at 1.26 μm. Thanks to the discrete band phase matching of this nonlinear process, high purity single photons without narrow band spectral filters are demonstrated. Intermodal four wave mixing enables a new class of classical and quantum sources, with unprecedent flexibility and spectral tunability. This process is particularly useful for the developing field of mid infrared photonics, where a viable integrated source of light is still missing.

Contents

Chapter 1

Multimode silicon photonics

Since the 60s, silicon has covered a central role in the technological development of modern society. Thanks to the abundance and good electrical properties of this material, the ultra large scale integrated microelectronics has been possible and has experienced an exponential performance increase and a widespread diffusion all across the different application markets. In the last fifty years silicon devices boosted the technological innovations, making accessible to a wide public high speed communication and and high frequency computing. Behind this success, there are the low costs and the huge research in complementary metal oxide semiconductor (CMOS) technology, which satisfied the continuously increasing demand of computational power and data rate traffic. Nowadays, microelectronics is facing a fundamental physical limit both in terms of minimum feature size and performance; these slow down a further development of the technology, despite the increasing demand of data bandwidth and operation frequency. A higher bandwidth would induce stronger parasitic effects in the metallic interconnects, with unacceptable signal losses and power dissipation [1]. In order to meet the data rate demand, a possible solution is to change the information carrier: photons instead of electrons. This motivates integrated photonics, with silicon the best ally for its widespread diffusion. With the pioneering work of Soref and Lorenzo [2], silicon was demonstrated to be a viable material for integrated optics in the telecommunication band, with promising perspectives for the integration of both optics and electronics on the same chip. The good optical properties, the already mature CMOS technology and the electronics compatibility, make silicon the most viable platform for the development of integrated photonics, which is currently revolutionizing the fields of telecommunication, computing, sensing and others. Silicon photonics can rely on years of microelectronics research, exploiting its dense integration and cheap mass-fabrication to bring optical circuits in the next generation devices [3]. The band gap of silicon (~1.1 eV), which makes it transparent in the spectral range used for optical transport (1.3 - 1.6 µm), explains the focused attention to the applications in telecommunication and computation. However, silicon photonics not only fits well with electronics, but also opens new perspectives with unprecedent functionalities in on-chip sensing and quantum technologies. The success of silicon in photonics is also related to its oxide, silica. Silica is used as cladding material in silicon photonics and the availability of silicon-on-insulator (SOI) wafer technology [4] makes SOI the paradigm for micro-fabrication. Silicon dioxide, with its lower refractive index (~1.45 at 1.55 µm wavelength), is used as the cladding surrounding the silicon core at a higher refractive index (~3.48 at 1.55 µm), as sketched in Fig. 1.1.

The large refractive index contrast ensures the guiding of light inside the core by means of the total internal reflection occurring at the interface between the core and the cladding [5]. This is the working principle of the optical waveguide, the

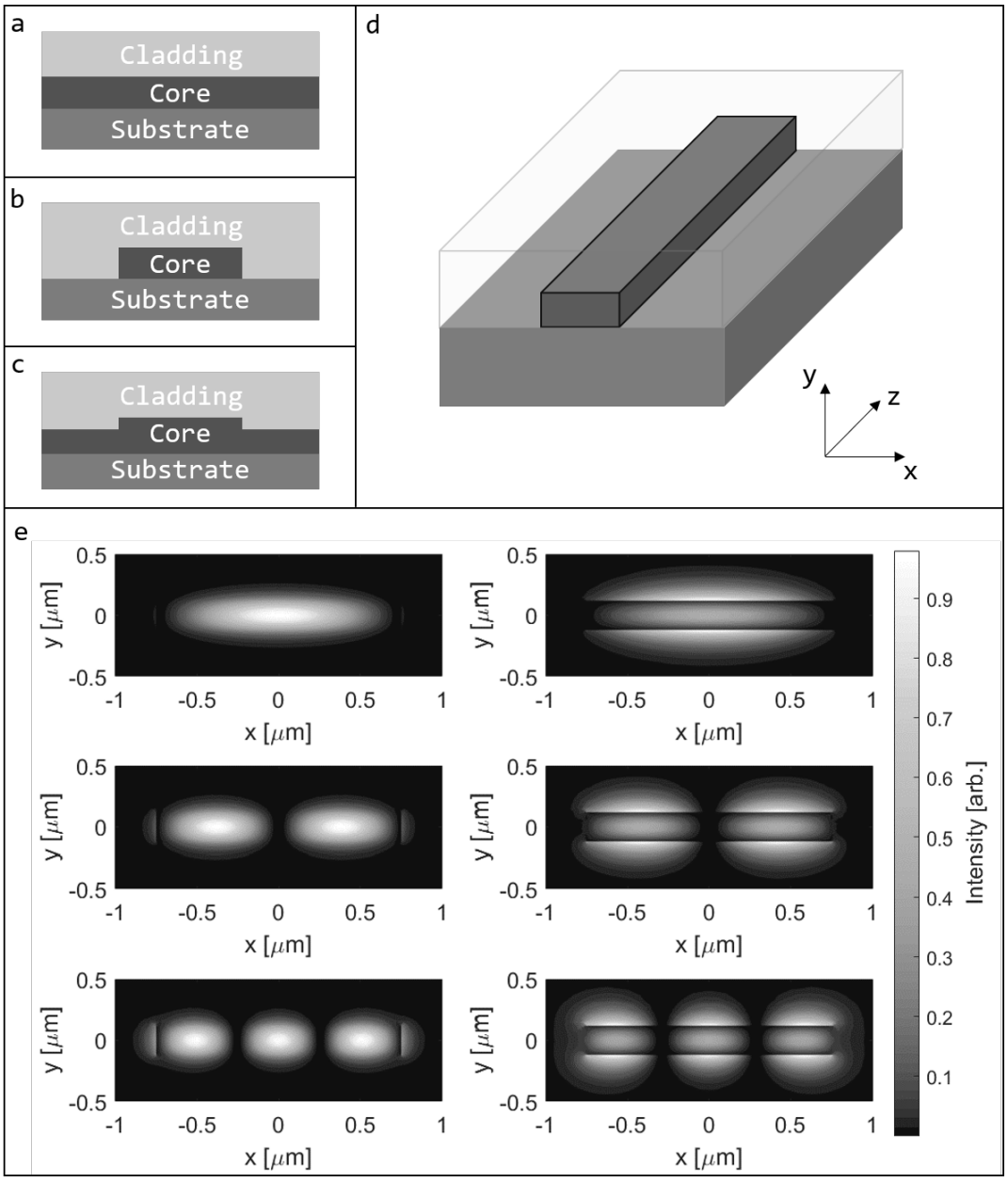

FIGURE 1.1: a) Cross section of a planar waveguide. b) Cross section of a channel waveguide. c) Cross section of a rib waveguide. d) 3D rendering of a channel waveguide, with the reference frame. e) First three modes in a channel waveguide for transverse electric (TE) (left column) and transverse magnetic (TM) (right column) polarization.

fundamental building block of integrated photonics. Thanks to the high confinement in the silicon core, the silicon waveguides have small cross section and are named silicon optical wires. Here, it is possible to achieve unprecedent high optical intensities, accessing nonlinear optical processes with low pump powers. Therefore, integrated nonlinear optical devices enabled on-chip all-optical processing such as filtering [6], wavelength conversion [7] or signal switching [8]. During the years, several devices followed the introduction of the waveguide, with increasing complexity and capabilities. Resonators, interferometers, couplers and many other micron-size

structures have been demonstrated, which allow fabricating complex and performing photonic integrated circuits. The number of integrated functions and devices is continuously increasing, as for the successful path of microelectronics. Even if the photonics technology is not ready for the widespread diffusion of optics, this platform could even surpass the achievements of microelectronics, exploiting possibilities that are accessible only through light-matter interaction. In particular, nonlinear optics opened a world of new functionalities that standard technologies based on electronics could not even imagine. The access to on-chip nonlinear phenomena is possible thanks to the waveguide technology, which guarantees a much higher optical intensity with respect to bulk or fiber optics, lowering the power requirements and making nonlinearities suitable for an integrated perspective [9]. Silicon exhibits a high nonlinear index with respect to other CMOS materials, making this material the best choice for the nonlinear applications in the telecommunication spectral window [10]. Nonlinear applications range from classical and quantum light generation to wavelength conversion, from sensing to all optical signal processing. The achievements in nonlinear silicon photonics boosted the growth of new fields of research, like mid infrared (MIR) photonics and quantum photonics. MIR photonics motivated much efforts in its development since it offers the unique opportunity to access the fingerprint region of several molecules, with potential applications in gas, biochemical and environmental sensing [11]. Moreover, the MIR (from 2 μm to 20 μm) exhibits two atmospheric windows suitable for astronomy and communication [12]. The great opportunities offered by the MIR spectral range have to face the fundamental limitation imposed by the transparency windows of the involved materials: silicon is transparent up to 8 μm, while silica has negligible absorption up to 2 μm. This motivates new researches on materials and structures to permit MIR photonics [12]. Another crucial point in MIR photonics is the lack of integrated sources and detectors for the MIR light. Currently wavelength conversion in nonlinear bulk or integrated devices appears to be a possible solution [13].

The same close interaction with nonlinear integrated optics is driving the research of integrated quantum light sources, a hot topic in photonics. Quantum photonics is becoming a reality thanks to the huge worldwide investments aimed at making quantum physics the main enabler of the next technological revolution. Photons are ideal q-bits, the carriers of the quantum information, since they weakly interact with the environment, move at the speed of light and can take advantage of the already mature optical communication infrastructure [14]. The vision is to develop an integrated quantum photonic chip, where all the building blocks required for the full processing of the quantum states of light are present [15]. In particular, three main components are: the source, the manipulation circuit and the detector of the quantum states. While the manipulation of the quantum states of light has reached good levels, a viable solution for the integration of both the source and the detection stages is still missing [16, 17]. For example, one of the possibilities currently investigated for the source of quantum states is based on parametric processes, which are used to create entangled or uncorrelated photon pairs [18]. In particular, of great interest is the on-chip production of single photons, which can be performed through heralded single photon generation, which is based on an uncorrelated pair of photons where one photon is used to certify the generation of the pair, while the other one is free to propagate in the quantum chip for processing [19].

Interestingly, most of linear and nonlinear silicon photonics developed on a single mode platform, thus considering high order waveguide modes as something

to be avoided. In fact, if higher order modes are supported by the optical waveguide, the information carried by the single mode can be lost through scattering on these modes. Because of this, a single mode architecture guarantees a better stability and reproducibility of the devices. Here, I want to show that high order modes are an opportunity for some applications. If higher order modes are treated properly, they constitute a new degree of freedom for the design of photonic devices. In fact, optical telecommunication, computing and signal processing have to handle an extremely large amount of data, with data rates that are rapidly increasing. To handle such a huge amount of data, dense wavelength division multiplexing (DWDM) is used. DWDM encodes the information in different wavelengths, thus using several communication channels on the same optical fiber. In addition, high order optical modes, which are orthogonal and not interacting, can be combined with DWDM to improve even more the capacity of the single fiber. The technology which exploits modes to multiplex data is called mode division multiplexing (MDM). Because of this, large interest in photonics is devoted to the implementation of optical devices able to use the higher order modes in integrated optical structures. In particular, research is looking for low dimensions, low crosstalk, low losses and large number of modes. In **chapter 2** of this thesis, I investigated a new approach to optical mode coupling based on the interference pattern arising from two superimposed tilted coherent beams. In order to prove the feasibility of the idea, I initially validated the approach through a free space experiment. Then, I studied through numerical simulations an integrated device based on this mode coupling strategy. The integrated interferometer promises small chip size, large number of data channels, unprecedent bandwidth and sufficient crosstalk, suggesting a new solution to the already well developed optical coupling technology.
Up to now, nonlinear optics has relied on single mode waveguides. This because single mode waveguides, with their small cross section, are the most suited structures to get the large intensity required to induce the nonlinearities. On the contrary, large multimode waveguides require larger optical powers to achieve the same nonlinear efficiencies. However, the introduction of higher order modes allows to improve the control over the efficiency and spectral properties of the nonlinear processes, providing at the same time an interesting connection with multimode optical processing. An example is the intermodal four wave mixing (FWM): a third order nonlinear optical process in which two photons coming from a powerful input beam are converted into two new photons at different frequencies. FWM is the most studied and exploited nonlinear process in silicon photonics, and it is usually used in its intramodal configuration, i.e. using only one waveguide mode. On the contrary, intermodal FWM is based on the excitation of higher order modes, enabling functionalities that are not easily accessible to single mode FWM. Thanks to intermodal FWM it is possible to generate light with controllable wavelength and bandwidth, enabling spectral conversions which can link the near infrared with the mid infrared part of the spectrum. These results are extremely attractive for integrated photonics, which looks for devices able to perform all optical wavelength conversion for signal processing and that can boost the currently developing field of mid infrared photonics, where sources and detectors of light can benefit of the spectral translation capability of intermodal FWM. In **chapter 3** of this thesis, I discuss intermodal FWM in silicon waveguides, which is the first experimental demonstration of this nonlinear process in an integrated platform. I report theory, simulations and measurements showing spectral conversions larger than 900 nm and tunable all over the telecom band. Intermodal FWM is also much more flexible in terms of phase matching and fabrication tolerance with respect to intramodal FWM.

For quantum applications, FWM can be used as a source of correlated photon pairs, that can be engineered as entangled or single photon states. In particular, the opportunity to generate quantum light in the mid infrared is appealing for applications in quantum sensing, which aims at probing with unprecedent sensitivity the fingerprint of gas molecules, or in quantum communications, which find in the MIR several transparent windows of the atmosphere for low loss free space data exchange. Intermodal FWM is a viable tool for controllable and broadband quantum light generation. In fact, one of the most detrimental issue of quantum photonics is the presence of Raman noise, which is at a well defined wavelength from the pump and that can be avoided by generating the quantum light far from its peak. Moreover, the discrete band generation of intermodal FWM can be used to create sources of heralded single photons which do not require post-filtering of the single photons. In **chapter 4** of this thesis, I discuss spontaneous intermodal FWM as a source of heralded single photons, with the single photon generated in the mid infrared. In this way, we want to exploit all the advantages of intermodal FWM, demonstrating the first integrated source of mid infrared heralded single photons. In the same chapter, I also discuss a new strategy for the purification of the biphoton wave function, exploiting the different group velocities of the higher order modes to achieve unprecedent purities of the generated single photons, whose theoretical estimation is around 99%.

In order to provide the basic tools for the understanding of multimode photonics, I introduce in **chapter 1** the basics of multimode waveguides, describing the modes formation and propagation, with a particular focus on the mechanisms related to their excitation.

1.1 Basics on multimode photonics

The fundamental building block of silicon photonics is the optical waveguide. Exactly like a metallic wire used to carry the electric current in a microelectronic chip, the optical waveguide interconnects the devices in an optical chip. An optical waveguide can be fabricated with different cross sections and geometries, and it can be basically separated into three parts: the core, the cladding and the substrate, as shown in Fig. 1.1.

The most widely used cross-sections are the channel and rib geometries, that exhibit slightly different confining properties. The core is made with a higher refractive index material than the one of the substrate and cladding materials, in order to have an index mismatch at the core borders. In fact, the light confinement in a waveguide arises due to the total internal reflection occurring at the interface between the core and the surrounding materials [5]. A waveguide, depending on its core area, can support one or more modes, where the mode is a solution of the Maxwell equations for the specific waveguide geometry. Each optical mode corresponds to a spatial distribution of optical energy whose lineshape does not change along the waveguide. In the following, the basics of the optical waveguide will be discussed, considering silicon as the core material and silica as the cladding and substrate material. Then, the attention will be focused on the multimode regime.

1.1.1 The optical waveguide

Light in a waveguide can travel exciting different modes, where each mode is a solution of the Helmholtz wave equation in the guiding geometry [5]. The Helmoltz equation is

$$\left(\nabla_{xy}^2 + \beta_m^2\right) e_m(x,y) = \frac{\omega^2}{c^2} n^2(x,y) e_m(x,y), \tag{1.1}$$

where $m = 1, 2, ..,$ β_m is the propagation constant of the m-th order waveguide mode, $e_m(x,y)$ is the electric field profile, ω the frequency of the optical wave, n the refractive index spatial distribution, c the light velocity. The propagation constant, which appears in the electric field $e_m(x,y,z;\omega) \simeq e_m(x,y)e^{iz\beta_m(\omega)}$, is a peculiar parameter for the description of the propagation of light in guiding structures and it is written as $\beta_m = \frac{\omega}{c} n_{eff,m}$; n_{eff} is the effective refractive index, which is a complex quantity that, with its real part, gives information on the phase acquired by the wave in its propagation, while its imaginary part is proportional to the losses experienced through the waveguide. In fact, the field intensity decreases while propagating along the waveguide as $e^{-\alpha_m z}$, where $\alpha_m = \frac{2\omega}{c} Im(n_{eff,m})$ is the attenuation coefficient. Each mode experiences a different effective index depending on the waveguide geometry and light polarization. This dependence is reflected also on the confinement of the optical mode, that can be quantified with the confinement factor Γ_{conf} [5],

$$\Gamma_{conf} = \frac{\iint_{core} n^2(x,y)|e_m(x,y)|^2 \mathrm{d}x\mathrm{d}y}{\iint_{A_\infty} n^2(x,y)|e_m(x,y)|^2 dxdy} \tag{1.2}$$

where $n(x,y)$ is the refractive index profile of the waveguide and the two integrals are performed over the core area (numerator) and the infinite plane A_∞ (denominator). As the core reduces in size, the optical mode is less and less confined, increasing its interaction with the low refractive index cladding. This results in a lower effective refractive index as the mode spread out from the core. Moreover, reducing Γ_{conf}, the optical modes approach the diffraction limit, losing the confinement. Considering the channel or rib cross-sections, the number of supported modes (with fixed polarization) is approximately $\frac{4}{\pi}\frac{wh}{\lambda^2}\mathrm{NA}^2$ [5], with w and h the width and height of the waveguide and $\mathrm{NA} = \sqrt{n_{core}^2 - n_{clad}^2}$ the numerical aperture. The modes depend also on the polarization, that can be transverse electric (TE), i.e. with the dominant electric field component along the x direction (reference frame in Fig. 1.1), or transverse magnetic (TM), i.e. with the dominant electric field along the y direction. With the typical geometries involved in integrated photonics, where $h < w$, the TM modes are less confined with respect to TE polarization. All these parameters (wavelength, polarization, waveguide geometry, core and cladding materials) influence the effective refractive index of the optical modes, which, in the case of micron-size structures, is largely dominated by the geometric dispersion rather than by the chromatic one. As a result, it is possible to engineer the dispersion of the waveguide modes simply by changing the geometrical dimensions of the waveguide. In order to carefully design the integrated structures with the desired dispersion properties, it is useful to expand the propagation constant β_m of the m-th order mode around a central frequency ω_0 [20]:

$$\beta_m(\omega) = \sum_q \frac{1}{q!} \beta_m^{(q)} (\omega - \omega_0)^q \tag{1.3}$$

where $\beta_m^{(j)} = \frac{d^j \beta_m}{d^j \omega}$ are the higher order dispersion coefficients ($j = 1, 2, ..$). Each beta coefficient provides a different information about the dispersion properties of the waveguide. For example, the first order coefficient gives directly the inverse of the group velocity v_g

$$\beta_m^{(1)} = \frac{d\beta_m}{d\omega} = \frac{n_{g,m}}{c} = v_g^{-1} \tag{1.4}$$

where n_g is defined the group index. The second order term $\left(\beta_m^{(2)}\right)$ is called group velocity dispersion (GVD). GVD gives information on how the dispersive character of the medium affects the pulse propagation due to the different group velocities experienced by each frequency component. From Eq. (1.4) it is also clear that different modes propagate with different group velocities in the same waveguide, making the multimode behaviour even more tricky. Another important parameter is the effective area A_{eff}, defined as

$$A_{eff,m} = \frac{\left(\iint_{A_\infty} |e_m|^2 dx dy\right)^2}{\iint_{A_0} |e_m|^4 dx dy} \tag{1.5}$$

where A_∞ is the infinite plane and A_0 is the core area. The effective area, also known as effective mode area, scales proportionally with the confinement factor Γ and inversely with the effective index. In fact, as also shown in Fig. 1.2, as the mode order increases, the effective index decreases and the effective area increases.

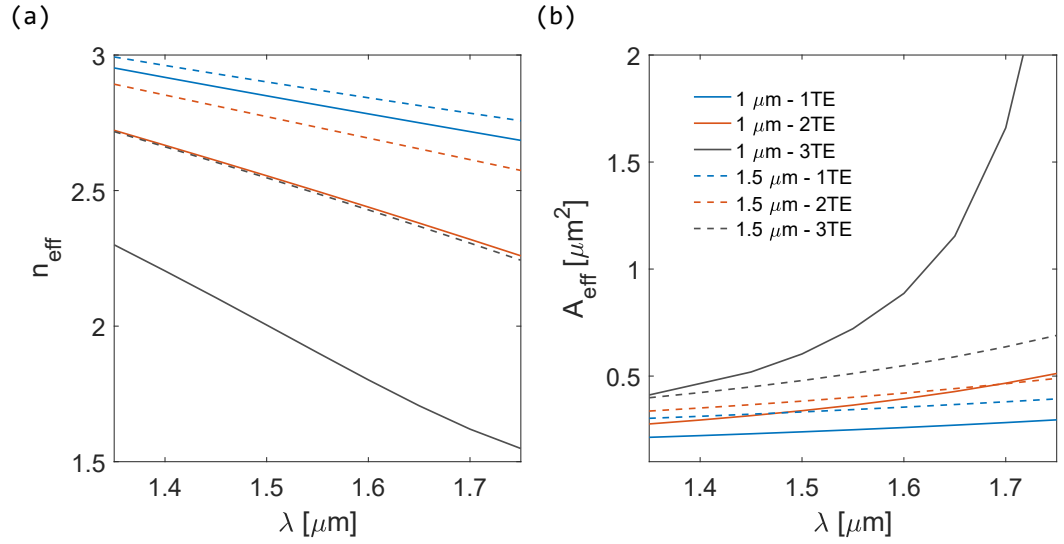

FIGURE 1.2: Simulation of the effective index and effective area for the first three TE modes in a channel waveguide of 243 nm height and 1 or 1.5 μm width (see legend). (a) Effective index as a function of the wavelength. (b) Effective area as a function of the wavelength.

When dealing with micron-size devices, the fabrication quality is of crucial importance in order to achieve the expected performance. The mature CMOS technology guarantees 140 nm of minimum feature size with a tolerance of few nm. Higher resolutions can be achieved by electron beam lithography, around tens of nanomenters, and with lower side walls roughness. Lower roughness means less scattering on the waveguide borders, resulting in lower propagation losses. In this thesis work, the devices, with channel or rib geometries, have been defined by 365

nm lithography, with 3 μm silica as the substrate, 900 *nm* silica deposited via plasma-enhanced chemical vapor deposition as the cladding, and silicon as the core material, with variable thickness depending on the cross-section of the waveguide. The samples here used have been fabricated by the Centre for Materials and Microsystems of Bruno Kessler Foundation (Trento, Italy).

1.1.2 Light coupling and propagation in multimode waveguides

In this section I follow the formalism used by Chang [21] [1].
Optical waveguides can support one or more waveguide modes depending on their cross section and refractive index of the materials used in their fabrication[2]. When light has to be loaded inside the waveguide structure, it can in principle excite all the guided modes supported by the waveguide. Thus these modes propagate together inside the optical device. Let us consider the excitation of the guided modes in a channel waveguide by means of free-space beams or optical fibers, which illuminate the input facet of the waveguide. The modes of a waveguide are solutions of the wave equation Eq. (1.1), and form a complete set. As a consequence, any electromagnetic field incident at the facet of the waveguide can be expressed as a linear combination of the modes supported by the waveguide, with the expansion coefficient of each mode proportional to the power coupled on that specific mode. Let us consider the input facet of the waveguide at $z = 0$ and the waveguide extending along the positive z axis, as in Fig. 1.3. Assume that a beam of laser light, arriving from $z < 0$, is impinging on the facet at $z = 0$. Given e_l the radiation field of the laser, the following relation holds

$$\mathbf{e}_l(x, y) = \mathbf{e}_x(x, y) + \mathbf{e}_y(x, y), \tag{1.6}$$

with $\mathbf{e}_{x/y}$ the transverse electric/magnetic radiation field. At $z < 0$, neglecting reflection and diffraction at the waveguide facet ($z = 0$), $\mathbf{e}_l$ consists only of the incident laser radiation. At $z \geq 0$, e_l consists of the guided waveguide modes and the field radiated in the cladding $e_{x,rad}$ and $e_{y,rad}$.

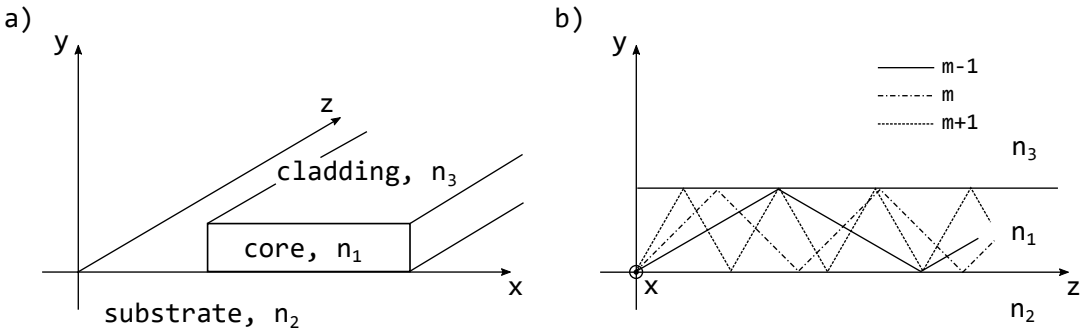

FIGURE 1.3: a) Schematic of the waveguide cross section and relative reference frame. b) Ray optics representation of mode propagation in dielectric waveguides. The higher the order mode, the higher the number of reflections at the boundaries of the core. In the legend is indicated the relative order mode of the three propagating modes drawn in the form of rays.

[1] Please notice that in this thesis the reference frame has been changed with respect to what used in [21], inverting the x and y axes.

[2] For an introduction on the formation of optical modes in waveguide, see Appendix A.

At $z = 0$ the field amplitudes e_x, e_y, for the TE and TM modes can be written as

$$e_x(x,y) = \sum_m A_m \psi_{x,m}(x,y) + e_{x,rad}, \tag{1.7a}$$

$$e_y(x,y) = \sum_m B_m \psi_{y,m}(x,y) + e_{y,rad}, \tag{1.7b}$$

with $\psi_{p,m}$ the field profile of the waveguide mode m with polarization p (x for TE and y for TM). The A_m and B_m coefficients are proportional to the amount of excitation of each mode, and can be calculated as

$$|A_m|^2 = \frac{\left| \int_{-\infty}^{\infty} \mathrm{d}x \int_{-\infty}^{\infty} \mathrm{d}y \left[e_x \psi_{x,m}^* \right] \right|^2}{\left[\int_{-\infty}^{\infty} \mathrm{d}x \int_{-\infty}^{\infty} \mathrm{d}y \left| \psi_{x,m} \right|^2 \right]^2}, \tag{1.8a}$$

$$|B_m|^2 = \frac{\left| \int_{-\infty}^{\infty} \mathrm{d}x \int_{-\infty}^{\infty} \mathrm{d}y \left[e_y \psi_{y,m}^* \right] \right|^2}{\left[\int_{-\infty}^{\infty} \mathrm{d}x \int_{-\infty}^{\infty} \mathrm{d}y \left| \psi_{y,m} \right|^2 \right]^2}, \tag{1.8b}$$

where $\int_{-\infty}^{\infty} \mathrm{d}x \int_{-\infty}^{\infty} \mathrm{d}y \, e_p \psi_{p,m}^*$ is the *overlap integral*, quantifying the field matching between the incident radiation and the $\psi_{p,m}$ mode. In the following, the field radiated in the cladding will be neglected, since it radiates away after a short distance and it is not of interest here. Related to the overlap integral is the *power overlap integral*, which quantifies the normalized amount of power coupled to the m-th mode given the input field profile e_p. The power overlap integral is written as

$$\Gamma_{p,m} = \frac{\left| \int_{-\infty}^{\infty} \mathrm{d}x \int_{-\infty}^{\infty} \mathrm{d}y \left[e_p \psi_{p,m}^* \right] \right|^2}{\left(\int_{-\infty}^{\infty} \mathrm{d}x \int_{-\infty}^{\infty} \mathrm{d}y \left| \psi_{p,m} \right|^2 \right) \left(\int_{-\infty}^{\infty} \mathrm{d}x \int_{-\infty}^{\infty} \mathrm{d}y \left| e_p \right|^2 \right)} \tag{1.9}$$

with $p = x, y$. $\Gamma_{p,m}$ does not takes into account coupling losses and it goes from 0 to 1; for example, if only the first TE order mode is excited in the waveguide, then $\Gamma_{x,1} = 1$ and $\Gamma_{x,n} = 0$ with $n > 1$. This parameter is quite useful since it provides an intuitive information about the coupling efficiency for separate modes given the same input radiation profile. Normalizing properly the input field e_p and the waveguide modes $\psi_{p,m}$ it is possible to rewrite Eq. (1.7) using the $\Gamma_{p,m}$'s as the expansion coefficienst, such that

$$e_x(x,y) = \sum_m \sqrt{\Gamma_{x,m}} \psi_{x,m}(x,y), \tag{1.10a}$$

$$e_y(x,y) = \sum_m \sqrt{\Gamma_{y,m}} \psi_{y,m}(x,y), \tag{1.10b}$$

where the radiative modes have been explicitly neglected, and $\int_{-\infty}^{\infty} \mathrm{d}x \int_{-\infty}^{\infty} \mathrm{d}y |e_p|^2 = \int_{-\infty}^{\infty} \mathrm{d}x \int_{-\infty}^{\infty} \mathrm{d}y |\psi_{p,m}|^2 = 1$ ($p = x, y$). With this normalization it results that $\sum_m \Gamma_{p,m} = 1$, as expected from the definition of the power overlap integral.
The overlap integral or the power overlap integral are powerful tools for the description and simulation of the higher order mode coupling techniques. In a more naive interpretation, the overlap integral quantifies how much the two field profiles involved in the calculation are similar, with the maximum of the overlap integral when the two profiles are identical. This means that the best coupling of a certain waveguide mode is achieved when the field profile provided at the input of the

waveguide resembles the profile of that mode as much as possible. This consideration is true because the tangential component of the electric field is continuous across the interface, as stated by the Maxwell boundary condition for the radiation field at the interface between two media [22].

When dealing with abruptly ended optical waveguides, a sudden change in the refractive index is experienced by the propagating mode (from 3.48 to 1 with Si/air interface at 1550 nm), giving rise to a non negligible reflection. This gives rise to a Fabry-Perot oscillation [23] in the waveguide transmission, due to the light being continuously reflected back and forth at the input and output facets of the waveguide. An example is shown in Fig. 1.4a. For a particular propagating mode order m, with wavelength λ at position z, the Fabry-Perot response $h_m(\lambda, z)$ is [24]

$$h_m(\lambda, z) = \frac{(1 - R_m)^2 e^{-\alpha_m z}}{\left(1 - \widetilde{R}_m\right)^2 + 4\widetilde{R}_m \sin^2(\Phi_m/2)}, \tag{1.11}$$

with $\Phi = 2k_m L + \Phi_0$. Φ is the phase acquired in one round trip and Φ_0 the phase added at each facet reflection, $\widetilde{R}_m = R_m e^{-\alpha z}$, R_m is the reflection coefficient at the waveguide/air interface calculated according to the Fresnel formula as $R = (n_{eff,m} - 1)^2/(n_{eff,m} + 1)^2$. Since many modes can co-propagate along the waveguide, as shown in Fig. 1.4, one has to consider their coherent superposition, and the resulting field profile at wavelength λ propagating in the waveguide, with polarization TE or TM, can be expressed by

$$\mathbf{e}_{wg}(\lambda; x, y, z) = \sum_m \sqrt{\Gamma_m(\lambda)}\sqrt{h_m(\lambda, z)}\mathbf{e}_m(\lambda; x, y), \tag{1.12}$$

where m runs over all the modes supported by the waveguide. In order to simplify the analysis, it is assumed that the mode profiles $\mathbf{e}_m(\lambda; x, y)$ are independent on λ, i.e. $\mathbf{e}_m(\lambda; x, y) \equiv \mathbf{e}_m(x, y)$.

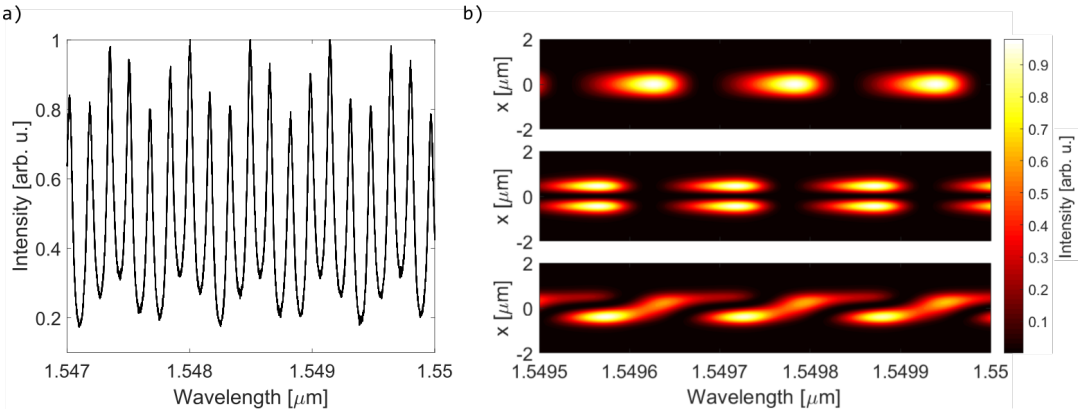

FIGURE 1.4: a) Measured spectrum of the transmitted intensity for the first TE order mode in a SOI rib waveguide with 600 nm width and 2.05 mm length. The Fabry-Perot fringes are clearly visible. b) Simulated intensity profiles for a SOI rib waveguide with only the 1TE mode (top), only the 2TE (middle) mode and with both 1TE and 2TE propagating (bottom) as a function of the wavelength. The profile in the bottom figure arises from the interference between the two modes. These plots have been simulated through Eq. (1.12), with $z = L$, $L = 2.05$ mm and a width of 1.4 μm.

1.1.3 The directional coupler

Controlling the light propagating inside an optical waveguide is required for almost all the applications involving integrated photonic circuits. This can be achieved directly on-chip using a device called directional coupler (DC). A DC consists of two parallel waveguides with a small gap in between, as shown in Fig. 1.5a, where a rib DC with two equal waveguides is shown. In fact, when two waveguides are placed sufficiently close such that the evanescent field from one overlaps with the field of the other, a power exchange between the two waveguides occurs. DCs can be used as power dividers, such as the 3-dB coupler simulated in Fig. 1.5c, which equally splits the power from the input port into two outports. When the two waveguides have different widths, like in Fig. 1.5b, the device is called an asymmetric directional coupler (ADC). The ADC is used as a mode coupler [25]. In fact, when a single mode waveguide is placed close to a multimode waveguide, it is possible to excite selectively one of the supported higher order modes. This is shown in the simulation reported in Fig. 1.5d, where an ADC is used to transfer all the input power into the second order mode of the multimode waveguide. DCs and ADCs can also be used in the opposite direction, i.e. to bring the power coming from more waveguides into a single output port, or to extract selectively the power carried by a certain waveguide mode.

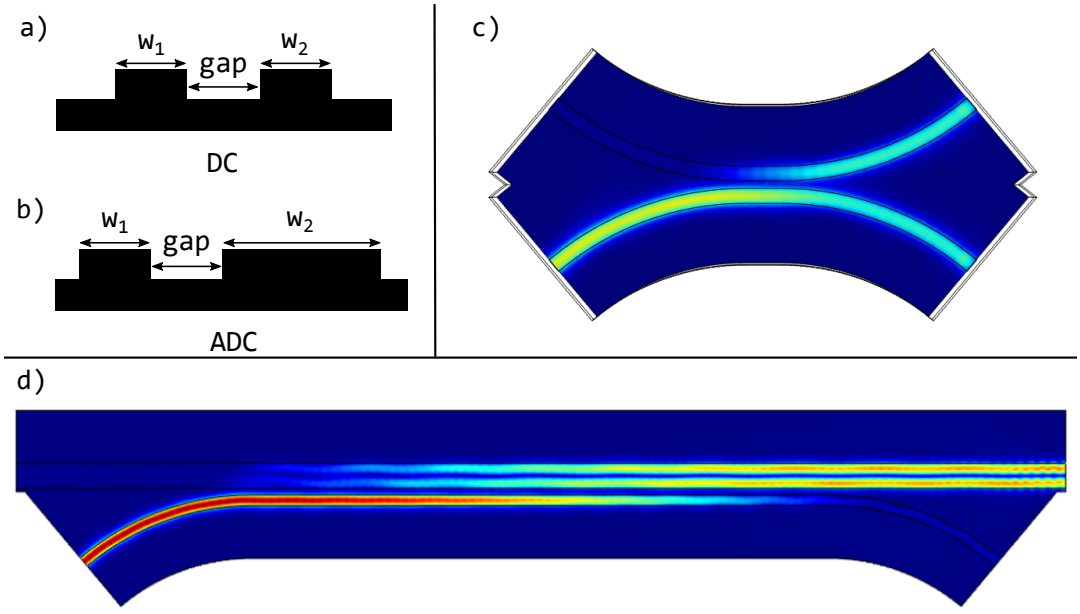

FIGURE 1.5: a) Directional coupler. b) Asymmetric directional coupler. c) Simulation of a 3-dB directional coupler. d) Simulation of an asymmetric directional coupler for the 2nd order coupling.

The working principle, for both the DC and ADC, can be explained by the coupled-mode theory (CMT). CMT is an approximate theory which assumes that the waveguides are weakly coupled [5]. Consider the geometry in Fig. 1.6a, where two planar waveguides, with thickness h, are placed close with a gap of $2a$. The upper waveguide has refractive index n_1, the lower waveguide has n_2, while the surrounding medium has refractive index n, such that $n < n_1 \sim n_2$. Let us label the waveguide with refractive index n_1 "waveguide 1" and the other one "waveguide 2". The CMT assumes that the coupling affects only the amplitude of the modes propagating in the two waveguides, without affecting their spatial profiles or propagation

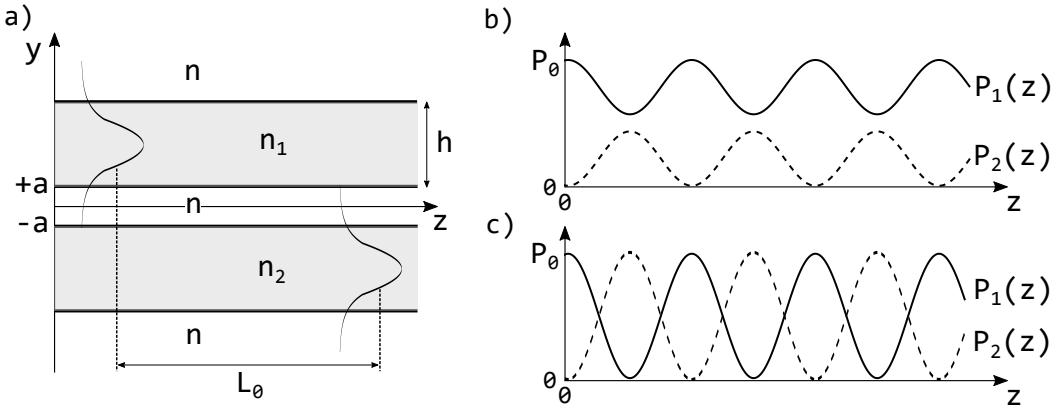

FIGURE 1.6: a) Schematic of the DC with equal waveguides of thickness h and gap $2a$. The refractive indexes are n_1, n_2 and n for the upper waveguide, the lower waveguide and the cladding, respectively. The upper waveguide is initially excited, and after a propagation length L_0 the power is completely transferred to the other waveguide. b) Power in the two coupled waveguides as a function of the propagation length. Here the two waveguide are not equal and the total power transfer is not achieved. c) Power in the two coupled waveguides as a function of the propagation length. Here the two waveguide are equal and the total power transfer is achieved.

constants. As a result, the amplitudes of the two waveguides are a function of z, the position along the propagation direction. The fields in the two waveguides can thus be written as

$$e_1(y,z) = a_1(z)u_1(y)\exp(-i\beta_1 z), \tag{1.13a}$$

$$e_2(y,z) = a_2(z)u_2(y)\exp(-i\beta_2 z). \tag{1.13b}$$

The CMT aims thus at the calculation of $a_1(z)$ and $a_2(z)$. The two waveguides interact through the corresponding evanescent tails, which provide the mutual excitation of the field in the opposite waveguide. This power exchange is modelled by the coupled differential equations for $a_1(z)$ and $a_2(z)$ [5]:

$$\frac{da_1}{dz} = -ic_{21}\exp(i\Delta\beta z)a_2(z) \tag{1.14a}$$

$$\frac{da_2}{dz} = -ic_{12}\exp(i\Delta\beta z)a_1(z) \tag{1.14b}$$

where $\Delta\beta = \beta_1 - \beta_2$ quantifies the phase mismatch per unit length, and

$$c_{21} = \frac{1}{2}(n_2^2 - n^2)\frac{k_0^2}{\beta_1}\int_a^{a+h} u_1(y)u_2(y)dy, \tag{1.15a}$$

$$c_{12} = \frac{1}{2}(n_1^2 - n^2)\frac{k_0^2}{\beta_2}\int_{-a-h}^{-a} u_2(y)u_1(y)dy, \tag{1.15b}$$

are the coupling coefficients. Assuming that waveguide 1 is excited with $a_1(0)$ amplitude and that $a_2(0) = 0$, then solving Eq. (1.14) yields

$$a_1(z) = a_1(0)\exp\left(\frac{i\Delta\beta z}{2}\right)\left(\cos(\xi z) - i\frac{\Delta\beta}{2\xi}\sin(\xi z)\right) \tag{1.16a}$$

$$a_2(z) = a_1(0)\frac{c_{12}}{i\xi}\exp\left(-\frac{i\Delta\beta z}{2}\right)(\sin(\xi z)) \tag{1.16b}$$

with

$$\xi^2 = \left(\frac{\Delta\beta}{2}\right)^2 + C^2 \tag{1.17}$$

and $C = \sqrt{c_{12}c_{21}}$. Considering that the optical power is proportional to the modulus squared of the amplitude, it is possible to write the optical powers $P_1(z)$ and $P_2(z)$ circulating in the coupled waveguides as

$$P_1(z) = P_1(0)\left[\cos(\xi z)^2 + \left(\frac{\Delta\beta}{2\xi}\right)^2 \sin^2(\xi z)\right], \tag{1.18a}$$

$$P_2(z) = P_1(0)\frac{|c_{12}|^2}{\xi^2}\sin^2(\xi z). \tag{1.18b}$$

Eqs. (1.18) show that the power is periodically exchanged between the two waveguides, as shown in Fig. 1.6b. When the waveguides are equal, i.e. $\beta_1 = \beta_2$, and $\Delta\beta = 0$, the phase matching condition is achieved, and Eq. (1.18) can be rewritten as

$$P_1(z) = P_1(0)\cos^2(Cz), \tag{1.19a}$$

$$P_2(z) = P_1(0)\sin^2(Cz). \tag{1.19b}$$

Eqs. (1.19) are plotted in Fig. 1.6c, showing that when the two waveguides are equal the power can be completely exchanged between them and the maximum coupling efficiency is possible. The length required to obtain the maximum power transfer is

$$L_0 = \frac{\pi}{2C}. \tag{1.20}$$

When designing a DC aiming at the total power transfer, a coupling length of L_0 has to be used. A 3-dB coupler is obtained with a coupling length of $L_0/2$. In the case of an ADC, thus involving different waveguide widths and spatial modes, it is sufficient to consider the propagation constants β for the corresponding modes and geometries. This means that while in the case of the DC the maximum coupling efficiency is achieved when the two waveguides have the same effective indexes, with the ADC the maximum efficiency is achieved when the first order mode of the single mode waveguide matches the effective index of the higher order mode to be excited in the multimode waveguide. Even though for the ADCs the CMT is more inaccurate than for DCs, it still provides a good approximation to the actual coupling, and it is widely used to design the devices.

Chapter 2

Interferometric mode coupling in silicon waveguides

This section has been largely taken from the work that I presented in Ref. [26].

2.1 Introduction

The main building block of the multimode platform is the mode coupler. When dealing with mode couplers, the main parameters used to characterize their efficiency are the cross talk (XT), that is the ratio between the power in the channel due to the wrong input ports and the power due to the right input port, the excess loss (EL), which is the ratio between the total output power on all the channels and the input power, the bandwidth (BW), measured as the wavelength range over which the XT remains lower than a reference value [27], and the number of channels (N_{ch}), which is the number of modes that can be used for the data transport. Clearly, with the perspective of highly dense on-chip integration, also the footprint becomes crucial when considering the quality of the device. At the moment, three main approaches to mode coupling are developing. The first one is based on multimode interference (MMI), see Fig. 2.1a, where multiple modes are excited in the same waveguide and their interference gives rise to a N-fold self imaging if the propagation length is properly chosen [28, 29]. With the MMI very small size devices can be designed, at the expenses of the insertion losses and the number of channels. The second approach relies on the mode evolution in an adiabatic structure. Here the width of the waveguide is slowly changed in order to couple all the power of the input mode into the target output waveguide mode [30, 31], as shown in Fig. 2.1b, where an example of such structure is proposed. Adiabatic coupling exhibits large footprint but guarantees low cross-talk and losses. The last technique exploits the selective excitation of higher order modes provided by evanescent coupling through ADCs, as in the example in Fig. 2.1c. The ADCs have the advantage of small footprint and easy design, at the expenses of fabrication tolerance, which is critical due to the precise gap and waveguide widths required for the device feasibility [32, 33].

Research in the field of integrated optical interconnects is moving towards the best compromise among the available mode coupling solutions. The final result should combine small footprint, high number of channels, low crosstalk and a bandwidth large enough to match the requirements of DWDM. Up to now, the proposed devices are not able to provide low crosstalk on a large number of channels keeping at the same time a reduced footprint. Within this framework, I studied a new approach to mode coupling, that should guarantee smaller size with respect to standard couplers, with a large number of channels and a much broader bandwidth (>

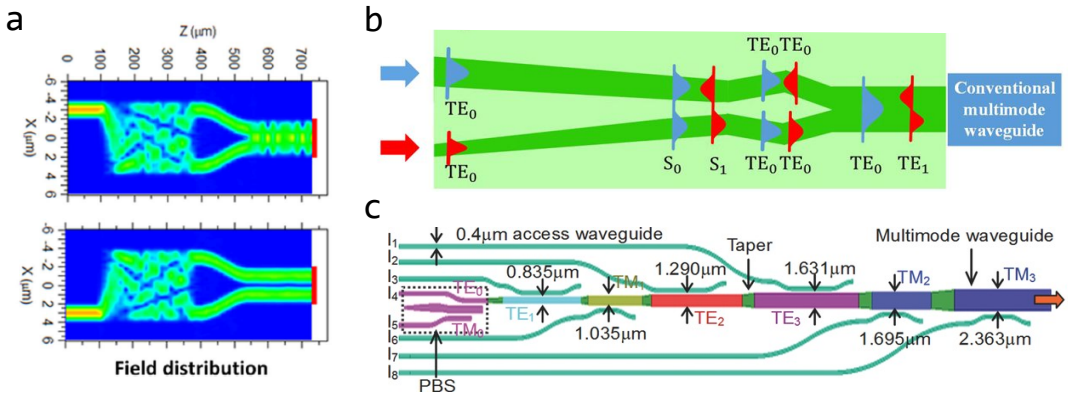

FIGURE 2.1: a) MMI based two mode (de)multiplexer with an y-junction to couple the first (top) or second (bottom) order mode. © 2016 IEEE [29]. b) Adiabatic coupler for the multiplexing of the first or second TE waveguide mode. Reprinted from Ref. [31] under CC BY 2.0. c) (De)multiplexer based on cascaded ADCs, with also a polarization beam splitter (PBS) to enable the simultaneous multiplexing of both TE and TM polarizations. Reprinted from Ref. [32] © 2014 Wiley-VCH.

200 nm) with respect to standard values ($\sim$ 100 nm). This approach to mode coupling takes directly into account the maximization of the overlap integral between the input exciting field and the desired waveguide mode. The input field is constituted by spatial interference fringes, whose period is tuned as close as possible to the period of the electric field lobes characterizing the target waveguide mode. This maximizes the overlap integral and, therefore, the excitation of the selected mode in the multimode waveguide. Moreover, the interferometer, exhibits extremely low crosstalk between even and odd modes. In fact, an odd (even) input profile cannot excite even (odd) modes. Also the fabrication tolerance is expected to be enhanced, since the minimum feature size here required is well above the resolution of standard CMOS fabrication technologies. In order to obtain the suitable interference pattern at the input facet of the multimode waveguide, two coherent tilted beams are superimposed within a planar waveguide region.

As a first step to design an integrated device compatible with the SOI platform, I experimentally investigated a free space implementation of the system in order to validate the principle. In particular, I studied the selection of higher order modes in channel SOI waveguides. After validating the principle, I simulated the integrated version of the device, evaluating the performance of the system and proposing several chip designs for both TE and TM mode coupling.

In this work, Dr. Mattia Mancinelli and Dr. Massimo Borghi supervised the development of the interferometric coupling approach. The samples used have been fabricated by the Centre for Materials and Microsystems of Bruno Kessler Foundation (Trento, Italy).

2.2 Theory

2.2.1 Oblique beams interference

Consider two coherent gaussian oblique beams with wavevectors $\mathbf{k_1}$ and $\mathbf{k_2}$ which form an angle 2θ between them, as in Fig. 2.2b. Let us make the two beams interfere on the waveguide input facet at $z = 0$.

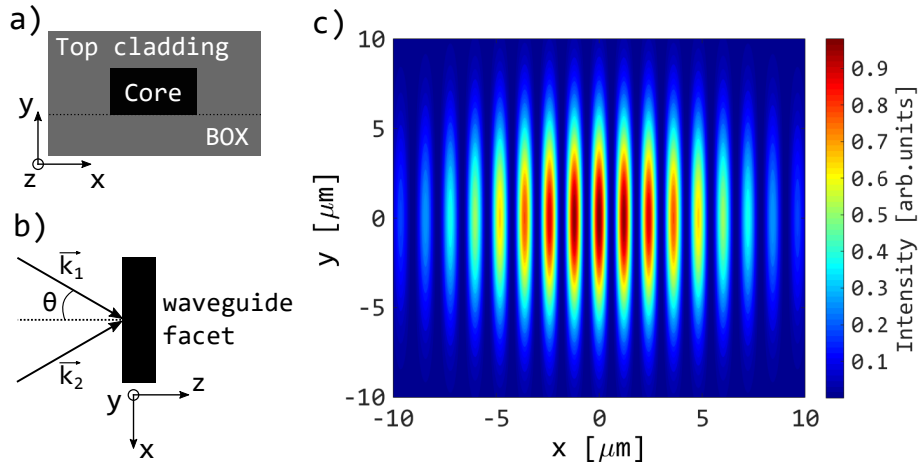

FIGURE 2.2: a) Cross-section of the waveguide used in the experiment. The top cladding is a 900 nm thick SiOx, the BOX is a 3 μm thick silicon dioxide and the core, i.e. the waveguide, is a 245 nm thick silicon. b) Scheme for the two oblique beams reaching the waveguide facet. 2θ is the angle between the beams. c) 2D plot of the simulated interference fringes forming on a screen placed in the (x,y)-plane, where the two tilted gaussian beams interfere. In this simulation a waist of 8 μm for the beams, a wavelength of 1550 nm, transverse magnetic polarization and $\theta = 40^o$ are considered.

The beams are assumed to propagate in the (x,z)-plane and are both polarized in the y-direction. Therefore, the interference pattern occurs along the x direction. Given $\mathbf{r}$ the spatial position and setting $z = 0$, within the Rayleigh range we can approximate the complex electric field amplitudes for the gaussian beams as [5]

$$U_1(x,y) = \sqrt{I_1(x,y)}e^{ik\sin(\theta)x} \tag{2.1}$$

$$U_2(x,y) = \sqrt{I_2(x,y)}e^{-ik\sin(\theta)x}e^{ik\Delta L} \tag{2.2}$$

where $I_1(x,y)$ and $I_2(x,y)$ are the gaussian profile intensities of the two beams, $e^{ik\Delta L}$ is a phase term that accounts for a path length mismatch ΔL between the two beams, $k_1 = k_2 = k = 2\pi n/\lambda$ is the wavevector of the beams and n is the refractive index of the medium where light is propagating with wavelength λ. The total intensity $I(x,y)$ is given by

$$\begin{aligned} I(x,y) &= |U_1(x,y) + U_2(x,y)|^2 = I_1(x,y) + I_2(x,y) \\ &+2\sqrt{I_1(x,y)I_2(x,y)}cos\left[\frac{4\pi n}{\lambda}sin(\theta)x - \frac{2\pi n}{\lambda}\Delta L\right]. \end{aligned} \tag{2.3}$$

$I(x,y)$ exhibits spatial interference fringes along x, with a period δ given by

$$\delta = \frac{\lambda}{2\,n\,sin(\theta)}. \tag{2.4}$$

δ can be changed by means of the θ angle. An example of $I(x,y)$ is reported in Fig. 2.2c, where the interference pattern is simulated for two beams with $\theta = 40^o$, $\lambda = 1.55\,\mu m$ and $n = 1$. The presence of ΔL provides a phase term that makes the interference fringes to experience a spatial shift along the x direction, as the wavelength is changed. Let us note that in the simulations we have used gaussian beams

even for $z = 0$.
A parameter that characterizes the interference is the *visibility* of the fringes. If A denotes the maximum intensity of the fringes and B their minimum intensity, the visibility V is defined as

$$V = \frac{A - B}{A + B}. \tag{2.5}$$

If the visibility is lower than 100%, a background intensity all over the interference region is present, leading to a partial excitation of all the modes supported by the waveguide in addition to the target higher order mode. The efficiency with which the modes are excited in the waveguide is evaluated by the power overlap integral.

Fig. 2.3 shows an example of mode selectivity, simulated for a SOI waveguide 3.65 μm wide and 250 nm high (details of the waveguide in Section 2.3.1). Here the power overlap integral is evaluated separately for even and odd modes as a function of the angle 2θ between the two gaussian beams. When $\Delta L = p\lambda$, with p an integer, the interference pattern exhibits its maximum value at (x,y) = (0,0), preventing the excitation of modes which have an electric field profile which is odd with respect to the center of the waveguide (y = 0 axis). The modes excited with this condition correspond to even mode orders. However, by inducing a path length mismatch $\Delta L = p\lambda/2$ the fringes are shifted by half a period, and the resulting pattern exhibits a dark fringe in the middle, allowing efficient odd mode orders excitation.
From Fig. 2.3, one can see that when one of the modes has its maximum excitation, the power coupled to the other modes is negligible, with a simulated cross-talk of 32 dB for the first order mode, 38 dB for the second, 34 dB for the third, 59 dB for the fourth and 20 dB for the fifth. For the simulations of Fig. 2.3, the 3-dB bandwidth is around $\Delta\theta = 35^o$ for all the waveguide modes considered. Moreover, it can be calculated that the maximum variation of the power overlap integral due to the variation of wavelength is about 2% in the C-band (1530nm - 1565nm), and so the coupling coefficient is almost insensitive to λ and it can be considered constant over all the C - band. This constitutes a large difference with respect to the ADC, in which light confinement enhances the geometrical dispersion, resulting in a more limited bandwidth [34, 35].

2.2.2 Mode beatings in a waveguide

When looking at the spectrum at the output of the waveguide, it is necessary to take into account also the Fabry-Perot (FP) behaviour of the waveguide itself. For a particular propagating mode order m, with wavelength λ at position z, the FP effect is considered through the transfer function in Eq. (1.11). Since many modes can co-propagate along the waveguide, one has to consider their superposition, and the resulting field profile can be expressed by Eq. (1.12). An example of the field E_{wg} at the output of the waveguide, as a function of the wavelength, is shown in Fig. 2.4b. Here we consider the simulation of the coupling through the interferometer in a waveguide of width 3.65 μm and length 1.4 cm, with $\theta = 40^o$ and $\Delta L = 40\,\mu m$. The θ angle is tuned for a third order mode selection.

In Fig. 2.4a the input exciting field profile coming from the interference process is reported as a function of the wavelength. According to eq. (2.3), the shift along x exhibited by the input fringes, as λ is changed, is due to a mismatch in the light path of the two interfering beams. In Fig. 2.4b the field propagating inside the waveguide

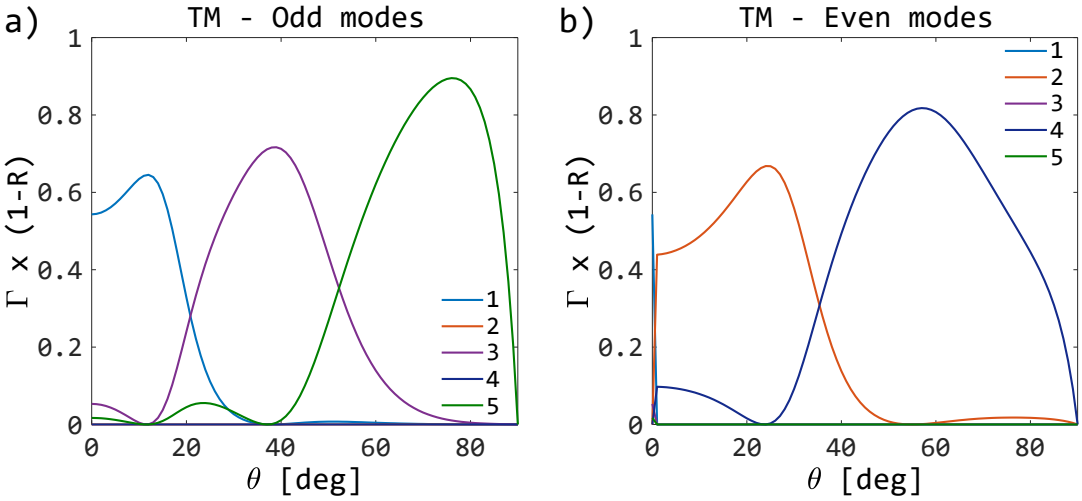

FIGURE 2.3: Simulated power overlap integral multiplied by the transmittance T through the input waveguide facet for the first five TM modes in the 3.65μm wide waveguide. The transmittance is evaluated according to Fresnel equations [5] for an air-silicon interface. The wavelength of the input light is 1550 nm. a) Even modes with $\Delta L = 0\,nm$. b) Odd modes $\Delta L = 775\,nm$. Note that the power of the even modes in a) and of the odd modes in b) is negligible.

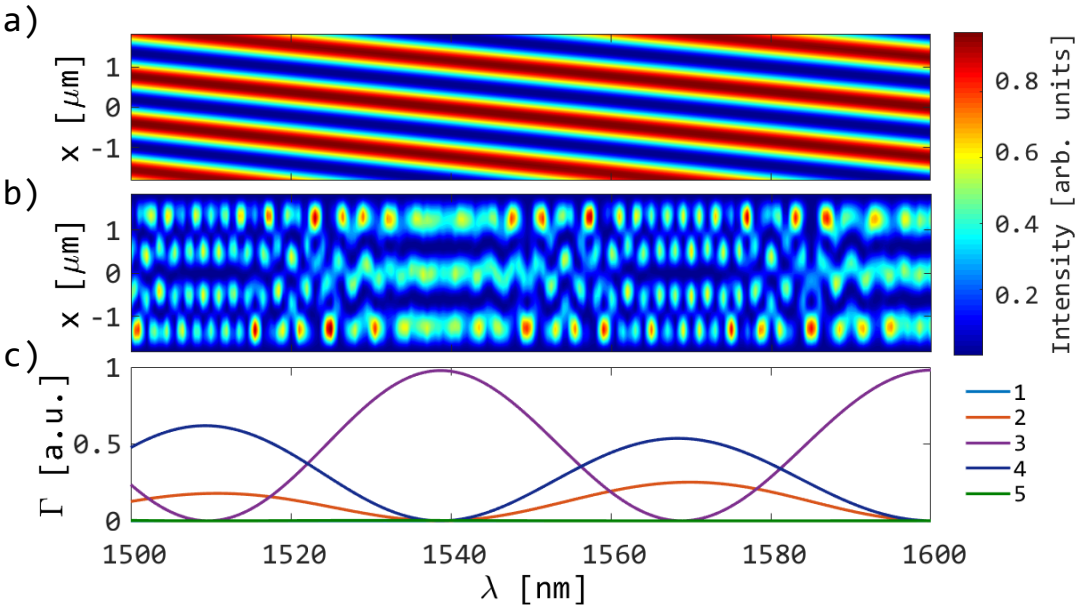

FIGURE 2.4: Simulation of light coupling in a waveguide of width 3.65 μm and length 1.4 cm, with $\theta = 40^o$ and $\Delta L = 40\mu m$. a) Shift of the input fringes with the wavelength. As the number of fringes illuminating the waveguide input changes, also the mode excited is different. b) Profile at the output of the waveguide exhibiting mode beatings as a function of the input wavelength. c) Power overlap integral as a function of the input wavelength for the modes in the waveguide. Only the first five modes are considered.

is shown. Depending on the alignment of the input fringes with respect to the input waveguide facet, a pure third order mode, which is the target one, or a mixture of modes, that give rise to beatings, will be excited. This behaviour is quantified by the

power overlap integral, plotted in Fig. 2.4c. The comparison between Fig. 2.4b and Fig. 2.4c makes evident that when the third order mode is mostly excited, near $\lambda = 1540\,nm$, the spatial profile at the output exhibits three lobes, which remains almost unchanged for small variations of the wavelength. In the other spectral regions, the profile is a mixture of the second and fourth order modes, or of all the excited modes.

2.3 Experiment

2.3.1 Experimental setup

The setup implemented to perform the interference of two oblique beams is reported in Fig. 2.5. It is composed by a tunable C - band laser source, followed by a polarization controlling stage, a beam expander and an interferometer. The interferometer is realized by a beam splitter, two equal gold mirrors and two equal lenses of $5\,cm$ of focal length. A tunable free space attenuator is placed in one of the arms, in order to balance the intensity of the two beams and, according to Eq. (2.5), maximizing the visibility. Furthermore, in one of the arms is inserted a delay stage that allows to tune the phase between the two splitted beams by adding a path difference ΔL. The spot diameter of the oblique beams is $(16 \pm 2)\,\mu m$. In order to probe the interference pattern at the input and at the output of the waveguide, a Scanning Near field Optical Microscopy (SNOM) fiber is used. The SNOM fiber has an aperture tip of $250\,nm$, which sets the resolution of the near field imaging system. The position of both the fiber and the waveguide is controlled by means of two XYZ-nanopositioning stages.

2.3.2 Measurement procedure

The selective mode excitation is performed in consecutive steps. Firstly, one has to verify the quality of the interference pattern in the region where the input facet of the waveguide will be placed and then the light paths of the two interfering beams have to be balanced ($\Delta L = 0$). At this point, the waveguide input facet has to be carefully aligned with the fringes of the interference pattern and, as a last step, the output field profile is probed. Two waveguides were chosen for the measurement, one $2.45\,\mu m$ wide for a second order mode selection, and the other $3.80\,\mu m$ wide for a third order mode selection. Transverse Magnetic (TM) polarization is used.

Creation of the input interference fringes

Firstly, the interferogram which will be formed on the input facet of the waveguide is characterized. In order to evaluate the interference period required for the excitation of the target modes, we performed a numerical simulation of the chosen waveguides with a Finite Elements Method (FEM) solver and we evaluated the distance between the lobes of the target modes. This yields $(1.31 \pm 0.02)\,\mu m$ for the second order mode in the $2.45\,\mu m$ wide waveguide and $(1.30 \pm 0.02)\,\mu m$ for the third order mode in the $3.80\,\mu m$ wide waveguide. The θ angle for these two cases was evaluated with Eq. (2.4) to be $(36.6 \pm 0.7)^o$ for the second order mode in the $2.45\,\mu m$ wide waveguide and $(36.3 \pm 0.6)^o$ for the third order mode in the $3.80\,\mu m$ wide waveguide.

Once that the θ angle is chosen, the visibility of the fringes was verified by looking at their spatial distribution in the (x,y)-plane by means of the SNOM fiber. One of the 1D slices is given in Fig. 2.6, where the experimental pattern is compared with the simulated one. A good agreement between simulation and experiment exists. By looking at the period of the experimental interferogram, and through Eq. (2.4),

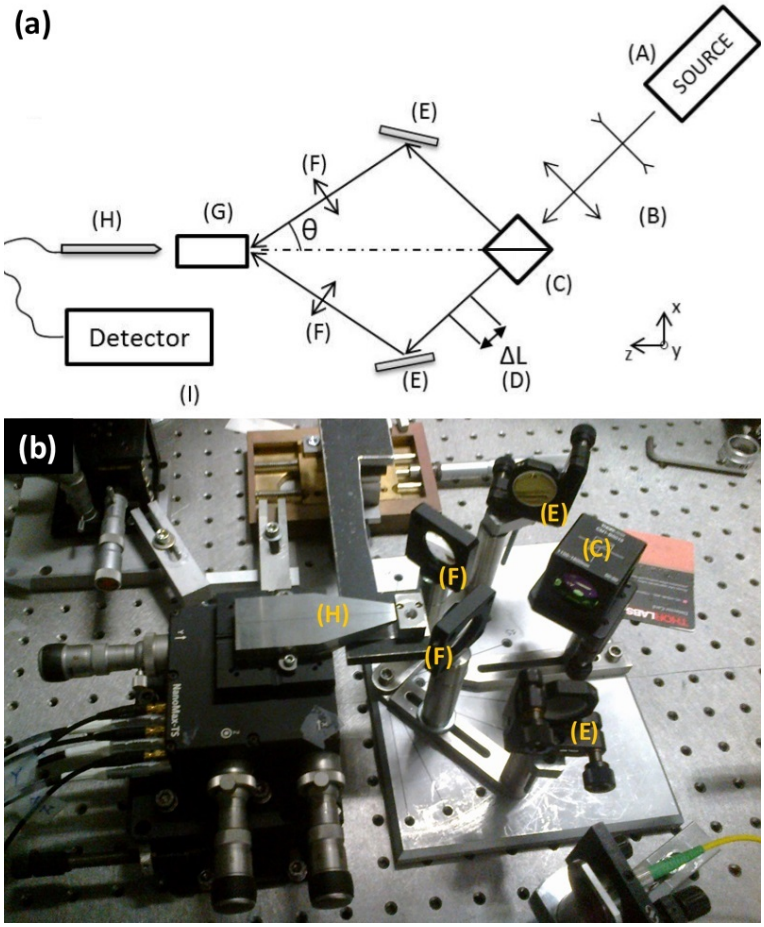

FIGURE 2.5: a) Sketch of the implemented setup observed from the top: (A) laser source, (B) beam expander, (C) beam splitter, (D) delay stage, (E) gold mirror, (F) lens, (G) waveguide, (H) collecting fiber, (I) detector. b) Photograph showing the interferometer in the experimental set up, with the letters indicating the corresponding element in a).

it is possible to evaluate the actual θ angle, that results to be $\theta = (36.6 \pm 0.3)^o$. The visibility is (0.95 ± 0.02).

Paths balancing

The last step before placing the waveguide on the interference pattern is setting $\Delta L = 0$. Indeed, if $\Delta L \neq 0$ the interference pattern at the input facet of the waveguide changes with the wavelength, as shown in Fig. 2.4, modifying the power overlap integral between the input profile and the target mode order.
In order to measure and tune the path mismatch ΔL, one has to look at the spectrum collected by the SNOM fiber while it is kept in the middle of the pattern profile and the wavelength is changed. According to Eq. (2.3), if the paths are balanced, fringes do not shift with wavelength, so the signal probed by the fiber is constant. Otherwise, the signal would oscillate, with a maximum when one maximum of interference shines on the tip, and a minimum when a dark fringe is probed.
In order to set ΔL to zero, the delay stage in Fig. 2.5 was tuned until no spectral

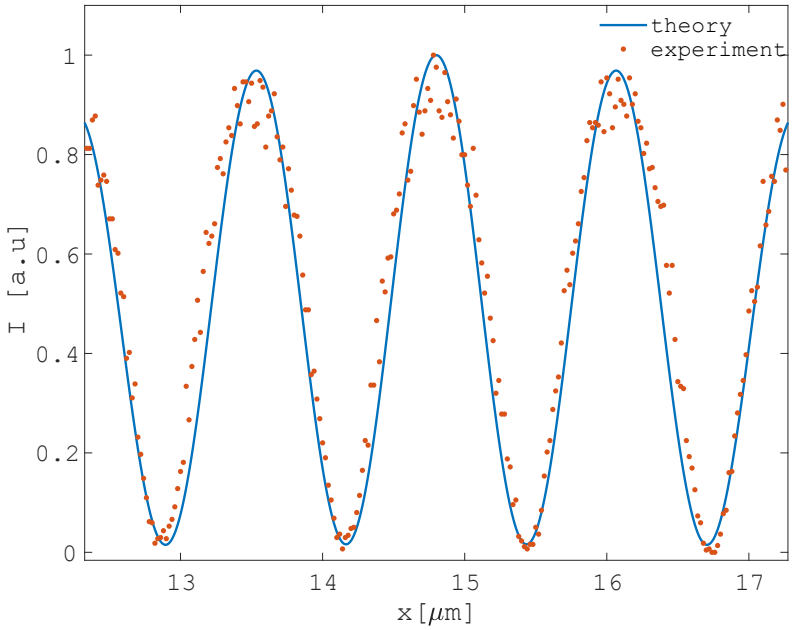

FIGURE 2.6: Measured and simulated 1D interference pattern of the two beams interferometer for $\theta = 36.6^o$ and $\lambda = 1550\,nm$. The measurement was carried out with the SNOM fiber.

shift was measured. In Fig. 2.7 the measured spectrum before and after the path balancing procedure is reported. ΔL is tuned from $(1.47 \pm 0.01)\,mm$ to $(8 \pm 1)\,\mu m$. ΔL is evaluated by fitting the experimental measurement. This value for the path mismatch provides a good stability, with the intensity greater than 95% of its maximum in a spectral range of $32\,nm$, that we consider sufficiently wide for the purposes of the experiment.

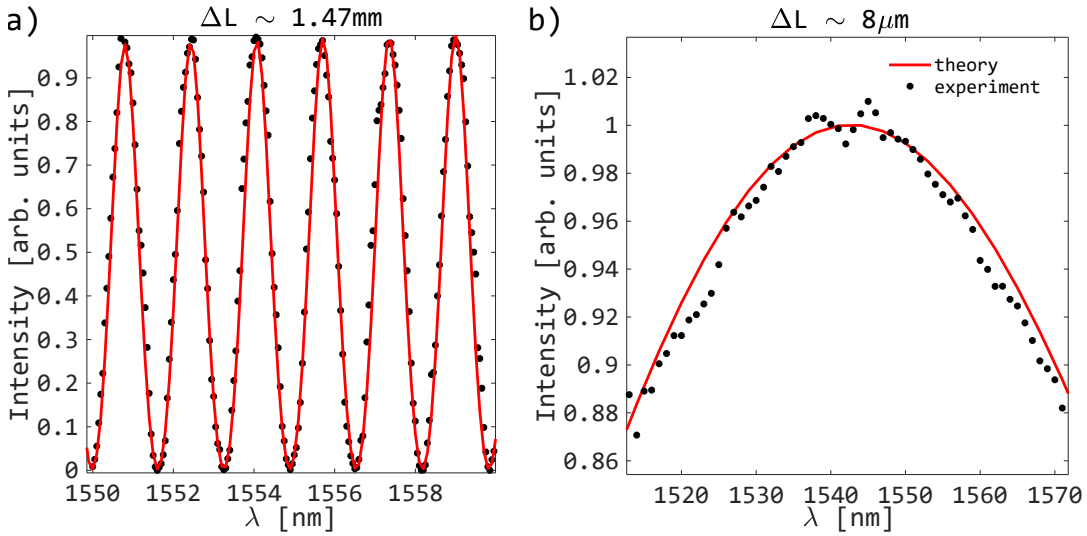

FIGURE 2.7: Measured and simulated spectrum a) before the balancing of light paths and b) after the balancing. (Notice the scale change.)

Selective excitation of the waveguide mode

The waveguide input facet was carefully placed in the plane where the interferogram was formed. In order to verify if the mode excited in the waveguide was actually the desired one, 1D spatial profiles of the transmitted signal at the waveguide output facet were taken for different wavelengths. The excited waveguide mode is pure if the profile does not change with wavelength. In fact, when more than one mode is excited, mode beatings occur and the field profile at the output of the waveguide changes periodically with the wavelength, as shown in Fig. 2.4b.

A XYZ-nanometric positioning stage is used in order to tune the waveguide position. If the first 1D slice did not exhibit a pure mode selection, the waveguide was moved along the x direction by steps of 10 nm, in order to match better the interference pattern with the input facet of the waveguide. This procedure was repeated until the evidence of pure mode selection was found. The field at the output of the waveguide is probed at wavelength steps of 1 nm.
The measured profiles are reported in Fig. 2.8.

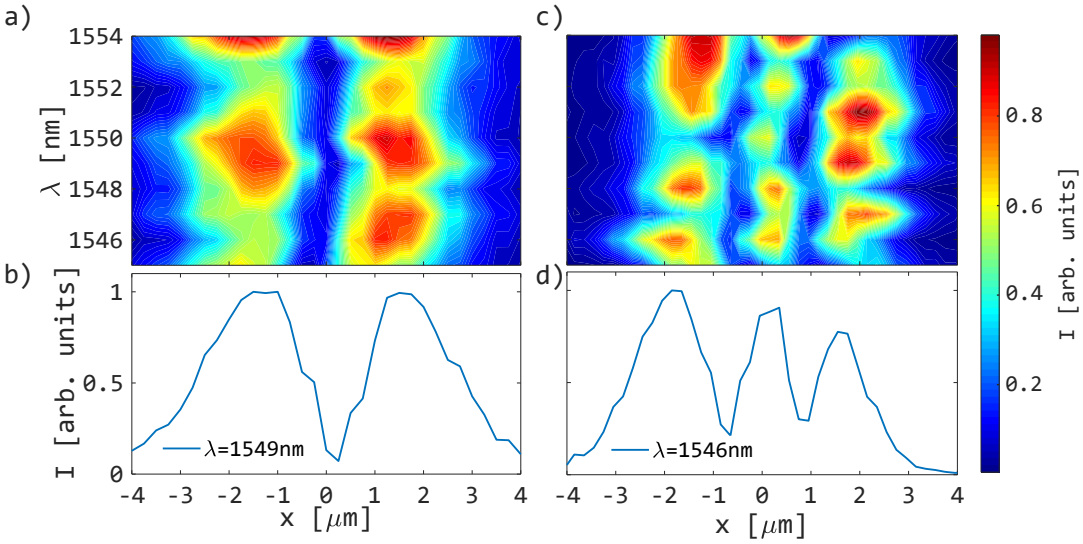

FIGURE 2.8: a) Experimental mode profile probed at the output of the 2.45 μm wide waveguide with the SNOM fiber. The measurement exhibits the selection of a second order mode in the waveguide. b) Slice from a) taken at 1549 nm. c) Experimental mode profile probed at the output of the 3.80 μm wide waveguide with the SNOM fiber. The measurement exhibits the selection of a third order mode in the waveguide. d) Slice from c) taken at 1546 nm.

The selective excitation of the second order mode in the 2.45 μm wide waveguide and of the third order mode in the 3.80 μm wide waveguide are shown in Fig. 2.8a and Fig. 2.8c respectively. The selected modes are identified by the number of lobes in the spatial profile. These lobes are not uniform in wavelength due to FP and to a partial excitation of other modes. Considering the bandwidth as the spectral range where the cross-talk is lower than 20 dB, the simulations suggested a bandwidth larger than the measured spectral region in Fig. 2.8a and Fig. 2.8c. In particular, the simulated bandwidth is around 20 nm (from 1540 nm to 1560 nm) both for the selection of the second order mode in the 2.45-μm-wide waveguide and for the selection of the third order mode in the 3.80-μm-wide waveguide. Experimentally, it was not possible to measure the field profiles for a wavelength range larger than the one in Fig. 2.8a and Fig. 2.8c, due to limitations in the mechanical stability of

our setup. Assuming, in the worst case, that the bandwidth is as large as the spectral range considered in Fig. 2.8a and Fig. 2.8c (1545 nm - 1554 nm), the simulated cross-talk has a minimum of 29 dB for the second order mode excited in the 2.45 μm wide waveguide and a minimum of 27 dB for the third order mode excited in the 3.80 μm wide waveguide. In both cases, the power overlap integral has an average value of 0.9 over the bandwidth considered. As a comparison, Fig. 2.9 reports a measurement where the mode selectivity was not accurate, resulting in the excitation of many modes in the waveguide that give rise to mode beatings.

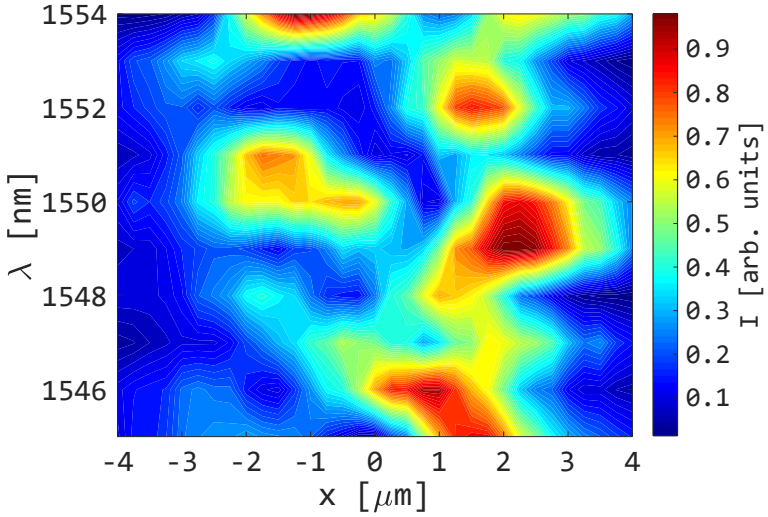

FIGURE 2.9: This is the same measurement performed in Fig. 2.8a, but in the case of a not pure mode selection. In this case the input pattern profile does not match correctly with the input facet of the 2.45 μm wide waveguide, preventing a pure second order mode selection.

The profiles in Fig. 2.8a and Fig. 2.8c are wider than the waveguides themselves, due to the point spread function of the SNOM fiber. We measured a value of (25.62 ± 0.02)dB of coupling losses, due to reflections at the input facet of the waveguide and to the large size of the input beams with respect to the size of the input facet. Insertion losses can be significantly reduced by optimizing the optics of the setup.

2.4 Perspectives: integrated interferometer

In order to integrate the interferometer directly on a chip, a planar waveguide region where the two oblique beams can interfere is required. With this aim, I studied a structure where the interference is achieved in a planar semicircular region, also known as star coupler. The basic design of the integrated device is reported in Fig. 2.10a: two input waveguides of width w_{in} are angled by θ with respect to the horizontal axis of the star coupler of radius R, and the higher order mode is coupled into the outgoing multimode waveguide with width w_{out}.

When designing the device, all these parameters are swept in order to find the best configuration for every mode to be coupled into the output. The insertion angle of the two beams in the star coupler is chosen according to the mode to be selected, as in the free-space case. However, the integrated interferometer has also to take into account the diffraction occurring in the planar waveguide: in fact, once the light exits the input waveguides the lateral confinement suddenly disappears, and the light

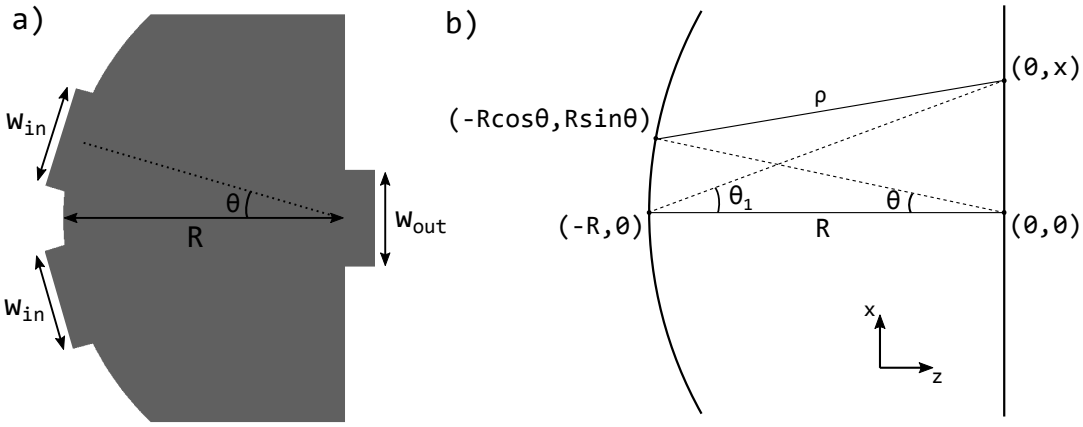

FIGURE 2.10: a) Basic chip design for the integrated interferometer, with the main quantities defining its geometry. b) Geometry of the integrated interferometer, representing the geometrical parameters involved in Eq. (2.6).

diffracts within the planar star coupler. This diffraction is modelled starting from the equation for the diffraction in a star coupler [21] adapted for the geometry of the interferometer. The equation used to calculate the diffracted field on the output port is

$$e_{out}(x) = -\sqrt{\frac{ik}{2\pi}} \int e_{in}(\theta) \exp\left(-ik\rho\right) \frac{R}{\sqrt{\rho}} \cos(\theta)\cos(\theta - \theta_1) \mathrm{d}\theta, \tag{2.6}$$

where the variables and parameters are as in Fig. 2.10, $x = R\tan(\theta_1)$, $e_{in}(\theta)$ is the field at the input port at θ angle and $e_{out}(x)$ is the output field at $z = 0$ and x. The integrated interferometer has also been studied with FEM simulations, as reported in Fig. 2.11, where the excitation of up to the fifth TE order mode is shown.

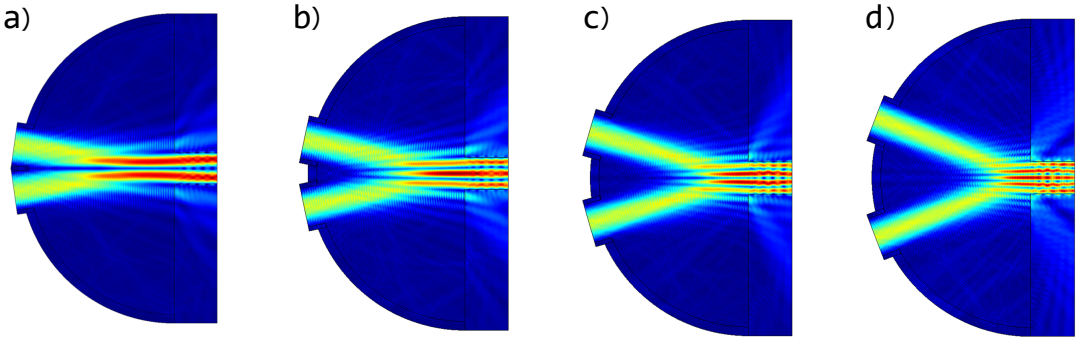

FIGURE 2.11: FEM simulations of the interferometer showing the coupling of different higher order modes: a) second order, b) third order, c) fourth order and d) fifth order mode.

The integrated interferometer should provide a mode order selectivity higher than the free space case, with lower coupling losses and better phase stability. In fact, while in the free space case the profile matching between the input beam and the waveguide mode is limited by the mismatch along the y-direction, in the integrated case the overlap along this direction is guaranteed by the vertical confinement. This vertical confinement allows to simplify the analysis of the overlap integral considering only the one dimensional profile along the x direction. In order to control the selection of the even or odd modes, the input field phase has to be prepared accordingly. To do so, a small part of one of the two input waveguide arms

has been designed with a larger width, as shown in the detail in Fig. 2.12, and whose length is such that a π phase shift between the two input beams is induced. Also an active control of the relative phase can be considered, which can be accomplished by placing thermal heaters on both the input arms, in order to fine tune the phase shift by changing the temperature of the two input waveguides. If the heaters are introduced, much more phase stability is obtained at the expenses of device footprint. In Fig. 2.12 the full design for the integrated interferometer is proposed. The input light propagates through a 3-dB coupler, whose outgoing arms, after the heater stage, reach the star coupler. The total length of the device depends on the presence or not of the heating stage, which doubles the length of the device, and on the quality of the fabrication technology, which affects the minimum length of both the 3-dB coupler and the tapered input waveguides.

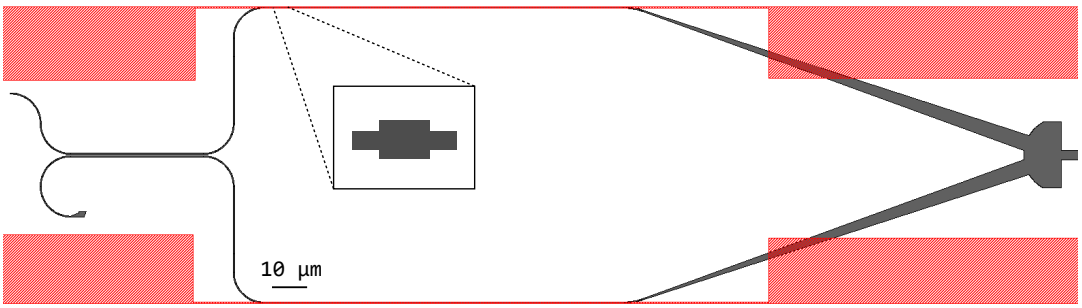

FIGURE 2.12: Final design of the integrated interferometer. In gray is the silicon structure, while in red are the metallic heaters. In the inset, it is shown the larger waveguide used to add a π phase shift on one of the arm, in order to excite the even mode orders.

As said before, in order to find the best geometrical configuration of the interferometer given a certain target mode, all the combinations of the parameters have been explored. I limited the analysis to the first five waveguide modes, since for higher order modes it is not possible to keep the same small footprint with low XT and losses at the same time. However, in principle there is not an upper limit to the mode order that can be excited, the only limit is θ, that cannot be too large in order to avoid strong reflections at the entrance of the multimode waveguide. In Table 2.1 and Table 2.2 are reported the best parameters up to the fifth TE and TM order mode respectively. The first waveguide mode has not been included in the tables since it is not useful to apply the interference method for the excitation of this mode, but it has been considered in the XT calculation. Γ is the power overlap integral, calculated between the input interference profile and the target mode within the cross section of the outgoing multimode waveguide. A common practice is to consider 3 dB as the maximum acceptable value for the EL. The BW refers to wavelengths with XT < -15 dB. As for the free space case, the interferometer exploits the symmetry of even and odd modes, so that the crosstalk of odd (even) modes cannot be affected by even (odd) modes. This results in low crosstalks, as shown in the Tables 2.1 and 2.2. From simulations, the bandwidth of the integrated interferometer is larger than 200 nm for all the modes and polarizations, as shown in Fig. 2.13.

Looking at the MDM application, one has to consider a slightly different design for the interferometer, in order to couple simultaneously more than one higher order mode. Considering a 2-mode multiplexer, the design should be like the one in Fig. 2.14, where two pairs of oblique beams are present, one for each mode. From this figure is evident the increasing complexity of the system, which should consider also

TE polarization							
Mode	θ [deg]	R [μm]	w_{in} [μm]	w_{out} [μm]	XT [dB]	EL [dB]	BW [nm]
2	15	20	5	2	-27.19	-2.85	>200
3	20	25	5	2.5	-25.95	-3.33	>200
4	22	25	4.5	3	-21.56	-3.63	>200
5	24	30	5	3.5	-20.20	-3.95	>200

TABLE 2.1: Geometrical parameters and efficiency of several simulated integrated interferometers for TE polarization. The first column refers to the target mode. BW refers to wavelengths with XT < -15 dB.

TM polarization							
Mode	θ [deg]	R [μm]	w_{in} [μm]	w_{out} [μm]	XT [dB]	EL [dB]	BW [nm]
2	16	15	4	2.5	-23.45	-3.70	>200
3	20	25	5	3.5	-22.05	-3.97	>200
4	23	25	5	4	-18.89	-3.98	>200
5	29	15	4.5	4	-14.73	-3.98	>200[a]

TABLE 2.2: Geometrical parameters and efficiency of several simulated integrated interferometers for TM polarization. The first column refers to the target mode. BW refers to wavelengths with XT < -15 dB.

[a]Only for the 5TM the bandwidth is calculated considering XT < -13 dB

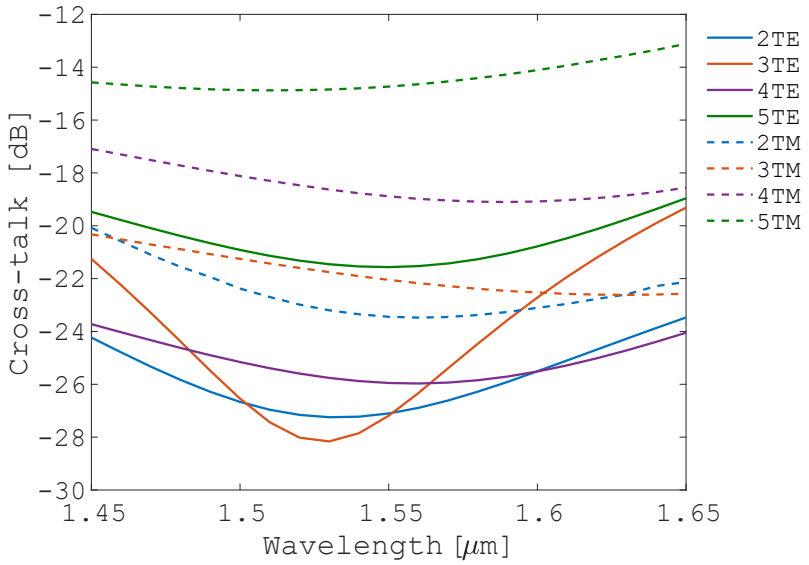

FIGURE 2.13: Simulated cross-talks as a function of the wavelength for the geometrical configurations in Table 2.1 and Table 2.2.

crossings, more heaters and 3-dB couplers. The full device for 2-mode multiplexing has a length greater than 350 μm, but it has to be considered that the heaters can be avoided if the phase shift by the larger waveguide (detail in Fig. 2.12) is reliable. Moreover, this design is limited by the low fabrication resolution, which imposes longer coupler lengths and tapering. With state of the art fabrication performance, and removing the heaters, the device can be reduced below 100 μm.

The integrated interferometer, due to the large dimensions involved, exhibits

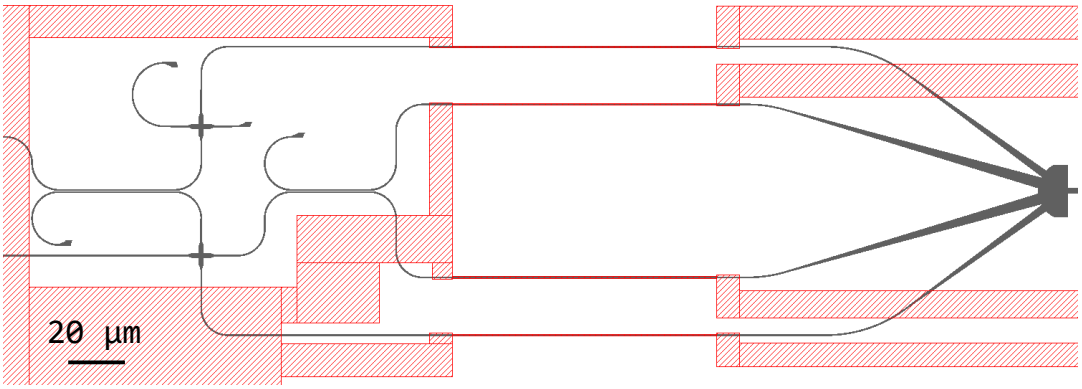

FIGURE 2.14: Full design of a 2-mode multiplexing interferometer.

large fabrication tolerance. To simulate the fabrication tolerance it has been considered the geometry for the selection of the 2TE mode, reported in Table 2.1. The parameters of the geometry have been varied one by one around their optimal value. The cross-talk variation with respect to the optimal one (δXT) is reported in Fig. 2.15. If $\delta\text{XT} = 0$ the fabrication tolerance is perfect. In Fig. 2.15a the most critical parameters are considered, θ and w_{out}, which exhibit a maximum δXT of about 3 dB, with parameter deviations larger than the experimental expectations. In Fig. 2.15b are considered R and w_{in}, which are almost insensitive to fabrication imperfections.

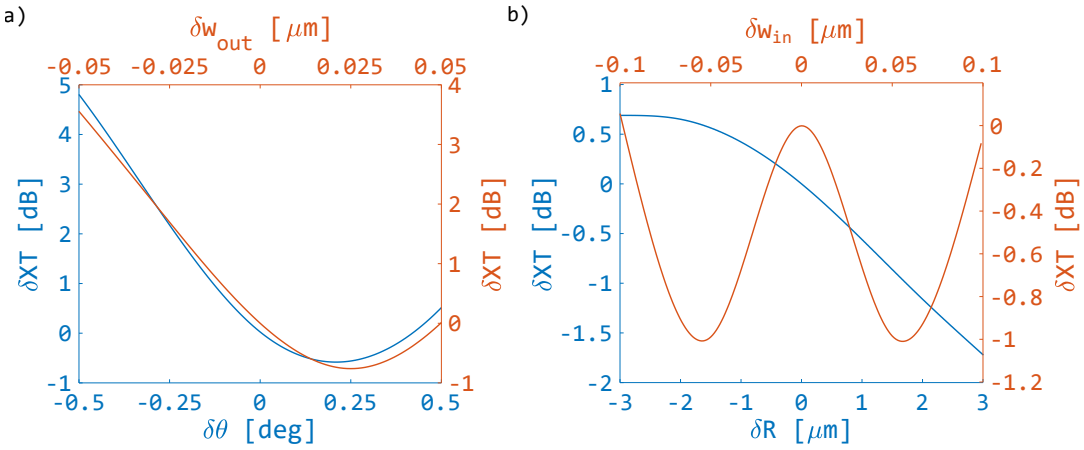

FIGURE 2.15: Deviation from the optimal cross-talk (δXT) as a function of the variation of the geometrical parameters from the optimal values ($\delta\theta$, δw_{in}, δR, δw_{out}). The simulation considers the geometry for the selection of the 2TE mode, given in Table 2.1. a) δXT for the variation of θ and w_{out}. b) δXT for the variation of R and w_{in}.

Some pictures of the fabricated devices have been taken with the microscope, focusing on the input 3-dB coupler (Fig. 2.16a), a single mode interferometer (Fig. 2.16b) and a 2-mode interferometer (Fig. 2.16c).

In Fig. 2.17 are reported two full 3D FEM simulations for the full device, for the second and third TE modes, with both the input and output couplers. These full 3D simulations are still under analysis and I report them here just as a qualitative description of the working principle of the integrated coupler.

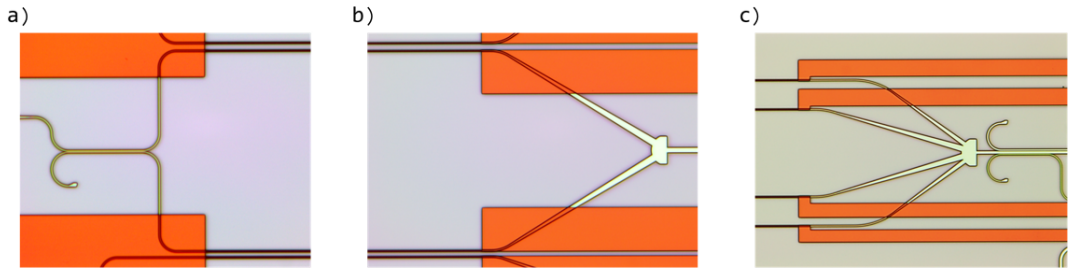

FIGURE 2.16: Colored microscope images of the fabricated integrated interferometers. In red the metallic heaters, in white the integrated devices. a) Detail of the input 3-dB coupler. b) Detail of the interferometer. c) Detail of the interferometer with double mode coupling. Photos by Dr. Mher Ghulinyan.

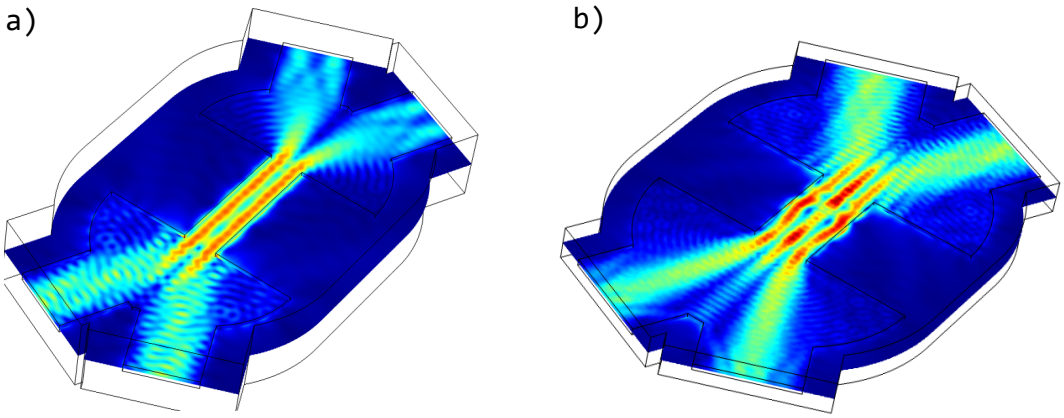

FIGURE 2.17: a) Full 3D FEM simulation of a second TE excited and extracted through the interferometer mode coupler. b) Full 3D simulation of a third TE excited and extracted through the interferometer mode coupler.

Ref.	Year	L [μm]	EL [dB]	XT [dB]	BW [nm]	N_{ch}	Technique
[36]	2012	80	1	-40	50	2	MMI
[37]	2014	∼200	0.2 ÷ 3.5	-20	∼100	8	ADC
[38]	2017	∼500	0.2 ÷ 1.8	-15 ÷ -25	∼90	10	Adiabatic
[39]	2018	5	<2.5	-19	>60	3	Y-junction
This thesis	2019	<200	2.85 ÷ 4	-15 ÷ -27	>200	>2	Interferometer

TABLE 2.3: State of the art of mode (de)multiplexers. The BW refers to wavelengths with XT < -15 dB and L is the length of the device. (Based on the report in Ref. [27]).

2.5 Conclusions

In this chapter I described a new approach to mode coupling based on the interference pattern arising from two superimposed tilted coherent beams. I initially validated experimentally the method for free space coupling. Then, I investigated the integrated version of the system. This integrated interferometer, compared with the already existing mode couplers in Table 2.3, exhibits smaller lengths (when heaters are not required) and superior bandwidths, without losing in cross talk. The main drawback of the integrated interferometer is the excess loss, which is larger than state of the art devices. The peculiarity of this device is the high selectivity on the

parity of the modes. In fact, even order modes does not affect the cross talk of the odd modes, and vice versa. The number of available channels can be very large, but its hard to define an upper limit without testing experimentally the system. In fact, despite the chip has been fabricated, some errors in the fabrication process affected irredeemably the propagation losses of the whole chip, preventing its experimental analysis.

Chapter 3

Intermodal four wave mixing in silicon waveguides

3.1 Nonlinear silicon photonics

The silicon photonics platform is one of the most successful technological advancements of the last decades. With their low costs and unique properties, silicon optical devices are bridging the gap between fundamental research and everyday applications. One of the key factor contributing to this success is the high nonlinear optical response of silicon, which enables plenty of new functionalities at the chip scale and that brought silicon photonics almost everywhere, from medical research to car industry, from data centers to telecommunication networks [20]. The fundamental reasons laying at the basis of the successful paradigm of nonlinear silicon photonics are:

- the high refractive index contrast of the SOI platform, which allows for very compact devices, that can be integrated in a huge number at the chip scale;
- the high optical densities that the small waveguide core permits, which reduce the input power requirements in order to trigger the nonlinear effects;
- the moderately high nonlinear index of silicon;
- the CMOS compatibility, which makes silicon preferable with respect to other semiconductor or polymers or organic materials with even higher nonlinear response.

While moving outside the labs, nonlinear silicon photonics is still facing new challenges at the fundamental research level. Among the most intriguing and promising research fields, mid infrared (MIR) and quantum applications are nowadays attracting most of the attention. In fact, these two fields are based on the nonlinear parametric processes arising in silicon devices [40], which enable on-chip wavelength conversion, useful for MIR light detection and generation [11], and correlated pairs production, which is at the basis of the developing quantum technologies [15].

The theory of optical nonlinearities starts from the polarization vector (or polarization density), which describes how the material responds to an applied electromagnetic field. At low optical powers, the relation between the applied electric field $\mathbf{E}$ and the polarization $\mathbf{P}$ is essentially linear, namely

$$\mathbf{P} = \epsilon_0 \chi^{(1)} \mathbf{E} = \epsilon_0 \sum_{ij} E_i \hat{\mathbf{a}}_j, \tag{3.1}$$

where ϵ_0 is the vacuum permittivity and $\chi^{(1)}$ is the first order susceptibility, a second rank tensor whose elements, $\chi^{(1)}_{ij}$, multiply the electric field component E_i and the unitary versor $\hat{\mathbf{a}}_j$ [20]. When the input optical power increases, stronger electric fields have to be considered, and the linear relation between the input electric field and the polarization no more holds. When such high optical fields are involved or free carriers have to be considered (which is often the case in semiconducting materials), the polarization vector can be rewritten as

$$\mathbf{P} = \mathbf{P}_L + \mathbf{P}_{NL} + \mathbf{P}_{FC}, \tag{3.2}$$

where $\mathbf{P}_L$ is the linear polarization, as in Eq. (3.1), $\mathbf{P}_{NL}$ is due to nonlinear optical interaction and $\mathbf{P}_{FC}$ is related to linear optical effects with free carriers involved. For sufficiently weak optical fields, the nonlinear polarization can be expanded as a Taylor series:

$$\begin{aligned}\mathbf{P}_{NL} &= \mathbf{P}^{(2)} + \mathbf{P}^{(3)} + ... \\ &= \epsilon_0 \left[\chi^{(2)} : \mathbf{E}^2 + \chi^{(3)} \vdots \mathbf{E}^3 + ... \right] \\ &= \epsilon_0 \left[\sum_{ijk} \chi^{(2)}_{ijk} E_i E_j \hat{\mathbf{a}}_k + \sum_{ijkl} \chi^{(3)}_{ijkl} E_i E_j E_k \hat{\mathbf{a}}_l + ... \right],\end{aligned} \tag{3.3}$$

where $\mathbf{P}^{(2)}$ and $\mathbf{P}^{(3)}$ are the second and third order polarization vectors respectively, while $\chi^{(2)}$ and $\chi^{(3)}$ are the second and third order susceptibilities, which are tensors of third and fourth order respectively. When amorphous or isotropic materials are involved (e.g. silica) the susceptibility can be treated as a scalar quantity, while for crystalline media (e.g. silicon) it has to be considered as a tensor. A further detail is that as the order of the nonlinear susceptibility increases, its value reduces rapidly. As an example, $\chi^{(2)} \sim 10^{-12} m/V$ and $\chi^{(3)} \sim 10^{-24} m^2/V^2$ [41]; as a result, second order nonlinear processes require weaker fields with respect to third order ones. This consideration motivates the photonics community to research primarily on $\chi^{(2)}$ materials, since on-chip integration requires low power functionalities. Unfortunately, silicon does not display second order nonlinearity, due to its centrosymmetric crystalline structure. In fact, when the material is centrosymmetric, it has an inversion symmetry, which prevents the existence of even order nonlinearities. This last conclusion comes from the comparison between the second order polarization without the application of the inversion operator

$$\mathbf{P}^{(2)} = \epsilon_0 \left[\sum_{ijk} \chi^{(2)}_{ijk} E_i E_j \hat{\mathbf{a}}_k \right], \tag{3.4}$$

and with the inversion operator applied

$$-\mathbf{P}^{(2)} = \epsilon_0 \left[\sum_{ijk} \chi^{(2)}_{ijk} (-E_i)(-E_j) \hat{\mathbf{a}}_k \right], \tag{3.5}$$

where $\chi^{(2)}_{ijk} = -\chi^{(2)}_{ijk}$ holds according to the inversion symmetry of silicon. As a consequence,

$$-\mathbf{P}^{(2)} = \epsilon_0 \left[\sum_{ijk} \chi^{(2)}_{ijk} (-E_i)(-E_j) \hat{\mathbf{a}}_k \right] = \epsilon_0 \left[\sum_{ijk} \chi^{(2)}_{ijk} E_i E_j \hat{\mathbf{a}}_k \right] = \mathbf{P}^{(2)}, \tag{3.6}$$

which is valid only for $\chi^{(2)}_{ijk} = 0$. Because of this the research in nonlinear silicon photonics moved towards third order nonlinearities. Moreover, higher order susceptibilities, like $\chi^{(4)}$ and higher, are usually not considered due to the tremendous power intensities required.

When dealing with nonlinear optics, a fundamental role is still covered by the linear susceptibility $\chi^{(1)}$, which is related to the electronic transitions induced in the medium by individual photons. $\chi^{(1)}$ is related to the refractive index n by

$$\chi^{(1)} + 1 = n^2, \tag{3.7}$$

which means that $\chi^{(1)}$ is related to the real part of the refractive index, while its imaginary part encloses information on loss or gain mechanisms in the material [42]. Related to the real and imaginary parts of the refractive index is the role of free carriers, whose presence gives rise to extra absorption and dispersion phenomena, named respectively free carrier absorption (FCA) and free carrier dispersion (FCD). The complex refractive index as a function of the wavelength λ and of the electron/hole densities N_e/N_h reads as [20]

$$n(\lambda, N_e, N_h) = n_0(\lambda) + \delta n_{FC}(N_e, N_h) + i\frac{\lambda}{4\pi}\left[\alpha_0(\lambda) + \delta\alpha_{FC}(N_e, N_h)\right], \tag{3.8}$$

where n_0 and α_0 are the standard refraction and absorption coefficients, while δn_{FC} and $\delta\alpha_{FC}$ are the refractive index change and extra losses induced by free carriers. These coefficients have been estimated at 1550 nm[43]:

$$\delta n_{FC} = -8.8 \times 10^{-22} N_e - 8.5 \times 10^{-18} N_h^{0.8}, \tag{3.9a}$$

$$\delta\alpha_{FC} = 8.5 \times 10^{-18} N_e + 6.0 \times 10^{-18} N_h. \tag{3.9b}$$

3.2 Second order processes

Despite silicon does not exhibit second order processes, these phenomena are extremely useful for off-chip applications and experiments, as will be shown in Section 4.5.2, where a $\chi^{(2)}$ process is used to up-convert and detect photons in the MIR. Second order processes arise from the combination of three photons, which, in terms of polarization vector, can be described as the superposition of two waves $\mathbf{E}_1$ and $\mathbf{E}_2$ with ω_1 and ω_2 frequencies respectively [20]:

$$\begin{aligned}
\mathbf{P}^{(2)}(\mathbf{r}, t) = \\
&\epsilon_0\chi^{(2)} : \left[\mathbf{E}_1^2(\mathbf{r}, \omega_1)\mathrm{e}^{-i2\omega_1 t}\right] \\
&+ \epsilon_0\chi^{(2)} : \left[\mathbf{E}_2^2(\mathbf{r}, \omega_2)\mathrm{e}^{-i2\omega_2 t}\right] \\
&+ \epsilon_0\chi^{(2)} : \left[2\mathbf{E}_1(\mathbf{r}, \omega_1)\mathbf{E}_2(\mathbf{r}, \omega_2)e^{-i(\omega_1+\omega_2)t}\right] \\
&+ \epsilon_0\chi^{(2)} : \left[2\mathbf{E}_1(\mathbf{r}, \omega_1)\mathbf{E}_2^*(\mathbf{r}, \omega_2)e^{-i(\omega_1-\omega_2)t}\right] \\
&+ \epsilon_0\chi^{(2)} : \left[\mathbf{E}_1(\mathbf{r}, \omega_1)\mathbf{E}_1^*(\mathbf{r}, \omega_1)\right] \\
&+ \epsilon_0\chi^{(2)} : \left[\mathbf{E}_2(\mathbf{r}, \omega_2)\mathbf{E}_2^*(\mathbf{r}, \omega_2)\right] \\
&+ c.c.
\end{aligned} \tag{3.10}$$

where *c.c.* is the complex conjugate. The first two lines in Eq. (3.10) refer to the second harmonic generation (SHG), where two photons at ω_1 (ω_2) annihilate resulting in the generation of one photon at $2\omega_1$ ($2\omega_2$). The third and fourth lines of Eq. (3.10) are the polarizations associated with the sum frequency generation (SFG) and difference frequency generation (DFG) respectively: in SFG two photons at ω_1 and ω_2 disappear to generate a new photon with frequency $\omega_1 + \omega_2$, while in DFG the generated photon has frequency $\omega_1 - \omega_2$. The last two terms of Eq. (3.10) refer to optical rectification (OR), which give rise to the generation of a DC component of the polarization [20]. All the processes involving the annihilation and generation of photons can be modelled in the quantum mechanical framework as a two level system, in which the upper level is a virtual state. According to the virtual state picture, SHG, SFG and DFG have been schematized in Fig. 3.1.

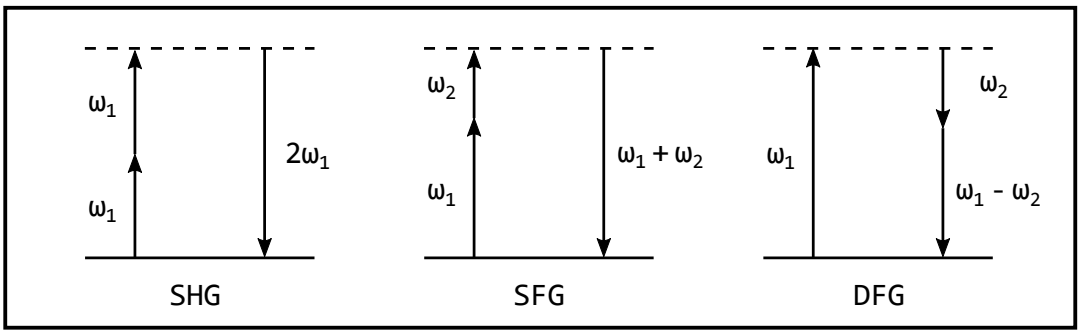

FIGURE 3.1: Virtual state diagram for SHG, SFG and DFG processes.

3.3 Third order processes

Like the second order nonlinearities, it is possible to describe the $\chi^{(3)}$ processes and the corresponding polarization vector considering the superposition of three waves $\mathbf{E}_1$, $\mathbf{E}_2$, $\mathbf{E}_3$ at respectively ω_1, ω_2, ω_3 frequencies:

$$\begin{aligned}
\mathbf{P}^{(3)}(\mathbf{r},t) = \\
&\epsilon_0\chi^{(3)}\vdots\left[\mathbf{E}_1^3(\mathbf{r},\omega_1)\mathrm{e}^{-i3\omega_1 t}\right] \\
&+\epsilon_0\chi^{(3)}\vdots\left[3\mathbf{E}_1^2(\mathbf{r},\omega_1)\mathbf{E}_2(\mathbf{r},\omega_2)\mathrm{e}^{-i(2\omega_1+\omega_2)t}\right] \\
&+\epsilon_0\chi^{(3)}\vdots\left[3\mathbf{E}_1^2(\mathbf{r},\omega_1)\mathbf{E}_2^*(\mathbf{r},\omega_2)\mathrm{e}^{-i(2\omega_1-\omega_2)t}\right] \\
&+\epsilon_0\chi^{(3)}\vdots\left[6\mathbf{E}_1(\mathbf{r},\omega_1)\mathbf{E}_2(\mathbf{r},\omega_2)\mathbf{E}_3(\mathbf{r},\omega_3)\mathrm{e}^{-i(\omega_1+\omega_2+\omega_3)t}\right] \\
&+\epsilon_0\chi^{(3)}\vdots\left[6\mathbf{E}_1(\mathbf{r},\omega_1)\mathbf{E}_2(\mathbf{r},\omega_2)\mathbf{E}_3^*(\mathbf{r},\omega_3)\mathrm{e}^{-i(\omega_1+\omega_2-\omega_3)t}\right] \\
&+\epsilon_0\chi^{(3)}\vdots\left[3|\mathbf{E}_1(\mathbf{r},\omega_1)|^2\mathbf{E}_1(\mathbf{r},\omega_1)\mathrm{e}^{-i\omega_1 t}\right] \\
&+\epsilon_0\chi^{(3)}\vdots\left[3|\mathbf{E}_2(\mathbf{r},\omega_2)|^2\mathbf{E}_1(\mathbf{r},\omega_1)\mathrm{e}^{-i\omega_1 t}\right] \\
&+c.c.
\end{aligned} \tag{3.11}$$

where all the permutations of the waves for reasons of compactness have not been considered. The first term in Eq. (3.11) describes third harmonic generation (THG), with the generation of one photon at $3\omega_1$ frequency after the annihilation of three

photons at ω_1. From the second to the fifth term in Eq. (3.11) different ways to achieve frequency mixing in a $\chi^{(3)}$ material are described, named four wave mixing (FWM), in which four photons combine to give rise to the generation of new harmonics. The sixth term in Eq. (3.11) describes both self phase modulation (SPM) and two photon absorption (TPA). SPM comes from the real part of $\chi^{(3)}$ and induces an intensity dependent modulation $\Delta n = n_2 I(t)$ to the nonlinear refractive index, with n_2 the Kerr coefficient and I the field intensity; as a result, the propagating pulse experiences a time-dependent phase shift which give rise to a spectral broadening of the pulse itself [44]. With TPA two input photons are absorbed by the excitation of one electron from the valence to the conduction band [41]. TPA leads to the production of free carriers in the medium, increasing the system losses. TPA occurs at wavelengths in which the band-gap energy is larger than the single photon energy, such that only multiple photons absorption can cover the energy gap of the material. Depending on the wavelengths propagating in the medium, also cross-two photon absorption (XTPA) can occur, which is the same mechanism of TPA but with two photons with non-degenerate frequency. Silicon is strongly affected by TPA at 1550 nm, which introduces FCA and FCD, and also imposes severe limitations at the maximum attainable on-chip power [45, 20]. A process analogous to SPM is the one described by the last term of the summation in Eq. (3.11), cross phase modulation (XPM), in which the phase shift experienced by the wave at ω_1 is not induced by itself but by another wave propagating simultaneously (ω_2 in the case of Eq. (3.11)). THG, FWM and SPM are also schematized in Fig. 3.2.

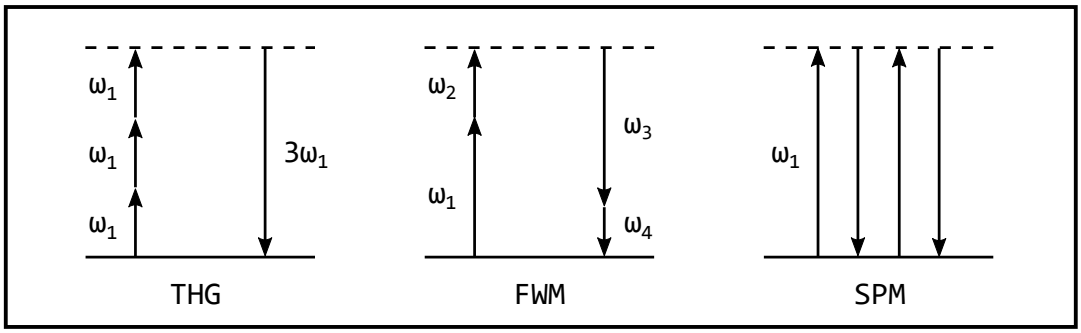

FIGURE 3.2: Virtual state schematics for THG, FWM and SPM processes.

Nonlinear processes can be grouped into two categories, parametric and non parametric processes. Parametric processes are characterized by identical initial and final quantum mechanical states of the system, thus allowing the excitation of the population in the ground state to a virtual state only for extremely brief time intervals. As a consequence, parametric processes are instantaneous and the energy of the system during the process remains in the form of photons [41]. On the contrary, in non parametric processes the energy can be exchanged with the material also through other forms, like heat or sound. All the processes described above, both $\chi^{(2)}$ and $\chi^{(3)}$, are parametric, with the exception of TPA, in which photon energy goes into the excitation of free carriers. Another common example of non parametric process is stimulated Raman scattering (SRS), which results from the interaction between propagating photons and vibrational modes of the material structure. In particular, a photon at frequency ω is annihilated and a Stokes-shifted photon at ω_s is generated, according to the energy conservation $\omega_s = \omega - \omega_V$, where $\hbar\omega_V$ is the phonon energy exchanged with the medium [46]. Most of the technological applications involving nonlinear optics are based on frequency mixing processes; however,

also the study of TPA and SPM is of crucial importance for nonlinear devices, since these processes directly affect the light propagation in photonics structures. As already stated, SPM leads to a nonlinear modulation of the refractive index, while TPA give rise to nonlinear losses both in terms of multiphoton absorption and FCA. The perturbation of the refractive index and of the absorption coefficient can be expressed as

$$n = n_0 + n_2 I + i\frac{\lambda}{4\pi}\left[\alpha_0 + \beta_{TPA} I\right], \tag{3.12}$$

with n_0 the refractive index, β_{TPA} the TPA coefficient and α_0 the absorption coefficient [20]. n_2 and β_{TPA} are related to the real and imaginary part of the susceptibility tensor as [20]

$$n_2 = \frac{3}{4\epsilon_0 c n^2}\,\mathrm{Re}\left(\chi^{(3)}_{eff}\right), \tag{3.13a}$$

$$\beta_{TPA} = \frac{3\omega}{2\epsilon_0 c^2 n^2}\,\mathrm{Im}\left(\chi^{(3)}_{eff}\right), \tag{3.13b}$$

where c is the speed of light, $\chi^{(3)}_{eff}$ the effective third order susceptibility, calculated considering the independent terms of the $\chi^{(3)}$ tensor [47]. From Eq. (3.13a) and Eq. (3.13b) it can be seen that SPM, and the nonlinearities in general, is directly dependent on the real part of $\chi^{(3)}_{eff}$, while TPA is related to its imaginary part. In fact, n_2 and β_{TPA} can be regarded as two sides of the same coin, in the sense that a high nonlinear coefficient, which is desirable for nonlinear photonics applications, is usually related to a high β_{TPA} coefficient, which introduces nonlinear losses and it is detrimental for integrated optics. Because of this the figure of merit (FOM) parameter has been introduced, calculated as

$$\mathrm{FOM} = \frac{n_2}{\beta_{TPA}\lambda}. \tag{3.14}$$

The FOM is used to evaluate the material suitability for nonlinear operation considering also the induced nonlinear losses [40]. The FOM of crystalline silicon (c-Si), for example, is between 0.32 and 0.86, much lower than silica (SiO2), whose FOM $\gg 1$. However, silica has an n_2 that is two orders of magnitude smaller than the one of silicon, and its refractive index is much lower than the silicon case; this means that devices based on silica has a much larger FOM, but they exhibit also a footprint that is enormous with respect to SOI structures [40]. Because of this the FOM alone is not sufficient to judge the quality of a material. Another parameter that is complementary to FOM is the effective nonlinearity γ, calculated as

$$\gamma = 2\pi\frac{n_2}{\lambda A_{eff}}. \tag{3.15}$$

The dependence on the effective area A_{eff} makes the γ parameter a reliable parameter to compare integrated structures. Silicon single mode waveguides (SMWs) exhibit $\gamma = 350 - 500\,W^{-1}m^{-1}$, much larger than the one of silica single mode fibers (SMFs), which have $\gamma \sim 0.001\,W^{-1}m^{-1}$. The role of γ is intuitively understood when considering the nonlinear phase shift ϕ_{NL}, that is the phase accumulated by the optical pulse due to the intensity-dependent refractive index. ϕ_{NL} is defined as

$$\phi_{NL} = \gamma P_p L_{eff}, \tag{3.16}$$

where P_p is the peak power of the pulse (or the average power in the continuous

wave (CW) case) and L_{eff} is the effective length. The effective length defines the length of a fiber/waveguide considering its linear losses. L_{eff} is calculated as

$$L_{eff} = \frac{1 - e^{-\alpha_0 L}}{\alpha_0}, \tag{3.17}$$

where the linear absorption coefficient α_0 and the geometrical length L of the device have been considered. In this way, ϕ_{NL} quantifies the nonlinear efficiency of the whole device, taking into account the intrinsic nonlinearity of the material, the actual interaction length of the device and the pump power required to trigger the nonlinear processes. By comparing the integrated structures with silica fibers, it can be noticed that integrated devices have larger linear losses with respect to fibers, but they exhibit much higher nonlinear phase shifts with insuperable shorter lengths [40]. Thus, integrated photonics is a suitable platform when looking for miniaturization and scalability of photonics devices, as also shown by Fig. 3.3, where the typical c-Si SMW is compared with the typical SiO2 SMF in terms of nonlinear phase shift per watt; it is evident that the Si platform exhibits much higher nonlinearity right at the centimeter scale, while the SMF becomes comparable only above kilometer lengths. In order to help the comparison between silicon waveguides and silica fibers, all the nonlinear parameters mentioned above have been summarized in table 3.1.

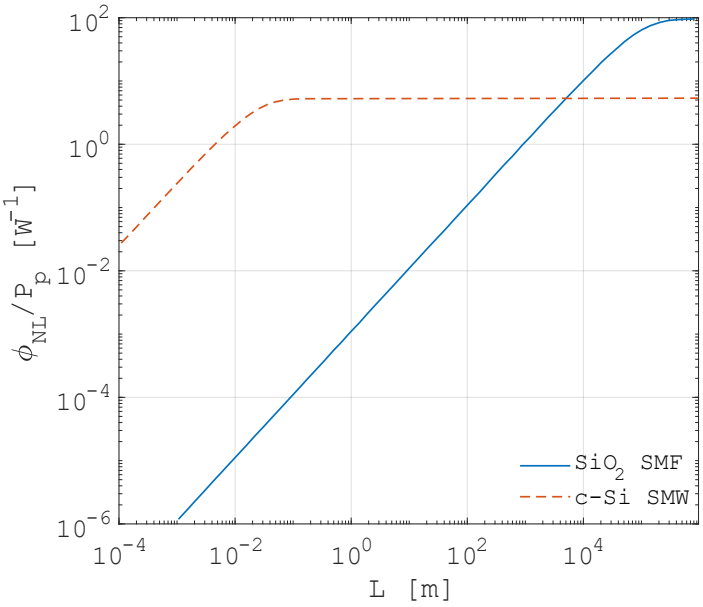

FIGURE 3.3: Nonlinear phase shift per unit of power versus the length of the device. Typical SiO2 SMF and typical c-Si waveguide are compared, showing that the latter is superior in terms of nonlinearity right at the chip scale. Data taken from Ref. [40].

3.4 Four wave mixing in silicon waveguides

Nonlinear optics enables several applications in silicon photonics, like wavelength conversion [48, 49], signal amplification [50], gas sensing [51, 12], light generation [52], photon pair sources [15] and many others. The common point among these functionalities is the nonlinear process used, that is FWM. FWM has been initially

Properties	**SiO_2 SMF**	**c-Si SMW**
A_{eff} [μm^2]	85	0.1
Core index	1.47	3.48
n_{eff}	1.47	2.3
n_2 [cm^2W^{-1}]	$\sim 2 \times 10^{-16}$	4.3 - 6 $\times 10^{-14}$
γ [$W^{-1}m^{-1}$]	~ 0.001	350 - 500
Linear loss [dB/cm]	1.8×10^{-6}	3
β_{TPA} [cm/GW]	0	0.45 - 0.87
FOM_{TPA}	$\gg 1$	0.32 - 0.86

TABLE 3.1: Optical properties of typical SiO2 SMF and typical c-Si SMW at a wavelength of 1550 nm. Data taken from Ref. [40].

discovered in bulk semiconductor materials [53, 54], then silica fibers were considered to improve the efficiency of the process [55] and only later the SOI platform was considered as a promising alternative for FWM [56]. Due to the lack of second order susceptibility in silicon, FWM is the most investigated and developed process on the SOI platform, and the opportunities offered by this phenomenon are still studied and developed, especially in the emerging fields of MIR and quantum photonics [12, 15]. FWM is a nonlinear third order process in which two (three) photons are annihilated with the instantaneous generation of two (one) photons at frequencies different from the starting ones. Several patterns for this interaction are possible, as shown in Fig. 3.4. The most common scheme is the one involving two input photons, called the *pump*, at the same ω_p frequency, that are converted into the *signal* and the *idler* photons at frequencies ω_s and ω_i respectively, with $\omega_i > \omega_s$[1]. Considering an optical waveguide, the process can be schematized as in Fig. 3.5, where the two input pump photons enter the waveguide and the two new frequencies, the signal and the idler photons, are emitted.

When the two input pump photons are equal in frequency, the process is said to be *degenerate*, otherwise it is called *non-degenerate*. Another distinction is when, together with the pump, also a stimulating signal is provided at the frequency of the signal or idler. In this case, the process is called *stimulated* FWM (sFWM), and the presence of the stimulating signal fosters the generation rate of the signal and idler pairs, which becomes much more efficient with respect to the case not involving the stimulus. This last case, is called *spontaneous* FWM (SFWM). While sFWM can be described with a classical electromagnetic theory, the SFWM requires a quantum picture. From a naive point of view, it is possible to consider the vacuum quantum fluctuations as the seed of the process [41], in analogy with the stimulated FWM. The main characteristic of spontaneous FWM is that the generated idler and signal photons are always emitted simultaneously in pairs, with a degree of correlation which depends on the bandwidths of both the pump and the process itself. The capability of generating correlated pairs lays at the basis of the use of FWM for the generation of entangled and single photon states for quantum applications in $\chi^{(3)}$ materials [57].

Both stimulated and spontaneous FWM are constrained by the same conservation rules. The first constraint is the **energy conservation**. Considering the most common FWM interaction, where the two input photons are annihilated to generate an idler-signal pair, the energy of the generated pair must equals the energy of the

[1] In literature, no clear definition exists of whether the idler is the photon at larger or lower frequency with respect to the signal. Because of this, here I prefer to make explicit my notation.

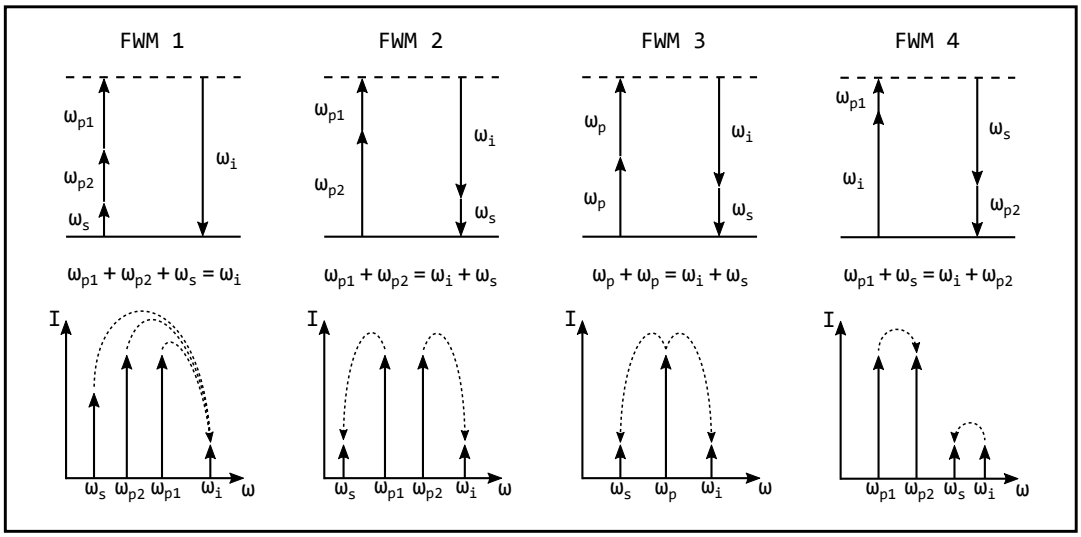

FIGURE 3.4: Different interaction schemes for the four photons involved in FWM. For each interaction, the energy diagram is reported (top). The energy conservation relation governing the particular interaction (middle) and the qualitative spectrum of the process (bottom). The length of the arrows in the energy diagram is proportional to the frequency of the photons, while the arrows in the spectrum represents the intensity of the wave. 'FWM 1' refers to the case of three photon annihilation for the production of one photon at higher energy. 'FWM 2' describes the annihilation of two input pump photons with different frequencies and the consequent generation of the signal and idler photons. 'FWM 3' is the degenerate FWM, where the two input pump photons have the same frequency. 'FWM 4' depicts the generation of pump and signal photons after the absorption of the other pump and idler photons. This last interaction is also known as FWM-Bragg scattering [40].

FIGURE 3.5: Schematized FWM process occurring in a waveguide. The input pump photons are injected from the facet of the waveguide and are converted into the signal and idler frequencies, which exit from the end facet of the structure.

input pump photons. This energy conservation is summarized with the equation

$$\hbar\omega_{p1} + \hbar\omega_{p2} = \hbar\omega_s + \hbar\omega_i, \tag{3.18}$$

which forces the idler and signal to be symmetric, in frequency, with respect to the pump. The second constraint comes from the phase-sensitive nature of FWM, which means that its efficiency depends on the phase relationship between the waves involved in the process. In fact, the generated waves in the medium add up constructively only when they are generated in phase, that is the so called *phase matching*

condition, which corresponds to the **momentum conservation**, written as

$$k_{p1} + k_{p2} = k_s + k_i. \tag{3.19}$$

When dealing with nonlinear processes the momentum conservation is not automatically satisfied, and particular techniques are required in order to phase match the waves, as will be discussed later in Section 3.5. The parameter used to quantify the lack of phase matching is the phase mismatch Δk, calculated as

$$\Delta k = k_{p1} + k_{p2} - k_s - k_i. \tag{3.20}$$

When $\Delta k = 0$ the phase matching condition is achieved and maximum FWM efficiency is obtained; when $\Delta k \neq 0$ the phase relationship between the waves in the process is not optimized, yielding lower generation efficiency [41]. Equations (3.18),(3.19) and (3.20) have been derived for the most common FWM interaction, 'FWM 2' in Fig. 3.4. Only this last FWM scheme will be considered in this thesis.

3.4.1 Classical theory of four wave mixing

Light propagation in media is described by the wave equation (see Section 1.1.1). When during the propagation also generation phenomena, such as FWM, are present, the wave equation has to be modified by considering the nonlinear polarization. In this way, the nonlinear wave equation is obtained [58]

$$\nabla^2 \mathbf{E}(\mathbf{r}, \omega) + \frac{\omega^2}{c^2} n^2 \mathbf{E}(\mathbf{r}, \omega) = -\frac{\omega^2}{\epsilon_0 c^2} \mathbf{P}_{NL}(\mathbf{r}, \omega). \tag{3.21}$$

In Eq. (3.21), the nonlinear polarization $\mathbf{P}_{NL}$ acts as a source that radiates in a linear medium of refractive index n. Considering a linearly polarized plane wave propagating along z, its electric field, with mode profile $\mathbf{e}(\mathbf{r}_\perp, \omega)$ and field envelope $u(z)$, can be written as [20]

$$\mathbf{E}(\mathbf{r}, \omega) = \frac{1}{2} \mathbf{e}(\mathbf{r}_\perp, \omega) u(z) e^{ikz}, \tag{3.22}$$

where $\mathbf{r}_\perp \in (x, y) -$ plane. The field envelope $u(z)$ is such that the optical power P carried by the wave is calculated as $P(z) = P_0 |u(z)|^2$, where P_0 is the total optical power of the wave before being perturbed by the interaction with the medium [20]. Considering homogeneous and isotropic materials, Eq. (3.21) becomes

$$\frac{1}{2} \mathbf{e}(\mathbf{r}_\perp, \omega) \left[\frac{\partial^2 u(z)}{\partial z^2} + 2ik \frac{\partial u(z)}{\partial z} \right] = -\frac{\omega^2}{\epsilon_0 c^2} \mathbf{P}_{NL}(\mathbf{r}, \omega) e^{-ikz}. \tag{3.23}$$

Eq. (3.23) can be further simplified by introducing the slowly varying envelope approximation, which states that if the envelope of a wave pulse varies slowly in space and time with respect to the wavelength of the field, the following relations hold

$$\left| \frac{\partial^2 u(z)}{\partial z^2} \right| \ll \left| k \frac{\partial u(z)}{\partial z} \right|, \tag{3.24a}$$

$$\left| \frac{\partial^2 u(t)}{\partial t^2} \right| \ll \left| \omega \frac{\partial u(t)}{\partial t} \right|. \tag{3.24b}$$

The slowly varying approximation allows to rewrite Eq. (3.23) as

$$ik\mathbf{e}(\mathbf{r}_\perp,\omega)\frac{\partial u(z)}{\partial z} = -\frac{\omega^2}{\epsilon_0 c^2}\mathbf{P}_{NL}(\mathbf{r},\omega)e^{-ikz}. \tag{3.25}$$

In order to simplify the analysis, without lacking of significance, I consider only the z component of the field and I take a weak nonlinear interaction, such that the undepleted pump approximation holds [20]. In this case, the nonlinear polarization can be approximated as a constant along the propagation direction, with k_{NL} the wavevector of the nonlinearly generated wave, therefore $\mathbf{P}_{NL}(\mathbf{r},\omega) \sim \xi_{NL}e^{ik_{NL}z}$, where the ξ_{NL} is proportional to the nonlinear efficiency and to the coupling with the input wave. With these assumptions, Eq. (3.25) can be rewritten as

$$\frac{\partial u(z)}{\partial z} = i\frac{\omega^2}{\epsilon_0 kc^2}\xi_{NL}e^{-i\Delta kz}, \tag{3.26}$$

where $\Delta k = (k - k_{NL})$ is the phase mismatch parameter. Solving Eq. (3.26) results that

$$u(z) = -\frac{\omega^2}{\epsilon_0 kc^2}\xi_{NL}\frac{e^{-i\Delta kz}-1}{\Delta k}. \tag{3.27}$$

Taking then the modulus square of the envelope and considering $z = L$, with L the length of the sample,

$$|u(L)|^2 = \left(\frac{\omega^2}{2\epsilon_0 kc^2}\xi_{NL}\right)^2 L^2\mathrm{sinc}^2\left(\frac{\Delta kL}{2}\right). \tag{3.28}$$

Eq. (3.28) describes the relation between the generated power, which is proportional to $|u|^2$, and the phase mismatch parameter Δk. When $\Delta k = 0$ the maximum efficiency of the process is achieved (Fig. 3.6a). Therefore, when the phase matching is perfect, the efficiency of the process increases with a square law as a function of the waveguide length, as shown in Fig. 3.6b. On the contrary, when $\Delta k \neq 0$, the nonlinear wavelets are not in phase for the whole length of the waveguide and the generated power scales as $L^2\mathrm{sinc}^2(L\Delta k/2)$, which is a periodic function of L. According to this description, the coherence length of the process L_{coh} is introduced,

$$L_{coh} = \frac{\pi}{\Delta k}, \tag{3.29}$$

which quantifies the length where the nonlinear interaction is constructive, or, in other terms, the length for the pump and the generated wave to get out of phase [41].

The result in Eq. (3.28) can be straightforwardly generalized for the FWM case, where the propagation of multiple waves has to be taken into account and four coupled differential equations have to be solved. Considering the FWM nonlinear polarization

$$\mathbf{P}_{NL,a}(\mathbf{r},\omega_a) = \epsilon_0\chi^{(3)}\vdots 6\mathbf{E}_b(\mathbf{r},\omega_b)\mathbf{E}_c(\mathbf{r},\omega_c)\mathbf{E}_d^*(\mathbf{r},\omega_d), \tag{3.30}$$

where the indices a, b, c, d indicates the four waves involved in the process, the coupled wave equations for FWM, neglecting the propagation losses, the free carriers effect and other nonlinear phenomena like SPM and XPM, can be written as [20],

$$\frac{du_1}{dz} = 2i\gamma_{1is2}\sqrt{\frac{P_2P_iP_s}{P_1}}u_iu_su_2^*e^{i\Delta kz}, \tag{3.31a}$$

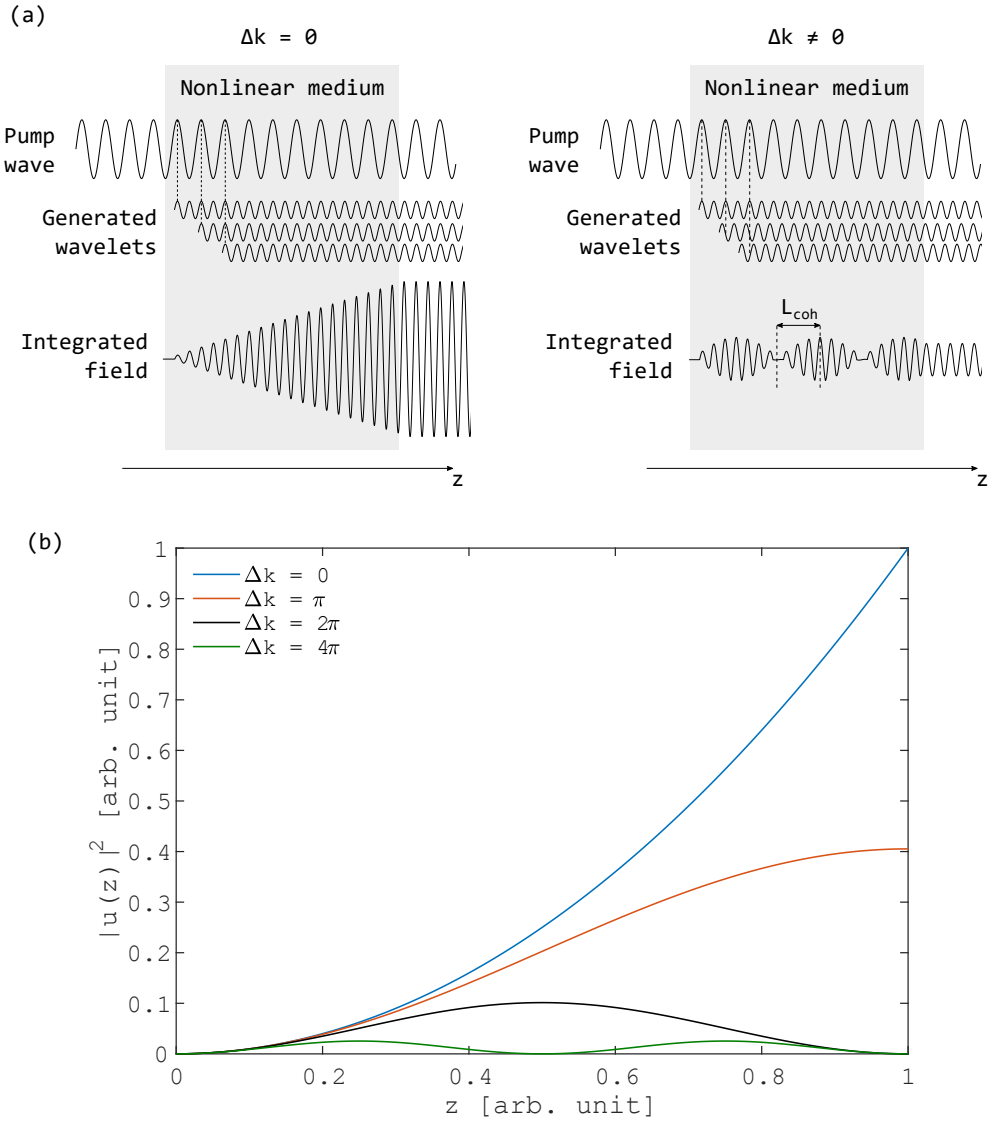

FIGURE 3.6: a) Schematic description of the nonlinear generation process at the wavelet level. When the phase matching condition is satisfied ($\Delta k = 0$), the generated wavelets add-up constructively along the whole medium, giving rise to a large total nonlinear field. The situation is different when the phase mismatch is non-zero ($\Delta k \neq 0$), which leads to limited regions of coherent summation among the wavelets. In this case, the total nonlinear field exhibits a modulation with a period that is twice the coherence length. b) $|u(z)|^2$ as a function of the propagation length z, according to Eq. (3.28). Depending on the phase mismatch parameter, the efficiency of the process scales quadratically with the propagation length ($\Delta k = 0$) or it is modulated by the sinc function as $L^2\text{sinc}^2(\Delta kL/2)$. The larger the Δk, the lower the maximum efficiency that can be obtained.

$$\frac{du_2}{dz} = 2i\gamma_{2is1}\sqrt{\frac{P_1P_iP_s}{P_2}}u_iu_su_1^*e^{i\Delta kz}, \tag{3.31b}$$

$$\frac{du_i}{dz} = 2i\gamma_{i12s}\sqrt{\frac{P_1P_2P_s}{P_i}}u_1u_2u_s^*e^{-i\Delta kz}, \tag{3.31c}$$

$$\frac{du_s}{dz} = 2i\gamma_{s12i}\sqrt{\frac{P_1P_2P_i}{P_s}}u_1u_2u_i^*e^{-i\Delta kz}, \tag{3.31d}$$

where the indices 1, 2 refer to the two input pumps, while i, s refer respectively to the idler and signal waves; P_j $(j = 1, 2, i, s)$ is the optical power of the waves, and

$$\gamma_{abcd} = \frac{3\omega_a\sqrt{n_{g,a}n_{g,b}n_{g,c}n_{g,d}}}{4\varepsilon_0 A_0 c^2}\Gamma_{abcd}, \tag{3.32}$$

with the labels a, b, c, d referring to $1, 2, s, i$, A_0 is the waveguide cross-section, $n_{g,\nu}$ the group index and

$$\Gamma_{abcd} = A_0\frac{\int_{A_0}\mathbf{e}_a^*(\mathbf{r}_\perp,\omega_a)\chi^{(3)}\vdots\mathbf{e}_b(\mathbf{r}_\perp,\omega_b)\mathbf{e}_c^*(\mathbf{r}_\perp,\omega_c)\mathbf{e}_d(\mathbf{r}_\perp,\omega_d)\ dA}{\prod_{\nu=abcd}\left(\int_{A_\infty}n_{wg}(\mathbf{r}_\perp,\omega_\nu)^2|\mathbf{e}_\nu(\mathbf{r}_\perp,\omega_\nu)|^2\ dA\right)^{1/2}}, \tag{3.33}$$

where A_∞ is the whole transverse plane and n_{wg} is the waveguide refractive index. The strength of the FWM interaction depends on the γ_{abcd} coefficients, which have been here proposed in the most general form, considering also the case in which the pump, signal and idler waves propagate with different waveguide modes $\mathbf{e}_j(\mathbf{r}_\perp,\omega_j)$. In this case, for symmetry reasons, certain modal combinations lead to a vanishing Γ_{abcd} coefficient.

Let us consider the case of single mode FWM, i.e. all the waves are on the same waveguide mode, and the undepleted pump approximation, which assumes that the pump power is not affected by the generation process. With these assumptions, the generated signal power at the end of the waveguide is

$$P_s(L) = 4\left|\gamma_{s12i}\right|^2 P_p^2(0)P_i(0)L^2\mathrm{sinc}^2\left(\frac{\Delta kL}{2}\right), \tag{3.34}$$

where $P_p(0)$, $P_i(0)$ are the input powers of the pump and idler waves. Like in the case of Eq. (3.28), the efficiency depends on the square of the propagation length modulated by the sinc function of the phase mismatch, and the same considerations apply. Moreover, Eq. (3.34) shows that the generated waves are characterized by a sinc^2 shaped bandwidth as a function of Δk or ω, as shown in Fig. 3.7, where also the role of the waveguide length is shown, with the phasematching bandwidth that increases with the reduction of L.

Eq. (3.34) highlights two key features of FWM: the linear dependence of the generated signal intensity on the stimulating idler wave intensity and the quadratic dependence on the pump power. When measuring FWM, these two dependences are used to demonstrate that the phenomenon under study is actually FWM.

3.4.2 Quantum theory of four wave mixing

In this section I will provide a brief introduction to the quantum description of the spontaneous FWM, that will be treated in much more detail in Chapter 4. Spontaneous FWM differs from the stimulated case since no stimulating wave is provided at the input of the waveguide. In this sense, the generation of signal and idler waves occurs spontaneously. Within the spontaneous FWM, the signal and idler photons are emitted simultaneously as a unique pair of photons, with the peculiar feature of being correlated in time [59]. In order to model this quantum process, the creation ($\hat{a}^\dagger$) and annihilation ($\hat{a}$) operators are introduced, which represent the generation of signal and idler photons from an initial vacuum state. In fact, from a naive point of

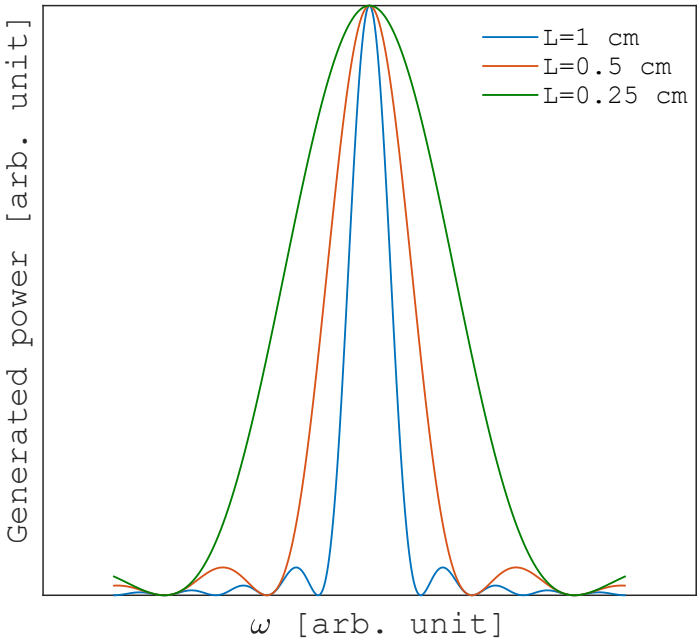

FIGURE 3.7: Normalized FWM generated signal power as a function of the frequency and waveguide length, reported in the legend. The generated signal exhibits a sinc^2 shape, with the bandwidth that increases as the waveguide length is shortened.

view, the spontaneous FWM can be interpreted with the same picture of the stimulated case, where the seed is provided by the vacuum quantum fluctuations [60]. Indeed, despite the electric field operator $\hat{\mathbf{E}}(\mathbf{r},t)$ evaluated over the vacuum state returns zero, this is not the case for the squared field operator, which results in

$$\langle 0|\,\hat{\mathbf{E}}^2(\mathbf{r},t)\,|0\rangle = \sum_j \frac{\hbar\omega_j}{2\epsilon_0 V} \tag{3.35}$$

where j runs over the radiation modes of the field and V is the quantization volume [60, 61]. Eq. (3.35) states that electric field fluctuations around the zero mean value are possible. Spontaneous FWM is fed by these fluctuations. The interaction of the electromagnetic field with the $\chi^{(3)}$ medium can be given as the sum of the linear ($\hat{H}_L$) and nonlinear ($\hat{H}_{NL}$) interaction hamiltonians as [62]

$$\hat{H}_3 = \hat{H}_L + \hat{H}_{NL}, \tag{3.36a}$$

$$\hat{H}_L = \int \mathrm{d}k\hbar\omega_k \hat{a}_k^\dagger \hat{a}_k, \tag{3.36b}$$

$$H_{NL} = -S \int \mathrm{d}k_{p1}\mathrm{d}k_{p2}\mathrm{d}k_s\mathrm{d}k_i \hat{a}_{p1}^\dagger \hat{a}_{p2}^\dagger \hat{a}_s \hat{a}_i \mathrm{e}^{i(k_{p1}+k_{p2}-k_i-k_s)z}, \tag{3.36c}$$

where S is a coefficient quantifying the strength of the interaction which includes also the γ parameter. In order to derive the two-photon state $|\Psi_2\rangle$ describing the signal-idler pair the perturbation theory is used [63], where the initial state $|\Psi_{in}\rangle$ is evolved as

$$|\mathrm{II}\rangle = \mathrm{e}^{-\frac{i}{\hbar}\int \hat{H}_3(t)dt}\,|\Psi_{in}\rangle\,. \tag{3.37}$$

In the case of degenerate spontaneous FWM, $|\Psi\rangle_{in} = |\alpha\rangle\,|0_s, 0_i\rangle$, since initially

the pump is described by a coherent state $|\alpha\rangle$ with $|\alpha|^2$ the average photon number and the signal and idler modes are unoccupied. The generated two-photon state results to be [61]

$$|\mathrm{II}\rangle = |\alpha\rangle\,|0_s, 0_i\rangle + \frac{\alpha^2 SL}{\sqrt{2}}\mathrm{sinc}\left(\frac{\Delta kL}{2}\right)|\alpha\rangle\,|1_s, 1_i\rangle\,, \tag{3.38}$$

where multipair states, like $|2_s, 2_i\rangle$, $|3_s, 3_i\rangle$, have been neglected due to their low generation probability at low input pump power. Starting from Eq. (3.38), it is possible to calculate the photon detection probability, which results to be proportional to $\frac{\alpha^4 S^2 L^2}{2}\mathrm{sinc}^2\left(\frac{\Delta kL}{2}\right)$. This resembles the result in Eq. (3.34) for the stimulated case, showing that the main parameters ruling the classical case are the same also for the spontaneous case. Another characteristic feature of the spontaneous process is that the signal and idler should be equal in terms of photon number per pulse, since they come in pairs.

In more general terms, the two-photon state can be given as

$$|\mathrm{II}\rangle \sim \int\int \mathrm{d}\omega_s \mathrm{d}\omega_i F(\omega_s, \omega_i)\hat{a}_s^\dagger \hat{a}_i^\dagger\,|0_s, 0_i\rangle\,, \tag{3.39}$$

with $\hat{a}_q^\dagger$ representing the generation of one photon in mode q and $F(\omega_s, \omega_i)$ the bi-photon wavefunction, which is a function of both the pump and phase matching envelopes and it will be described in detail in Chapter 4. Depending on the shape of the bi-photon wavefunction, the idler and signal paired photons can display a variable degree of entanglement, which can range from a perfect time-energy entanglement to a completely decorrelated state [59].

3.5 Phase matching considerations

As already introduced in Section 3.4.1, one of the crucial conditions for the efficiency of FWM is the phase matching. The phase matching problem comes from the chromatic dispersion of the material, by which the refractive index of the medium increases nonlinearly and monotonically with the frequency [41]. Because of this, in a bulk material the wavevector iscreases as a function of the frequency, $k(\omega) = n(\omega)\omega/c$, thus the phase mismatch $\Delta k = k_{p1} + k_{p2} - k_s - k_i$ cannot vanish whatever the frequencies involved [41]. This feature is strictly related to the GVD of the material, which in bulk media is usually normal ($\beta_2 > 0$) and prevents the phase matching. Aiming at $\Delta k = 0$, it is necessary to control the wavevectors of the involved waves, in such a way that the phase mismatch parameter can be designed to zero.

One of the first approaches to the perfect phase matching for SHG in bulk crystals was the phase matching based on **birefringence** [41]. The phase matching condition for SHG [41],

$$n(\omega_p) = n(2\omega_p), \tag{3.40}$$

according to the dispersion argument of before, is impossible. However, several crystals display a birefringent nature, by which the light experiences a different refractive index value depending on its polarization; in fact, in the case of uniaxial materials, if the light is polarized in the direction of the optical axis of the crystal, the experienced refractive index is said to be *extraordinary* (n_e), and it is different from the one saw by light polarized perpendicular to the optical axis, which is called *ordinary* (n_o). n_e and n_o are different functions of the frequency, as qualitatively shown in

Fig. 3.8a. Their different values can be exploited to phase match the SHG process by taking the pump as the ordinary wave and the generated light as the extraordinary wave, as depicted in Fig. 3.8a, such that $n_o(\omega_p) = n_e(2\omega_p)$. The case of birefringence phase matching, which can be analogously applied also to FWM [64], well explains the basic approach to perfect phase matching, that is considering directly and independently the refractive index value experienced by the waves involved in the nonlinear process. However, despite birefringence is common in many crystals, bulk silicon has a negligible birefringence, around five orders of magnitude lower than silica [65], making this technique not attractive for integrated photonics.

Another well developed approach to phase matching is the so called **quasi-phasematching**. As already introduced in Section 3.4.1, if a phase mismatch is present, the nonlinear waves can interact constructively only for a limited length in the medium, namely the coherence length. In the case of SHG, when a phase mismatch is present, as soon as the the interaction exceeds the coherence length, destructive interference occurs due to the generation of counter-phased harmonic wavelets. Within this picture, to recover constructive interference it is sufficient to reverse the sign of $\chi^{(2)}$. In practical terms, this procedure is known as *poling* and periodically poled materials are structures fabricated such that the orientation of one of the crystalline axes is inverted periodically as a function of the position along the material [66]. This results in a modulated nonlinear coefficient, as depicted in the inset of Fig. 3.8b. The poling can be modelled as a square wave going from $+c_{NL}$ to $-c_{NL}$ (being c_{NL} the nonlinear coefficient) with $\Lambda = 2L_{coh}$ spatial periodicity. In the phase matching relation for poled materials, it appears as an extra phase, such that

$$\Delta k = 2k_p - k_{SHG} - \frac{2\pi}{\Lambda}. \tag{3.41}$$

Quasi-phasematching is a very successful technique when working with materials that does not display any birefringence, e.g. for FWM in silicon [67], but it requires a fabrication process not straightforward, especially in silicon photonics. Moreover, perfect phasematching is always preferable because it is more efficient than the quasi-phase matching, as shown in Fig. 3.8b.

3.5.1 Phase matching in a waveguide

Focusing now on phase matching in silicon photonics, the first consideration is that the medium is highly nonlinear and other $\chi^{(3)}$ effects, different from the one to be phase matched, may arise, modifying the phase matching relation. It is the case of SPM, which directly affects the phase of the propagating pump wave, affecting the phase mismatch as [20]

$$\Delta k = k_{p1} + k_{p2} - k_s - k_i - 2\gamma \left(P_{p1} + P_{p2}\right). \tag{3.42}$$

The presence of the phase induced by SPM becomes important only when very high pump intensities are involved, thus with small cross-section waveguides or with high peak powers. It contributes shifting the position of the phase matching. In order to simplify the description, without losing in generality, I will neglect this term from here on. This is also justified because the work reported in this thesis is exclusively performed with multimode waveguides, where the large cross-section lowers the involved intensity.

When light is confined in a waveguide the propagation properties are affected by the confinement and by the surrounding materials. Thanks to this, it is possible

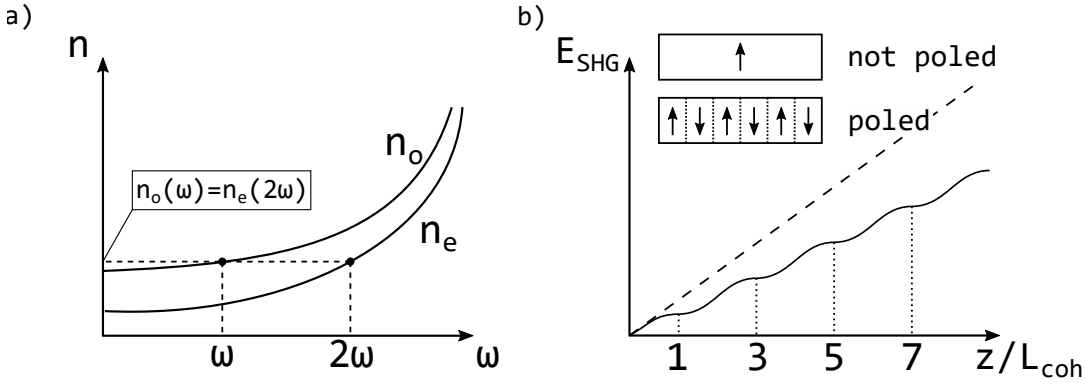

FIGURE 3.8: a) Extraordinary and ordinary refractive index for birefringent phase matching. The case of phase matched SHG is shown, where the fundamental wave at ω has the same refractive index of the SHG wave at 2ω. b) Quasi-phasematching technique. In the inset the schematics of the periodically poled material is shown, where the arrow represents the nonlinear coefficient orientation with and without the poling. The graph describes the increase in the generated SHG field amplitude in the case of perfect phasematching (dashed line) and quasi-phasematching (continuous line). The perfect phasematching exhibits higher performance with respect to the quasi-phasematching case.

to tailor the dispersion experienced by the guided light by acting on the geometry of the waveguide, controlling the wavevectors of the propagating waves [47]. This feature is of crucial importance in nonlinear photonics, where the opportunity to engineer the dispersion of the device allows to tune the phase mismatch parameter, controlling its value and achieving the phase matching condition. The first step is to consider the propagation constant β and its Taylor expansion around ω_0,

$$\begin{aligned}\beta(\omega) =&\beta_0(\omega_0) + \beta_1(\omega_0)(\omega-\omega_0) + \frac{1}{2}\beta_2(\omega_0)(\omega-\omega_0)^2 + \\ &+ \frac{1}{6}\beta_3(\omega_0)(\omega-\omega_0)^3 + \frac{1}{24}\beta_4(\omega_0)(\omega-\omega_0)^4 + \dots,\end{aligned} \tag{3.43}$$

where β_n are the group velocity dispersion terms. Let us consider a degenerate FWM process, with all the waves on the same waveguide mode, that is the standard FWM condition. The phase matching condition is

$$\Delta k = 2k(\omega_p) - k(\omega_s) - k(\omega_i). \tag{3.44}$$

or, considering that $k \equiv \beta$,

$$\Delta\beta = 2\beta(\omega_p) - \beta(\omega_s) - \beta(\omega_i). \tag{3.45}$$

The propagation constants can be Taylor expanded around ω_p according to Eq. (3.43), such that

$$\beta(\omega_p) = \beta_0, \tag{3.46a}$$

$$\beta(\omega_i) = \beta_0 + \beta_1\Delta\omega + \frac{1}{2}\beta_2\Delta\omega^2 + \frac{1}{6}\beta_3\Delta\omega^3 + \frac{1}{24}\beta_4\Delta\omega^4 + \dots, \tag{3.46b}$$

$$\beta(\omega_s) = \beta_0 - \beta_1\Delta\omega + \frac{1}{2}\beta_2\Delta\omega^2 - \frac{1}{6}\beta_3\Delta\omega^3 + \frac{1}{24}\beta_4\Delta\omega^4 + \dots, \tag{3.46c}$$

where $\Delta\omega = \omega_i - \omega_p = \omega_p - \omega_s$ and β_j $(j = 0, 1, 2, 3, 4)$ are evaluated in ω_p. In Eq. (3.46), $\beta(\omega_p)$ does not exhibit higher order terms since in this expansion $\Delta\omega = \omega_p - \omega_p = 0$. It has also to be noticed that odd terms in $\beta(\omega_s)$ have the opposite sign with respect to the odd terms in $\beta(\omega_i)$, because $\omega_i - \omega_p = -(\omega_s - \omega_p)$. By inserting the expanded propagation constants of Eq. (3.46) into Eq. (3.45), $\Delta\beta$ becomes

$$\Delta\beta = -\beta_2(\omega_p)\Delta\omega^2. \tag{3.47}$$

Eq. (3.47) states that the perfect phase matching can be achieved with $\beta_2(\omega_p) = 0$, that, in terms of wavelengths, corresponds to the zero dispersion wavelength (ZDW) [5]. If also a small negative contribution is present in the phase mismatch, like the nonlinear phase induced by SPM, then $\beta_2(\omega_p)$ should be negative, which corresponds to the anomalous GVD. This means that in order to fabricate the right geometry to phase match the process at a certain pump wavelength, a careful numerical modelling of the waveguide dispersion is required. In Fig. 3.9a are reported the β_2 functions for three channel waveguides with different widths and the same height of 243 nm; from the figure it is evident the difficult task of engineering the waveguide to have exactly the desired value of β_2, which varies critically with the width. In fact, just a variation from 0.5 to 1 μm in waveguide width induces a large variation in the ZDW and GVD behaviour. Eq. (3.47) gives also information on the bandwidth of the phase matching. In fact, looking at Eq. (3.34), we can consider $\Delta\beta_{max} = 4/L$ the maximum tolerable phase mismatch; therefore, by plugging $\Delta\beta_{max}$ into Eq. (3.47), the relation between the process bandwidth BW and the length L of the sample is found as [20]

$$\mathrm{BW} \simeq \sqrt{\frac{\Delta\beta_{max}}{\beta_2(\omega_p)}} = \sqrt{\frac{4}{L\beta_2(\omega_p)}}, \tag{3.48}$$

which is compatible with the qualitative spectra reported in Fig. 3.7. It has to be noticed that this kind of phase matching has the phase matching band centered at the pump wavelength, giving rise to the so called *continuous band phase matching*.

Eq. (3.47) holds till $\Delta\omega$ is small; as soon as the detuning increases, also higher order terms in the expansion become important, and the phase mismatch has to be rewritten as

$$\Delta\beta = -\beta_2(\omega_p)\Delta\omega^2 - \frac{1}{12}\beta_4(\omega_p)\Delta\omega^4. \tag{3.49}$$

In this case the phase matching is achieved when $\beta_2(\omega_p)$ and $\beta_4(\omega_p)$ have opposite sign [68]. Therefore β_4 can be used to compensate the phase mismatch carried by the β_2 term, giving rise to a phase matching bandwidth centered at the phase matching wavelength, that is different from the pump wavelength. This kind of situation is called *discrete band phase matching* [7]. This technique has been used to perform a spectral translation from 2440 nm to 1620 nm [48]. However, relying on the GVD terms for the phase matching is not always the best choice when considering a practical implementation, because the higher order terms might be much more important than what expected, as shown in Fig. 3.9b. Here the phase mismatch is calculated using the full effective index dispersions of the waves (dashed line). This is compared with the phase mismatch calculated with the higher order β terms. The Δk calculated with the β's at the pump wavelength considered (1.55 μm) does not predict the phase matching in the spectral position expected by the exact calculation with the effective index; to recover the phase matching at the same wavelength, the pump has to be moved to 1.94 μm. Moreover, also a small variation of the waveguide

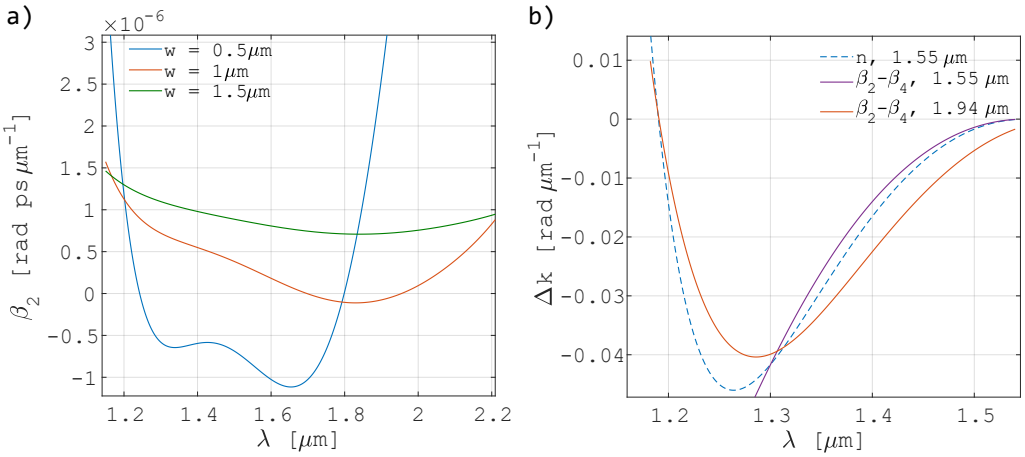

FIGURE 3.9: a) β_2 as a function of the wavelength for different waveguide widths. The β_2 value is critically dependent on the geometry of the waveguide, which makes the engineering of the dispersion a non trivial task. b) Phase mismatch as a function of the idler wavelength for a 2 μm wide waveguide with 243 nm height. The Δk calculated considering the full effective indices of the waves (dashed line) is compare with those calculated with the dispersion compensation ($\beta_2 - \beta_4$). The phase matching is calculated around 1.19 μm by the full effective index treatment with 1.55 μm pump wavelength, while the dispersion compensation method fails to calculate its spectral position with the same pump wavelength (purple line). The phase matching in the expected position is recovered with 1.94 μm pump wavelength (red line).

affects critically the phase matching. These examples show that the phase matching based on the higher order terms is efficient, but is affected by errors in real devices.

Thus far we have considered only the first order waveguide mode, which forces the engineering of the GVD terms. However, it is possible to use different propagation constants of different order modes to earn one more degree of freedom in designing the phase matching. This is the case of intermodal phase matching, where higher order waveguide modes are used, with their different effective index profiles, as shown in Fig. 3.10. This allows tuning the propagation constant of each wave independently, thus improving the control on the phase matching condition. Up to now, intermodal FWM has been demonstrated only in high-order-mode optical fibers [55, 69, 70] and in photonic crystal optical fibers [71]. The only example of intermodal phase matching in an integrated device was reported with Brillouin scattering [72], but FWM has never been investigated. With our work we reported the first experimental demonstration of intermodal FWM in waveguides [73], which was rapidly followed by several other works exploiting this kind of phase matching approach for FWM in integrated platforms [74, 75, 76, 77]. The full description, analysis and experimental demonstration of intermodal FWM are reported in the next section.

3.6 Intermodal four wave mixing in silicon waveguides: theory and experimental demonstration

This section has been largely derived from my work in Ref. [73].

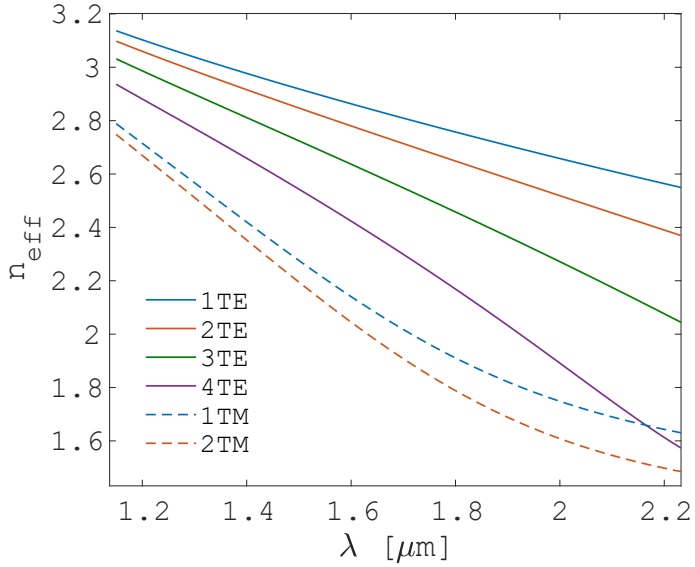

FIGURE 3.10: Effective indices in a $(2 \times 0.243)\ \mu m^2$ waveguide. In the legend are reported the polarization and the waveguide mode order.

As already introduced in Section 3.5, tailoring the dispersion of waveguides is a good solution for high efficient FWM, but it also has few limitations. First of all, phase matching by GVD compensation can be achieved only far from the pump wavelength, making this process not suitable for all those applications requiring a tunable wavelength conversion in the C-band (1530-1565 nm). Then, it exhibits a critical dependence on the geometry, which on one side enables high control on the generation process by means of the geometrical features, but on the other side makes the device fabrication intolerant. In order to face these drawbacks, it is possible to take advantage of the higher order modes propagating in a multimode waveguide, whose different effective index profiles can be used to phase match the FWM waves [73]. Moreover, introducing actively the higher order modes in the silicon platform opens new perspectives in terms of interfacing the nonlinear process with the developing multimode integrated platform. As an example, it has been recently investigated a new functionality based on higher order intramodal FWM providing mode-selective wavelength conversion for high-speed and controllable on-chip data transfer [78, 79, 80]. However, the multimode nonlinearities are even more interesting under the intermodal point of view. Intermodal FWM has the advantage of not requiring anomalous GVD (group velocity dispersion), which is usually considered for intramodal FWM to achieve phase matching [81, 82]. This results in an easier handling of the phase matching condition [70], which exhibits also much more flexibility thanks to the extra degree of freedom introduced by the waveguide modes. What it is interesting in intermodal phase matching is the fact that, depending on the excited optical modes and on the geometry of the waveguide, the wavelength of the phase matched discrete bands can be easily controlled. We demonstrate that this allows getting largely tunable spectral conversions, from nearby to the pump up to very large detunings. In fact, we show spontaneous FWM with an idler ranging from 1469 nm to 1202 nm, when the pump is at 1550 nm. To the best of our knowledge, this is the largest spectral detuning achieved by FWM in a SOI waveguide with a C-band pump. This paves the way to the application of intermodal FWM for MDM within

the telecom technology. In addition, broadband and highly tunable on-chip wavelength conversion can be applied in gas sensing [83], mid infrared (MIR) detection [84] and MIR light generation [49]. Moreover, the large detuning combined with the spontaneous generation can be used to get on-chip heralded single photon sources with the heralder photon generated at short wavelengths, where high efficient single photon detectors are available, and the heralded photon generated beyond 2 μm, as will be extensively explained in Chapter 4. The high controllability is also of great advantage when dealing with the Raman noise, which is always present due to the nonlinear process of Raman scattering, which appears as an intense peak shifted by 15.6 THz with respect to the pump frequency [15]. Generating the discrete band of photons far from the Raman peak is of great interest for quantum devices, where the presence of the Raman noise has detrimental effects over the purity of the generated quantum states [85].

In this section, I describe the intermodal phase matching technique, reporting the experimental demonstration of intermodal FWM in silicon waveguides. I extensively investigated a particular modal combination involving the pump on both the first and second TE modes and the signal and idler on, respectively, the second and first TE modes. Moreover, I report also of other modal combinations, involving up to the third order mode and with both TE and TM polarizations.

3.7 Theory

3.7.1 Multimode waveguides

The cross-section of the waveguides used in the experiment is reported in Fig. 3.11a. These waveguides have been fabricated on a SOI 6' wafer, with a BOX of 3 μm and a silicon device layer of 243 nm. The waveguides were defined by 365 nm lithography. Reactive ion etching was used to pattern the waveguides, which were then cladded by 900 nm thick SiO_2 deposited by plasma-enhanced chemical vapor deposition (PECVD). The waveguide width ranged from 2 μm to 3.8 μm.
By using a commercial finite element method (FEM) software (COMSOL), we computed the modal field profiles and the effective indices for these multimode waveguides. It is possible to control the effective index value of the propagating wave by selective excitation of a specific optical mode, as shown in Fig. 3.10. Moreover, the index dispersion depends critically also on the waveguide width, as reported in Fig. 3.11c and in Fig. 3.11d. As alredy said, tailoring the index dispersion through the geometry of the waveguide is of crucial importance for the control of the phase matching condition [86].

3.7.2 Intermodal phase matching for four wave mixing

Let us consider the degenerate FWM, which is the most used FWM process. Despite the two pumps have the same frequency, in a multimode waveguide they can propagate on different waveguide modes, thus with different effective indices n_{eff}. Since the wavevector is written as $k = \frac{\omega}{c} n_{eff}$, with c the light velocity, the result is that the two pumps have the same frequency but different wavevectors.
FWM is ruled by the usual energy conservation relation (3.50) and momentum conservation relation (3.51),

$$\omega_p + \omega_p = \omega_s + \omega_i, \tag{3.50}$$

$$k_{p1} + k_{p2} = k_s + k_i, \tag{3.51}$$

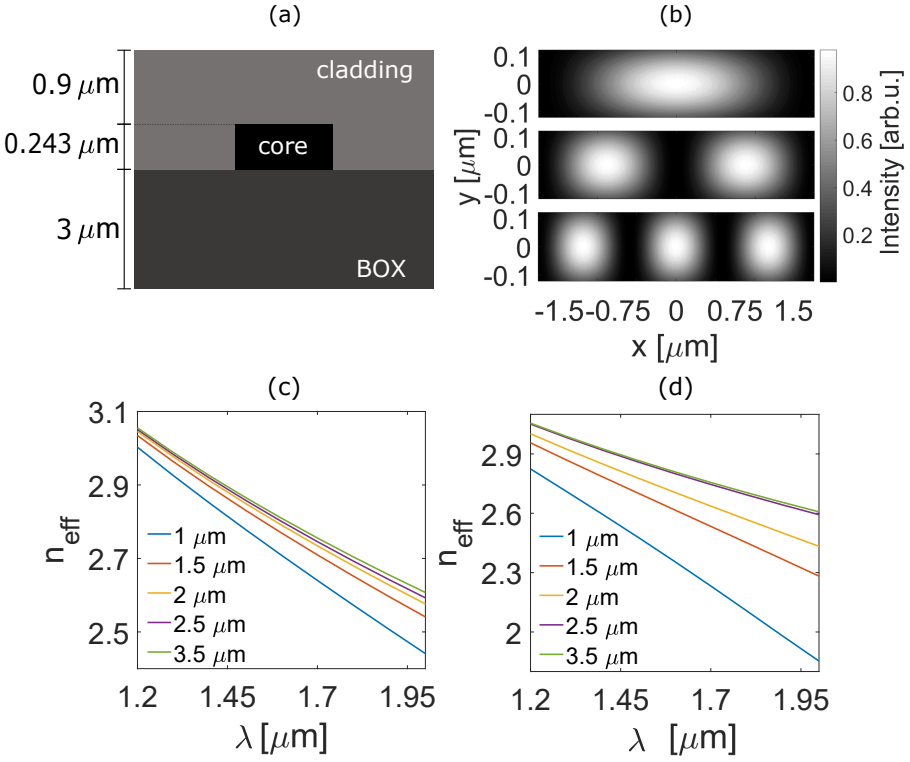

FIGURE 3.11: a) Cross-section of the waveguides used in this work. BOX refers to the buried oxide. The core is made of crystalline Si, and the cladding by a deposited SiO_2. b) Computed intensity profiles in the core region of the first three TE modes supported by a 3.5 μm wide waveguide. c) Effective index as a function of the wavelength for the 1^{st} TE mode for the different waveguide widths reported in the legend. d) Effective index as a function of the wavelength for the 2^{nd} TE mode for the different waveguide widths reported in the legend.

where the indices $p1$, $p2$, s, i refer to the first pump, second pump, signal and idler, respectively.

I rewrite here the already introduced phase mismatch Δk for FWM,

$$\Delta k = \Delta k_L + \Delta k_{NL}, \tag{3.52}$$

where $\Delta k_L = k_s + k_i - k_{p1} - k_{p2}$ is the linear phase mismatch and $\Delta k_{NL} = \gamma_{p1} P_{p1} + \gamma_{p2} P_{p2}$ quantifies the phase contribution to Δk due to SPM of the pumps [87]. γ_{p1} and γ_{p2} are the nonlinear coefficients for the two pumps [20], and P_{p1}, P_{p2} are the powers of the two pumps.
Δk_L in a multimode waveguide can be written as [88]

$$\Delta k_L = \frac{\omega_p}{c} n^j_{eff}(\omega_p) + \frac{\omega_p}{c} n^q_{eff}(\omega_p) - \frac{\omega_s}{c} n^l_{eff}(\omega_s) - \frac{\omega_i}{c} n^m_{eff}(\omega_i), \tag{3.53}$$

where j, q, l, m are as in (3.57). In the following we use the convention that the modal combination involved in the FWM process is indicated as (j, q, l, m), i.e. one pump photon on the j-th order mode, the other pump photon on the q-th order mode, the signal photon on the l-th order mode and the idler on the m-th order mode. Looking at Eq. (3.53), and indicating the waveguide modes of the pumps, signal and idler

with the labels $p1, p2, s, i$, the most feasible scenarios are:

1. $p1 = p2 = s = i$, that is the intramodal FWM with generalized mode order,
2. $p1 = p2 \neq s = i$, which correspond to the pumps on one mode and the signal and idler on another one,
3. $p1 = s \neq p2 = i$, or $p1 = i \neq p2 = s$, where one pump has the same mode of the idler, and the other pump propagates on the same mode of the signal.

While for the first case, intramodal FWM, the phase matching analysis is the same carried out in Section 3.5, for the second and third cases the treatment is different, and will be studied in the following considering the Taylor expansion of the propagation constants β on the group velocity terms.

Intermodal FWM with p1 = p2 ≠ s = i

When dealing with higher order modes, each mode has a different propagation constant β_m, with m the mode order, whose group velocity terms are indicated as $\beta_{n,m}$, with n the order of the expansion term. The phase mismatch $\Delta\beta$, considering the higher order modes and the expansion in Eq. (3.43) around ω_p, becomes

$$\Delta\beta = 2\left(\beta_{0,p1} - \beta_{0,s}\right) - \beta_{2,s}\Delta\omega^2 - \frac{1}{12}\beta_{4,s}\Delta\omega^4, \tag{3.54}$$

where the expansion has been truncated at the fourth term. Depending on the magnitude of $\Delta\omega = \omega_i - \omega_p = \omega_p - \omega_s$, the terms in Eq. (3.54) can be neglected at different expansion orders, exactly like in the intramodal case. This intermodal combination is very similar to the intramodal case, with the only difference that an extra constant is present due to the mismatch between the zero order expansion terms $\beta_{0,p1}$ and $\beta_{0,s}$. This means that the same considerations for the β_2 and β_4 terms already done in the intramodal case in Section 3.5 are valid here with the proper modifications due to the zero order term, which is also the peculiarity of this intermodal combination. In fact, with respect to the intramodal case, the phase matching cannot be achieved at very small values of detuning ($\Delta\omega \sim 0$), due to $\left(\beta_{0,p1} - \beta_{0,s}\right)$, which cannot vanish since $\beta_{0,p1} \neq \beta_{0,s}$ if $p1 \neq s$.

Intermodal FWM with p1 = s ≠ p2 = i or p1 = i ≠ p2 = s

Considering again the expansion around ω_p in Eq. (3.43) for the higher order modes, the phase mismatch parameter, with $\Delta\omega$ small, can be rewritten truncating the expansion at the second order dispersion term as

$$\Delta\beta = -\left(\beta_{1,i} - \beta_{1,s}\right)\Delta\omega - \frac{1}{2}\left(\beta_{2,i} + \beta_{2,s}\right)\Delta\omega^2. \tag{3.55}$$

Eq. (3.55) suggests that the group velocity mismatch, first term in the equation, can be compensated by the β_2 terms of idler and signal, which do not need to be negative if $\beta_{1,i} < \beta_{1,s}$, i.e. no anomalous dispersion is required if the idler mode order is lower than the signal mode order. In fact, the higher the order mode, the higher the β_1 term. On the contrary, if $\beta_{1,i} > \beta_{1,s}$, anomalous GVD is required by at list one of the two modes. As soon as the spectral detuning increases, also the higher

order terms in the expansion have to be considered, giving

$$\begin{aligned}\Delta\beta = &-(\beta_{1,i}-\beta_{1,s})\,\Delta\omega - \frac{1}{2}(\beta_{2,i}+\beta_{2,s})\,\Delta\omega^2 \\ &-\frac{1}{6}(\beta_{3,i}-\beta_{3,s})\,\Delta\omega^3 - \frac{1}{24}(\beta_{4,i}+\beta_{4,s})\,\Delta\omega^4.\end{aligned} \tag{3.56}$$

As already seen with the intramodal phase matching in Fig. 3.9b, also for the intermodal case the best design practice is to consider the full effective index profiles in the phase matching relation, especially when dealing with large spectral translations. Comparing the intermodal phase matching with the intramodal, the first conclusion is that, when no dispersion compensation is introduced for the intramodal case, the intermodal exhibits a discrete phase matching that can be tuned away from the pump, while the intramodal displays phase matching only close to the pump wavelength, as simulated in Fig. 3.12, with a continuous band.

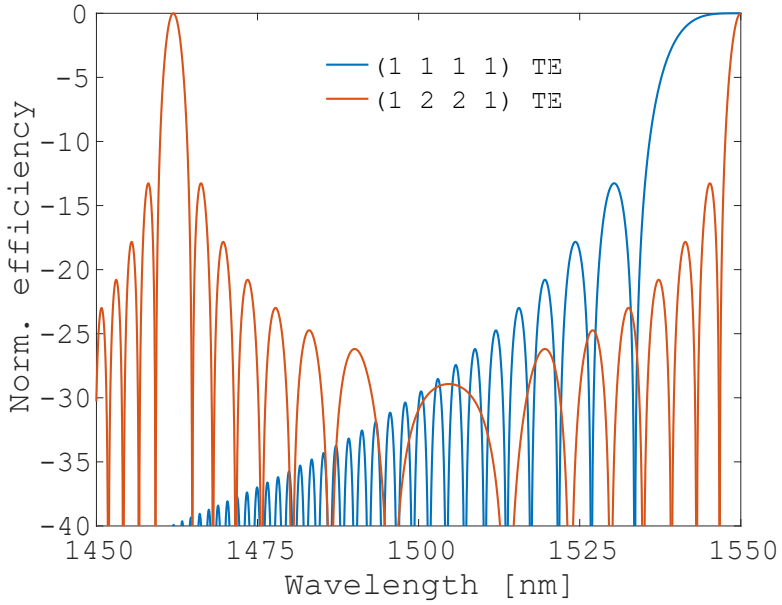

FIGURE 3.12: Spectral dependence of the idler generation efficiency for the (1,1,1,1) intramodal FWM and for the (1,2,2,1) intermodal FWM. All waves have TE polarization. A silicon waveguide with a cross-section 3.5 $\mu m \times 243\,nm$ was assumed in the calculation. Each efficiency is normalized to its maximum.

In the case of far detuning phase matching (PM), where the β_4 compensation is needed for the intramodal case, the intermodal PM allows generating an idler at $\sim 1.2\ \mu m$ with a pump at $1.55\ \mu m$ with lower sensibility to the geometry or pump deviations from the nominal values, see Fig. 3.13. Here, I considered the 1221TE combination in a $(1.98 \times 0.243)\ \mu m^2$ waveguide for the intermodal PM and a $(0.5 \times 0.243)\ \mu m^2$ waveguide for the intramodal case. In order to quantify the tolerance to the fabrication imperfections, I considered a deviation of $\pm 50 nm$ from the nominal waveguide width. The change in the phase matched idler wavelength as a function of the width deviation is reported in Fig. 3.13a.

By fitting with a linear function ($y = a + bx$) these simulated points, I found that, in these particular conditions, the intramodal PM has $b = -0.819\,(-0.931, 0.707)$ while the intermodal PM has $b = 0.55\,(0.53, 0.57)$, where in the parenthesis are

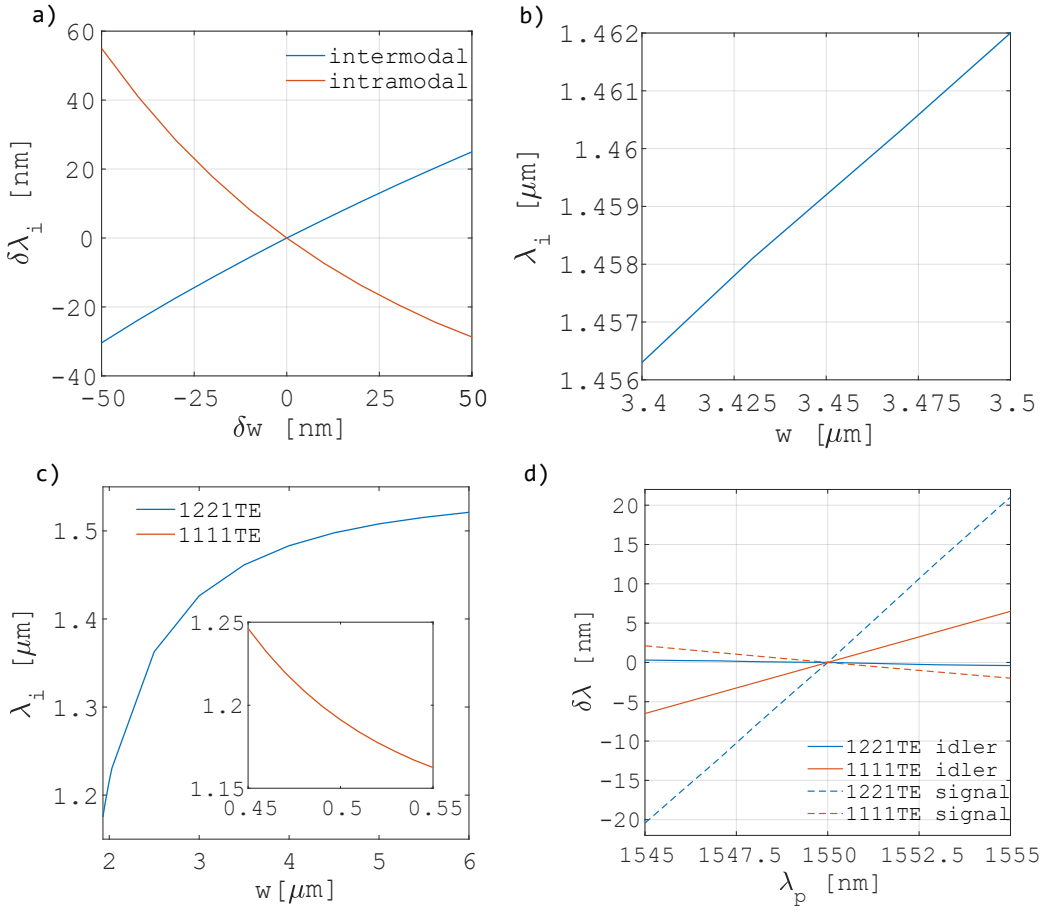

FIGURE 3.13: a) The fabrication tolereance of intramodal FWM in a 0.5 μm wide waveguide is compared with the one of intermodal 1221TE FWM in a 1.98 μm wide waveguide (height = 243 nm). The graph reports the simulated deviation from the idler phase matching position $(\delta\lambda_i)$ with respect to the deviation from the nominal waveguide width (δw). b) Idler wavelength (λ_i) for 1221TE combination as a function of the waveguide width (w). c) Idler phase matching wavelength as a function of the waveguide width. The intramodal FWM can be achieved only in a limited spectral range with respect to the intermodal case. d) Deviation from the phase matching position with 1.55 μm pump wavelength $(\delta\lambda)$ versus the pump wavelength (λ_p). The intermodal combination exhibits much larger signal sensitivity to pump wavelength.

reported the 95% confidence bounds. Intuitively b represents the deviation of the idler wavelength in nm given a deviation of $1nm$ in the width. Therefore the intramodal PM exhibits a sensitivity to the width deviations that is 49% higher than the intermodal case. Almost the same relative sensitivity is obtained considering the signal wavelength, with $b = 2.735\,(2.475, 2.995)$ for the intramodal PM and $b = -1.806\,(-1.930, -1.683)$ for the intermodal PM. Considering the typical fabrication deviation for standard lithography technologies, $\sim \pm 20nm$, the idler can be generated, around the nominal idler wavelength, within a range of $32nm$ in the intramodal case and $20nm$ in the intermodal PM. Regarding the intermodal PM, if a generation closer to the pump wavelength was considered, for example with a 3.45 μm waveguide width generating the idler at 1.459 μm with 1.55 μm pump wavelength, the idler would be found in a range of 2.2 nm with the same width deviation

of $\pm 20\,nm$, as shown in Fig. 3.13b. Therefore, it can be concluded that as the waveguide width increases, generating the wavelength closer to the pump wavelength, the fabrication tolerance also increases, with a good fabrication robustness. Moreover, intermodal FWM has the possibility to generate over a wide spectral range with respect to the intramodal PM. In Fig. 3.13c is reported the idler wavelength as a function of the waveguide width for the 1221TE intermodal PM (blu line) and the 1111TE intramodal PM (inset, red line), both with 1.55 μm pump wavelength. While the generated idler for the intermodal process spans from 1.2 μm to 1.52 μm, the intramodal idler is limited to the 1.15 - 1.25 μm range, due to the large dispersion change occurring outside this width range. This means that while the intermodal PM can be used to generate light almost everywhere above 1.15 μm, the intramodal approach is limited to a narrow spectral region. Clearly, this analysis has been carried out with a fixed pump wavelength; by modifying the pump wavelength it is possible to tune even more the spectral position of the generated light. From the comparison here reported it is possible to conclude that the intermodal PM exhibits larger fabrication tolerance, it is able to cover all the spectrum above 1.15 μm and does not require a careful control of the ZDW and anomalous GVD like the intramodal phase matching. Moreover, an interesting feature, peculiar of the intermodal approach, arises when considering the variation of the pump wavelength with fixed waveguide geometry. In Fig. 3.13d are reported the wavelength deviations of the idler and signal wavelengths as the pump is moved from 1.55 μm. The wavelength deviation is fitted with a linear function. The intramodal 1111TE combination in a 0.5 μm wide waveguide is compared with the intermodal 1221TE combination in a 1.98 μm wide waveguide; both the waveguides have 243 nm height. For the intramodal 1111TE, the idler and signal slopes are respectively 1.3000 (1.3001,1.2999) and -0.4119 (-0.4168,-0.4069), while for the intermodal 1221TE the slopes are -0.0736 (-0.0788,-0.0685) for the idler and 4.158 (4.133,4.182) for the signal. It is immediately evident that while the intramodal PM exhibits a notable variation with both the signal and idler, with slightly higher slope for the idler, the intermodal case, due to the different dispersion profile of the two modes involved, has a negligible variation for the idler while the signal is highly sensitive to the pump wavelength. This feature is extremely interesting for the application in the field of gas sensing, where it is required a good tunability of the signal generation to span the gas absorption spectrum keeping at the same time a low device complexity [12]. These characteristics can be achieved with this intermodal process, where the signal can be largely modified by small variations of the pump wavelength and the idler can be used as the stimulating signal which, as shown in Fig. 3.13d, does not require any spectral tuning, making the device even more simple.

3.7.3 Mode field overlap and efficiency

Provided that Eq. (3.50) is fulfilled, the efficiency η of FWM in a waveguide of length L scales with the phase mismatch Δk as in Eq. (3.34),

$$\eta_{jqlm} \propto |f_{jqlm}|^2 \, L^2 \, \mathrm{sinc}\left(\Delta k \frac{L}{2}\right)^2, \tag{3.57}$$

where the dependence on the mode field overlap f_{jqlm} is made explicit, with j, q, l, m indicating, respectively, the mode orders for the two pump photons, the signal and the idler photons. f_{jqlm} is similar to the Γ_{abcd} parameter of Eq. (3.33), except for the absence of the $\chi^{(3)}$ tensor, and for the combination (j, q, l, m), assuming all the waves

(j,q,l,m)	$\lvert f_{jqlm}^{norm}\rvert$		η_{jqlm}^{norm} [dB]	
	TE	TM	TE	TM
1111	1	0.852	0	-1.391
2222	0.996	0.842	-0.035	-1.494
3333	0.989	0.821	-0.096	-1.713
1221	0.665	0.562	-3.544	-5.005
1122	0.665	0.562	-3.544	-5.005
1331	0.661	0.554	-3.596	-5.130
1113	0.333	0.293	-9.551	-10.663

TABLE 3.2: Normalized mode field overlap and normalized efficiency for various TE and TM modal combinations in a $2 \times 0.243\ \mu m^2$ waveguide. The fields are evaluated at 1.55 μm wavelength.

with the same polarization, is given by [87]

$$f_{jqlm} = \frac{\int_{A_0} e_j(r_\perp,\omega_j) e_q(r_\perp,\omega_q) e_l^*(r_\perp,\omega_l) e_m^*(r_\perp,\omega_m)\,\mathrm{d}A}{\prod_{i=jqlm}\left[\int_{A_\infty} n_{wg}(r_\perp,\omega_i)^2 |e_i(r_\perp,\omega_i)|^2\,\mathrm{d}A\right]^{\frac{1}{2}}}, \tag{3.58}$$

where $r_\perp$ is the spatial coordinate in the cross-section plane, n_{wg} is the waveguide refractive index, A_0 is the waveguide cross-section, A_∞ is the whole transverse plane, and $e_{j/q/l/m}$ is the mode field profile of each wave involved in the intermodal FWM. f_{jqlm} quantifies the coupling between the fields involved in the process, thus implying that maximum FWM efficiency requires maximum overlap. Eq. (3.58) suggests also that not all the modal combinations are available for FWM: in fact, when the modal combination is such that the integrand at the numerator is odd, f_{jqlm} vanishes. Therefore, only modal combinations resulting in an even integrand are possible. This parameter depends also on the confinement of the modes, it is in fact measured as μm^{-2}, resulting in a higher value when the modes are more confined in the waveguide core. In order to compare the role of the mode field overlap when different modal combinations are considered, I reported in Table 3.2 the normalized mode field overlap $f_{jqlm}^{norm} = f_{jqlm}/f_{1111}$ and the corresponding normalized efficiency $\eta_{jqlm}^{norm} = \eta_{jqlm}/\eta_{1111}$ for various modal combinations in a $2 \times 0.243\,\mu m^2$ waveguide. All the values reported in the table have been calculated with all the modes evaluated at a wavelength of 1.55 μm. It can be seen that intramodal combinations are similar in terms of efficiency, while the intermodal combinations are all similar when of the type *aabb* or *abba* and lose more than 3 dB with respect to the intramodal case. As soon as the combination is asymmetric, with only one mode different from the others, the relative efficiency decreases dramatically to ~ -10 dB. The situation is analogous when comparing intermodal and intramodal TM combinations, which, with respect to the TE case, are even less efficient due to their larger mode area. The lower efficiency of the intermodal combinations with respect to the 1111 combination is mainly due to the spatial profile mismatch between the fields rather than to the larger effective area of the involved modes. In fact, the intramodal combinations with higher order modes, and therefore with larger mode area, have efficiencies close to the 1111 combination.

A similar analysis can be carried out with respect to the waveguide width. I consider the two modal combinations more efficient for the intermodal and intramodal

w [μm]	$\lvert f_{jqlm}^{norm} \rvert$		η_{jqlm}^{norm} [dB]	
	1111	1221	1111	1221
0.5	1	-	0	-
1	0.552	0.359	-5.161	-8.898
2	0.282	0.187	-10.995	-14.563
3	0.189	0.126	-14.471	-17.993

TABLE 3.3: Normalized mode field overlap and normalized efficiency for various waveguide widths and the same height of 0.243 μm. The fields are evaluated at 1.55 μm wavelength with TE polarization.

case, i.e. 1221TE and 1111TE. From Table 3.3 it can be seen the dramatic dependence of the efficiency on the waveguide width. Therefore, it is evident that the traditional intramodal FWM in the single mode waveguide of 0.5 μm is much more efficient than the intermodal phase matching, but it has to be considered that here losses are not taken into account. In fact, multimode waveguides experience lower losses with respect to single mode waveguide, due to the higher confinement. Moreover, when considering the typical cross sections used for state of the art broad wavelength conversion, around 1 μm width [48], the intermodal 1221 combination in the 2 μm waveguide is less efficient by -9.4 dB with respect to the 1111 combination in the 1 μm waveguide. This efficiency becomes -9.379 dB when considering the wavelengths involved in the spectral translation under analysis, i.e. $\lambda_i = 1.2\mu m$, $\lambda_p = 1.55\mu m$, $\lambda_s = 2.2\mu m$, meaning that the mode field overlap can be estimated with sufficient accuracy using the pump wavelength for all the fields. Despite the lower efficiency, the intermodal FWM enables larger spectral translations with respect to intramodal FWM with dispersion compensation [89, 7, 48]. Fig. 3.14 shows the calculated Δk for FWM in a 2-μm-wide waveguide with the 1221TE intermodal combination. It is observed that, as the pump wavelength is increased, the spectral position of the phase matching condition moves towards longer wavelengths. In this way, a very large spectral translation is obtained, with the generation of 3.5 μm signal photons when the pump approaches 1.9 μm wavelength, with a total spectral translation of about 2.2 μm, larger than the state of the art result of 860 nm with similar pump wavelength [48].

3.8 Experimental demonstration of intermodal four wave mixing

In order to demonstrate experimentally the intermodal FWM, using samples that had been already fabricated, we worked as follow. First of all, I numerically simulated the multimode waveguides, using a FEM solver to extract their effective indices. With these index profiles I solved Eq. (3.53) finding the phase matched intermodal combinations. Then, I solved the coupled wave equations of FWM with the higher order modes involved in the intermodal combinations, finding the expected efficiencies and the spectral properties. Once the simulated results were ready, it was possible to verify experimentally the process. The samples under study where simple straight multimode waveguides, without any input coupler able to excite selectively the higher order modes. Because of this, we studied an alternative approach to mode coupling based on the misalignment of the fibers used to inject and

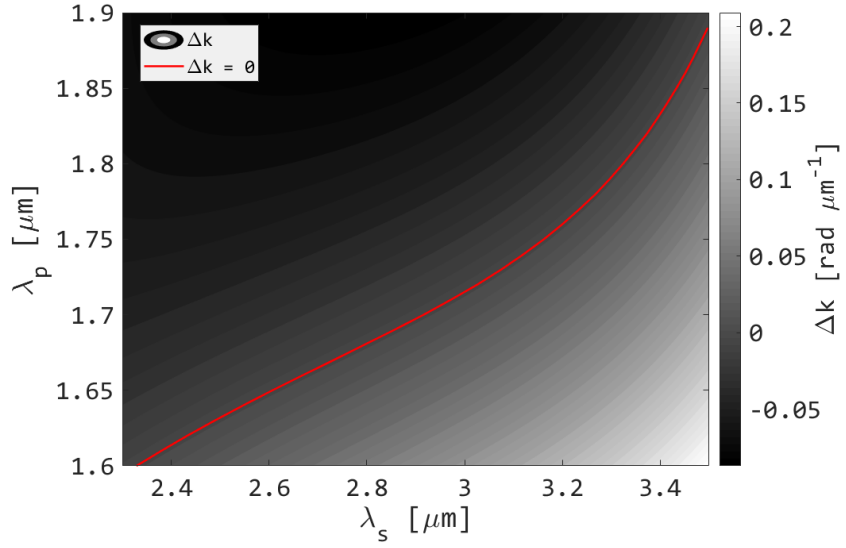

FIGURE 3.14: Numerical simulation of Δk according to Eq. (3.52) for a 2-μm-wide waveguide with (1,2,2,1) intermodal combination and TE polarization. In gray scale the Δk parameter as a function of the pump wavelength and the signal wavelength. The red line highlights the perfect phase matching spectral position.

extract the light. We studied both stimulated and spontaneous intermodal FWM with several waveguide widths, demonstrating the occurence of spontaneous and stimulated intermodal FWM over a broad spectral range (1.2 - 1.5 μm).

The samples used have been fabricated by the Centre for Materials and Microsystems of Bruno Kessler Foundation (Trento, Italy). Dr. Mattia Mancinelli and Dr. Fernando Ramiro Manzano developed the monochromator. Dr. Mattia Mancinelli and Dr. Massimo Borghi suggested the investigation of the intermodal FWM in waveguide.

3.8.1 FWM simulation and phase matching analysis

In order to extract the index profiles of the waveguide modes a FEM solver is used (COMSOL). This kind of software solves the Maxwell equations for the electromagnetic fields within the waveguide geometry. The mode solver requires the cross-section of the guiding structure with the refractive index of the materials used. In Fig. 3.15a is reported the cross-section used for the simulation of the waveguides of our experiment. The core is silicon (Si) with 243 nm height, the substrate is thermal grown silicon oxide (ThOx) 2 μm high, a layer of tetraethyl orthosilicate (TEOS) of 200 nm is deposited over the core and the top cladding is silica deposited via plasma enhanced chemical vapour deposition (PECVD). To have the lowest mismatch with respect to the experimental situation, it is fundamental to provide to the software the exact refractive index of the materials used. In our case, the foundry gave us the measured refractive indices, that I report in Fig. 3.15b.

I then numerically solved the phase matching relation derived from Eq. (3.53) as

$$\frac{2\pi}{\lambda_p} n^j_{eff}(\lambda_p) + \frac{2\pi}{\lambda_p} n^q_{eff}(\lambda_p) - \frac{2\pi}{\lambda_s} n^l_{eff}(\lambda_s) - \frac{2\pi}{\lambda_i} n^m_{eff}(\lambda_i) = 0, \tag{3.59}$$

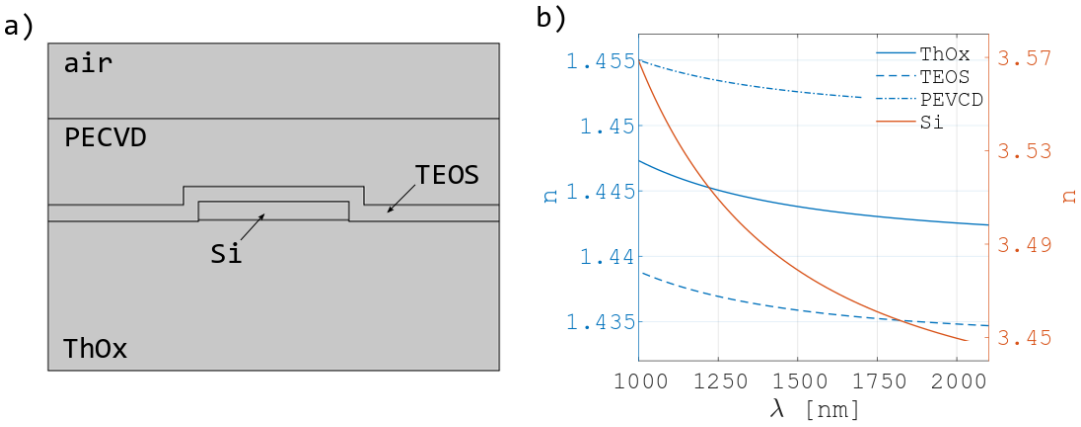

FIGURE 3.15: a) Cross-section used in the FEM solver to extract the optical properties of the modes. b) Measured refractive indices of materials used in the fabrication of the waveguides (Data from FBK-CMM center).

where $\lambda_p = 1.55\mu m$, λ_i spans over 1.15 - 2.38 μm and λ_s is moved according to the energy conservation, such that

$$\lambda_s = \left[\frac{2}{\lambda_p} - \frac{1}{\lambda_i}\right]^{-1}. \tag{3.60}$$

By cycling over all the permutations of the modal indices (j,q,l,m) it is possible to find those combinations phase matched within the spectral range considered. Both TE and TM polarizations have been considered. Through the comparison between the simulated phase matching and the experimental spectra it is possible to experimentally verify the excited modal combinations.

3.8.2 FWM coupled wave equations

We simulated the process by numerically solving the coupled wave equations of FWM [20]. In our experiment we used a pulsed laser with 40 ps pulse duration. Therefore, since the dispersion length $L_D = T_0^2/\beta_2$ [58], with T_0 the pulse duration and β_2 the GVD ($1.42 \times 10^{-6}\,\mathrm{ps}^2\mu m^{-1}$) is much longer than the waveguide length (e.g. $L_D > 1$ km for the first TE mode in a 2-μm-wide waveguide at $\lambda = 1.550\,\mu m$), we neglected the temporal dependence and we considered continuous waves in the coupled equations. For the power, the peak power of the pulses is used. The dependence on frequency and position of the wave amplitude u is omitted in the notation for reasons of compactness.
The coupled amplitude wave equations that we used describe FWM, SPM and XPM, considering also the presence of free carriers (FCs). The coupled equations used are:

$$\begin{aligned}\frac{du_1}{dz} = &-\frac{\alpha_1}{2}u_1 - \frac{F_1}{2}u_1 + \\ &+ i\left[\gamma_1 |u_1|^2 + 2\left(\gamma_{12}|u_2|^2 + \gamma_{1s}|u_s|^2 + \gamma_{1i}|u_i|^2\right)\right]u_1 + \\ &+ 2i\gamma_{1is2}\sqrt{\frac{P_2P_iP_s}{P_1}}u_iu_su_2^*e^{i\Delta k_L z},\end{aligned} \tag{3.61a}$$

$$\begin{aligned}\frac{du_2}{dz} =& -\frac{\alpha_2}{2}u_2 - \frac{F_2}{2}u_2 + \\ &+ i\left[\gamma_2 |u_2|^2 + 2\left(\gamma_{21}|u_1|^2 + \gamma_{2s}|u_s|^2 + \gamma_{2i}|u_i|^2\right)\right]u_2 + \\ &+ 2i\gamma_{2is1}\sqrt{\frac{P_1P_iP_s}{P_2}}u_iu_su_1^*e^{i\Delta k_L z},\end{aligned} \tag{3.61b}$$

$$\begin{aligned}\frac{du_i}{dz} =& -\frac{\alpha_i}{2}u_i - \frac{F_i}{2}u_i + \\ &+ i\left[\gamma_i |u_i|^2 + 2\left(\gamma_{i1}|u_1|^2 + \gamma_{i2}|u_2|^2 + \gamma_{is}|u_s|^2\right)\right]u_i + \\ &+ 2i\gamma_{i12s}\sqrt{\frac{P_1P_2P_s}{P_i}}u_1u_2u_s^*e^{-i\Delta k_L z},\end{aligned} \tag{3.61c}$$

$$\begin{aligned}\frac{du_s}{dz} =& -\frac{\alpha_s}{2}u_s - \frac{F_s}{2}u_s + \\ &+ i\left[\gamma_s |u_s|^2 + 2\left(\gamma_{s1}|u_1|^2 + \gamma_{s2}|u_2|^2 + \gamma_{si}|u_i|^2\right)\right]u_s + \\ &+ 2i\gamma_{s12i}\sqrt{\frac{P_1P_2P_i}{P_s}}u_1u_2u_i^*e^{-i\Delta k_L z},\end{aligned} \tag{3.61d}$$

where $\hat{\mathbf{z}}$ is the propagation direction, the labels $\nu = 1, 2, s, i$ refer respectively to the first pump photon, the second pump photon, the signal and the idler, α_ν is the attenuation coefficient due to propagation, P_ν is the power. Regarding the FCs,

$$F_\nu = \sigma_\nu (1 + i\mu_\nu) N, \tag{3.62}$$

where N is the free carrier density generated by the pumps, evaluated through the rate equation with 30 ns FCs lifetime [47], and

$$\sigma_\nu = \frac{1}{N}\frac{c\kappa_\nu}{n(\omega_\nu)v_{g,\nu}}\delta\alpha_{FC} \quad \mu_\nu = -\frac{1}{\sigma_\nu N}\frac{2\omega_\nu\kappa_\nu}{n(\omega_\nu)v_{g,\nu}}\delta n_{FC}, \tag{3.63}$$

with n the bulk Si refractive index, ω_ν the frequency, $v_{g,\nu}$ the group velocity, $\delta\alpha_{FC}$ the FCA coefficient, δn_{FC} the FCD coefficient, and

$$\kappa_\nu = \frac{n(\omega_\nu)^2 \int_{A_0} |E_\nu(r,\omega_\nu)|^2 \; dA}{\int_{A_\infty} n_{wg}(r,\omega_\nu)^2 |E_\nu(r,\omega_\nu)|^2 \; dA}. \tag{3.64}$$

Consider that in the case of nonlinear optical processes the FCs are mainly generated through TPA, with the same density of electrons and holes; because of this, we calculated the coefficients $\delta\alpha_{FC}$ and δn_{FC} as [20]

$$\delta\alpha_{FC} = 14.5 \times 10^{-18} N, \tag{3.65}$$

$$\delta n_{FC} = -8.8 \times 10^{-22} N - 8.5 \times 10^{-18} N^{0.8}. \tag{3.66}$$

Regarding the γ coefficients, with the labels a, b, c, d referring to $1, 2, s, i$, γ_{abcd} is like in Eq. (3.32), $\gamma_{ab} = \gamma_{abba}$, $\gamma_a = \gamma_{aaaa}$ and Γ_{abcd} is like in Eq. (3.33). In (3.61) the higher order modes are taken into account by using their field profiles and effective index dispersions. We assumed the same attenuation coefficient for all the waves. For further details regarding Eqs. (3.61), see [20].

3.8.3 Mode selection

The excitation of higher order modes in a multimode silicon waveguide is achieved by illuminating properly the input facet of the waveguide. The efficiency with which the modes are excited in the waveguide is calculated through the power overlap integral ξ, that we already introduced in Chapter 1 as

$$\xi_{x,m} = \frac{\int_{-\infty}^{\infty} dx \int_{-\infty}^{\infty} dy\, \psi_x E_{x,m}^* \int_{-\infty}^{\infty} dx \int_{-\infty}^{\infty} dy\, \psi_x^* E_{x,m}}{\int_{-\infty}^{\infty} dx \int_{-\infty}^{\infty} dy |\psi_x|^2 \int_{-\infty}^{\infty} dx \int_{-\infty}^{\infty} dy |E_{x,m}|^2}, \tag{3.67}$$

with the index x indicating TE polarization (y is used for TM polarization), ψ_x is the incident TE field profile, $E_{x,m}$ is the m-th TE order mode field profile. ξ quantifies how the input power is distributed among the modes supported by the waveguide. Depending on the input field profile, it is possible to excite a single waveguide mode or multiple modes [26].
In our experiment, we used a tapered lensed fiber to couple the light in the waveguide. The field profile of the tapered lensed fiber is gaussian, with a measured waist of $(1.17 \pm 0.01)\ \mu m$ at $1550\ nm$. We simulated the coupling efficiency as a function of the horizontal fiber position, i.e. along the waveguide width, keeping the vertical position at half of the height of the waveguide. The fiber was assumed to be normal with respect to the waveguide facet. The power coupled in the different modes is calculated by

$$P_{p,m}^{wg} = (1 - R)\xi_{p,m} P_p, \tag{3.68}$$

where m is the order mode, $p = x, y$ refers to the polarization, R is the facet reflection coefficient, P_p is the input power. In Fig. 3.16 the computed power coupled in the first three waveguide modes is shown, considering $1\ W$ power in the input fiber and a waveguide width of $3.5\ \mu m$. Fig. 3.16 shows that higher order modes can be excited by moving the input fiber along the waveguide width, with $0\ \mu m$ corresponding to the center of the waveguide. The same coupling method was used also for the output signal collection.

3.8.4 Experimental set-up

We used the same set-up for the measurement of both the stimulated FWM and spontanoues FWM, Fig. 3.17. The only difference is that in the spontaneous case no seed signal is required. A pulsed pump beam, with $1550\ nm$ wavelength, $40\ ps$ pulse duration and $10\ MHz$ repetition rate, is mixed through a free-space beam splitter with the continuous wave (CW) seed signal, whose wavelength can be tuned in the range $1480\ nm$ - $1670\ nm$. On both the beams a polarization controller stage is present. The two beams are then coupled in a tapered lensed fiber through a collimator. To excite the proper waveguide mode, the input fiber is moved along the x-axis with a piezocontrolled translator stage. The SOI chip used has several multimode waveguides with different waveguide widths. An infrared camera coupled to a microscope allows controlling the selected waveguide. The light transmitted by the waveguide is then collected at the output by another tapered lensed fiber mounted on a piezocontrolled translator stage. Then, the signals are analyzed by a monochromator when their optical power is lower than $0.1\ nW$ or by an optical spectrum analyzer (OSA) for larger powers. The monochromator was homemade, using a grating in a double pass configuration, as shown in Fig. 3.18. The monochromator is coupled to an InGaAs single photon counter, allowing for a dynamic range of 10^5, i. e. from $1\ fW$ to $0.1\ nW$. This large dynamic range is possible thanks to

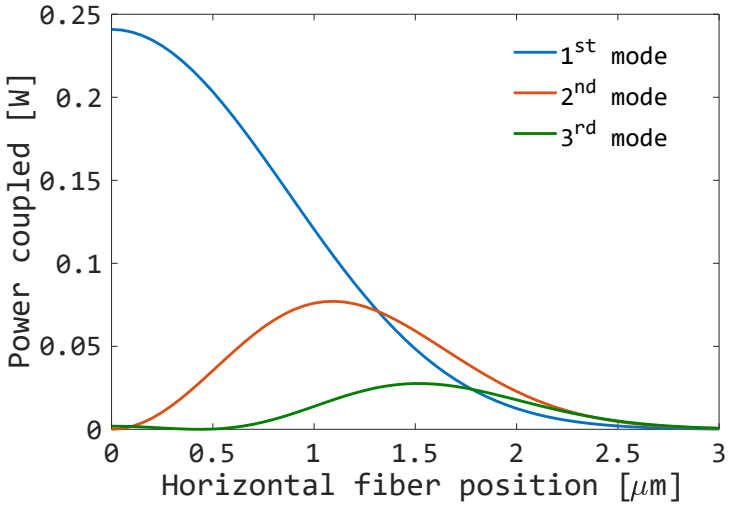

FIGURE 3.16: Computed power coupled into the different modes of a waveguide by a tapered lensed fibre as a function of the fibre position with respect to the centre of the waveguide. It is assumed a 3.5-μm-wide waveguide and 1 W at the input fibre with a wavelength of 1550 nm. When the fibre position is 0 μm, the fibre is in the middle of the waveguide. These values of coupled power have been rescaled such that the losses simulated for the first TE order mode are equal to the measured ones.

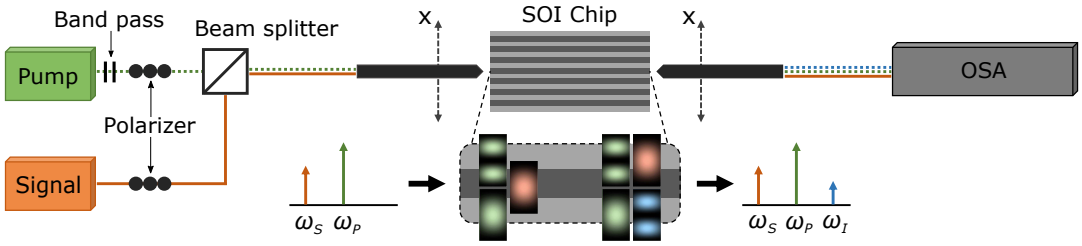

FIGURE 3.17: Set-up for the sFWM. The pump is initially filtered with two 1550 nm - bandpass filters. Then, the pump and the signal, after a polarization controller stage, are mixed by a free space beam splitter and coupled in the same tapered lensed fiber through a collimator. The input fiber injects the light in the desired waveguide on the SOI chip. The light is collected from the waveguide by another tapered lensed fiber. The position of both fibers is controlled by means of two XYZ - nanopositioning stages via piezo controllers. The collected light is analysed with an OSA or a monochromator, depending on the power of the generated signal. In the inset, the waveguide modes involved in the intermodal FWM are sketched by showing the mode profiles at the input and at the output of the waveguide; as an example, the case of the (1,2,2,1) modal combination is considered. For the SFWM, the set-up is exactly the same, except for the lack of the input signal.

a gated measurement with the pump laser trigger. Note that the use of the InGaAs photodetector limits our measurements to the wavelength region 1200-1700 nm.

We characterized a 3.5-μm-wide waveguide, measuring the propagation losses (4.6 dB/cm) and the coupling losses (-5.3 dB) for the 1^{st} TE order mode at a wavelength of 1550 nm. The coupling losses for the 2^{nd} TE order mode (-10.0 dB) are

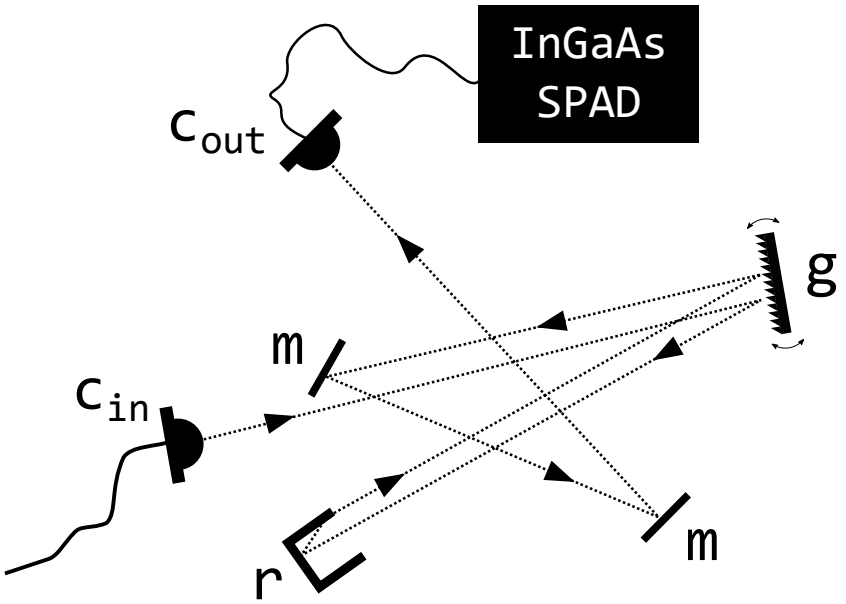

FIGURE 3.18: Schematics of the monochromator used in our experiment. The light is injected in the system through a collimator (c_{in}), then it is firstly reflected on a monochromator (g) placed on a motorized rotating stage; then, a retroreflector (r) is used to reflect back the beam with a vertical offset, and another passage over the grating is made. In the end, after being reflected by two mirrors (m) the light is outcoupled with another collimator (c_{out}) and measured through the photon counter. The whole system is controlled through a software which synchronizes the photon counter and the grating rotation such that spectra can be measured automatically.

estimated from the simulation (Fig. 3.16). The coupling losses are evaluated considering the position of the fibre that maximizes the coupling of the considered mode (1^{st} mode - $x = 0\,\mu m$, 2^{nd} mode - $x = 1.1\,\mu m$). Finally, in our simulations, we assumed for the 2^{nd} order mode the same propagation losses of the 1^{st} one, which is an optimistic assumption.

3.8.5 Measurements and results

We investigated several modal combinations for the intermodal FWM: (1,2,2,1)-TE, (1,2,2,1)-TM, (1,1,2,2)-TE, (1,3,3,1)-TE and (1,3,3,1)-TM. Here we focus mainly on the (1,2,2,1)-TE modal combination. We performed the measurements on 15 different waveguides with the same nominal width of 3.5 μm and 1.5 cm length. We measured an average idler wavelength $\bar{\lambda_i} = 1467.6nm$ with standard deviation $\sigma = 3.5\,nm$. This finding is in agreement with the numerical computed idler peak wavelength of 1467 nm. The deviation from the computed value is mainly due to fabrication imperfections, that led to waveguide widths different from the nominal one. In Fig. 3.19a the spectrum of the spontaneous FWM for one of the 3.5-μm-wide waveguides is reported. In this particular case, we measured $\lambda_i = 1469\,nm$ and $\lambda_s = 1640\,nm$. The measurement was performed with the input fibre at $x = 0.83\,\mu m$, position that maximizes the product between the coupled power on the first and second order mode. The input on-chip peak pump power is about 3.1 W (2.1 W on the first order mode and 1.0 W on the second one). For this measurement, the fiber-to-fiber losses are 17.9 dB or 22.6 dB, coupling at the output the first or the second TE mode respectively.

For this calculation we are considering the input fibre fixed at 0.83 μm, with -5.7 dB total coupling losses for the pump.

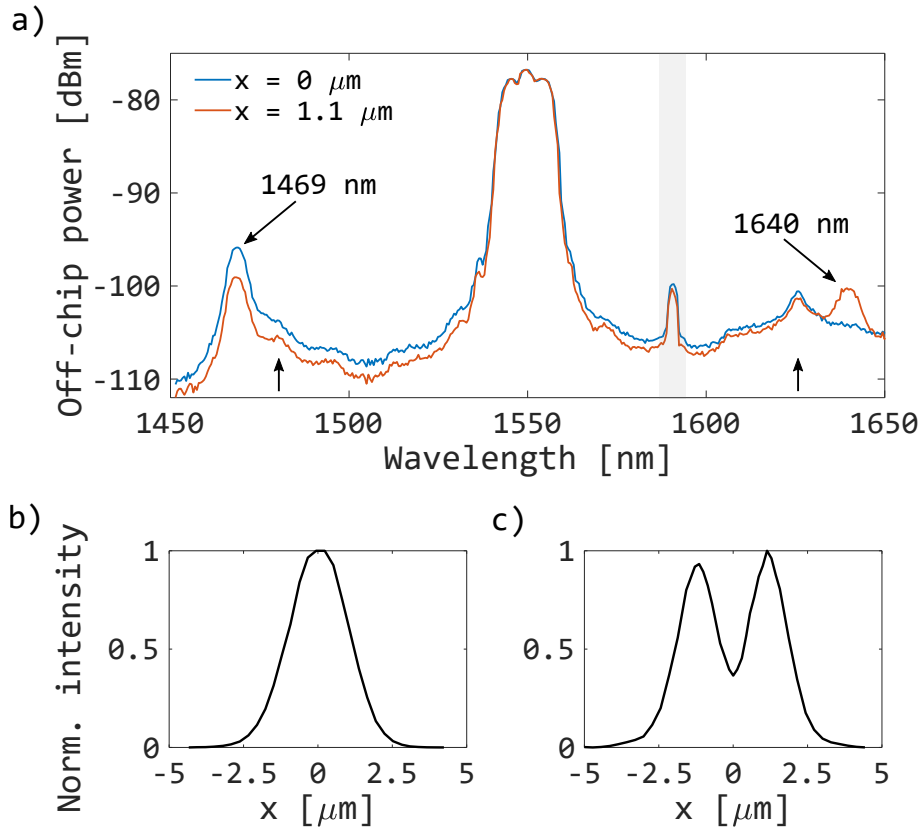

FIGURE 3.19: a) Spectrum of the SFWM in a 3.5-μm-wide waveguide, with (1,2,2,1) combination and TE polarization. The pump is at 1550 nm. The different lines refer to different position of the output fiber: the blue line refers to the spectrum measured with the output fiber in the middle of the waveguide, the red line refers to the spectrum measured with the output fiber at 1.1 μm with respect to the center of the waveguide. The two vertical arrows indicate a spurious signal due to Raman scattering occurring in the input fibre. The shaded gray box indicates a spurious peak. b) Intensity profile at the output facet of the waveguide, for the peak at 1469 nm in a. c) Intensity profile at the output facet of the waveguide, for the peak at 1640 nm in a).

As stated in Section 3.4.1, to confirm the FWM origin of these peaks the generated light must be quadratic with the pump power. In Fig. 3.20, the average on-chip generation rate is reported as a function of the on-chip average pump power. The expected quadratic dependence is measured for pump powers $P_P < 0.5\ mW$, see the inset in Fig. 3.20, while for higher powers the efficiency of the process decreases due to TPA, which depletes the pump power. We estimate an average generation rate of $24.6 \pm 0.8 \left(\frac{MHz}{mW^2}\right) P_P^2$ for the 3.5-μm-wide waveguide in the pump power range $[0 - 0.5]\, mW$. This measurement was performed by monitoring the idler photon counts.

We verified the intermodal nature of the process by measuring the spectrum with two different horizontal positions of the output fiber. In fact, since the idler is generated on the 1^{st} order mode and the signal on the 2^{nd} order mode, according to Fig. 3.16, we expect to observe the maximum intensity for the idler when the output fiber

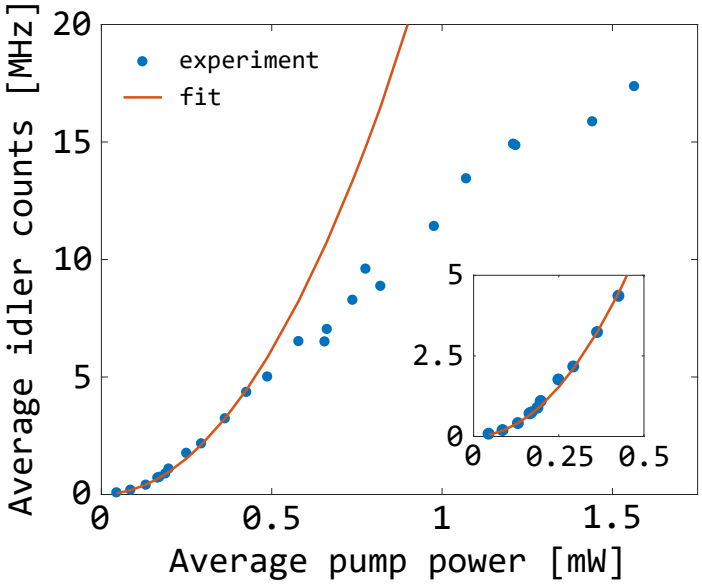

FIGURE 3.20: Average on-chip photon generation rate for the SFWM process as a function of the on-chip average pump power. The blue circles are the experimental measurements, while the red line is the quadratic fit of the data belonging to the [0 - 0.5] mW range. The inset shows the low pump power region.

position is $x = 0\,\mu m$, i.e. in the middle of the waveguide, and the maximum intensity for the signal when the position of the output fiber is at 1.1 μm, i.e. when the coupling of the second order mode is maximized. In Fig.3.19a the spectrum measured with the output fiber at $x = 0\,\mu m$ exhibits only one peak at 1469 nm, the idler peak. In fact, from simulation in Fig. 3.16, we expect, at $x = 0\,\mu m$, a negligible coupling efficiency for the second order mode. When the output fiber is placed at 1.1 μm, also the signal peak appears at 1640 nm, as expected.
Another evidence of the intermodal nature of the SFWM is the spatial profile of the generated idler and signal waves on the output waveguide facet. To do this measurement, we set the monochromator to resolve either the signal or the idler peak wavelengths, and then we performed an intensity profile scan on the output facet of the waveguide along the x axis (see Fig.3.17). In Fig. 3.19b and c we report the measured profiles for the idler and signal, respectively, that exhibit the expected one-lobe (first-order) and the two-lobes (second-order) shapes.
The stimulated FWM was measured in the same 3.5-μm-waveguide with 1.5 cm length. An example of the measured spectrum is shown in Fig. 3.21a. For this measurement, the on-chip input peak pump power was about 1 W (0.7 W on the 1^{st} mode and 0.3 W on the 2^{nd}) at 1550 nm and the input on-chip signal power was about 47 μW at 1640 nm on the second order mode. An idler peak at 1469 nm is generated with -14.7 dB maximum conversion efficiency, calculated as the ratio between the on-chip idler peak power and the on-chip signal power, evaluated at the end of the waveguide [2].

[2]The input on-chip signal power was about 47 μW ($= -13.3 dB$) at 1640 nm on the second order mode. At the end of the waveguide, considering 4.6 $dBcm^{-1}$ of propagation losses and 1.5 cm waveguide length, the signal power on the second order mode is -20.2 dBm. The off-chip generated average idler power is about -74.2 dBm, as shown in Fig. 3.21a. Considering the coupling losses for the first order mode, 5.3 dB, the on-chip *average* idler power is -68.9 dBm. Considering that the pump laser has 10 MHz repetition rate and 40 ps pulse width, the on-chip idler *peak* power, at the end of the waveguide,

The input on-chip powers are estimated from the off-chip power reported in Fig. 3.21a and considering the propagation and coupling losses. Regarding the coupling losses, the measurement reported in Fig. 3.21a was performed with the input fibre at $x = 0.83\,\mu m$ and the output fibre at $x = 0\,\mu m$.

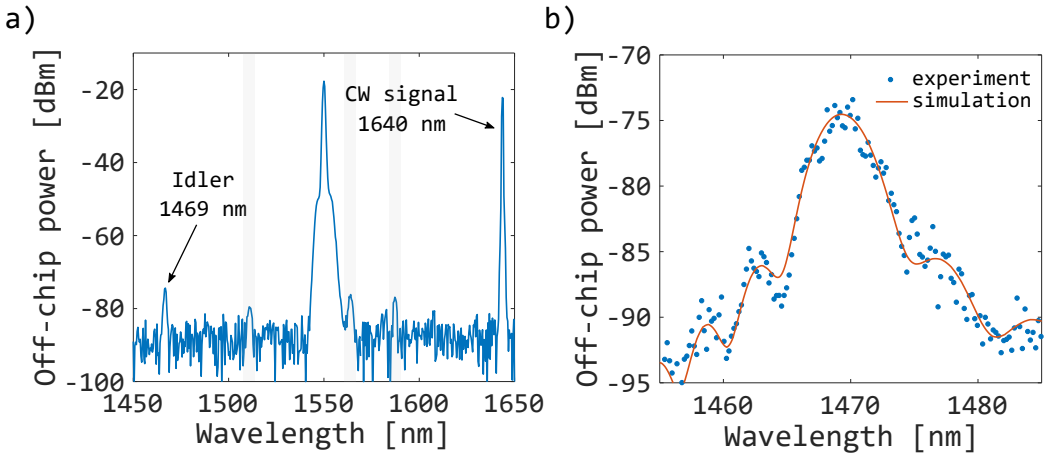

FIGURE 3.21: a) Spectrum of the sFWM with (1,2,2,1) - TE intermodal combination in a 3.5-μm-wide waveguide. The stimulating CW signal at 1640 nm is converted into the pulsed idler at 1469 nm. The smaller peaks (shaded gray boxes) are spurious signals due to the OSA. b) Spectrum of the stimulated idler generation efficiency with the intermodal FWM combination (1,2,2,1) TE in a 3.5-μm-wide waveguide. The simulation was performed with a 3.66-μm-wide waveguide. The blue dots are the measured data, while the orange line is the simulation. This measurement was performed by synchronously scanning the signal wavelength and the monochromator wavelength, in order to read the idler power corresponding to the input signal. The simulated spectrum was shifted by -3.3 dBm, in order to match the experimental data.

By synchronously scanning the signal wavelength and the monochromator wavelength according to the energy conservation equation, it is possible to measure the spectrum of the stimulated FWM. We considered again the (1,2,2,1) TE combination in the 3.5-μm-wide waveguide. Fig. 3.21b compares the measured and simulated spectrum of the stimulated idler. A good agreement is observed. The simulation considered a width of 3.66 μm for the waveguide, in order to match the peak wavelength. This could be due to a difference of 0.16 μm with respect to the nominal 3.5 μm width. The measured 3-dB bandwidth is $4.7 \pm 0.2\,nm$, compatible with the simulated 4.8 nm 3dB-bandwidth. Regarding the bandwidth of the process, we measured the 3-dB bandwidth as a function of the waveguide length L for a 3.5 μm wide waveguide, obtaining the results in Fig. 3.22, where also the simulated points are shown. The measured and simulated results are in good agreement, with the bandwidth that decreases, as expected, with the length.

According to Eq. (3.52), it is possible to tune the phase matching position by controlling the effective index of the modes involved in the intermodal FWM, i.e. by changing the waveguide cross-section. Therefore, we measured the intermodal spontaneous FWM with (1,2,2,1) modal combination and TE polarization in several

is -34.9 dBm. Therefore, the conversion between the signal power, -20.2 dBm, and the idler peak power, -34.9 dBm, is -14.7 dB.

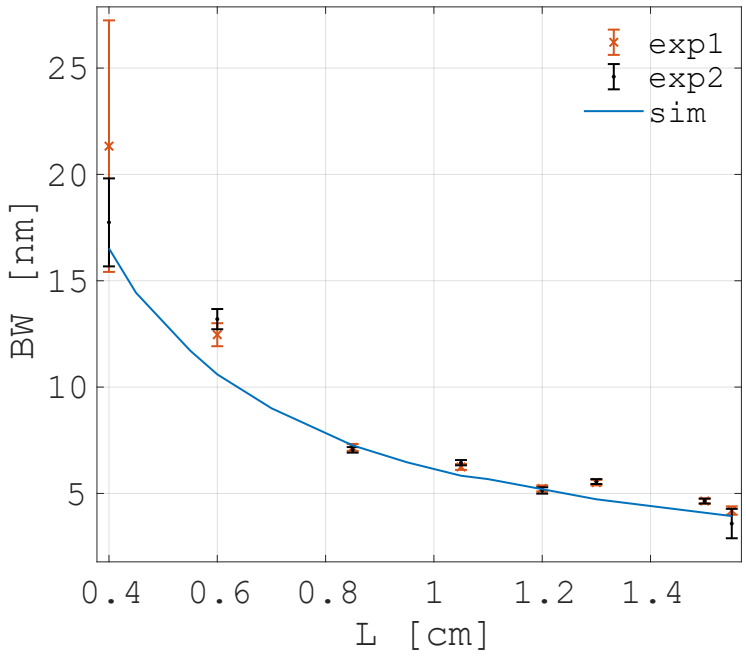

FIGURE 3.22: 3-dB bandwidth as a function of the waveguide length for two waveguides with the same width of 3.5 μm. The experimental points are the dots, while the line represents the simulated values.

waveguides, with widths ranging from 2 μm to 3.8 μm. Due to the use of the InGaAs detector we could only trace the evolution of the idler spectral position while we computed the corresponding spectral position of the signal imposing the energy conservation. As the waveguide width is increased, the spectral distance between the signal and idler reduces, as shown in Fig. 3.23. Fig. 3.23 shows that the waveguide geometry and the spectral translation $\Delta\lambda = \lambda_s - \lambda_i$ are tightly correlated, which allows an easy tunability of the phase matched wavelengths. Moreover, the intermodal phase matching approach allows for extremely large spectral translation in waveguide. An example is shown in Fig. 3.24, where the SFWM spectrum for a 2-μm-wide waveguide pumped at 1550 nm is shown. The generated idler is at 1202 nm and the expected signal is at 2181.6 nm, resulting in 979.6 nm spectral distance between signal and idler. This is the largest detuning ever reported for FWM on a silicon chip with a C-band pump source. Note that in Fig. 3.24, it is also possible to see the anti-stokes Raman peak at 1434 nm, which can be used as a reference for the efficiency of the process.

We also investigated other modal combinations. We performed the SFWM measurements in a waveguide with a nominal width of 3.8 μm, with 1.5 cm length, observing peaks corresponding to the modal combinations reported in Fig. 3.25. Three spectra are shown, two for the TE combinations and one for the TM combinations. The TE measurements were performed with an on-chip peak power of about 16.1 W on the first mode, 0.2 W on the second mode and 0.4 W on the third mode. The on-chip peak power for the TM case was about 10.4 W on the first mode, 5.2 W on the second mode and 0.4 W on the third mode. The TE combinations required two spectra, one with the output fibre at $x = 0\,\mu m$ and one at $x = 1.25\,\mu m$, in order to enlighten the different modes involved in the combinations (1,3,3,1) and (1,1,2,2). In fact, the idler on the first order mode is better coupled when $x = 0\,\mu m$, while the idler of the second order mode when $x = 1.25\,\mu m$. Table 3.4 compares the measured

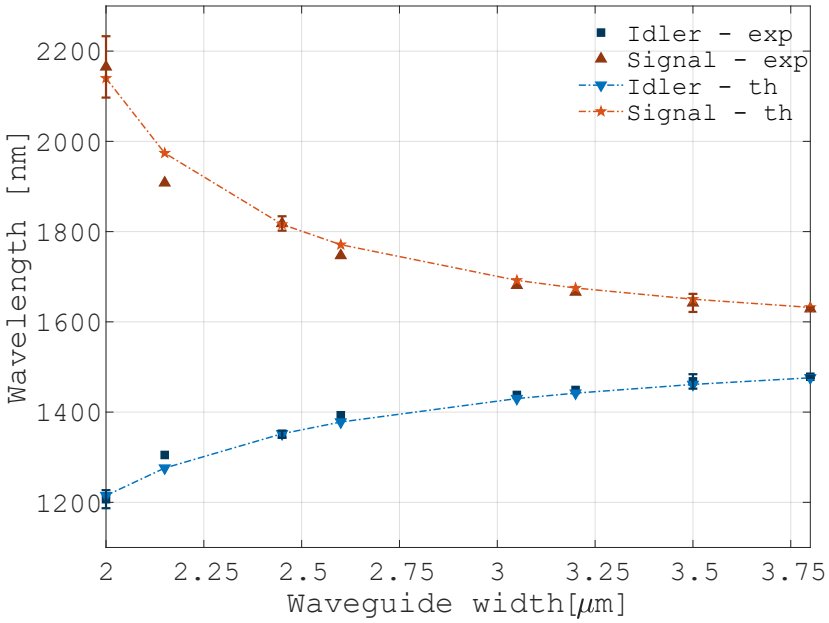

FIGURE 3.23: Phase matched wavelengths as a function of the waveguide width for the (1,2,2,1) combination, TE polarization and 1550 nm pump. The experimental idler and signal are reported in blue and red respectively, while the corresponding simulated values are reported by the light blue and orange points. The lines are a guide for the eye. The phase matched signal wavelengths have been deduced by using Eq. (3.50) and the measured idler wavelengths. For some widths (those with the errorbars), we performed repeated measurements (ten measurements) on nominally identical waveguides.

and simulated idler wavelengths for the combinations shown in Fig. 3.25. A good agreement is observed.

(j,q,l,m)	Polarization	$\lambda_i^{sim}\,[nm]$	$\lambda_i^{exp}\,[nm]$
$(1,1,2,2)$	TE	1211	1205
$(1,2,2,1)$	TE	1479	1479
$(1,3,3,1)$	TE	1346	1340
$(1,2,2,1)$	TM	1525	1531
$(1,3,3,1)$	TM	1480	1492

TABLE 3.4: Intermodal combinations measured in Fig. 3.25. λ_i^{sim} and λ_i^{exp} are the simulated and the measured idler wavelengths. The simulation is performed with a 3.84-μm-wide waveguide.

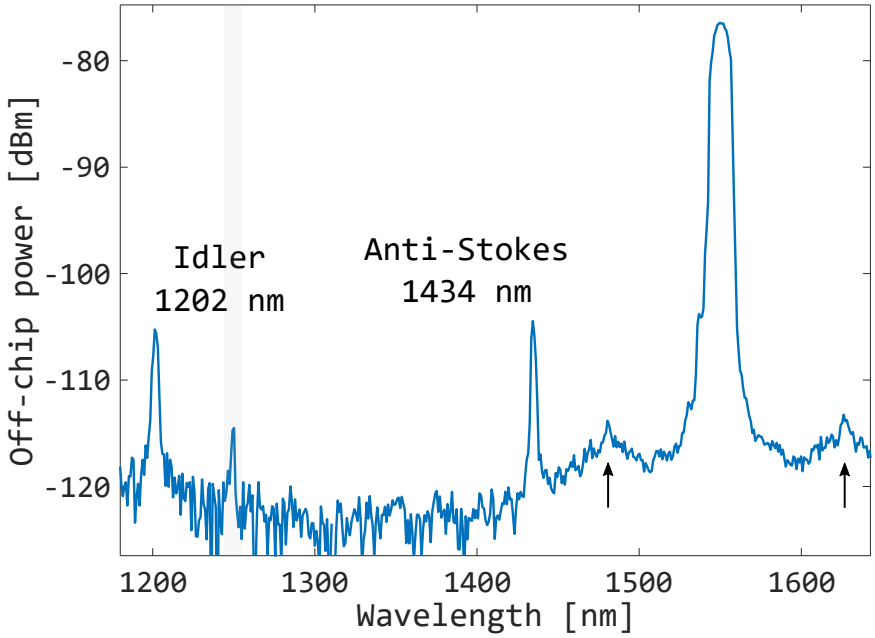

FIGURE 3.24: Spectrum of the SFWM for the (1,2,2,1) combination, TE polarization and a 2-μm-wide waveguide. The pump is at 1550 nm with an on-chip peak power of about 3.9 W (3.3 W on the first order mode, 0.6 W on the second one). The idler is generated at 1202 nm. The peak at 1434 nm is the anti-stokes peak of the Si Raman scattering. The two vertical arrows indicate the generated light due to Raman scattering occurring in the input fibre. The shaded gray box indicate a spurious peak due to the monochromator.

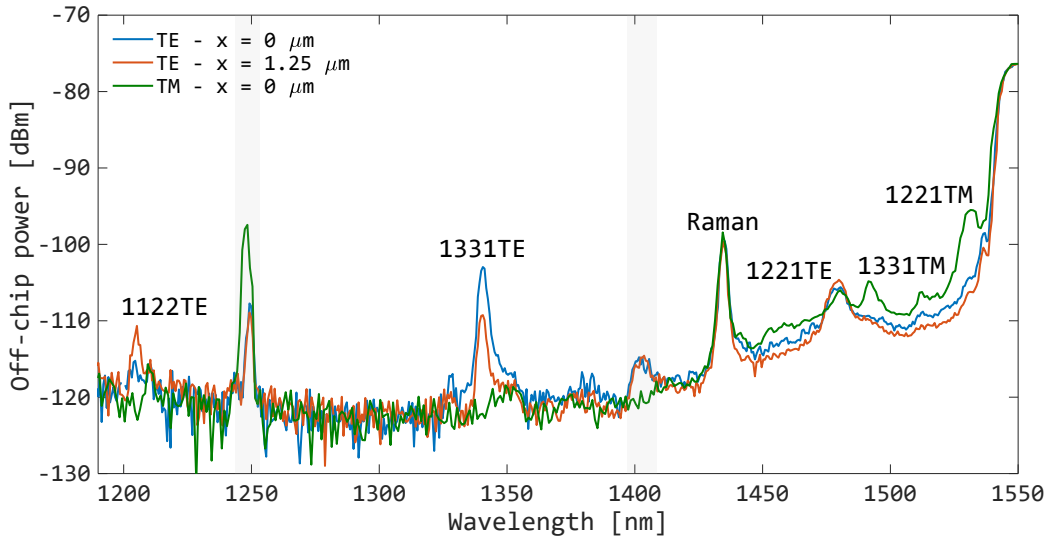

FIGURE 3.25: Spectra of intermodal SFWM in a 3.8-μm-wide waveguide. Both TE and TM measurements are reported. The position of the output fibre is reported in the legend. The peaks refer to the indicated combinations. The pump is at 1550 nm. The shaded gray boxes indicate spurious signals.

3.9 Conclusions

In this chapter I initially briefly reviewed the basics of nonlinear optics, describing how the nonlinear polarization arises in integrated devices and giving a general introduction to the available nonlinear processes, focusing on the second and third order nonlinearities. I then extensively described the FWM process, the most investigated nonlinear phenomenon in silicon photonics, with particular attention to the various phase matching mechanisms currently available. Within the framework of spectral conversion and compatibility with technologies like DWDM and MDM, I have introduced intermodal FWM. Thanks to the different effective index dispersions of each waveguide mode, it is possible to engineer easily the phase matching condition of the process, achieving large and tunable spectral translations for several intermodal combinations. In the chapter we demonstrated both spontaneous and stimulated FWM via intermodal phase-matching in SOI waveguides. We exploited the large spectral translation of intermodal FWM to achieve spontaneous generation of 1202 nm light in a 2-μm-wide waveguide, with 979.6 nm spectral distance with respect to the twin signal photon. Since the phase matching with higher order modes does not rely on the fourth-order dispersion coefficient β_4 of the GVD, the phase matched wavelengths are less affected by fabrication imperfections with respect to discrete band phase matching based on the compensation of the higher order GVD terms, that we compared with the intermodal FWM. The multimode waveguides are larger than common single mode waveguides, with lower losses and less issues in terms of relative deviations from the nominal waveguide dimensions. Involving higher order modes in the FWM process clearly affects negatively the efficiency of the process, that reduces with the decreased mode field overlap. Despite this lower efficiency with respect to common intramodal FWM, the intermodal approach enables larger spectral translations and opens new functionalities for technologies involving higher order modes. Moreover, we measured several modal combinations, demonstrating the flexibility of the intermodal FWM, whose application is not limited at the first two order modes. Thanks to the discrete phase matched bands and the tunability of the generation, intermodal FWM can provide a suitable mechanism for the creation of heralded single photon sources with high brightness and low noise, since the large spectral distance between the involved photons allows an easy filtering of the pump and Raman light.
The approach here proposed has been demonstrated by using silicon photonics, however it can be easily extended to other classes of materials. Specifically, the use of other materials is relevant to overcome the detrimental effect of TPA, which is particularly large in Si waveguides.

Chapter 4

Heralded single photons

When the photon flux is reduced such that the average beam energy corresponds to the single photon energy, quantum optical phenomena arise. Working at the single photon level makes possible to unveil and exploit the quantum properties of light, that are nowadays defining a whole new field of photonics technology. Currently, quantum technologies are gaining importance due to the unprecedent applications and improvements that they promise to unlock and photons appear as the most suitable carriers of such quantum revolution [90]. In fact, photons do not interact with the environment, resulting in limited decoherence. Photons can be transmitted at high speed and within the already deployed optical fiber network. Finally, sources of quantum states of light are readily available at room temperature and at the chip level [91]. In particular, the opportunity to realize low cost and mass manufacturable devices offered by integrated photonics is a strong motivation to investigate photonics for quantum applications, looking at the widespread diffusion of such technologies.

In the last ten years, quantum photonics has experienced a prominent rise, with outstanding and pioneering results in quantum communication, computation, sensing, cryptography and metrology [14]. Laying at the basis of such quantum applications are the peculiar properties of quantum physics, such as the wavefunction collapse, the superposition principle and the entanglement. These properties can be exploited either through entangled photon pairs or through single photons [15, 92]. Two photons are said to be entangled when the quantum system constituted by the pair can be described only as a whole [59]. On the other hand, a single photon lacks any correlation with other systems, and it can be described individually. Depending on the application, single or paired photons can be used. Entangled pairs are mainly generated through nonlinear parametric processes, like SPDC and SFWM, and find particular employment in the field of secure communications [93]. Single photons can be generated from different types of sources and can be used for a large spectrum of technologies. Single photon sources can be atom-like emitters, as trapped ions or quantum dots [91], or heralded sources based on correlated photon pairs [94]. The ideal single photon source should emit deterministically exactly one and only one photon at a time with 100% generation probability [95]. This is the concept of the "photon gun" [96], the naive description of the ideal single photon source, where by pressing a button a single photon is emitted instantaneously and with unit probability. Atom-like emitters are the closest example of "photon gun", due to their two-level energy diagram, which prevents the emission of more than one photon. In fact, much effort has been devoted to the development of such sources and to their integration on the silicon platform; however, the hard manufacture and low spectral flexibility hinder the establishment of such sources as the standard for quantum photonics [15]. Moreover, the large majority of quantum applications are based on the interference between indistinguishable single photons; this means that

different sources should emit single photons that perfectly overlaps over all the field modes (energy, polarization, time, ...) [97, 98]. The indistinguishability of emitted single photons is currently a main topic for atom-like emitters [99, 100], since such sources, due to their fabrication technology, exhibit broad and not reproducible spectra, resulting in distinguishable sources. Indistinguishability can be achieved also by filtering the generation bandwidth, such that within the filter band the sources are identical, but at the expenses of their brightness.

The limited reproducibility and difficult scalability of atom-like emitters (quantum dots, NV centers in diamond,...) together with the cryogenic working temperatures required [101, 102, 103] pushed the photonics research to explore and develop more feasible single photon sources. The most investigated alternative to atom-like emitters are heralded single photon sources. Heralded single photon sources exploit the temporal correlation between pairs generated by means of spontaneous parametric nonlinear processes, as SPDC or SFWM. In fact, the paired photons generated through spontaneous processes are emitted at the same time. Thus the idea is to use one of the two photons as the *herald*, whose detection confirms that the pair generation has occurred, and the remaining twin photon, that is the *heralded* photon, can be used as a single photon in the quantum device. However, heralded sources are intrinsically probabilistic, since they are based on nonlinear parametric processes, thus lacking on-demand generation, which, on the contrary, characterizes atom-like emitters [101]. Nevertheless, the probabilistic emission of heralded sources can be mitigated by means of multiplexing, whose basic idea is to use several identical heralded sources in parallel, such that the generation probability scales with the number of such sources and recovering the single photon statistics through post selection [59].

Single photons are evaluated looking at well defined parameters. First of all, it has to be verified if they are indeed *single* photons, i.e. if they are emitted alone within the generation process. Then, the *purity* of the single photon state is a main parameter to characterize the source, since it quantifies how close the quantum state is to a single mode system [104]. This last parameter is crucial when dealing with quantum interference between single photons coming from individual sources, since the maximum visibility is obtained with single mode photons [59]. Purity is inversely proportional to correlation, and it is therefore in contrast to entanglement. In fact, what is generally pursued is the factorizability of the biphoton wavefunction, i.e. the complete loss of any correlation between signal and idler in order to maximize the purity of the state. Looking at the quantum interference between single photons, also *indistinguishability* has to be considered. This parameter measures the similarity between the single photons in terms of the source parameters (spectrum, polarization, ...) and it is proportional to the visibility of the quantum interference [105, 98]. Fundamental for the feasibility of the source is the *brightness*, which is the emission rate of single photons. The former parameters are equivalently used for both atom-like emitters and heralded sources, but these latter are characterized by a property that is peculiar of the heralding scheme, namely the *heralding efficiency*; this parameter is proportional to the probability of detecting the heralded photon once the herald photon has been detected. The heralding efficiency is strictly related to the losses of the system [59].

A well established strategy for the generation of heralded single photons is SPDC in periodically poled crystals [106, 107, 108, 109]. Despite the good results that can be obtained with poled crystals, these cannot be the ultimate solution for integrated quantum photonics. On one side because the photons generated by the poled crystals are affected by losses when coupled to the guiding structure. On the other side

because they are not compatible with CMOS technology, thus requiring higher costs and hindering the mass production of the devices. In order to move towards the goal of an efficient fully integrated quantum chip, as the one proposed in Fig. 4.1, it is therefore required the adoption of a source that can be implemented directly on-chip. The requirement of an integrated source of quantum states comes from the necessity to reduce drastically the coupling losses, that are detrimental when dealing with the low photon rate proper of the quantum devices. Moreover, having all the building blocks at the chip level makes the system much more robust, easy to fabricate and compact. These advantages are promoting the development of the quantum silicon photonics platform, which is dealing with the optimization and full integration of all the devices required for the generation, manipulation and detection of the quantum states of light. Moreover, the silicon photonics platform meets all the criteria for an efficient mass productivity. As an example, in Fig. 4.1 is reported the rendering of a possible quantum photonic chip, in which all the required structures for the generation, pump filtering, control and detection of quantum light are integrated together.

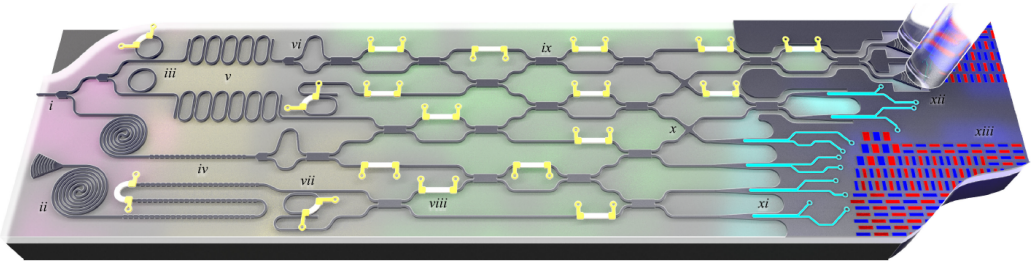

FIGURE 4.1: Schematics of a possible quantum photonic chip, in which the generation stage (magenta), filtering (yellow) manipulation (green) and detection (cyan) are integrated together. The labels indicate: (i) input and 3-dB splitter, (ii) spiralled waveguide, (iii) ring resonator, (iv) Bragg reflector, (v) coupled resonator optical waveguide, (vi) asymmetric Mach-Zender, (vii) ring resonator filter, (viii) thermal phase tuner, (ix) MMI, (x) waveguide crossing, (xi) superconducting nanowire single-photon detector (SNSPD), (xii) grating coupler, (xiii) control electronics. Reprinted from Ref. [15] ©2016 IEEE.

The source of quantum light is the starting point of the chain leading to the final quantum operation of the device. Within the silicon photonics platform, heralded photons can be generated in spiralled waveguides, ring resonators or simple straight waveguides, whose schematic design is reported in Fig. 4.2. Spiralled waveguides are essentially an improvement of the simple straight waveguide, since they exploit their longer length to enhance the probability generation. Straight and spiralled waveguides are much more fabrication tolerant with respect to ring resonators, which need precise control of the waveguide-ring gap in order to exhibit a high degree of indistinguishability [62]. On the other hand, ring resonators require much lower pump power, have a smaller fingerprint and improve the spectral purity of the single photon state [15]. Nevertheless, resonators are much more sensitive to phase deviations due to free carriers and they are feasible only for the generation of photons close to the pump wavelength [15]. This latter limitation comes from the triply resonant condition required for the generation of SFWM, where pump, signal and idler must be all resonant in the same cavity. This condition is true only for an almost flat dispersion, which occurs when all the waves are close in wavelength.

This hinders the use of ring resonators for applications requiring broad band generation of single photons, such as quantum sensing or free space communications, which need quantum light in the MIR part of the spectrum.

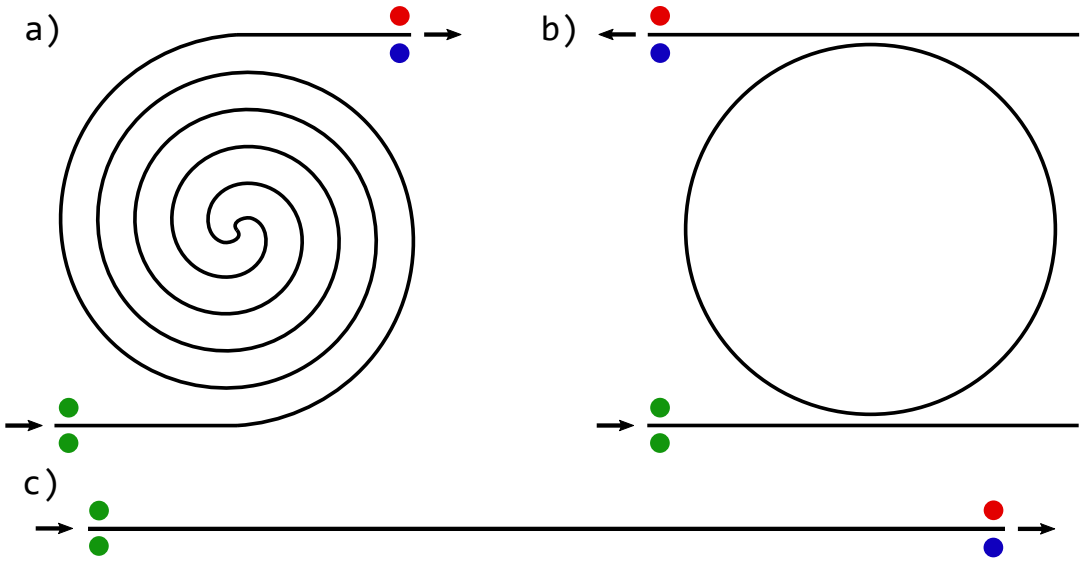

FIGURE 4.2: Sketch of three typical integrated heralded single photon sources in the case of SFWM generation. In green are the pump photons and in blue and red are respectively the idler and signal photons emitted in pairs. a) Spiralled waveguide, b) ring resonator, c) straight waveguide.

Owing to the promising perspective of having an efficient integrated source of single photons, heralded sources have experienced a rapid development in the last years, with the achievement of bright, pure and indistinguishable single photons [19, 110, 98, 109]. However, heralded single photons are still at the development level and several challenges are currently under further investigation. Among these is the requirement of having an easy spectral tunability of the generated single photons with high purity and without recurring to narrow band filters. In fact, the most common approach to pure and tunable generation in silicon is to perform broadband SFWM in a spiralled single mode waveguide, which is then filtered in order to reduce the multimode character of the generated photons, selecting at the same time the spectral position of the source [59]. This approach is extremely practical and readily available at the chip level with high purities [111, 112], but spectral filters improve purity at the expenses of source brightness. Obtaining high purities together with high generation rates is nevertheless possible by using ring resonators, whose generated single photons are naturally filtered by the linewidth of the ring spectrum. However, as said before, the generation is limited to a narrow spectral range around the pump wavelength, with limited single photon spectral control.

In order to combine the large and tunable detuning offered by waveguides with the high purity and brightness of ring resonators, it is required a phase matched process which exhibits a tunable discrete band phasematching, in order to naturally filter the generated photons. These requirements can be fulfilled within the intermodal phasematching scheme. As introduced in Chapter 3, intermodal FWM is characterized by a discrete band generation, whose bandwidth and central wavelength can be controlled by changing, respectively, the length and cross section of the waveguide [73]. The introduction of intermodal SFWM as a source for heralded single photons could open a new route towards the realization of integrated quantum sources that

exhibit high purity and brightness together with large detunings from the pump wavelength [113]. This last feature, in particular, allows to get large spectral distance between the generated photons and the pump and Raman light, improving greatly the rejection of such noise sources [114]. Moreover, the capability of generating the herald photon in the NIR spectral range, where feasible single photon detectors are already present, and the heralded above two microns opens interesting perspectives for the field of quantum MIR photonics, where an integrated source of quantum states of light is still missing [115, 116]. Several fields of science and technology would greatly benefit of single photons in the MIR, like medical imaging [117], free-space quantum communications [118], absorption measurements in the few photon regime [119] and lidar technologies [120]. Therefore, the research in MIR heralded photons through on-chip intermodal SFWM is strongly motivated and of great interest for all the quantum photonics platforms, not only within the SOI technology. The high spectral tunability is regarded as the main peculiarity of intermodal FWM; nonetheless, the different propagation properties of the higher order modes involved offer an additional tool for the control of the state purity. In fact, by exploiting the different group velocities of the pump waveguide modes, it is possible to implement a dual pump delayed scheme [121] for the generation of heralded single photons with unprecedent purities ($\sim 99\%$).

During my research I investigated the application of intermodal FWM to the generation of heralded single photons in silicon. I investigated both the generation of single photons above 2 μm and the high purity offered by this intermodal process. The chapter is organized as follow: initially a brief introduction to the basic concepts of quantum states of light is provided; then, particular attention is devoted to the purification strategies for the heralded states, including group velocity matching and dual pump delay approaches; in conclusion, experimental results regarding the generation of 2 μm single photons are discussed, and simulation results for the dual pump delay scheme are provided.

4.1 Basics of quantum optics

4.1.1 State vector

Considering an ensemble of objects (e.g. photons) with states $\{|\psi_i\rangle\}$, if all the objects occupy the same state, this ensemble is represented by a pure state. Pure quantum states correspond to vectors in the Hilber space, whose observables are associated with an operator. The operator acts on the state vectors, while the eigenvalues are the possible outcomes for the observables [122]. Each eigenvalue has its own eigenvector/eigenstate, which is a quantum state with a well defined value of the observable considered (i.e. no quantum uncertainty). However, a quantum system can be in a linear combination of several eigenstates, and in this case it has quantum uncertainty, since each eigenstate has a different eigenvalue. A state which is the result of a linear combination of eigenstates can be written as

$$|\psi(\mathbf{r},t)\rangle = \sum_{n=0}^{\infty} c_n(\mathbf{r},t)\,|\phi_n\rangle \tag{4.1}$$

where c_n are complex coefficients, from which the quantum interference arises, $|\phi_n\rangle$ is the n-th eigenstate. Due to the kind of analysis that we require for the study of single photon sources, from here on we will consider as the quantum state the

photon number state, i.e. $|\phi_n\rangle \equiv |n\rangle$. In order to operate on the photon number states, the following operators are introduced:

$$\hat{a}^\dagger |n\rangle = \sqrt{n+1}\,|n+1\rangle\,, \tag{4.2a}$$

$$\hat{a}\,|n\rangle = \sqrt{n}\,|n-1\rangle\,, \tag{4.2b}$$

where the first one is the creation operator, adding one photon to the $|n\rangle$ state, and the second one the destruction operator, subtracting one photon to the photon number state. The number states are eigenstates of the single-mode number operator $\hat{n}$,

$$\hat{n}\,|n\rangle = \hat{a}^\dagger\hat{a}\,|n\rangle = n\,|n\rangle\,. \tag{4.3}$$

Eq. (4.1) is a particular quantum state, since it is a single mode state. An example of a single-mode state, with j the label of the mode, is a plane-wave, a monochromatic field with frequency ω_j, wave vector $\mathbf{k}_j$ and polarization given by the unit vector $\mathbf{e}_j$. A more general notation, involving multimodes, can be given as

$$|\psi(\mathbf{r},t)\rangle = \sum_{n_1,n_2,n_3,\ldots} c_{n_1,n_2,n_3,\ldots}(\mathbf{r},t)\,|n_1\rangle_1\,|n_2\rangle_2\,|n_3\rangle_3\,\ldots, \tag{4.4}$$

with n_1, n_2, n_3... the number of photons in the modes $1, 2, 3, \ldots$ respectively. The multimode state product can be written as

$$|n_1\rangle_1\,|n_2\rangle_2\,|n_3\rangle_3\,\ldots = \prod_{j=1,2,3,\ldots} \frac{(\hat{a}_j^\dagger)^{n_j}}{\sqrt{n_j!}}\,|0\rangle\,, \tag{4.5}$$

with $|0\rangle$ the global vacuum state, meaning no photons in any mode. These multimode number states form a complete orthonormal basis set, therefore the following relation holds

$$[\hat{a}_j, \hat{a}_k^\dagger] = \delta_{j,k}. \tag{4.6}$$

Considering again the single-mode case, it is possible to simplify the notation by omitting the time and space dependence when these are included in the mode definition or do not affect the state over the region of interest:

$$|\psi\rangle = \sum_n^\infty c_n\,|n\rangle\,, \tag{4.7}$$

which in the case of an ideal single photon source becomes

$$|\psi\rangle = |1\rangle\,. \tag{4.8}$$

Till now we have considered pure states, but also statistical mixtures of states are possible, which are statistical ensembles of independent pure states. An ensemble here is considered as the collection of a large number of independent replicas of the system. A statistical mixture does not involve complex coefficients in the combination of states, but real positive values which describe the probability that choosing randomly a system in the ensemble this will be in the n-th state. While the mixed state exhibits classical probabilities, the quantum superposition of pure states is still a pure state, therefore based on probability amplitudes which give rise to quantum interference. Mixed states come from a statistical mixture of the initial state or they could be due to the uncertainty in the state preparation.

When dealing with heralded single photon states the degree of purity is inversely proportional to how much a state is mixed; this means that in order to have a pure single photon coming from a photon pair, all the correlations between the twin photons have to be broken in order to avoid the production of a mixed state instead of a pure photon state [123]. These concepts are further analysed in Sections 4.1.3 and 4.1.4.

4.1.2 Quantized electric field

The quantized electric field at $\mathbf{r}$ position and t time is [95]

$$\hat{\mathrm{E}}(\mathbf{r},t) = \sum_j \left[\hat{\mathrm{E}}_j^{(+)}(\mathbf{r},t) + \hat{\mathrm{E}}_j^{(-)}(\mathbf{r},t)\right], \tag{4.9}$$

with $\hat{\mathrm{E}}_j^{(\pm)}(\mathbf{r},t)$ the positive and negative frequency components of the quantized electric field in mode j; each mode is characterized by a particular spatial distribution, central wavelength, wave vector, polarization and spectral and temporal profiles. The two components are linked through the relation $\hat{\mathrm{E}}_j^{(-)}(\mathbf{r},t) = \left[\hat{\mathrm{E}}_j^{(+)}(\mathbf{r},t)\right]^\dagger$, with the † indicating the Hermitian conjugate [122]. The Hamiltonian for the electromagnetic field, which is treated as a quantized harmonic oscillator, is

$$\hat{H} = \sum_j \hbar\omega_j \left(\hat{a}_j^\dagger \hat{a} + \frac{1}{2}\right), \tag{4.10}$$

with $\hbar = h/2\pi$ and h the Planck constant. To be noticed that the energy of the vacuum fluctuations in mode j is $\frac{1}{2}\hbar\omega_j$. Considering a plane wave, its positive frequency component can be written as

$$\hat{\mathrm{E}}_j^{(+)}(\mathbf{r},t) = \varepsilon_j \mathbf{e}_j \hat{a}_j e^{i(\mathbf{k}_j\cdot\mathbf{r}-\omega_j t)} \tag{4.11}$$

with $\varepsilon_j = i\sqrt{\hbar\omega_j/2\epsilon_0 V}$, ϵ_0 the vacuum permittivity and V the mode volume. When dealing with non-monochromatic fields, the continuous-mode creation and annihilation operators are introduced, $\hat{a}_j^\dagger(\omega)$ and $\hat{a}_j(\omega)$, such that [95]

$$\left[\hat{a}_j(\omega), \hat{a}_j^\dagger(\omega')\right] = \delta(\omega-\omega'). \tag{4.12}$$

The number operator becomes

$$\hat{n}_j = \int \mathrm{d}\omega\, \hat{a}_j^\dagger \hat{a}_j(\omega), \tag{4.13}$$

and the positive frequency component of the field

$$\hat{\mathrm{E}}_j^{(+)}(\mathbf{r},t) = \int \mathrm{d}\omega\, \varepsilon_j \mathbf{e}_j \hat{a}_j(\omega) e^{i(\mathbf{k}_j\cdot\mathbf{r}-\omega_j t)}. \tag{4.14}$$

If pulsed light is considered, the photon wave packet creation operator is taken into account as follow

$$\hat{a}_{j,p}^\dagger = \int \mathrm{d}\omega\, F_j(\omega)\hat{a}_j^\dagger(\omega), \tag{4.15}$$

where $F_j(\omega)$ is the spectral profile of the photon wavepacket in mode j. The normalization is $\int \mathrm{d}\omega\, |F_j(\omega)|^2$. The positive frequency component, for the wave

packet case, becomes

$$\hat{\mathrm{E}}_j^{(+)}(\mathbf{r},t) = \int \mathrm{d}\omega\, \varepsilon_j \mathbf{e}_j F_j^*(\omega)\hat{a}_j(\omega)e^{i(\mathbf{k}_j\cdot\mathbf{r}-\omega_j t)}. \tag{4.16}$$

If the non-zero band of the spectrum is much smaller than ω_j, then the following approximation holds

$$\hat{\mathrm{E}}_j^{(+)}(\mathbf{r},t) \simeq \varepsilon_j \mathbf{e}_j e^{i(\mathbf{k}_j\cdot\mathbf{r}-\omega_j t)} \int \mathrm{d}\omega\, F_j^*(\omega)\hat{a}_j(\omega). \tag{4.17}$$

All this formalism can be given also in the time domain, that is linked to the frequency domain through the Fourier Transform.

4.1.3 Density matrix and purity

The density matrix is used to provide a more general quantum representation of the states. It can be used for both pure and mixed states, and the corresponding operator (the density-matrix operator) is [122]

$$\hat{\rho} = \sum_i p_i \left|\psi_i\right\rangle \left\langle\psi_i\right| \tag{4.18}$$

where p_i is the probability that the system is in $|\psi_i\rangle$ state and $\sum_i p_i = 1$. Eq. (4.18) represents a general quantum state: if only one of the p_i coefficients is non-zero the state is pure and $\hat{\rho} = \hat{\rho}^2$ holds, otherwise it is a mixture. Representing a state through the density matrix is an equivalent alternative to the representation based on the ket or the statistical ensemble of kets. The density matrix contains all the information needed in order to derive any property of the state. Regarding the measurable properties of the state, given the observable $\hat{O}$, its average over the ensemble is

$$\langle\hat{O}\rangle = \mathrm{Tr}\{\hat{\rho}\hat{O}\}, \tag{4.19}$$

from which arise the normalization condition $\mathrm{Tr}\{\hat{\rho}\} = 1$.

When the photon number probabilities have to be calculated, the photon number states are used as the basis, such that

$$P(n) = \mathrm{Tr}\{\hat{\rho}\left|n\right\rangle\left\langle n\right|\} = \left\langle n\right|\hat{\rho}\left|n\right\rangle, \tag{4.20}$$

with $P(n)$ the probability that the source will emit n photons at a time. So $P(n>1) = \sum_{n=2}^{\infty} P(n)$ is the probability of multi-photon emission. With a pulsed source, $P(n)$ gives the probability of n photons emitted per pulse, with $\mu = \mathrm{Tr}\{\hat{\rho}\hat{n}\}$ the average number of photons per pulse. The elements on the diagonal (ρ_{nn}) of the density matrix give the population in the basis considered. The off-diagonal elements (ρ_{nm}) are called *coherences* and are related to the interference between the states $|n\rangle$ and $|m\rangle$ [95].

The density matrix is also a powerful tool when the physical system under study is composed by several subsystems. In this case, the *reduced* density operator is used. A composite system of A and B subsystems is described by the density operator $\hat{\rho}_{AB}$. The reduced density operator for system A is given by

$$\hat{\rho}_A \equiv \mathrm{Tr}_B\{\hat{\rho}_{AB}\}, \tag{4.21}$$

where Tr_B is the partial trace over B [123], that, in terms of state vectors, is defined by

$$\mathrm{Tr}_B\{|a_1\rangle\langle a_2| \otimes |b_1\rangle\langle b_2|\} \equiv |a_1\rangle\langle a_2|\,\mathrm{Tr}\{|b_1\rangle\langle b_2|\}, \tag{4.22}$$

with $|a_i\rangle$ and $|b_i\rangle$ $(i = 1, 2)$ vectors in A and B spaces respectively. From the formalism of the reduced density operator, it is trivial to understand that this tool provides the right measurement statistics for measurements on the subsystems. In fact, considering a quantum composite system in the product state $\hat{\rho}_{AB} = \hat{\rho} \otimes \sigma$, where $\hat{\rho}$ and $\hat{\sigma}$ are density operators for A and B subsystems respectively, the following relation holds [123]

$$\hat{\rho}_A = \mathrm{Tr}_B\{\hat{\rho} \otimes \hat{\sigma}\} = \hat{\rho}\mathrm{Tr}\{\hat{\sigma}\} = \hat{\rho}, \tag{4.23}$$

where Eq. (4.21) and the normalization condition for the density operator have been considered. This means that the partial trace allows to access the correct observable quantities for subsystems involved in a composite quantum system. This last concept is of particular importance in the treatment of heralded single photons, where the composite system is composed by signal and idler photons, and the measurement performed on one of these two photons corresponds to a partial trace over the other photon state.

Through the density matrix formalism it is possible to quantify the purity of a state as

$$\mathcal{P} = \mathrm{Tr}\{\hat{\rho}^2\} \tag{4.24}$$

where $\mathcal{P} = 1$ corresponds to a pure state, while $\mathcal{P} = 1/N$ is the lower purity limit for a mixed state with N dimensions [122]. Therefore maximum purity is achieved when the state has the lowest degree of mixing, namely $N = 1$. When dealing with entangled states, the purity of the states of the subsystems involved in the entanglement defines the degree of the entanglement itself. If the system is maximally entangled, then the states composing the system are completely mixed ($N \gg 1$) because it is impossible to assign a definite pure state to the subsystems; on the contrary, if the system is not entangled at all ($N = 1$), the states of the subsystems are pure and the state describing the composite system is separable in the product state of the subsytems [122].

4.1.4 Entanglement and separability

A composite quantum system is composed by two or more quantum subsystems. The Hilbert space of the composite system is given by the tensor product of the individual Hilbert spaces associated to the embedded subsystems as $\mathcal{H} = \mathcal{H}_1 \otimes \mathcal{H}_2 \otimes \mathcal{H}_3 \cdots$.
Considering the case of a bipartite system, such that $\mathcal{H} = \mathcal{H}_1 \otimes \mathcal{H}_2$, we can prepare a system $|\Psi_s\rangle \in \mathcal{H}$ that is the product of the pure states $|\psi_1\rangle \in \mathcal{H}_1$, $|\psi_2\rangle \in \mathcal{H}_2$ of the two subsystems, such that

$$|\Psi_s\rangle = |\psi_1\rangle \otimes |\psi_2\rangle\,. \tag{4.25}$$

In this case, $|\Psi_s\rangle$ is separable, and physically corresponds to the fact that the measurement on one of the subsystems does not affect the outcome on the other one. This uncorrelation between the measurement outcomes of the subsystems indicates the absence of entanglement [124]. Consider now a state $|\Psi_e\rangle \in \mathcal{H}$ that is the result of the superposition of states $|\psi\rangle_i \neq |\phi\rangle_i$, $(i = 1, 2)$ belonging to the respective Hilbert

spaces $\mathcal{H}_i$, $(i = 1, 2)$, for example,

$$|\Psi_e\rangle = \frac{1}{\sqrt{2}} \left(|\psi\rangle_1 \otimes |\psi\rangle_2 + |\phi\rangle_1 \otimes |\phi\rangle_2 \right). \tag{4.26}$$

In this case, measuring an observable only over one of the two subsystems will affect the outcome of the other subsystem. In fact, the expectation value of an observable $\hat{a}$ over the subsystem 1 will be

$$\langle \hat{a} \rangle = \mathrm{Tr}_1(\hat{a}\hat{\rho}_1), \tag{4.27}$$

with $\hat{\rho}_{1(2)} = \mathrm{Tr}_{2(1)} |\Psi_e\rangle \langle\Psi_e|$ the reduced density matrix of subsystem 1(2) [124]. This means that the states of the individual subsystems are given by $\hat{\rho}_i$, $(i = 1, 2)$, but the state of the composite system is not equal to the product of the reduced density matrices $\hat{\rho} = |\Psi_e\rangle \langle\Psi_e| \neq \hat{\rho}_1 \otimes \hat{\rho}_2$. As a result the composite system state $|\Psi_e\rangle$ cannot be expressed as a product state like Eq. (4.25), with the direct consequence that a local measurement on one subsystem will affect the entire state, and thus also the outcome of the other subsystem will be conditioned. When such a correlation between the subsystems is present, the state of the composite system $|\Psi_e\rangle$ is an *entangled state*, and it is not separable. This description of entanglement and separability explains the importance of having a full factorization of the two-photon state when the pair is used within the heralded single photon framework. In fact, only if the two photons of the pair are uncorrelated, the herald detection does not affect the heralded state.

As just explained, the separability of the state is related to the degree of entanglement of the corresponding quantum system, and such a state is said to be separable if a decomposition into product states exists. Generally, a basis able to make explicit the entanglement properties is always present, and the representation of the state with this basis is indicated as the Schmidt decomposition [125].

4.1.5 The Schmidt decomposition

Any state $|\Psi\rangle$ belonging to a given composite system whose Hilbert space is $\mathcal{H} = \mathcal{H}_u \otimes \mathcal{H}_v$, where $\mathcal{H}_{u/v}$ are the Hilbert spaces of the two subsystems $\mathcal{U}$ and $\mathcal{V}$ of the composite system, can be written as

$$|\Psi\rangle = \sum_{i,j=1} c_{i,j} |a_i\rangle \otimes |b_j\rangle \tag{4.28}$$

where $\{|a_i\rangle, i = 1, 2, ...\}$ and $\{|b_j\rangle, j = 1, 2, ...\}$ are the bases of $\mathcal{H}_u$ and $\mathcal{H}_v$ respectively, and $c_{i,j}$ are complex non-negative coefficients such that $\sum_{i,j} |c_{i,j}|^2 = 1$. If the state of the composite system $\mathcal{U} + \mathcal{V}$ is pure, described by $\hat{\rho} = |\Psi\rangle \langle\Psi|$, then an orthonormal basis $\{|u_i\rangle\}$ for $\mathcal{H}_u$ and $\{|v_j\rangle\}$ for $\mathcal{H}_v$ such that [126]

$$|\Psi\rangle = \sum_i g_i |u_i\rangle \otimes |v_i\rangle \tag{4.29}$$

exists, where $\sum_i |g_i|^2 = 1$. This is the Schmidt decomposition, where $|u_i\rangle$ and $|v_i\rangle$ are the Schmidt modes and g_i are the Schmidt coefficients [125]. The power of this decomposition is that only one summation index is required, instead of two, as in a usual change of basis. From Eq. (4.29) it is evident that if $|\Psi\rangle$ is in a pure state, only one non-zero Schmidt coefficient should be present, resulting in a factorizable state;

on the contrary, if more than one Schmidt coefficient is different from zero, then $|\Psi\rangle$ is no more separable and the state is not pure.

Within the heralded single photon picture, thus involving pair of photons generated through parametric processes, the Schmidt decomposition is mainly used as a mean for the definition of a metric for the purity of the heralded single photon state [127]. Say $|\mathrm{II}\rangle$ the two-photon state. Considering the density matrix description for the two-photon state, the purities of the individual idler and signal photon states, respectively P_i and P_s, are given as in Eq. (4.24),

$$P_i = \mathrm{Tr}\left(\hat{\rho}_i^2\right), \tag{4.30a}$$

$$P_s = \mathrm{Tr}\left(\hat{\rho}_s^2\right), \tag{4.30b}$$

where the reduced density matrices are calculated from the density matrix of the two-photon state $\hat{\rho}_{\mathrm{II}}$ as in Eq. (4.23)

$$\hat{\rho}_i = \mathrm{Tr}_s\left(\hat{\rho}_{\mathrm{II}}\right), \tag{4.31a}$$

$$\hat{\rho}_s = \mathrm{Tr}_i\left(\hat{\rho}_{\mathrm{II}}\right). \tag{4.31b}$$

As said before, the number of elements in Eq. (4.29) needed in order to express $|\mathrm{II}\rangle$ quantifies its factorizability, or purity. The number of Schmidt modes involved in the entanglement between the photons in the pair can be measured through the Schmidt number K,

$$K \equiv \frac{1}{\sum_i g_i^4} \equiv \frac{1}{\mathrm{Tr}\left(\hat{\rho}_s^2\right)} \equiv \frac{1}{\mathrm{Tr}\left(\hat{\rho}_i^2\right)}. \tag{4.32}$$

K is related to the individual single photon purities of the two-photon state as [125],

$$P_s = P_i = \sum_i g_i^4 = \frac{1}{K}, \tag{4.33}$$

thus $K = 1$ corresponds to perfect purity of the single photon state, while the greater is K the larger is the entanglement between signal and idler, therefore minimizing the factorizability of the two-photon state.

4.1.6 The two-mode squeezed state

When dealing with parametric light generation, the photon pairs that are generated are described as two-mode squeezed states, in analogy with a system of two oscillators. This state is characterized by reduced uncertainty on the conjugate variables describing the entire system of oscillators, i.e. on the linear combinations of variables of both oscillators; in fact, squeezing is not evident on the fluctuations of each oscillator taken separately. A particular feature of the two-modes state is that considering individually the modes, they will exhibit a thermal behaviour [128].

A coherent state can be described in terms of its quadrature dimensionless variables $\hat{X} = (\omega/\hbar)^{1/2}\hat{q}$ and $\hat{Y} = (\hbar\omega)^{-1/2}\hat{p}$, where $\hat{q}$, $\hat{p}$ are the canonical variables of the harmonic oscillator [128]. According to the Heisenberg uncertainty principle, for minimum uncertainty states, the relation $\Delta q \Delta p = \hbar/2$ holds [129]. In the case of the ground state (vacuum) of the quantum harmonic oscillator, it can be derived that [128]

$$\Delta p_0 = \left(\frac{1}{2}\hbar\omega\right)^{1/2}, \tag{4.34a}$$

$$\Delta q_0 = \left(\frac{\hbar}{2\omega}\right)^{1/2}. \tag{4.34b}$$

As a consequence, the uncertainties over the quadrature variables are equal,

$$\Delta X_0 = \Delta Y_0 = \frac{1}{\sqrt{2}}. \tag{4.35}$$

However, when squeezed states are taken into account, the equality between the uncertainties is no more valid, and the squeezed state uncertainties Δq_s, Δp_s can be written as a function of the ground state uncertainties as

$$\Delta q_s = e^{-r}\Delta q_0, \tag{4.36a}$$

$$\Delta p_s = e^{+r}\Delta p_0, \tag{4.36b}$$

with r the squeeze parameter, whose role is to reduce the uncertainty on one of the variables ($\hat{q}$ or $\hat{p}$) at the expenses of the uncertainty on the conjugate one, whose fluctuations increase. More in general, an oscillator is said to be squeezed if one of the conjugate variables exhibits a lower uncertainty with respect that of a coherent state, while the other variable can be affected by a much larger uncertainty, resulting in a product of the conjugate uncertainties larger than the Heisenberg limit. The most studied squeezers are the single-beam squeezers and twin-beam squeezers. Single-beam squeezers generate the squeezed state only in one optical mode, with the squeezing operator $\hat{S} = \exp\left(-\xi\hat{a}^{\dagger 2} + \xi^*\hat{a}^2\right)$, while twin-beam squeezers involve the inter-beam squeezing operator $\hat{S}^{ab} = \exp\left(-\xi\hat{a}^\dagger\hat{b}^\dagger + \xi^*\hat{a}\hat{b}\right)$ [130]. ξ is a parameter quantifying the squeezing strength and $\hat{a}^\dagger$ and $\hat{b}^\dagger$ are the creation operators for the mode a and b respectively. Tipically, parametric processes like SFWM and SPDC generate broadband squeezed states, meaning that they are characterized by a large amount of squeezers each in a different orthogonal spectral mode. Therefore, the generated parametric light is characterized by a multitude of spectral modes, which corresponds to the $K > 1$ condition discussed in Section 4.1.5. These kind of squeezers are called multimode squeezers, opposed to single mode squeezers, which generate the signal and idler photons, individually, in one squeezed beam. The number of mode squeezers is thus directly related to the correlations present between the signal and idler beams. The two-photon state can be written in terms of the squeezing operator starting from the Hamiltonian of the parametric process [130],

$$\hat{H}_{SFWM} = A\int\int \mathrm{d}\omega_i \mathrm{d}\omega_s F(\omega_s,\omega_i)\,\hat{a}_s^\dagger(\omega_s)\,\hat{a}_i^\dagger(\omega_i) + h.c., \tag{4.37}$$

where A is proportional to the efficiency of the process, $F(\omega_s,\omega_i)$ is the bi-photon wavefunction or the joint spectral amplitude (JSA), $\hat{a}_s^\dagger(\omega_s)$ and $\hat{a}_i^\dagger(\omega_i)$ are the creation operators for the signal and idler beams respectively. The two-photon state is obtained through [122],

$$|\Psi_{SFWM}\rangle = \hat{U}_{SFWM}\,|0\rangle_s\,|0\rangle_i\,, \tag{4.38}$$

where

$$\hat{U}_{SFWM} = \exp\left[-\frac{i}{\hbar}\hat{H}_{SFWM}\right]. \tag{4.39}$$

By applying now the singular value decomposition theorem [131], which is analogous to the Schmidt decomposition for the factorization of the two-photon state,

the unitary operator $\hat{U}_{SFWM}$ can be rewritten as the tensor product of N individual twin-beam squeezers,

$$\hat{U}_{SFWM} = \bigotimes_{k=0}^{N-1} \hat{S}_k^{ab}\left(-r_k\right), \tag{4.40}$$

with r_k the squeezing parameter and $\hat{S}_k^{ab}\left(-r_k\right) = \exp\left[r_k \hat{A}_k^\dagger \hat{B}_k^\dagger - h.c.\right]$ [132]. Therefore, the generated state after the SFWM interaction is the product of the independent squeezers, such that

$$\left|\Psi_{SFWM}\right\rangle = \bigotimes_{k=0}^{N-1} \hat{S}_k^{ab}\left(-r_k\right)\left|\Psi_0\right\rangle, \tag{4.41}$$

where $\left|\Psi_0\right\rangle$ is the initial state before the interaction, that usually corresponds to the vacuum state [133]. To perform the transformation in Eq. (4.40) the new broadband mode basis has been introduced,

$$\hat{A}_k = \int \mathrm{d}\omega_s \psi_k(\omega_s)\hat{a}_s(\omega_s), \tag{4.42a}$$

$$\hat{B}_k = \int \mathrm{d}\omega_i \phi_k(\omega_i)\hat{a}_i(\omega_i), \tag{4.42b}$$

where $\{\psi_k(\omega_s)\}$ and $\{\phi_k(\omega_i)\}$ each form a complete set of orthonormal functions [134]. These are the Schmidt modes for the decomposition of the bi-photon wavefunction as

$$-\frac{i}{\hbar} AF\left(\omega_s, \omega_i\right) = \sum_k r_k \psi_k^*\left(\omega_s\right)\phi_k^*\left(\omega_i\right), \tag{4.43a}$$

$$-\frac{i}{\hbar} A^* F^*\left(\omega_s, \omega_i\right) = -\sum_k r_k \psi_k\left(\omega_s\right)\phi_k\left(\omega_i\right). \tag{4.43b}$$

Consider now a two-mode squeezed state characterized by a single mode emission per idler and signal beams. Its state can be written, according to Eq. (4.41), as

$$\left|\Psi_{SFWM}\right\rangle = \hat{S}^{ab}(-r)\left|0\right\rangle_a\left|0\right\rangle_b = \sum_{n=0}^{\infty} \kappa_n \left|n\right\rangle_a \left|n\right\rangle_b, \tag{4.44}$$

with photon number distribution $p(n) = |\kappa_n|^2 = \mathrm{sech}^2(r)\tanh^{2n}(r)$, and where $\hat{A}_k$ and $\hat{B}_k$ have been transformed according to the Heisenberg representation [130]

$$\hat{A}_k \to \cosh(r_k)\hat{A}_k + \sinh(r_k)\hat{B}_k^\dagger, \tag{4.45a}$$

$$\hat{B}_k \to \cosh(r_k)\hat{B}_k + \sinh(r_k)\hat{A}_k^\dagger, \tag{4.45b}$$

and the index k is removed in the case of two-photon squeezed states with single mode emission. The photon number distribution $p(n)$ in Eq. (4.44) is a thermal distribution, as expected for each individual single mode contributing to the two-mode squeezed state [133]. Therefore, it can be derived that when the two-mode squeezed state is characterized by multiple modes emission, its photon number distribution is given by the convolution of all the thermal distributions of the independent squeezers involved [133]. This means that when only one mode contributes to the emission ($N = 1$) the photon source exhibits thermal statistics; when other modes come into play ($N > 1$) the resulting photon number distribution gradually loses its thermal statistics becoming Poissonian in the limit of $N \to \infty$, because the convolution of thermal distributions converges to the Poissonian one [60]. This description well

fits with the heralded state purity as a function of the degree of entanglement, that I discussed in Section 4.1.5. In fact, the higher the frequency correlations between the signal and idler fields, i.e. the photons are entangled, the larger the number of squeezed modes required to fully describe the two-mode squeezed state. This analogy is quantitatively introduced in the estimation of the generated squeezers via SFWM or SPDC by relating the squeezed parameter r_k with the Schmidt coefficients g_k, such that

$$r_k = B g_k, \tag{4.46}$$

with $B \in \mathbb{R}^+$ the overall gain of the process and g_k related to the probability of different squeezers occupation in the corresponding optical quantum state [130]. Within this formalism, the Schmidt number $K = 1/\sum_k g_k^4$ measures how many modes contribute to the multimode twin-beam state.

4.1.7 The bi-photon wave function and the joint spectral intensity

In the case of the nonlinear spontaneous parametric processes like SPDC or SFWM, the two-photon state is generated thanks to the vacuum fluctuations, which seed the conversion of the input pump photons into the correlated signal and idler photons. In the particular case of SFWM in waveguide with co-polarised photon generation, the two-photon squeezed state describing the generated idler-signal pair, both on the same waveguide mode, is written, according to Section 4.1.6, as [135]

$$|II\rangle = \int\int \mathrm{d}\omega_s \mathrm{d}\omega_i F(\omega_s, \omega_i) \left|\omega_s\right\rangle_s \left|\omega_i\right\rangle_i, \tag{4.47}$$

with $\left|\omega\right\rangle_q \equiv \left|1\right\rangle_{q,\omega} = \hat{a}_q^\dagger(\omega)\left|0\right\rangle$ representing one photon in mode q with frequency ω. $F(\omega_s, \omega_i)$, already introduced in Eq. (4.37), embeds the information relative to the bandwidth of the pump, signal and idler photons, and it is given by

$$F(\omega_s, \omega_i) = \int_{-\infty}^{+\infty} \mathrm{d}\omega \alpha(\omega)\alpha(\omega_s + \omega_i - \omega)\phi(\omega_s, \omega_i, \omega), \tag{4.48}$$

where $\alpha(\omega)$ is the complex amplitude of the pump spectrum centered in ω_p, usually considered with a gaussian profile, and

$$\phi(\omega_s, \omega_i, \omega) = \exp\left(\frac{i\Delta k L}{2}\right) \mathrm{sinc}\left(\frac{\Delta k L}{2}\right) \tag{4.49}$$

is the phase matching function, with L the waveguide length and Δk the phase mismatch parameter [136]. The JSA quantifies the probability density for the generation of the first photon of the pair in the ω_s mode and the second photon in the ω_i mode. The modulus square of the JSA, namely $|F(\omega_s, \omega_i)|^2$, is called joint spectral intensity (JSI), which is considered more frequently than the JSA, cause the JSI deals directly with the intensity of the field, that is the actual measurable quantity. The JSI is used to characterize the degree of correlation between the signal and idler photons [127]. In fact, since the JSI takes into account all the frequencies and bandwidths of the involved waves (pump, signal, idler), it directly reflects the spectral distribution associated with the signal/idler once the frequency of the idler/signal is given. In more quantitative terms, the capability of the JSI to quantify the degree of correlation, and so the purity of the system, is made evident by the Schmidt decomposition.

In fact, the JSA can be decomposed according to Eq. (4.29) [135],

$$F(\omega_s, \omega_i) = \sum_n g_n u_n(\omega_s) v_n(\omega_i) \tag{4.50}$$

with u_n and v_n two complete sets of orthonormal functions. As introduced in Section 4.1.5, through the Schmidt number $K = \left(\sum_n g_n^4\right)^{-1}$ the degree of entanglement in the system can be quantified, with K that can be interpreted as the effective number of populated eigenmodes (see Section 4.1.6): with $K = 1$, corresponding to only one non-zero Schmidt coefficient, the system is completely uncorrelated; if multiple non-zero Schmidt coefficients are present, $K > 1$ and the system exhibits entanglement. However, the decomposition in Eq. (4.50) is not possible with the JSI, and the JSA is not easily accessible experimentally [135]. Anyway, usually it is considered a singular value decomposition of the square root of the JSI, which provides a lower bound for the true Schmidt number [137], from which it is possible to calculate the purity of the heralded single photon as $P = 1/K$ [138]. Despite the JSI does not exhibit the correlations present in the joint spectral phase, it is in any case directly related to the degree of correlation, and its shape ranges from a thin line (perfect correlation) to a circular shape (perfect decorrelation) [107], as shown in Fig. 4.3.

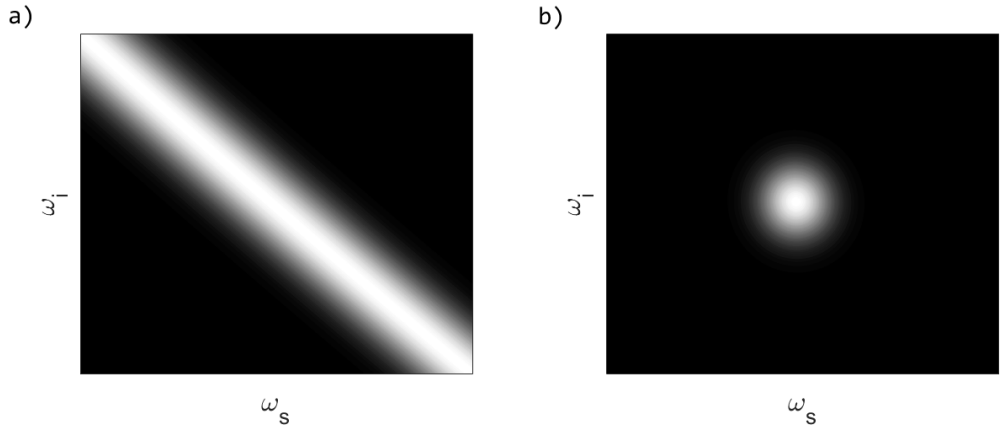

FIGURE 4.3: JSI in the case of (a) correlated and (b) decorrelated photon pairs.

The circular shape case directly resembles the case in which the two-photon system is in a separable state, which means maximum purity, $P = 1$. When the JSI is circular, it means that the JSA can be factorized, such that $F(\omega_s, \omega_i) = F_s(\omega_s)F_i(\omega_i)$ [95]. The case of separable bi-photon wave function is exactly the pursued condition for the heralded single photon operation, where the maximum purity for the single photon state can be attained only by eliminating the correlation between the twin photons [95]. The JSI can thus be used as a tool for the evaluation of the purity P of the heralded single photon, which can be calculated as [139]

$$P = \int\int \mathrm{d}\omega \mathrm{d}\omega' |q_s(\omega, \omega')|^2, \tag{4.51}$$

where it is considered the signal photon as the heralded single photon and $q_s(\omega, \omega') =$

$\int \mathrm{d}\omega'' F(\omega'', \omega) F^*(\omega'', \omega')$, with q_s related to the density matrix of the heralded photon as

$$\rho_s = \mathrm{Tr}_i\{|II\rangle \langle II|\} = \int\int \mathrm{d}\omega \mathrm{d}\omega' q_s(\omega, \omega') \hat{a}_s^\dagger(\omega) |0\rangle \langle 0| \hat{a}_s(\omega'). \tag{4.52}$$

4.2 Elements of photon statistics for single photon experiments

4.2.1 The $g^{(2)}$ correlation function

When dealing with quantum light sources, it is of fundamental importance knowing the statistics of the photons involved, in order to predict the emission properties of the source itself. The most powerful tool when characterizing a single photon source is the second order coherence $g^{(2)}$, which quantifies the multi-photon emission probability. The second order coherence between two modes (mode j, at position $\mathbf{r}_1$ and time t_1, and mode k, at position $\mathbf{r}_2$ and time t_2) is

$$g^{(2)}_{j,k}(\mathbf{r}_1, t_1; \mathbf{r}_2, t_2) = \frac{\langle \hat{\mathbf{E}}_j^{(-)}(\mathbf{r}_1, t_1) \hat{\mathbf{E}}_k^{(-)}(\mathbf{r}_2, t_2) \hat{\mathbf{E}}_k^{(+)}(\mathbf{r}_2, t_2) \hat{\mathbf{E}}_j^{(+)}(\mathbf{r}_1, t_1) \rangle}{\langle \hat{\mathbf{E}}_j^{(-)}(\mathbf{r}_1, t_1) \hat{\mathbf{E}}_j^{(+)}(\mathbf{r}_1, t_1) \rangle \langle \hat{\mathbf{E}}_k^{(-)}(\mathbf{r}_2, t_2) \hat{\mathbf{E}}_k^{(+)}(\mathbf{r}_2, t_2) \rangle}, \tag{4.53}$$

where the angled brackets indicate the average on the ensemble, i.e. over a large number of photons [95]. When only one mode is measured ($j = k$), at a single position ($\mathbf{r}_1 = \mathbf{r}_2$) and with a stationary source (e.g. CW source), i.e. only the time delay $\tau = t_2 - t_1$ determines the properties of the source , Eq. (4.53) can be rewritten in terms of creation and annihilation operators as

$$g^{(2)}(\tau) = \frac{\langle \hat{a}^\dagger(t) \hat{a}^\dagger(t+\tau) \hat{a}(t+\tau) \hat{a}(t) \rangle}{\langle \hat{a}^\dagger(t) \hat{a}(t) \rangle^2}, \tag{4.54}$$

which becomes, in terms of the time dependent number operator $\hat{n} = \hat{a}^\dagger \hat{a}$, at $\tau = 0$,

$$g^{(2)}(0) = \frac{\langle \hat{n}(t)(\hat{n}(t) - 1) \rangle}{\langle \hat{n}(t) \rangle^2}. \tag{4.55}$$

$g^{(2)}(0)$ characterizes the photon number probabilities of the source of photons, and it is especially used when characterizing the single photon sources. In fact, $g^{(2)}(0)$ can be directly related to the probability of photon emission $P(n)$, as will be shown in a while. It has to be emphasized that $g^{(2)}$ does not change if the field under study is affected by losses, if all the modes experience the same amount of losses [95]. The same treatment can be done also for pulsed sources, where the continuous $g^{(2)}$ is substituted with its discrete analogous,

$$g^{(2)}[m] = \frac{\langle \hat{a}^\dagger[l] \hat{a}^\dagger[l+m] \hat{a}[l+m] \hat{a}[l] \rangle}{\langle \hat{a}^\dagger[l] \hat{a}[l] \rangle \langle \hat{a}^\dagger[l+m] \hat{a}[l+m] \rangle}, \tag{4.56}$$

where l and m are integer numbers indicating the pulse number and the average is taken over the l index. When treating pulsed sources, the photon statistics is averaged over the duration of the pulse. As in the CW case, $g^{(2)}[0]$ is directly related to the multi-photon probability associated with the source, and, using the photon

number operator $\hat{n} = \hat{a}^{\dagger}[l]\hat{a}[l]$, it becomes

$$g^{(2)}[0] = \frac{\langle \hat{n}(\hat{n}-1)\rangle}{\langle \hat{n}\rangle^2}, \tag{4.57}$$

where $\hat{n}$ measures the number of photons in the pulse. Therefore, when only one photon is present in the pulse, i.e. $\langle \hat{n}\rangle = 1$, from Eq. (4.57) it can be understood that $g^{(2)}[0] = 0$. Eq. (4.57) can be written maxing explicit the $P(n)$ as

$$g^{(2)}[0] = \frac{\mathrm{Tr}\{\hat{\rho}\hat{n}(\hat{n}-1)\}}{(\mathrm{Tr}\{\hat{\rho}\hat{n}\})^2} = \frac{\sum_{n=0}^{\infty} n(n-1)P(n)}{\left[\sum_{n=0}^{\infty} nP(n)\right]^2}, \tag{4.58}$$

where the density matrix has been considered and only its diagonal elements contribute to $g^{(2)}[0]$ [95].

If the source is characterized by $P(1) \gg P(2) \gg P(n>2)$, which is often the case when dealing with low-efficiency sources, the following expression can be derived

$$g^{(2)}[0] \simeq \frac{2P(2)}{\mu^2} \simeq \frac{2P(2)}{P(1)^2}, \tag{4.59}$$

where μ is the average number of photons per pulse and $\mu \simeq P(1)$ comes from the assumption $P(1) \gg P(2)$. Eq. (4.59) states that as soon as the source of single photons is characterized by $P(1) > \sqrt{2\,P(2)}$, a $g^{(2)}(0) < 1$ occurs, approaching zero as $P(1)^2/P(2)$ increases. This is the first signature of single photon statistics, as will be better described in Section 4.2.2, and it can be measured by means of an interferometric approach, that is the Hanbury Brown and Twiss interferometer.

Hanbury Brown - Twiss interferometer

In order to characterize a single-photon source it would be desirable to compare $P(1)$ with the analogous probabilities for multi-photon emission $P(2), P(3), ...$ Unfortunately, photon-number-resolving detectors are still limited in combining low jitter, low dead time and high efficiencies [140, 141]. Because of this, click/no-click detectors, with lower efficiency but better timing properties, are the most used approach to the photon statistics measurement. The basic experiment used to resolve the $g^{(2)}$ of a single-photon source is the Hanbury Brown-Twiss (HBT) interferometer, also reported in Fig. 4.4. Within this experimental scheme, the single-photon field enters from one input of the beam splitter (port 1 in Fig. 4.4) and it is then measured by one of the two detectors (D_3 and D_4) placed in the trasmitted (port 4) and reflected (port 3) ports; the electric signal due to detection is then processed by a correlator or a start/stop timing system. The basic idea of the HBT experiment is that if only one photon at a time enters the beam splitter, there is no possibility that both the detectors can detect him, yielding zero coincidences at zero delay, which means $g^{(2)}(0) = 0$. Via the HBT interferometer it is also possible to explore the $g^{(2)}(\Delta t)$ at subsequent or precedent times with respect to the coincidence at zero delay, by applying a temporal shift or electronic delay Δt to one of the two detectors. In the case of single photon statistics, it is expected $g^{(2)}(0) < g^{(2)}(\Delta t)$, $\forall \Delta t \neq 0$. The HBT experiment is particularly suitable for the second-order coherence estimation thanks to some distinguishing properties [95]:

- unbalanced transmission and reflection coefficients of the beam splitter do not affect the $g^{(2)}$ measurement;

- the two detectors do not require 100% efficiency or balanced efficiencies;
- click detectors are suitable for the HBT experiment without losing in accuracy if $P(1) >> P(2) >> P(n > 2)$;
- losses does not modify the $g^{(2)}$ measurement.

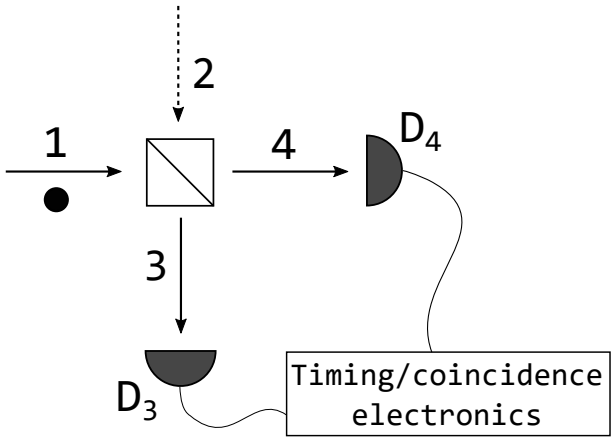

FIGURE 4.4: Schematics of the HBT interferometer, with the light field only in the input port 1, while in the input port 2 the vacuum field is present. The output detection signals coming from the two detectors are analyzed by suitable electronics (like a correlator or a start/stop system) in order to provide the measured $g^{(2)}(\tau)$.

4.2.2 Poisson statistics and the bunching/antibunching behaviour

The well known coherent state exhibits Poissonian photon number statistics, meaning random distribution of the photon arrival times and a $g^{(2)}(\tau) = 1$, $\forall\tau$. A source characterized by Poissonian statistics exhibits neither bunching nor antibunching behaviour, where *bunching* means that photons arrive more probably closely spaced in time rather than far apart, as depicted in Fig. 4.5, and *antibunching* refers to the opposite condition, i.e. with the photon arrivals far apart than close in time. In order to link the photon statistics to the $g^{(2)}$ measurement, it has to be considered that second order coherence relates the average photon number to the variation of the photon number.

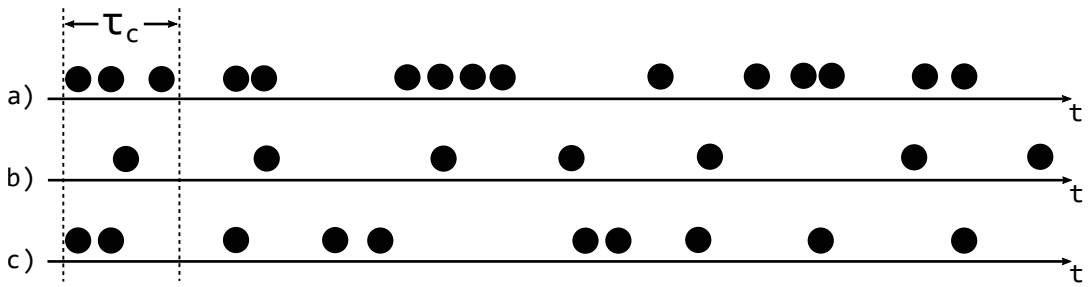

FIGURE 4.5: Photon detections as a function of time, with τ_c the temporal coherence. a) Super-poissonian behaviour, exhibiting photon bunching. b) Sub-poissonian behaviour, exhibiting photon antibunching. c) Poissonian behaviour, with random distribution of photons and no bunching or antibunching.

For the bunched case $g^{(2)}(0) > g^{(2)}(\tau \neq 0)$, while the antibunched process has $g^{(2)}(0) < g^{(2)}(\tau \neq 0)$. Considering the pulsed case, one can derive from Eq. (4.55) the relation linking the $g^{(2)}[0]$ to the mean photon number $\mu = \langle \hat{n} \rangle$ and the variance $(\Delta n)^2 = \langle \hat{n}^2 \rangle - \langle \hat{n} \rangle^2$ as

$$g^{(2)}[0] = 1 + \frac{(\Delta n)^2 - \mu}{\mu^2}. \tag{4.60}$$

For a Poissonian source $g^{(2)}[0] = 1$, and in fact $\mu = (\Delta n)^2$. If $g^{(2)}[0] > 1$ then the variance is larger than the mean value, typical of the bunching behaviour of a super-Poissonian field. When $g^{(2)}[0] < 1$ the variance is smaller than the mean value, signature of the antibunching occurring with sub-Poissonian light, which is the statistics required for single photon operation. In Fig. 4.6 is reported the $g^{(2)}$ for various photon statistics as a function of the temporal delay Δt between the two arms of the HBT interferometer; the case of perfect sub-Poissonian ($g^{(2)}(0) = 0$), perfect super-Poissonian ($g^{(2)}(0) = 2$, that is the thermal statistics) and Possonian ($g^{(2)}(0) = 1$) statistics are shown.

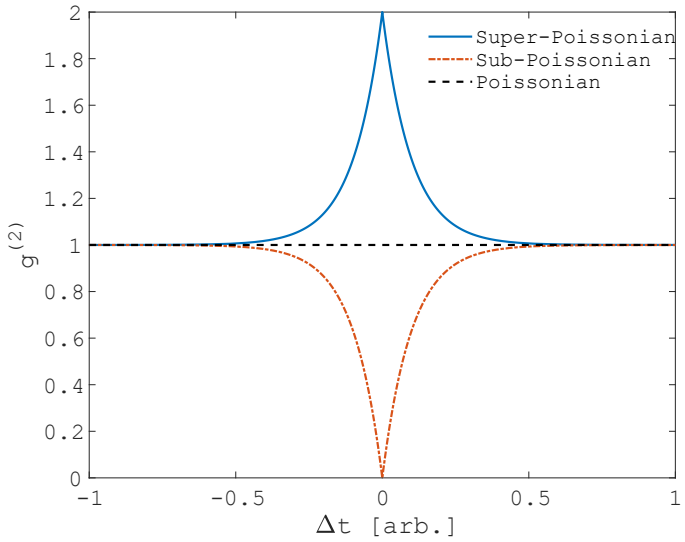

FIGURE 4.6: $g^{(2)}$ for super-Poissonian, sub-Poissonian and Poissonian light. The super- and sub-Poissonian statistics exhibit respectively the expected bunched and anti-bunched behaviour.

4.3 Experimental parameters of heralded single photon sources

In this section, a short introduction to the main features of the detectors and timing electronics involved in single photon experiments (Section 4.3.1) is provided and then it follows a brief introduction to the main experimental parameters for the characterization of the heralded sources (Section 4.3.2).

4.3.1 Detection in single-photon experiments

Considering a free-space coupled detector, the detection efficiency is related to the probability of obtaining an electrical signal, measurable for the readout electronics, as a result of a photon illuminating on the active area of the detector. η_{DE} is the result of other sub-processes, whose efficiencies affect the overall detection efficiency as

[95]

$$\eta_{DE} = \eta_{coupl}\eta_{abs}\eta^{i}_{QE}\eta_{th} \tag{4.61}$$

where η_{coupl} is the coupling efficiency due to the collection optics used to deliver the optical signal to the detector active-area, η_{abs} quantifies the probability that a photon impinging on the active-area is absorbed, η^{i}_{QE} is the internal quantum efficiency of the detector and η_{th} is the efficiency associated to the registration of the generated electrical signal by the electronics external to the detector. In fact, each electrical signal is registered and processed by means of electronic devices which are usually separated from the optical detector. In a real detector, other parameters have to be considered in order to deal with the detection process in the proper manner. These parameters are mainly related to the working principle of the detector itself, which is schematized in Fig. 4.7. These parameters are:

- **timing latency**, t_{lat}, which is the time delay between the arrival of the photon on the detector and the time at which the photogenerated output electrical pulse crosses a defined threshold level;
- **rise time**, t_{rise}, which is the time needed by the output detection electrical pulse to pass from the 10 % to the 90 % of its maximum value;
- **timing jitter**, which is the pulse-to-pulse variation in the t_{lat};
- **dead time**, t_{dead}, which is the time interval over which the detector is not capable of giving an output electrical pulse;
- **reset time**, t_{reset}, which is the time required by the detector to restore its maximum detection efficiency after the dead time;
- **recovery time**, $t_{recovery} = t_{dead} + t_{reset}$, which is the time needed by the detector to recover to its maximum detection efficiency after a detection event;
- **dark count rate**, R_{DC}, which is the average counts per second registered by a detector when no input light is present;
- **afterpulse probability**, $P_{afterpulse}$, which is the probability of an additional output detection signal, as a dark count, after a previous detection event.

The detection efficiency enters as a crucial parameter when calculating the probability that the detector gives an output if one or more photons have reached the active area; in ideal (no afterpulsing or dark counts) threshold detectors (detectors that are not able to resolve the number of photons related to the detection event but only whether the photons have been detected), like the single photon avalanche detectors (SPADs), the probability that the detector does not give any output,$p_{DE}(0)$, with $P(n)$ probability of the incident light flux is

$$p_{DE}(0) = \sum_{n=0}^{\infty}(1-\eta_{DE})^{n}P(n), \tag{4.62}$$

while the probability for a "click" on the detector (i.e. the detector gives an electric output) is

$$p_{DE}(1) = \sum_{n=1}^{\infty}[1-(1-\eta_{DE})^{n}]P(n). \tag{4.63}$$

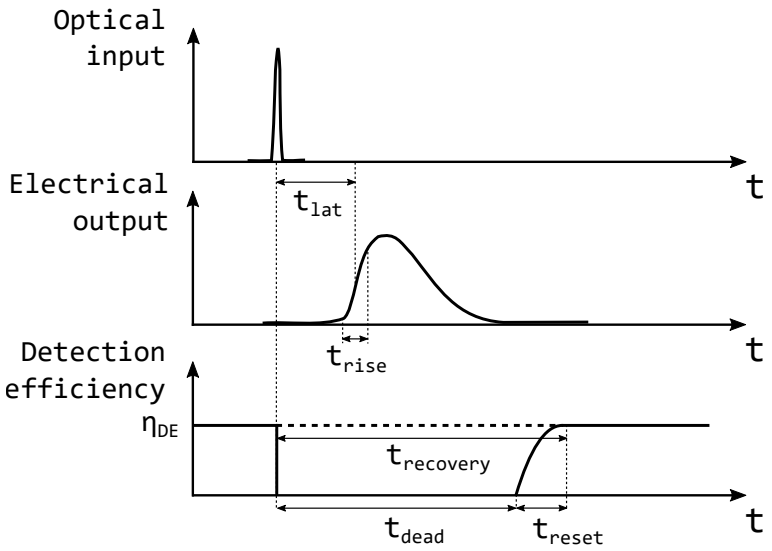

FIGURE 4.7: Parameters involved in the detection process and their timing relationship.

4.3.2 Measurement parameters

Coincidence to accidental ratio

When dealing with the pair generation through parametric processes, it is useful to introduce a parameter which quantifies the overall coincidence detection efficiency between signal and idler. In fact, the higher the losses on the idler or signal detection arm, the lower the probability that the detection of a signal/idler photon implies the simultaneous detection of his twin partner. The losses thus reduce the coincidence rate, promoting the occurrence of coincidences between the signal (idler) with other detections, coming from noise or subsequent/previous idler (signal) photons. The coincidence occurring between the signal and idler belonging to the same pair are the actual coincidences characterizing the temporal correlation of the emitted pairs. The coincidences occurring between signal and idler photons belonging to distinct pairs, or occurring between one photon of the pair and the noise, or between two noise photons, are indicated as accidental coincidences. An efficient source of photon pairs is characterized by a rate of "good" coincidences much greater than the accidental ones, and this concept is formalized through the coincidence to accidental ratio (CAR) parameter [59],

$$\mathrm{CAR} = \frac{R_{si}}{R_{ac}}. \tag{4.64}$$

with R_{si} the idler-signal coincidence rate and R_{ac} the accidental coincidence rate. This parameter is closely related to the signal-idler cross-correlation $g^{(2)}_{si}$ as

$$g^{(2)}_{si}(\tau) = \frac{\langle \hat{a}^\dagger_s(t+\tau)\hat{a}^\dagger_i(t)\hat{a}_i(t)\hat{a}_s(t+\tau)\rangle}{\langle \hat{a}^\dagger_s(t+\tau)\hat{a}_s(t+\tau)\rangle\langle \hat{a}^\dagger_i(t)\hat{a}_i(t)\rangle} = \frac{R_{si}(\tau)}{R_s\, R_i\, \tau_b}, \tag{4.65}$$

with R_s the signal generation rate, R_i the idler generation rate and τ_b the coincidence time window. When a CW laser is used,

$$\mathrm{CAR} = \frac{R_{si}(0)}{R_{si}(\infty)}, \tag{4.66}$$

while if pulsed pump is employed,

$$\mathrm{CAR} = \frac{R_{si}(0)}{R_{si}(n\,T)}, \tag{4.67}$$

with T the period of the laser pulses and $n > 0$ an integer number, since all the side peaks should be at the same height [106]. For both pulsed and CW light, the $g^{(2)}_{si}$ is normalized such that

$$\mathrm{CAR} = g^{(2)}_{si}(0). \tag{4.68}$$

Experimentally, the CAR value is measured as in Fig. 4.8, with the typical outcome in the right part of the picture, normalized as in Eq. (4.68). To carry out the measurement, a start/stop timing electronics or a correlator can be used equivalently in the case of CW pumping. If the pump is pulsed, the correlator can be used only if the pair generation rate is so low that the probability of detecting more than one pair in the correlator time window is negligible. In fact, the correlator works by shifting the individual detection traces of the two detectors, cross-correlating also good coincidence events, giving rise to an over estimation of the accidental counts.

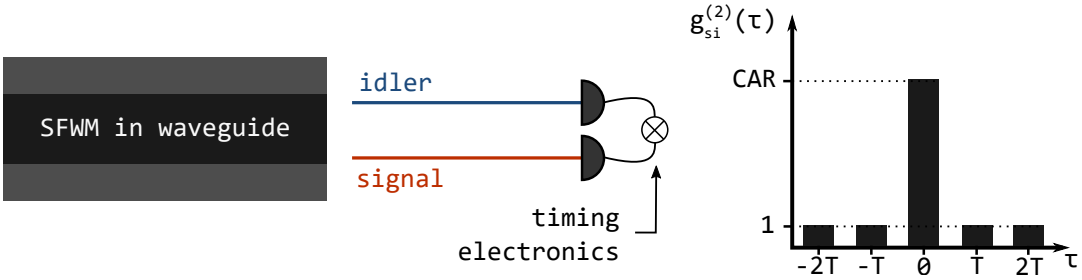

FIGURE 4.8: CAR measurement set-up with pulsed SFWM in waveguide, with 1/T repetition rate of the pump. The timing electronics can be a start/stop TDC or a correlator.

The CAR is therefore a fundamental parameter when characterizing the quality of a source in terms of reliability of its pair emission, or, equivalently, it estimates the amount of noise photons together with the wanted correlated pairs. A useful metric for the CAR has been introduced in Ref. [142], where it is derived the expected maximum CAR attainable given the dark counts and coupling losses for the detection of signal and idler photons. The maximum CAR is calculated as

$$\mathrm{CAR}_{max} = 1 + \frac{1}{\left(\sqrt{\frac{d_s}{\alpha_s}} + \sqrt{\frac{d_i}{\alpha_i}}\right)^2}, \tag{4.69}$$

with d_s, d_i the dark counts (in ns^{-1}) for the signal and idler detectors respectively and α_s, α_i the transmittance for the signal and idler paths respectively.

Purity

As already introduced in former sections, purity is the measurement of the single mode emission character of the generated single photon. In the case of parametric processes, this single mode character refers to the signal and idler beams individually, whose purity is inversely proportional to their degree of entanglement. It has been described in Section 4.1 that the purity of the single photon state is given as the trace over the system density matrix squared, or in terms of the inverse

of the Schmidt number, that are almost equivalent approaches to the definition of the purity. Single mode emission, absence of correlations/entanglement, or single squeezer description of the state are all synonyms to indicate a unit purity heralded single photon state. It can be experimentally quantified in several ways. As stated in Eq. (4.51), the purity of the state can be accessed directly through the map of the JSI, which can be measured exploiting the larger efficiency of the stimulated process [143]. This technique is called stimulated emission tomography, and is based on the use of a tunable stimulating seed and the subsequent spectrum measurement of the generated light. In this way the JSI is rapidly and easily reconstructed, with a resolution depending on the seed tunability and spectrometer's resolution. However, the JSI cannot map the phase correlations involved in the two-photon state, since it is a measure of the intensity of the fields rather than of their amplitude. The estimation of the state purity considering the contribution of the spectral-phase correlations can be accessed through the degree of second order coherence [144]. Within the squeezed state description, we saw in Section 4.1.6 that each individual squeezer exhibits a thermal statistics and the single mode emission corresponds to the contribution of only one squeezer to the single photon beam; as a result, when the state is pure, a thermal behaviour is expected for the heralded single photon. As introduced in Section 4.2, the statistics of a light source can be measured through the $g^{(2)}$ correlation function, expecting $g^{(2)}(0) = 2$ for a thermal source and $g^{(2)}(0) = 1$ when the light is Poissonian. Therefore, the signal/idler single photon beam is expected to exhibit a behaviour in between these two boundaries, such that

$$1 \leq g^{(2)}(0) \leq 2, \tag{4.70}$$

that is, in general, a super-Poissonian statistics if the g^2 does not equal the boundaries of the inequality. The maximum and minimum purity are therefore achieved when $g^{(2)} = 2$ and $g^{(2)} = 1$ respectively, and the purity parameter, and also the Schmidt number K, can thus be estimated as

$$P = \frac{1}{K} = 1 - g^{(2)}(0). \tag{4.71}$$

From an experimental point of view, the measurement of the $g^{(2)}$ is typically carried out through the HBT interferometer explained in Section 4.2.1, adapted to the SFWM analysis as in Fig. 4.9a, where the setup for the signal statistics measurement is shown together with the typical outcome. The measured g^2 exhibits a peak at zero delay between the two detectors, which corresponds to the coincidences within the same pulse or coherence time, while the side peaks arise due to the correlated detection with subsequent or precedent pulses, that are indicated as the accidental counts. The quantity that is measured through the correlator or start/stop electronics is the rate of coincidences R_{cc} between the two detectors of the HBT; the $g^{(2)}$ as a function of the delay τ between the detections at the two detectors in the HBT is then calculated as

$$g^{(2)}(\tau) = \frac{R_{cc}(\tau)}{R_1 R_2 \tau_b}, \tag{4.72}$$

where R_1, R_2 are the individual detection rates of the detectors and τ_b is the coincidence time window. With this normalization, the $g^2(0)$ will be between 1 and 2, providing a direct measurement of the purity of the state. Notice that the denominator in Eq. (4.72) corresponds to the accidental counts in the correlation measurements, therefore the $g^{(2)}(0)$ can be also seen as the rate of the "good" coincidences (peak at $\tau = 0$) normalized for the rate of accidental counts in the self correlation

measurement (side peaks at $\tau > 0$).

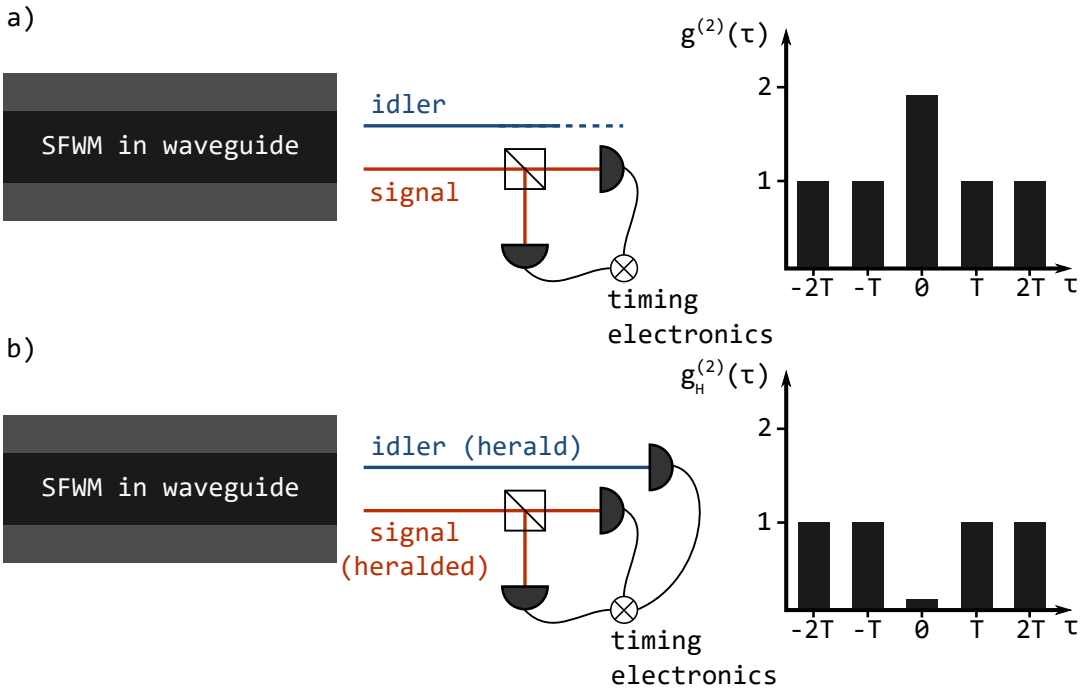

FIGURE 4.9: a) Setup (left) and typical outcome (right) of the $g^{(2)}$ measurement for the SFWM process, exhibiting super-Poissonian statistics. The pump is pulsed with repetition rate $1/T$. b) Setup (left) and typical outcome (right) for the measurement of the heralded second order correlation function, $g_H^{(2)}$, in the case of SFWM, with the typical anti-bunching dip, signature of the non-classical single photon (sub-Poissonian) statistics. The pump is pulsed with repetition rate $1/T$.

A third approach to measure the heralded single photon state purity is through the Hong-Ou-Mandel (HOM) interference [145] between two independent sources of heralded single photons. If the heralded photons are indistinguishable and pure, they will interfere with maximum visibility, since they are not in a mixed state with limited quantum interference. The two arms of the interferometer are delayed in time by τ, and the resulting measurement is the plot, as a function of τ, of the coincidence counts between the single photons heralded by the corresponding photon partner. When the state is pure, a dip is present at zero delay, whose vicinity to zero is proportional to the degree of purity and distinguishability of the states [125]. Despite the HOM interference directly deals with the measurement that is mostly involved in practical quantum applications, it returns the total state purity, meaning that it is not possible to separate the contribution to the purity coming from the mixedness of the state or from the distinguishability of the photons involved. Therefore, the HOM interference visibility does not give an exact measurement of the purity, but sets a lower bound on the mean photon purity [125].

True single photons

The definition of purity for heralded photons has a different meaning with respect to atom-like emitters. With atom like emitters, in fact, the $g^{(2)}$ exhibits a clear anti-bunching dip at zero delay, caused by the intrinsic single photon emission of the

source. This is not the case for squeezed states generated through parametric processes, which display a peak at $g^{(2)}(0)$, due to their super-Poissonian statistics. In order to recover the sub-Poissonian behaviour, and thus the single photon operation of the parametric source, the heralding scheme is introduced. Let us name the idler the herald and the signal the heralded photon. When the heralding procedure is considered, the second order self correlation for the signal is conditioned on the detection of the herald idler, thus changing the expression of the $g^{(2)}$. Therefore, the conditioned second order correlation function $g_H^{(2)}$ is introduced, that is the self correlation of the signal beam triggered by the detection of its twin idler. The experimental set-up for this kind of measurement is shown in Fig. 4.9b; also for the conditioned $g^{(2)}$ the experiment is based on a HBT interferometer but with the idler (herald) arm added in the timing electronics (correlator,start/stop,...). The effect of the herald arm is to trigger the detection of the signal-signal coincidences only when an idler has been detected, giving rise to the anti-bunching dip in Fig. 4.9b (right). In this sense the $g^{(2)}$ is now conditioned. To understand the origin of the dip in the $g_H^{(2)}$, I introduce a suitable formalism for this conditioned correlation function, which is written as

$$g_H^{(2)}(t_1, t_2|t_i) \equiv \frac{\langle \hat{a}_s^\dagger(t_1)\hat{a}_s^\dagger(t_2)\hat{a}_s(t_2)\hat{a}_s(t_1)\rangle_{pm}}{\langle \hat{a}_s^\dagger(t_1)\hat{a}_s(t_1)\rangle_{pm}\langle \hat{a}_s^\dagger(t_2)\hat{a}_s(t_2)\rangle_{pm}}, \tag{4.73}$$

where $\hat{a}_s^\dagger(t), \hat{a}_s(t)$ are respectively the creation and destruction operators for a photon in the signal mode at time t and $\langle\cdot\rangle_{pm}$ is the average over the post-measurement state upon the detection of the herald idler at time t_i [146]. Eq. (4.73) can be rewritten making explicit the conditioning operated by the idler photon as [147]

$$g_H^{(2)}(t_1, t_2|t_i) = \frac{R_{ssi}(t_1, t_2, t_i)R_{pair}}{R_{si}(t_1 - t_i)R_{si}(t_2 - t_i)}, \tag{4.74}$$

with $R_{pair} = \langle \hat{a}_i^\dagger(t)\hat{a}_i(t)\rangle = \langle \hat{a}_s^\dagger(t)\hat{a}_s(t)\rangle$ the pair generation rate, $R_{ssi}(t_1, t_2, t_i)$ the rate of triple coincidence between the idler detected at t_i and two signal photons detected at t_1 and t_2, and $R_{si}(\tau)$ the coincidence rate of signal and idler with a delay τ in between. These quantities are written as [147]

$$R_{ssi}(t_1, t_2, t_i) = \langle \hat{a}_i^\dagger(t_i)\hat{a}_s^\dagger(t_1)\hat{a}_s^\dagger(t_2)\hat{a}_s(t_2)\hat{a}_s(t_1)\hat{a}_i(t_i)\rangle, \tag{4.75a}$$

$$R_{si}(\tau) = \langle \hat{a}_s^\dagger(t+\tau)\hat{a}_i^\dagger(t)\hat{a}_i(t)\hat{a}_s(t+\tau)\rangle. \tag{4.75b}$$

In order to characterize the heralded source, it is of interest to investigate the particular case of $g_H^{(2)}(0, \tau|0)$, meaning that one signal detector clicks at the same time of the idler detector, and the second signal detector has a τ delay with respect to them. Intuitively, this particular case measures if the statistics of the heralded source is actually resembling the single photon one, expecting a dip at $\tau = 0$ and reaching 1 as the delay approaches ∞ or readily at the subsequent pump periods if the experiment is carried out in the pulsed regime. Therefore Eq. (4.73) is rewritten in a more useful and practical form as

$$g_H^{(2)}(0, \tau|0) = \frac{R_{ssi}(0, \tau, 0)R_{pair}}{R_{si}(0)R_{si}(\tau)}, \tag{4.76}$$

where all the terms comes from the direct measurement of the three-fold or two-fold coincidences. In order to understand the importance of the CAR quality in determining the sub-Poissonian statistics, I rewrite Eq. (4.76) as a function of the

cross correlation between signal and idler $g_{si}^{(2)}$ of Eq. (4.65):

$$g_H^{(2)}(\tau) = \frac{\langle \hat{a}_i^\dagger(0)\hat{a}_s^\dagger(0)\hat{a}_s^\dagger(\tau)\hat{a}_s(\tau)\hat{a}_s(0)\hat{a}_i(0)\rangle}{g_{si}^{(2)}(0)g_{si}^{(2)}(\tau)}\frac{1}{R_{pair}^3}, \tag{4.77}$$

that is expected to display a dip close to zero at $\tau = 0$ and a value of 1 for $\tau \to \infty$. The same result is expected, analogously, in the pulsed case, with τ equal at an integer number of pump periods. As clear from Eq. (4.77), any dip in the $g_H^{(2)}$ at zero delay should arise from a strong peak at $\tau = 0$ in the denominator; in fact, the numerator in Eq. (4.77) is just the triple coincidence of the signal and idler, that can be seen as the signal-signal self correlation sampled at the idler rate, thus resembling the super-Poissonian statistics of the signal beam. As anticipated before, the key parameter determining the anti-bunching is the $g_{si}^{(2)}(0)$, which peaks at the CAR value. Hence, a relation between $g_H^{(2)}(0)$ and $g_{si}^{(2)}(0)$ exists, that is [148]

$$g_H^{(2)}(0) = \frac{G^{(3)}(0)}{G^{(3)}(\tau)}\frac{1}{g_{si}^{(2)}(0)} = \frac{G^{(3)}(0)}{G^{(3)}(\tau)}\frac{1}{\mathrm{CAR}}, \tag{4.78}$$

with $G^{(3)}(\tau) = \langle \hat{a}_i^\dagger(0)\hat{a}_s^\dagger(0)\hat{a}_s^\dagger(\tau)\hat{a}_s(\tau)\hat{a}_s(0)\hat{a}_i(0)$. The higher the CAR, the closer to the anti-bunched statistics is the heralded photon. In other terms, the act of heralding can be seen as a procedure to kill the probability of detecting zero signal photons, i.e. $p(0) = 0$. The signal beam, in fact, exhibits a super-Poissonian statistics with typically a very low number of pairs per pulse, that is the typical condition for the single photon operation [59], and hence resulting in a photon number distribution such that $p(0) \gg p(1) \gg p(2)$..., as in Fig. 4.10a. As soon as the herald trigger is applied, the signal detectors look at the presence of the photons only when the pair has actually been generated, thus minimizing $p(0)$, as in Fig. 4.10b, and increasing the average photon number per pulse $\mu \simeq p(1) \gg p(2)$ [95]. Therefore, according to Eq. (4.59),

$$g_H^{(2)}(0) \simeq \frac{2p(2)}{\mu^2} \ll 1, \tag{4.79}$$

displaying the single photon sub-Poissonian statistics, which is closer and closer to zero as the pump power is reduced.

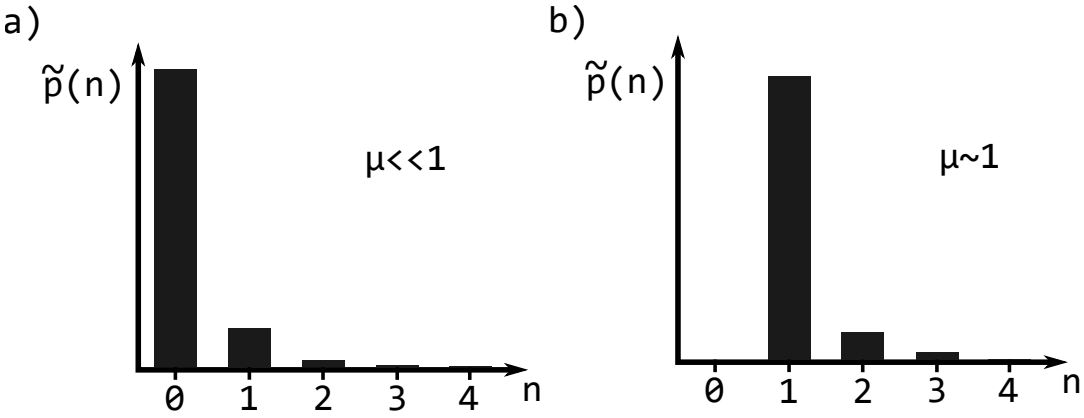

FIGURE 4.10: a) Normalized photon number distribution for a super-Poissonian signal beam. b) Normalized photon number distribution for a super-Poissonian signal beam when the heralding detection is applied. μ is the mean photon number per pulse.

Heralding efficiency

When dealing with heralded single photons one of the parameters that characterizes the practical feasibility of the source of such photons is the heralding efficiency η_H. Such parameter quantifies the probability that, given the detection of the herald photon, also the heralded photon will be detected. The heralding efficiency, with the idler as the herald photon, is measured as

$$\eta_H = \frac{R_{si}}{R_i} \tag{4.80}$$

where R_{si} is the rate of coincidences between signal and idler photons, while R_i is the generation rate of the idler photons.

Close to the concept of heralding efficiency is the preparation efficiency η_P, a parameter which get rid of the quantum efficiency of the detector, quantifying the probability that given a detection on the herald counter, the heralded photon will be successfully delivered to its application. In these terms, η_P is a generalization of the heralding efficiency, since it is independent of the detection system used for the heralded photon. Heralding and preparation efficiencies are mainly limited by losses occurring along the path from the source to the detectors, that in the case of integrated sources of single photons (waveguides, fibers, crystals...) correspond to propagation and coupling losses. Because of this, integrated waveguide single photon sources are a good solution to keep the preparation efficiency high, thanks to the low optical loss and high mode matching to the optical fiber [95].

Limits to efficient single-photon generation

When working with on-chip parametric processes, several side processes may occur together with the wanted nonlinear pair generation. These side processes typically are detrimental for the quality of the heralded source, by inducing losses or limiting the single photon behaviour of the source. The most common effects are TPA, XTPA, FCA and multipair generation. TPA, XTPA and FCA have been already introduced in Section 3.1, and here involve the pump photons or the pump and a generated photon, inducing losses on the generated frequencies and therefore limiting all the main features of the heralded single photon source. Multipair generation is related to the statistics of the generation process, and it directly affects the single photon statistics of the source. Multipairs arise as the terms $p(n > 2)$ of the photon number distribution. Their impact scales proportionally with the average number of photons per pair, thus with pump power. In general, they affect CAR, $g^{(2)}_{ss}(0)$ and the $g^{(2)}_{H}(0)$, being a main obstacle to the implementation of feasible heralded sources [149], since when multipairs are generated at least two photons will be heralded, not only one. As a common practice, to avoid multipair no more than 0.1 signal-idler pairs per pulse have to be generated [59]. Therefore, heralded sources are forced to work at very low pump powers, with limited brightness, making the linear and coupling loss one of the key limitations for the realization of efficient and bright integrated sources of single photons.

4.4 Purification of the heralded single photon state

Achieving high purity single photon states is a fundamental task for the practical implementation of single photon based quantum technologies. In fact, most of its

applications relay on the interference between two or more indistinguishable pure single photons [123, 150], like quantum logic gates [151] or quantum computing [152]. Maximum purity is achieved when the single photon emission has a single mode character, thus hindering the projection of the heralded photon into a mixed state of all possible modes [19], which would inevitably degrade the single photon purity. Without treating adequately the parametric generation process, the emitted pairs are naturally entangled in both spatial and spectral degree of freedom, due to the energy and momentum conservation [121]. As a result, the photons in the pair are individually in a mixed state, as shown by the reduced density matrix of the pure two-photon state. Within the heralding picture, this means that once the herald photon is measured, the heralded one will be projected into a mixture of states due to the correlations that hold between the two twin photons, thus preventing a high quantum interference visibility between independent sources [121]. Because of this, high attention is devoted to the development of measurement techniques able to provide a reliable estimation of the state purity and of feasible strategies for the purification of heralded single photon states [143]. The single mode character of the photon generation, and so the purity, can be evaluated with a plenty of methods, e.g. via the JSI tomography, the $g^{(2)}$ measurement, or through the HOM interference. The tomography of the JSI is a more intuitive description of the process of purification. Purification occurs through the engineering of the two photon state produced by the nonlinear parametric process. The idea is to tailor the process so that the two photon state approaches as much as possible a separable state, thus exhibiting high single photon purity. Looking at the JSA formulation in Eq. (4.48) it is evident the role of the pump bandwidth $\alpha(\omega)$ and the phase matching function $\phi(\omega_s, \omega_i, \omega)$ in manipulating its shape. In particular, the pump bandwidth controls the width of the JSA along the anti-diagonal direction, labelled with **A** in Fig. 4.11a, while the width on the diagonal (**B** in Fig. 4.11a) depends on the phase matching function. Within this picture, the task of making the JSA factorizable reduces to engineer properly the spectral profiles of the pump and phase matching functions in such a way that the final JSI takes the shape of a circle, like in Fig. 4.3b. This can be done through several approaches, each with its pros and cons.

The simplest technique adopted when dealing with SFWM heralded states is the spectral filtering: filters are placed on both the heralding and heralded beams, shaping the JSA by eliminating the unwanted frequency modes [19]. The filtering process is sketched in Fig. 4.11b, where δ_s and δ_i are the filter bandwidth for the signal and idler beams respectively. The effect of the filters can be included into the description of the bi-photon wavefunction by multiplying $F(\omega_s, \omega_i)$ in Eq. (4.47) by two gaussian functions of the form

$$f_j(\omega_j) = \frac{1}{\Gamma} \exp\left[\frac{(\omega_{j0} - \omega_j)^2}{\delta_j^2} 4\ln(2)\right], \tag{4.81}$$

with Γ a normalization factor, ω_{j0} the central filter frequency, δ_j the filter pass-band and $j = i, s$ labelling the idler and signal, respectively. This approach applies a drastic manipulation on the JSA, achieving the task of high purity single photon state, as shown in Fig. 4.12, where the JSI is qualitatively shown before and after the filtering. However, applying filters has the detrimental effect of lowering the brightness and heralding efficiency of the source, since the photons occupying the unwanted modes are irredeemably lost.

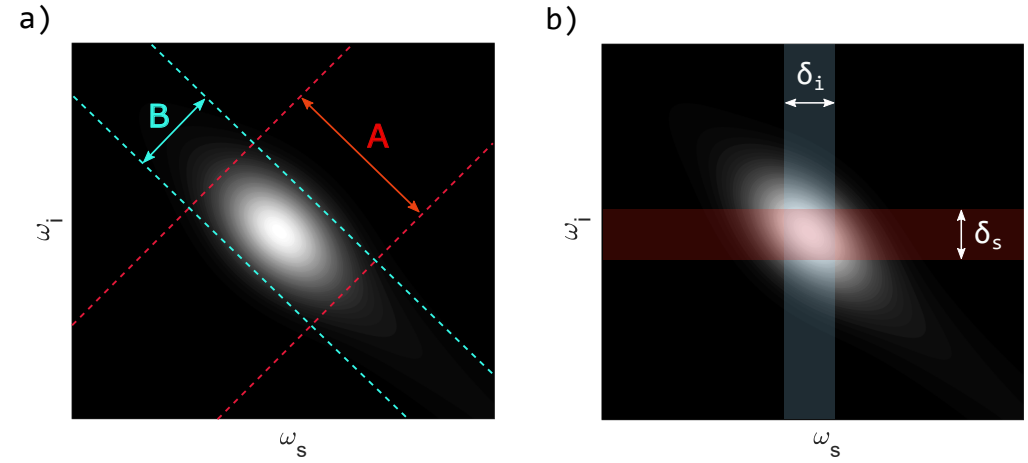

FIGURE 4.11: JSI as a function of signal and idler wavelengths. a) The JSA, and so the JSI, can be manipulated by engineering properly the phase matching function and pump spectral profiles, which affect the A and B widths respectively. b) The factorization of the JSA can be achieved by filtering adequately the signal and idler beams

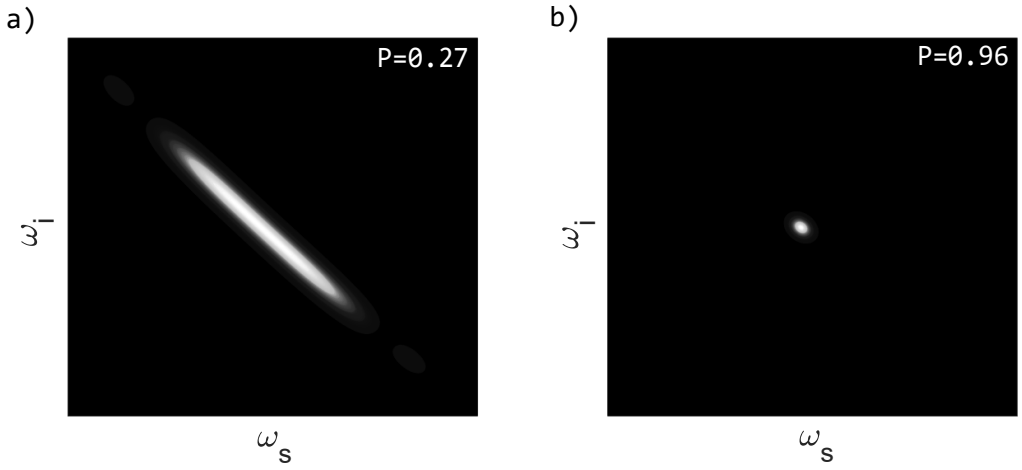

FIGURE 4.12: Qualitative plot for the JSI (a) before and (b) after the application of filters on both the signal and idler arms.

4.4.1 Group velocity matching for high purity states

An alternative approach to the factorization of the JSA is based on the group velocity matching. The JSA function in Eq. (4.48) depends strongly on the phase mismatch parameter Δk (or $\Delta\beta$) in $\phi(\omega_s, \omega_i, \omega)$. For the SFWM case and neglecting the self and cross phase modulation contribution, $\Delta\beta$ is written as

$$\Delta\beta = \beta_1(\omega_1) + \beta_2(\omega_2) - \beta_s(\omega_s) - \beta_i(\omega_i), \tag{4.82}$$

where the labels $1, 2, s, i$ refer respectively to the first pump, second pump, signal and idler. Following the treatment in [136], expanding $\Delta\beta$ in Taylor series around the frequencies ω_{0j} $(j = 1, 2, s, i)$ at which perfect phase matching is attained, $\Delta\beta$ can be rewritten as a linear approximation

$$L\Delta\beta_{lin} = L\Delta\beta_0 + T_s\Delta\omega_s + T_i\Delta\omega_i, \tag{4.83}$$

with

$$\Delta\beta_0 = \beta_1^{(0)}(\omega_{01}) + \beta_2^{(0)}(\omega_{02}) - \beta_s^{(0)}(\omega_{0s}) - \beta_i^{(0)}(\omega_{0i}), \tag{4.84a}$$

$$T_j = \tau_j + \tau_p \frac{\sigma_1^2}{\sigma_1^2 + \sigma_2^2}, \tag{4.84b}$$

$$\tau_j = L\left[\beta_2^{(1)}(\omega_{02}) - \beta_j^{(1)}(\omega_{0j})\right], \tag{4.84c}$$

$$\tau_p = L\left[\beta_1^{(1)}(\omega_{01}) - \beta_2^{(1)}(\omega_{02})\right], \tag{4.84d}$$

$$\beta_j^{(n)}(\omega) = \frac{\partial^n \beta_j}{\partial \omega^n}\Big|_{\omega=\omega_{0j}}, \tag{4.84e}$$

with σ_1 and σ_2 the bandwidths of the two pumps. By plugging $\Delta\beta_{lin}$ into Eq. (4.48), it is possible to get rid of the integral, thus rewriting the JSA within the linear approximation as [136]

$$F_{lin}(\Delta\omega_s, \Delta\omega_i) = \alpha(\Delta\omega_s, \Delta\omega_i)\phi(\Delta\omega_s, \Delta\omega_i), \tag{4.85}$$

with

$$\alpha(\Delta\omega_s, \Delta\omega_i) = \exp\left[\frac{(\Delta\omega_s + \Delta\omega_i)^2}{\sigma_1^2 + \sigma_2^2}\right], \tag{4.86}$$

and $\phi(\Delta\omega_s, \Delta\omega_i)$ is the same of Eq. (4.49) but with $\Delta\beta = \Delta\beta_{lin}$. At this point the idea of factorization of JSA can be understood simply by looking at its approximated function F_{lin}, which is simply the product of two independent functions. Considering the case of degenerate pump, $\alpha(\Delta\omega_s, \Delta\omega_i)$, due to the energy conservation, has a shape which forms an angle of -45° with the signal frequency axis in the JSA plot, with a width equal to the pump bandwidth, as shown in Fig. 4.13a. The phase matching function $\phi(\Delta\omega_s, \Delta\omega_i)$, on the other hand, forms an angle θ_{pm} with respect to the signal frequency axis which depends on the group velocities as [95]

$$\theta_{pm} = -\arctan\left[\frac{\delta_i}{\delta_s}\right], \tag{4.87}$$

with $\delta_j = L\left(\beta_p^{(1)}(\omega_{p0}) - \beta_j^{(1)}(\omega_{j0})\right)$. If $\theta_{pm} = +45°$, as in Fig. 4.13b, the final JSA will be the one in Fig. 4.13c, exhibiting a circular shape, signature of a factorizable JSA, i.e. of a pure heralded single photon state. By solving Eq. (4.87) for $\theta_{pm} = +45°$ it is found the proper relationship between the group velocities $\left(\beta_j^{(1)}\right)^{-1}$,

$$\beta_p^{(1)}(\omega_{0p}) = \frac{\beta_3^{(1)}(\omega_{03}) + k_4^{(1)}(\omega_{04})}{2}, \tag{4.88}$$

with p labelling the pump. The condition in Eq. (4.88) is called symmetric group velocity matching. Group velocities can be engineered also according to another condition, called asymmetric group velocity matching, which provides the factorization of the JSA but with $\theta_{pm} = 0°$ or $90°$ [95]. The group velocity matching technique for SFWM has been extensively used with optical fibers exploiting their birefringence [136, 153, 154], which allowed to control the phase matching condition of the waves involved in the process by taking advantage of the different group velocities characterizing the ordinary and extraordinary rays.

Despite the group velocity matching technique gets rid of the narrow spectral

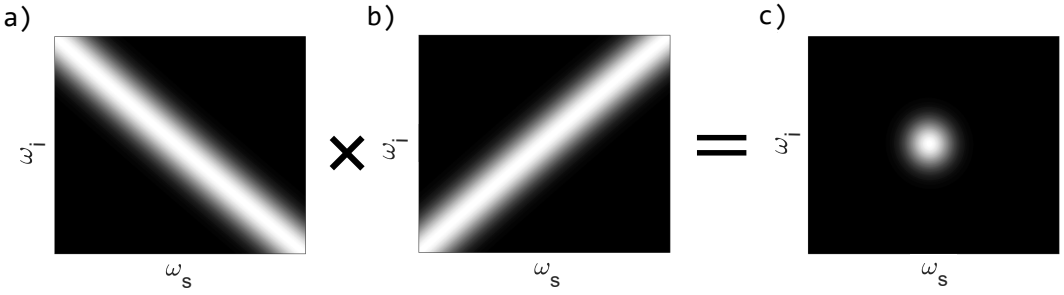

FIGURE 4.13: JSA engineering via the symmetric group velocity matching technique. a) Pump spectral envelope $\alpha(\Delta\omega_s, \Delta\omega_i)$. b) Phase matching function $\phi(\Delta\omega_s, \Delta\omega_i)$ with $\theta_{pm} = +45^o$. c) JSA resulting from the product of the pump envelope (a) and the phase matching function (b). Within the symmetric group velocity matching, JSA exhibits the factorization required for a pure heralded single photon state.

filtering guaranteeing at the same time high single photon purities, it is a viable solution only within the fiber platform, while for silicon chip devices it is not suitable due to the modest birefringence. However, it is still possible to apply the group velocity matching technique in the silicon platform if the higher order modes of a multimode waveguide are considered, where the different group velocities characterizing the different waveguide modes can be used [155]. Nevertheless, the group velocity matching technique requires non trivial dispersion engineering and it is reliable only when dealing with small generation detunings from the pump, otherwise higher order dispersion terms come into play [156]. Because of this, more robust and reliable strategies have been recently investigated, focusing on the other degrees of freedom available in SFWM, such as the temporal delay that can be introduced between the pumps [121].

4.4.2 Dual-pump delay approach

The standard approach to pair generation through SFWM relays on degenerate processes, where the two pump photons come from the same pump pulse and are thus indistinguishable. However, as explained in Section 3.4, FWM can occur also within the non-degenerate picture, which involves two pump waves which differ spectrally. The possibility of performing the process in the degenerate or non-degenerate scheme gives additional flexibility to the SFWM over the SPDC process. Moreover, the non-degenerate scheme proper of FWM has been shown to be a powerful tool for the achievement of almost unit purity single photons, as theoretically proposed by Fang et al. [121]. In this work, it is proposed to use a controlled temporal delay between the two pump pulses for the generation of spectrally pure single photons through non degenerate FWM. In fact, by tuning adequately the delay it is possible to shape the phase matching function to a gaussian envelope, thus obtaining a circular JSI with unit purity. This concept is shown in Fig. 4.14 in the case of a waveguide, where the purity is maximized when the two pump pulses with different group velocity and proper delay are used. When the pumps are degenerate, they are equal in all the degrees of freedom and have equal group velocities. Therefore, they are injected in the waveguide (gray box in the figure) without any temporal delay τ and propagate till the end of the waveguide without any walk-off. In this case the JSI exhibits an elongate anti-diagonal profile with reduced state purity.

When the pumps are not degenerate, whatever the degree of freedom involved (polarization, wavelength, spatial mode), they can be prepared with different group velocities. By applying a temporal delay between the two pulses ($\tau < 0$), it is possible to make them interact only when they are both already in the sample. Then, due to the walk-off, the faster pulse move forward ceasing the interaction before the end of the sample. As a result, at the end of the waveguide the faster pulse is ahead with respect to the slower one ($\tau > 0$). By choosing adequately τ it is possible to shape the JSI as a circle, thus with near unit purity.

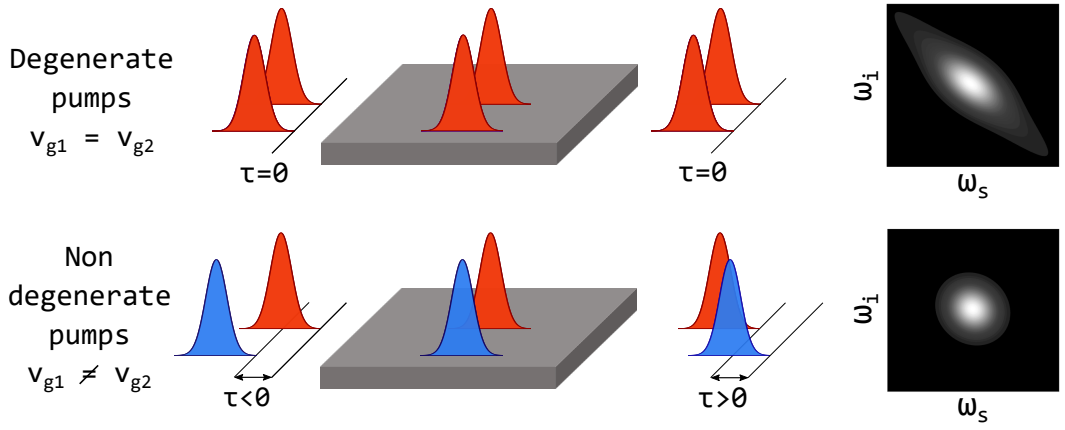

FIGURE 4.14: This figure provides an intuitive description of the dual pump delay scheme for the purification of the single photon purity with SFWM. When the pumps are degenerate, they are equal in all the degrees of freedom and have equal group velocities. Therefore, they are injected in the waveguide (gray box in the figure) without any temporal delay τ and propagate till the end of the waveguide without any walk-off. In this case the JSI exhibits an elongated anti-diagonal profile with reduced state purity. When the pumps are not degenerate, whatever the degree of freedom involved (polarization, wavelength, spatial mode), they can be prepared with different group velocities. By applying a temporal delay between the two pulses ($\tau < 0$), it is possible to make them interact only when they are both already in the sample. Then, due to the walk-off, the faster pulse move forward ceasing the interaction before the end of the sample. As a result, at the end of the waveguide the faster pulse is ahead with respect to the slower one ($\tau > 0$). By choosing adequately τ it is possible to shape the JSI as a circle, thus with near unit purity.

We propose to apply the same idea of Fang et al. but exploiting the different group velocities characterizing the higher order modes involved in intermodal FWM. We focus on the case where the pumps are degenerate in frequency and with the same pump profile, but are loaded on different waveguide modes.

The treatment starts from the JSA function already introduced in Eq. (4.48), that I rewrite by making explicit the integral over the propagation direction z and considering a gaussian profile for the pumps:

$$F(\omega_s,\omega_i) = N\int_0^L \int \mathrm{d}\omega_p \exp\left[-\left(\frac{\omega_p-\omega_p^0}{\sigma}\right)^2\right]\exp\left[-\left(\frac{\omega_s+\omega_i-\omega_p-\omega_p^0}{\sigma}\right)^2\right] \times \exp\left[-i\omega_p\tau\right]\exp\left[-i\Delta k z\right], \tag{4.89}$$

where N is a normalization factor, L is the waveguide length, ω_p, ω_s, ω_i the pump, signal and idler frequencies, ω_p^0 the central pump frequency, σ defines the bandwidth of the pump pulse, τ is the temporal delay between the two pumps and Δk is the phase mismatch parameter as defined in Eq. (3.53), i.e.

$$\Delta k = \frac{\omega_p^0}{c} n_{eff}^j(\omega_p^0) + \frac{\omega_p^0}{c} n_{eff}^q(\omega_p^0) - \frac{\omega_s^0}{c} n_{eff}^l(\omega_s^0) - \frac{\omega_i^0}{c} n_{eff}^m(\omega_i^0), \tag{4.90}$$

where ω_j^0 $(j = p, s, i)$ are the frequencies corresponding to the perfect phase matching, i.e. yielding $\Delta k = 0$.

By Taylor expanding Δk around the phase matching frequencies and considering only the linear terms, as already shown with Eq. (4.50), Eq. (4.89) can be simplified as a function of $\Delta\omega_s = \omega_s - \omega_s^0$ and $\Delta\omega_i = \omega_i - \omega_i^0$ [136],

$$F_{lin}(\Delta\omega_s, \Delta\omega_i) = N\alpha\left(\Delta\omega_s, \Delta\omega_i\right)\phi\left(\Delta\omega_s, \Delta\omega_i\right), \tag{4.91}$$

where the pulse envelope is given by

$$\alpha\left(\Delta\omega_s, \Delta\omega_i\right) = \exp\left[-\frac{\left(\Delta\omega_s + \Delta\omega_i\right)^2}{2\sigma^2}\right] \tag{4.92}$$

and the phase matching function is written as

$$\begin{aligned}\phi\left(\Delta\omega_s, \Delta\omega_i\right) &= \exp\left[-\left(\frac{\tau_s\Delta\omega_s + \tau_i\Delta\omega_i}{\sigma_{eff}\tau_p}\right)^2\right] \\ &\times\left[\operatorname{erf}\left(\frac{\sigma_{eff}(\tau+\tau_p)}{2} + i\frac{\tau_s\Delta\omega_s + \tau_i\Delta\omega_i}{\sigma_{eff}\tau_p}\right) - \operatorname{erf}\left(\frac{\sigma_{eff}\tau}{2} + i\frac{\tau_s\Delta\omega_s + \tau_i\Delta\omega_i}{\sigma_{eff}\tau_p}\right)\right],\end{aligned} \tag{4.93}$$

with $\sigma_{eff} = \sigma/\sqrt{2}$ the effective bandwidth; the group delays are given as

$$\tau_s = L\left(\frac{\beta_{1,p1}(\omega_p^0) + \beta_{1,p2}(\omega_p^0)}{2} - \beta_{1,s}(\omega_s^0)\right), \tag{4.94a}$$

$$\tau_i = L\left(\frac{\beta_{1,p1}(\omega_p^0) + \beta_{1,p2}(\omega_p^0)}{2} - \beta_{1,i}(\omega_i^0)\right), \tag{4.94b}$$

$$\tau_p = L\left(\beta_{1,p1}(\omega_p^0) - \beta_{1,p2}(\omega_p^0)\right), \tag{4.94c}$$

with $\beta_{1,j}(\omega) = \mathrm{d}k_j(\omega)/\mathrm{d}\omega$ $(j = p, s, i)$ the inverse of the group velocity for the pump, signal and idler waveguide modes. The phase matching angle, already defined in Eq. (4.87), can be rewritten as a function of the temporal delays as [136]

$$\theta_{pm} = -\arctan\left(\tau_s/\tau_i\right). \tag{4.95}$$

In order to have a factorizable single photon state, the θ_{pm} should be in the range $[0°, 90°]$, therefore requiring that [121]

$$\tau_s\tau_i \leq 0. \tag{4.96}$$

Eq. (4.96) sets a requirement for the factorizability, that can occur only if the idler and signal are anti-symmetric in terms of β_1 with respect to the average β_1 of the pumps, i.e. if $\beta_{1,i} > \langle\beta_{1,p}\rangle$ then the $\beta_{1,s} < \langle\beta_{1,p}\rangle$, and viceversa, with $\langle\beta_{1,p}\rangle = \frac{\beta_{1,p1}+\beta_{1,p2}}{2}$. This condition implies a correlation in the group velocities of the signal and idler: the two generated waves must have respectively greater and lower v_g than the threshold set by the pump group velocities. Since different group velocities are involved, inevitably the process will be affected by a reduced interaction length, thus resulting in a lower efficiency. Because of this the effective length L_{eff} is introduced, which quantifies the effective interaction length over which the FWM process takes place. In computing L_{eff} I consider $\tau = \tau_p/2$, such that the two pump pulses will be perfectly overlapped in the center of the waveguide ($z = L/2$), thus maximizing the available interaction. The effective length is defined as [121]

$$L_{eff} = \frac{\int_0^L \mathrm{d}z \int \mathrm{d}t I_{p1}(z,t) I_{p2}(z,t)}{\int \mathrm{d}t I_{p1}(z = L/2, t) I_{p2}(z = L/2, t)}, \tag{4.97}$$

where $I_{p1}(z,t)$, $I_{p2}(z,t)$ are the intensities of the two pumps at spatial position z and time t. A value of τ that does not lead to the pump pulses to be perfectly matched at $z = L/2$ results in a limited generation efficiency and purity. If the pump waves have the same group velocity, the interaction between the pumps does not vary along the waveguide and $L_{eff} = L$.

Negligible walk-off

Considering the case of negligible temporal walk-off, i.e. $\beta_{1,p1}(\omega_p^0) \sim \beta_{1,p2}(\omega_p^0)$, then the interaction between the pump pulses starts as soon as they enter the medium and stops at the end of the waveguide, with almost perfect overlap all over the propagation. The effective length is L and the resulting phase matching function exhibits the usual sinc behaviour as

$$\phi\left(\Delta\omega_s, \Delta\omega_i\right) = \mathrm{sinc}\left(\frac{\tau_s\Delta_s + \tau_i\Delta_i}{2}\right). \tag{4.98}$$

The sinc function is the typical shape of the phase matching function for parametric processes, and its oscillatory behaviour hinders the achievement of a factorizable JSA without resorting to spectral filtering, as shown in Fig. 4.15, where the JSI of a sinc shaped phase matching function is shown; despite the circular shape of the central lobe, centered at the phase matching position, the side lobes limits the factorizability of the state [156].

Optimal walk-off

Let us now consider the case in which the slower pump pulse is $\tau_p/2$ in advance with respect to the faster one. In these conditions, the interaction between the two pulses starts only when they are both already in the sample, gradually increasing to the maximum overlap at $z = L/2$, and then decreasing and switching off before the end of the waveguide. This situation occurs when $|\sigma_{eff}\tau_p| \gg 1$, which corresponds to long waveguides, large difference between the pump group velocities, or short pulse duration of the pumps [121]. The interaction length in this case becomes

$$L_{eff} = \frac{\sqrt{2}}{|\sigma_{eff}\tau_p|}L, \tag{4.99}$$

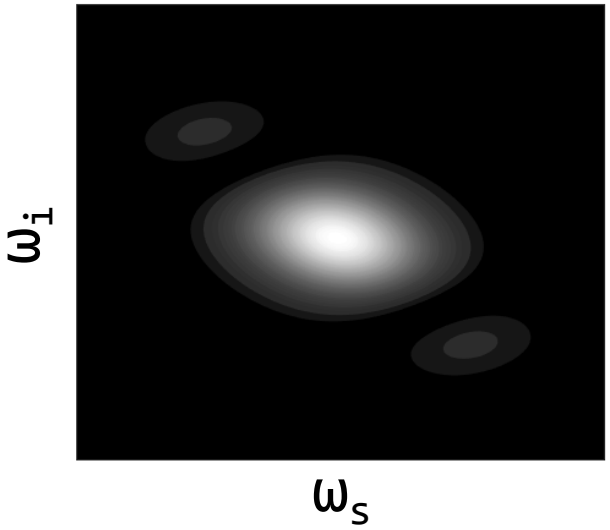

FIGURE 4.15: JSI exhibiting a sinc behaviour for the phase matching function. The side lobes limits the achievement of a factorizable single photon state.

thus scaled proportionally to $1/|\sigma_{eff}\tau_p|$, which is a large value when the optimal delay is considered. Despite the reduced interaction length and, therefore, the lower efficiency, the phase matching function now exhibits a gaussian shape,

$$\phi\left(\Delta\omega_s, \Delta\omega_i\right) = \exp\left[-\left(\frac{\tau_s\Delta\omega_s + \tau_i\Delta\omega_i}{\sigma_{eff}\tau_p}\right)^2\right]. \tag{4.100}$$

At this point, the JSA in Eq. (4.91) is given by the product of two gaussian shaped functions, the pulse envelope in Eq. (4.92) and the phase matching function in Eq. (4.100), such that

$$F_{lin}\left(\Delta\omega_s, \Delta\omega_i\right) \approx \exp\left[-\frac{\left(\Delta\omega_s + \Delta\omega_i\right)^2}{2\sigma^2}\right] \exp\left[-\left(\frac{\tau_s\Delta\omega_s + \tau_i\Delta\omega_i}{\sigma_{eff}\tau_p}\right)^2\right]. \tag{4.101}$$

By using Eq. (4.101) and Eq. (4.51), an analytical expression for the purity P is found [121],

$$P = \sqrt{\frac{\left(\frac{\tau_i}{\tau_p} - \frac{\tau_s}{\tau_p}\right)^2}{\left(\frac{1}{2} + 2\left(\frac{\tau_s}{\tau_p}\right)^2\right)\left(\frac{1}{2} + 2\left(\frac{\tau_i}{\tau_p}\right)^2\right)}}. \tag{4.102}$$

Please notice that Eq. (4.102) states that the purity is only a function of the delay ratios, namely τ_i/τ_p and τ_s/τ_p, and it does not depend on the length of the sample. In fact, the interaction length has an upper limit fixed by the delay between the pumps and by the group velocities of the waves involved in the process. Therefore extending the waveguide beyond the maximum effective interaction length does not result in an increased interaction time. In other words, when the faster pump pulse surpasses the slower one, the interaction switches off whatever the remaining waveguide length to go through.

Looking now at the condition for unit purity, by solving Eq. (4.102) for $P = 1$ the following relation is found,

$$\tau_s \tau_i + \frac{\tau_p^2}{4} = 0, \tag{4.103}$$

which gives the conditions for perfect factorizability of the JSA, i.e. unit purity of the single photon state. By investigating deeper Eq. (4.103), it is possible to extract a fundamental relation between the group velocities of the waves for the achievement of unit purity. From here on I will neglect the frequency dependence of the β_1's, such that $\beta_{1,j}\left(\omega_j^0\right) \equiv \beta_{1,j}$, $(j = p1, p2, s, i)$. Defining the average β_1 of the pumps as

$$\langle \beta_{1,p} \rangle = \frac{\beta_{1,p1} + \beta_{1,p2}}{2}, \tag{4.104}$$

and considering that

$$\beta_{1,p1} - \beta_{1,p2} = 2\left(\langle \beta_{1,p} \rangle - \beta_{1,p2}\right) = 2\left(\beta_{1,p1} - \langle \beta_{1,p} \rangle\right), \tag{4.105}$$

it is possible to rewrite τ_p^2 and $4\tau_s\tau_i$ as

$$\tau_p^2 = 4L^2\left(\langle \beta_{1,p} \rangle - \beta_{1,p2}\right)\left(\beta_{1,p1} - \langle \beta_{1,p} \rangle\right), \tag{4.106}$$

and

$$4\tau_s\tau_i = 4L^2\left(\langle \beta_{1,p} \rangle - \beta_{1,i}\right)\left(\langle \beta_{1,p} \rangle - \beta_{1,s}\right). \tag{4.107}$$

Therefore, by Eq. (4.106), Eq. (4.107) and Eq. (4.103), it follows

$$\left(\langle \beta_{1,p} \rangle - \beta_{1,p2}\right)\left(\beta_{1,p1} - \langle \beta_{1,p} \rangle\right) = \left(\langle \beta_{1,p} \rangle - \beta_{1,i}\right)\left(\beta_{1,s} - \langle \beta_{1,p} \rangle\right), \tag{4.108}$$

which is satisfied when

$$\beta_{1,p1} = \beta_{1,s}, \tag{4.109a}$$

$$\beta_{1,p2} = \beta_{1,i}. \tag{4.109b}$$

or

$$\beta_{1,p1} = \beta_{1,i}, \tag{4.110a}$$

$$\beta_{1,p2} = \beta_{1,s}. \tag{4.110b}$$

The relations in Eq. (4.109) and Eq. (4.110) set a fundamental constraint between the group velocities of the waves involved in the SFWM, stating that maximum purity can be achieved only when the idler has the same group velocity of the faster pump and the signal the same of the slower pump, or vice versa. This condition for factorizable JSA finds natural implementation with the intermodal combinations of the type (a,b,b,a) or (a,b,a,b) (see Section 3.7.2), thus with the first pump with the same mode of the idler and the other pump sharing the same mode with the signal, or vice versa. These conditions can be achieved with both TM and TE polarizations, as shown in Fig. 4.16, where I report the simulated purity when 1212TM and 1221TE combinations are involved in a SOI channel waveguide with respectively $(2.5 \times 0.340)\mu m^2$ and $(2.5 \times 0.220)\mu m^2$ cross-sections. Fig. 4.16a shows the β_1 of the 1TM and 2TM modes, highlighting the phasematching position with the 1.55 μm pump. Only at the perfect phase matching wavelengths, Eq. (4.109) holds, and purity approaching 1 can be achieved, as depicted by the JSI in Fig. 4.16c. Analogously,

the same result can be obtained with the symmetric condition in Eq. (4.110), that is satisfied with 1221TE combination. This second case is reported in Fig. 4.16b, where the β_1 are plotted with the phasematched wavelengths emphasized when the pump is at 1.55 μm. The corresponding JSI is shown in Fig. 4.16d, with a purity of 0.999. From Fig. 4.16 it can be seen that by moving the pump wavelength it is possible to move accordingly the phase matching position, always satisfying the high purity condition of Eq. (4.109) and Eq. (4.110). In the simulated JSI of Fig. 4.16c,d the waveguide has a length of 1 cm and the pump FWHM is 10 nm, in order to satisfy the condition $\sigma_{eff}\tau_p \gg 1$ assumed in deriving the expression of the purity in Eq. (4.102).

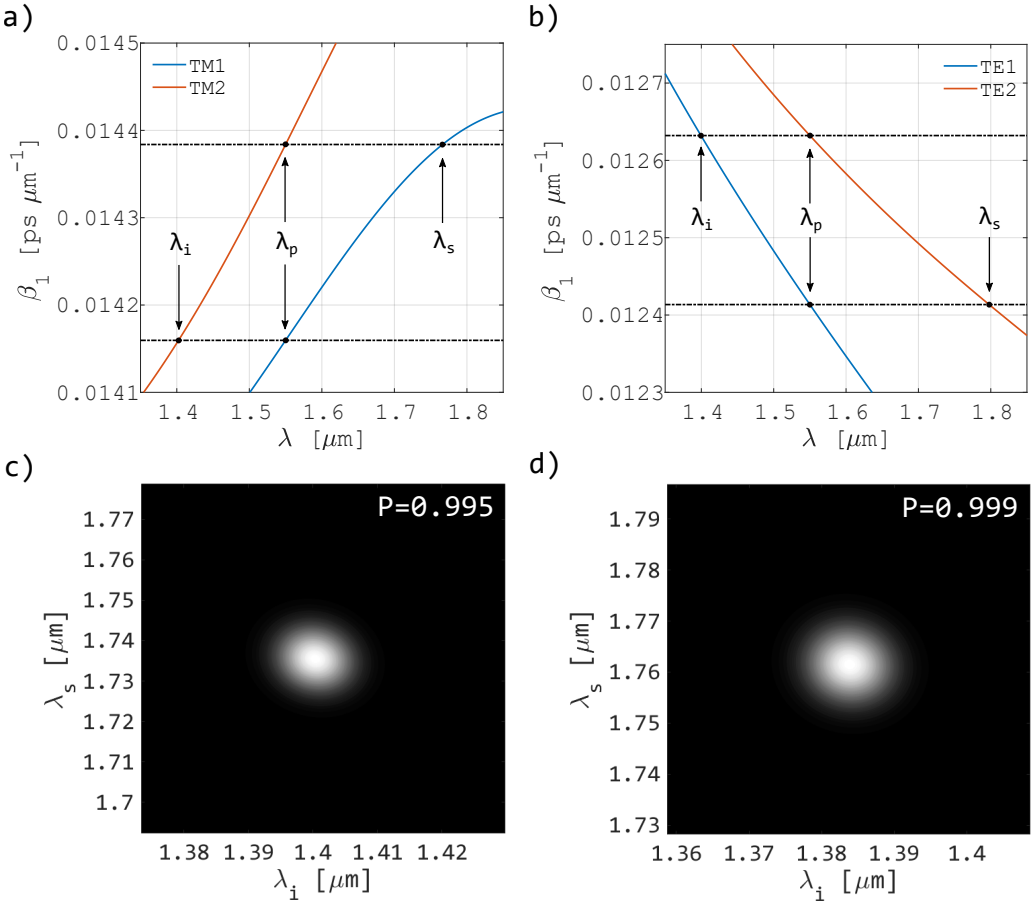

FIGURE 4.16: β_1 as a function of the wavelength for channel cross section waveguide. a) 1212TM intermodal FWM combination with $(2.5 \times 0.340)\mu m^2$ cross section. b) 1221TE intermodal FWM combination with $(2.5 \times 0.220)\mu m^2$ cross section. In both the plots the black lines are a guide to the eye, which highlight the matching between the β_1's of the pumps and those of the signal and idler waves. c) JSI corresponding to the 1212TM combination in a), with purity P = 0.995 evaluated through the exact JSA of Eq. (4.48). d) JSI corresponding to the 1221TE combination in b), P = 0.999 evaluated through the exact JSA of Eq. (4.48).

Considering now a fixed pump wavelength of 1.55 μm, I want to investigate the purity of the state as a function of the generated wavelength and, also, how the purity changes with a not phase matched intermodal combination. Looking at the case of 1212TM phase matched process of Fig. 4.16a, the idler is on the 2TM and the signal on the 1TM; if the idler was on the 1TM mode and the signal on the 2TM,

namely 1221TM combination, the resulting purity as a function of the idler wavelength would be like the one plotted in Fig. 4.17a (blue line). In fact, the 1221TM combination is phase matched only in the degenerate case, with all the waves at the same wavelength of the pump, where the conditions for unit purity hold. On the contrary, if we consider the 1212TM combination, the maximum purity is achieved in the expected phase matching position. The purity of the phase matched combination decreases when the idler wavelength moves away from the phasematching position, reaching $P = 0$ when $\beta_{1,s} = \beta_{1,i}$, as can be seen from the β_1 plot in Fig. 4.16a. $\beta_{1,s} = \beta_{1,i}$ is equivalent to $\tau_s = \tau_i$, that is the lower bound for the factorization given in Eq. (4.103). As λ_i increases to the pump wavelength, the purity grows again, since $\tau_s \tau_i < 0$. The same analysis holds for the 1221TE case in Fig. 4.16b, with the purity for the 1221TE that is maximized at the phase matching wavelength, while it does not peak at one with the not phase matched 1212TE, as shown in Fig. 4.17b. The purity of Fig. 4.51 has been calculated via Eq. (4.102).

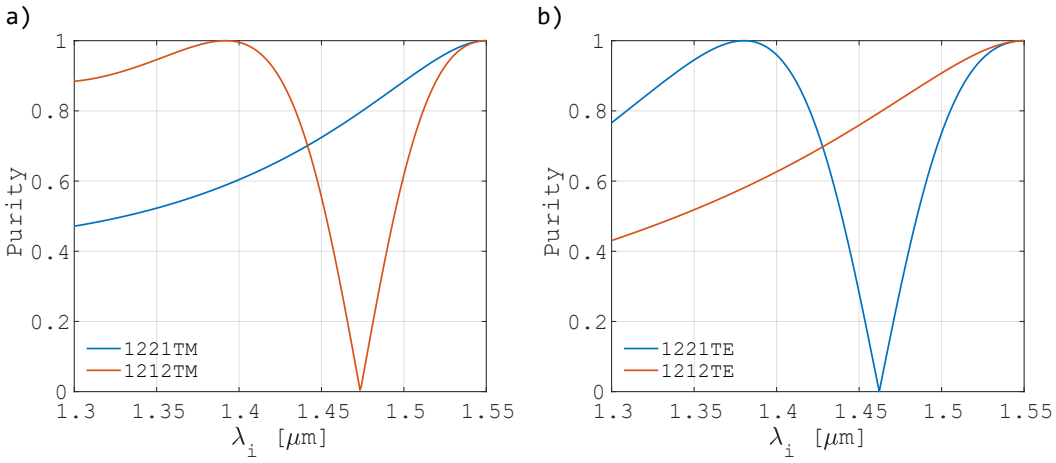

FIGURE 4.17: Purity calculated through Eq. (4.102) as a function of the idler wavelength, a) for the case of Fig. 4.16a and b) for the case of Fig. 4.16b. Only when the intermodal combination is such that the conditions in Eq. (4.109) and Eq. (4.110) are satisfied, purity reach unit value.

I showed that the dual pump delay approach to factorizable JSA can be performed within the intermodal FWM scheme and at degenerate pump wavelength. This strategy offers the opportunity to achieve unit purity without resorting to spectral filtering usually involved in heralded sources based on SFWM; by filtering it is possible to obtain single mode single photon states, but with $P = 1$ only in the limit of zero filter bandwidth [125]. Avoiding filter based purification strategies is therefore a fundamental step towards the development of feasible and efficient single photon sources. In Section 4.7 I discuss the experimental implementation on a SOI chip of the intermodal dual pump delay strategy here proposed.

4.5 2 μm heralded single photons via intermodal four wave mixing

This experiment was carried out with the help of Ms. Sara Piccione, who developed the up-converter detector, and Mr. Matteo Finazzer, who contributed to the

measurements. Mr. Giorgio Fontana developed the electronics for the photon coincidence measurements. The samples used have been fabricated by the Centre for Materials and Microsystems of Bruno Kessler Foundation (Trento, Italy).

Instead of using the common intramodal FWM, involving only the first order mode in a single mode waveguide, we propose to apply the peculiar properties of intermodal FWM (see Section 3.7.2) to solve some of the limitations experienced by heralded single photon sources. There are two main characteristics of intermodal FWM that are of interest: the discrete band phase matching, that can be exploited to obtain a filter free single photon generation; the large detuning between signal and idler, which offers on one side a mean to filter better the pump and Raman noise and on the other side can enable a new family of sources able to generated quantum light in the MIR.

In this section I present the results obtained for a heralded single photon source based on intermodal FWM on a SOI multimode waveguide, generating the idler photon at 1.26 μm and the signal photon at 2.011μm. This configuration is particularly advantageous, having the herald photon where standard InGaAs SPAD are highly efficient and the signal photon that is still below the absorption edge of silica. The chip device, the experiment and the outcomes are discussed, with a particular focus to the 2 μm light detection system.

4.5.1 Chip design and experimental set-up

From the results and simulations obtained with the intermodal FWM experiment in Section 3.6, I designed a device optimized for the coupling and outcoupling of higher order modes in a multimode waveguide. I focused on the generation of intermodal FWM with the intermodal combination 1221 TE, whose superior overall efficiency has been proven experimentally (Section 3.6). Moreover, the rib geometry chosen does not propagate the TM polarization. Therefore, the main process investigated involves the pumps on both the first and second waveguide mode, the idler on the first mode and the signal on the second one, as sketched in Fig. 4.18. The theory describing the process is exactly the same already introduced in Section 3.6.

The design of the integrated SOI device, sketched in Fig. 4.19, has been realized with a rib cross section where h = 300 nm, h_s = 190 nm, h_{clad} = 900 nm and h_{clad} = 2 μm (see Fig. 4.18 for the parameters). The same cross section is used for the simulations. Several waveguide widths have been fabricated, such that controllable spectral generation of the pair was possible. The device aims at generating heralded single photon states through intermodal FWM; in particular, the design in Fig. 4.19 works with intermodal combinations involving one pump photon and the idler on the first order mode and the other pump photon and the signal on higher order modes. The input and output ports are tapered to a width of 3.7 μm, in order to maximize the coupling with the tapered lensed fibers used to inject and extract the light. The input pump is splitted through a 3 dB directional coupler (DC), A in Fig. 4.19, in order to excite the first order mode with 50 % of the power, arm 2 in Fig. 4.19, and the higher order waveguide mode with the remaining half of the power, arm 1 in Fig. 4.19.At point B in the figure, there is the asymmetric directional coupler (ADC) used to couple the higher order mode in the waveguide where half of the pump is already propagating on the first order mode. The waveguide in B is then tapered up to the width w_{FWM} required for the phase matching of the intermodal FWM under consideration, C stage in Fig. 4.19. The last part of the device is used to separate the signal and the idler. Since the signal has been generated on a higher order mode, it can be extracted by using another ADC, D in Fig. 4.19. At the

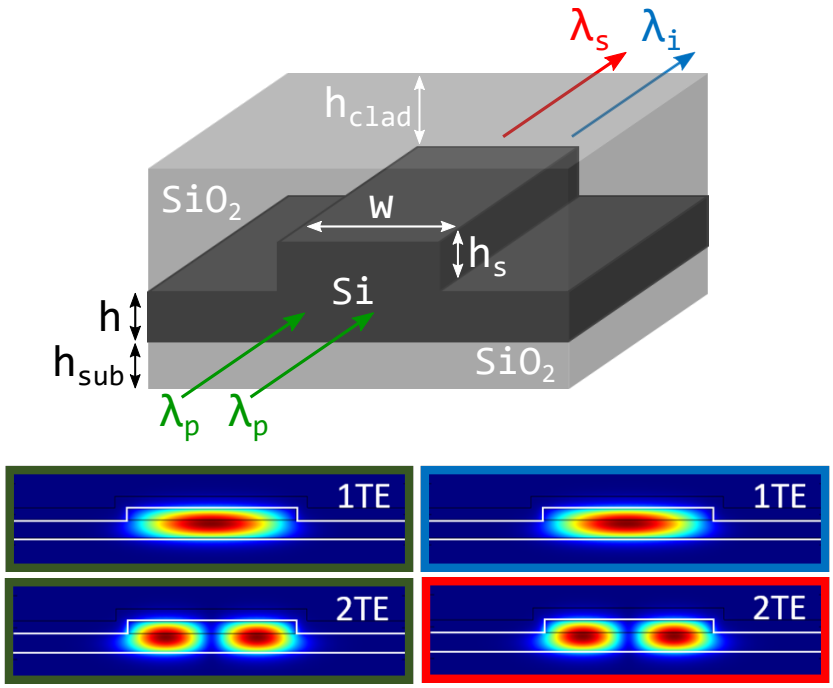

FIGURE 4.18: SOI rib geometry of the waveguides for heralded single photons via intermodal FWM. w is the width of the waveguide, h_s the height of the strip, h the height of the slab, h_{clad} the height of the cladding over the strip and h_{sub} the height of the substrate. The two input pump photons, at λ_p, are converted into signal and idler photons, respectively, at λ_s and λ_i. In the bottom panels, the simulated intensity profiles of the spatial modes excited in the rib waveguide are shown within boxes with the same colors of the corresponding waves in the top diagram.

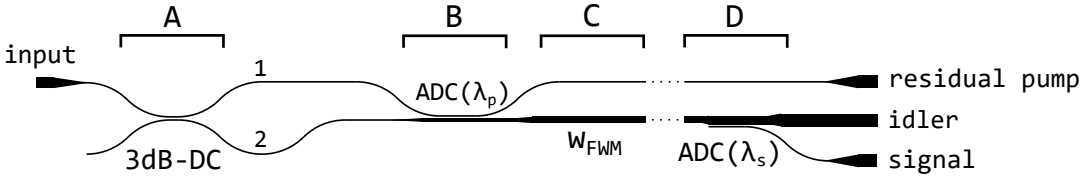

FIGURE 4.19: Design of the device used to generate heralded single photons via intermodal FWM. The pump is injected through the input port and then splitted through a 3 dB coupler (3dB-DC) (A). The power in the reflected arm (1) is coupled on the second TE order mode of the waveguide of the transmitted arm (2) through an asymmetric directional coupler (ADC(λ_p)) (B). At this point half of the pump power is travelling on the first TE order mode while the other half excited the second TE order mode in the same waveguide. This waveguide is then tapered up to the width (w_{FWM}) required for the phase matched intermodal FWM (C). The last stage of the device (D) consists of an asymmetric directional coupler (ADC(λ_s)) used to extract the signal wavelength from the idler and pump waves. The idler and signal are in this way separated on-chip. At the output of the device three ports are present: one for the residual pump not completely coupled through the ADC(λ_p), one for the idler photons and the last for the signal photons. All input and output ports are tapered to a width of 3.7 μm.

output of the device, there are three ports, one for the residual pump, that was not completely coupled into the main waveguide through the ADC in B; the second port carries the idler wave and the remaining pump; the third port allows the extraction of the signal photons. The design of the DC and ADCs used is exactly like the one shown in chapter 1, Fig. 1.5. Depending on the width of the multimode waveguide, different values for the idler and signal wavelengths are generated. As a result, each ADC has been designed in order to optimize the outcoupling of the predicted wavelength. In any case, the ADC is a broad band device, thus tolerant to deviations from the expected target wavelength. The DCs and ADCs have been characterized experimentally with repeated measurements, finding a splitting of 0.57(4) for the 3dB-DCs, and a light coupling efficiency of 0.72(8), both at 1.55μm. In the particular devices used for the 1.95 μm wide waveguide, the 3-dB DC had an efficiency of 0.58 and for the ADC a coupling efficiency of 0.92. Measuring the pump power on the residual output waveguide, it was estimated the amount of power actually propagating in the multimode waveguide, that was 96% of the total coupled power, without considering the propagation losses.

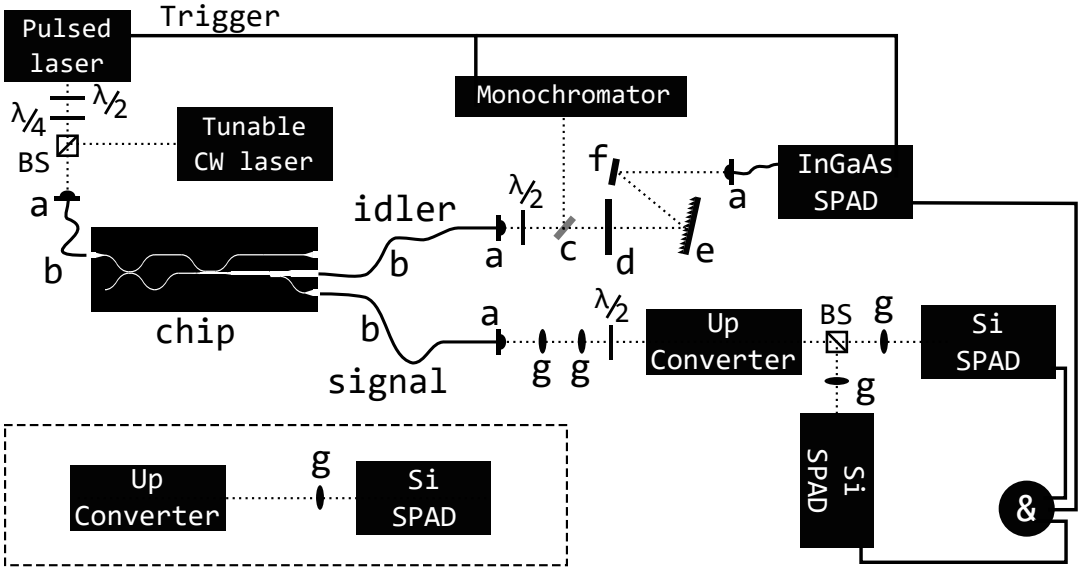

FIGURE 4.20: Setup for the heralding experiment. See text for description.

The setup used in the heralding experiment is shown in Fig. 4.20. The pulsed pump is injected through a collimator (a) into a tapered lensed fiber (b) that is used to couple the pump into the chip. For stimulated FWM also a tunable CW laser is mixed with the pump into the fiber. The optical pulse passes through the device, and the generated signal and idler photons are outcoupled via two tapered lensed fibers (b) and injected into two collimators. A flipping mirror is placed on the idler beam, such that the photon can be either sent to the monochromator, that is the same of Fig. 3.18, or to the InGaAs SPAD after passing through a long-pass filter (d) (1400 nm cut-off wavelength), a grating (e) and a mirror (f). The signal photon is generated above 2 μm; therefore it cannot be measured with standard detection systems. Thus, we used an up-conversion approach to the signal detection. Starting from the collimator, the signal wave is coupled inside the up-converter system through several lenses (g), and up-converted to visible light. When a HBT measurement is needed, the light is splitted through a beam splitter (BS) and focalised through two lenses into SPADs. When the HBT is not required, as in the measurement of the CAR, the up-converted

light is directly detected by one Si-SPAD, as in the inset of Fig. 4.20. Further details on the signal detection stage are reported in Section 4.5.2. The idler is measured in gated mode, triggered by the pump laser. Upon detection, the SPADs generate an electrical signal, that is sent to the coincidence electronics (&). The light polarization is controlled through half ($\lambda/2$) and quarter ($\lambda/4$) waveplates. The long pass filter (d) and the grating (e) are used to suppress the pump and Raman noise. The large frequency shift of the idler (< 1260 nm) allows to filter completely these sources of noise. Other instruments are

- the laser pump, which is a pulsed laser at 1.55 μm, with 40 ps pulse duration and operating at 100 MHz;
- the CW seed laser, which is a tunable laser in the range 1260 - 1640 nm;
- the InGaAs SPAD, which is an ID Quantique ID 210, used in gated mode at 25% detection efficiency and with 100 ns deadtime;
- the visible SPADs, which are Excelitas SPCM-AQRH-14 with 100 Hz of dark counts.

The losses of the whole system have been characterized. The fiber-chip coupling losses are 6.0 dB each facet and the propagation losses are 3.0 dB cm^{-1} in the single mode waveguide (600 nm width) at 1.55 μm; therefore the multimode waveguide is expected to experience much lower losses. The overall losses for the idler line, from the collimator to the InGaAs SPAD are 7 dB, to which the 28 % (-5.5 dB) detection efficiency of the detector has to be added. Therefore, the detected idler counts differ by about 18.5 dB from the on-chip generated photon pairs. By comparing the expected on-chip photon pairs, calculated with the idler, with the detected signal photons, an overall loss from the collimator to the Si-SPAD greater than 20 dB is expected, with a factor of 26.6 dB to have the on-chip photons from the detected counts (with the configuration of the inset in Fig. 4.20). The higher losses in the signal optical line are due to the low efficiency of the up-conversion module and the use of optical elements not optimized for wavelengths beyond $2\mu m$.

Particular attention has to be paid to the coincidence detection stage. We are interested in measuring the signal-idler cross correlation $g^{(2)}_{si}$, the signal second order coherence $g^{(2)}_{ss}$ and the heralded second order coherence $g^{(2)}_{H}$. For details on such quantities see 4.2. To measure the coincidences, we used a time-to-digital converter (TDC) start/stop counter, shown in Fig. 4.21. As soon as an electrical signal triggers the start, the internal timing counter of the TDC (minimum temporal resolution 50 ps) starts to count, and it is stopped only when an electric signal triggers the stop. The TDC measures in this way the delay between the start and stop detections, and its software returns the histogram of the detected delays. The maximum delay measurable by the TDC is 500 ns. For the measurement of the CAR, i.e. signal-idler coincidence, we used the configuration in Fig. 4.21a, where the idler acts as the start and the signal as the stop. Careful control of the delay between signal and idler photons is required, in order to be sure to have the idler arriving before the signal. Also noise can result in start and stop photons, but the corresponding delays will be distributed randomly all over the delay range of the TDC. The idler-signal delay, on the contrary, is expected to have a large peak corresponding to the delay between the signal and idler of the same pair (zero-peak), and lower peaks at delays equal to multiples of the laser period (side-peaks), which arise when the idler is stopped by a signal not belonging to its same pulse. This occurs when the signal photon is

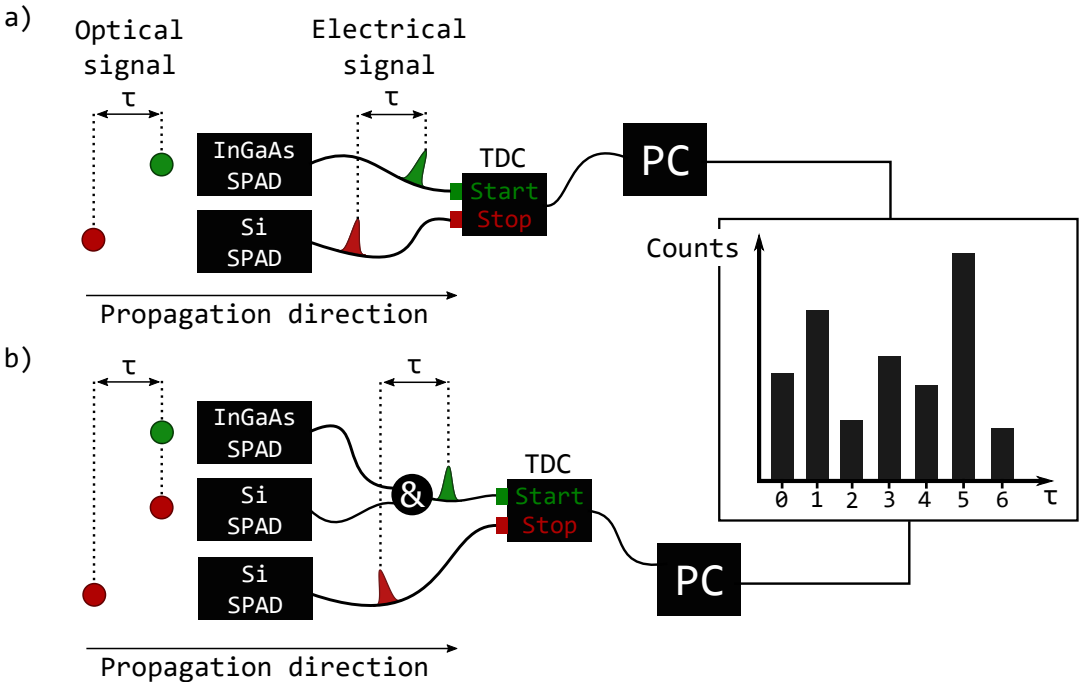

FIGURE 4.21: Schematics of the coincidence measurement setup. The temporal delay (τ) between the photons is reflected in a delay in the electric pulses, which can be measured through the TDC. a) Configuration for the two-fold coincidence measurement through the TDC start/stop. The detection of the idler triggers the counter start while the Si-SPAD gives the stop to the delay measurement. The measured delays are reported in a histogram produced by the TDC software in the personal computer (PC). b) Configuration for the three-fold coincidence measurement. The start is triggered only when the InGaAs and one Si-SPAD have a simultaneous detection, evaluated through a logic AND (&). Then the same as in a) follows.

lost due to losses in the detection stage. Therefore, the ratio between the zero-peak and the side peaks is a direct measurement of the CAR value. The same detection configuration is used for the signal-signal $g^{(2)}_{ss}$, with one Si-SPAD as the start and the other as the stop. The ratio between the zero-peak and the side-peaks gives $g^{(2)}_{ss}(0)$. For the heralded second order coherence, it has been used the configuration in Fig. 4.21b. The start is given by the logic AND between the idler InGaAs and one signal SPAD. The other signal SPAD acts as the stop in the TDC. Therefore, the start begins only at a coincidence between signal and idler, and the triple coincidence peak correspond to the zero-peak delay. The $g^{(2)}_{H}(0)$ is measured as the ratio between the triple zero-peak and the triple side-peaks multiplied by the CAR, as in Eq. (4.78).

4.5.2 Detecting 2 μm photons

In order to access the signal counts, we used a detection system able to measure photons with wavelength $> 2\,\mu m$ and with sensitivity down to the single photon level. While in the visible and NIR windows well established detection systems are readily available with sufficient efficiencies, in the MIR feasible solutions have been proposed based on nonlinear up-conversion [84]. In fact, superconducting nanowire single photon detectors (SNSPDs), that are the state of the art in terms of detection efficiencies (up to 90%) and dark counts ($\sim$ 1000 Hz) in the NIR [157], cannot be

applied with similar performances in the MIR. In this spectral region, SNSPDs are limited at about 2 μm wavelength, with 2% quantum efficiency and with high dark counts [158]. Moreover, SNSPDs require cryogenic temperatures, thus posing further complications to the experimental setup. With the up-conversion approach, single photon detection can be performed at room temperature and can be tuned over the MIR spectrum [84]. The basic idea is to exploit the sum-frequency generation (SFG) process (see Section 3.2), in a periodically poled lithium niobate crystal (PPLN) to up-convert the 2 μm signal photon into a visible single photon. This can be then detected by high efficiency silicon SPADs. The PPLN is quasi-phase matched at the target wavelength. The SFG respects the following energy and momentum conservation relations

$$\frac{1}{\lambda_s} + \frac{1}{\lambda_p^{SFG}} = \frac{1}{\lambda_{up}}, \tag{4.111a}$$

$$2\pi \frac{n(\lambda_p^{SFG}, T)}{\lambda_p^{SFG}} = 2\pi \left(\frac{n(\lambda_s, T)}{\lambda_s} + \frac{n(\lambda_{up}, T)}{\lambda_{up}} + \frac{1}{\Lambda} \right), \tag{4.111b}$$

where λ_s, λ_p^{SFG} and λ_{up} are, respectively, the 2 μm signal coming from the SFWM process, the pump for the SFG process and the up-converted wavelength. T is the temperature of the nonlinear medium and Λ the poling period. In Eq. (4.111b) the temperature dependence of the refractive index has been made explicit to highlight the phase matching tunability of the process via T. In order to improve the efficiency of the system, in Ref. [159] it has been proposed to place the PPLN inside a free-space Fabry-Perot cavity, in order to take advantage of the high circulating power induced by the cavity itself. In our experiment, we are using exactly the same up-converter of Ref. [159], reported in Fig. 4.22a, with PPLN crystals fabricated for $\sim 2\mu m$ with $\Lambda = 15.8\mu m$. Integrated with the up-conversion cavity is the pump source, composed by a broad area diode laser (BAL) that pumps at 880 nm a Nd:YVO_4 crystal, such that the generated light circulating in the cavity is $\lambda_p^{SFG} = 1.064\mu m$. The pump circulates in the cavity composed by mirrors (labelled with M in the figure), short-pass (M6) and long-pass (M7) filters, such that the pump wavelength cannot exit the cavity while the MIR photon and the up-converted photon are free to enter and exit the system. Also a germanium long-pass filter (cut-off wavelength $\sim 1.9\mu m$) is placed at the entrance of the cavity, in order to block the pump of the SFWM process at 1.55 μm. The PPLN in our experiment has a length of 2 cm and several waveguides with height of 1 mm and different widths depending on the wavelength to phase match. We used a poled waveguide with 1 mm width, in order to phase match the signal photon at $\sim 2.011\mu m$. In Fig. 4.22b, the simulated phase matching curve as a function of the temperature is proposed. For our heralding experiment, we used the phase matching temperature of 63°C.

A main feature of the up-converter, especially for quantum measurements, is the spectral bandwidth of the process; in fact, the up-conversion acts as a filtering stage for the single photon. In Fig. 4.23a is reported the simulated conversion efficiency, at $63°C$, for the poled waveguide used, that is compared with the experimental one in Fig. 4.23b. The simulated efficiency spectral position is slightly mismatched with respect to the measured one. The measurement of the up-converter bandwidth has been carried out at a fixed temperature of 63 $°C$ by performing a wavelength scan with a CW laser in the range 2 - 2.020 μm; the laser was directly coupled to the collimator where we usually couple the signal fiber, such that the optical path is exactly the same. By fitting the spectrum in Fig. 4.23b with a gaussian function,

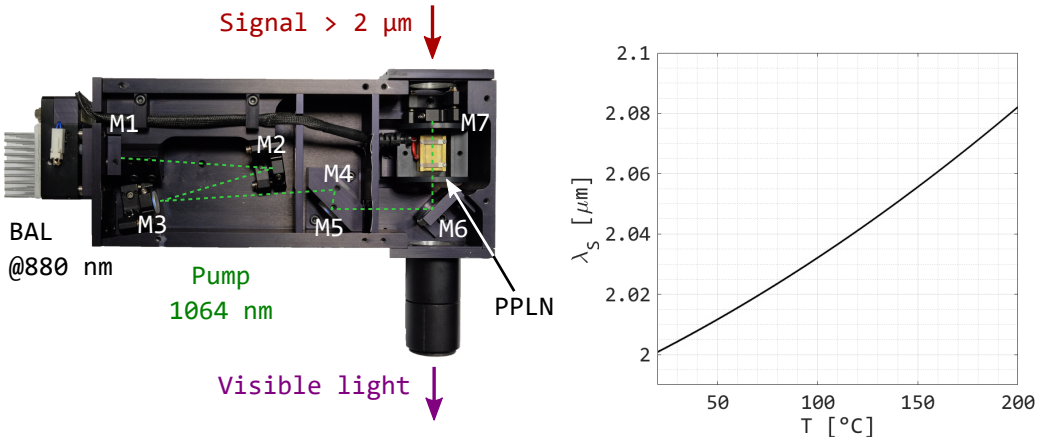

FIGURE 4.22: a) Up-converter cavity scheme. The mirrors composing the cavity are labelled by M. b) Phase matched wavelength as a function of the PPLN temperature.

namely

$$y = ae^{-\frac{(x-b)^2}{c^2}} + d; \tag{4.112}$$

the central wavelength of the up-conversion is $b = 2011.0\,(2010.9, 2011.1)nm$, and the FWHM = $2\sqrt{\ln(2)}c = 2.37\,(2.25, 2.50)nm$; the other parameters of the fit are $a = 0.44\,(0.42, 0.46)$ and $d = 0.566\,(0.555, 0.577)$. From this measurement it is clear that the peak has a FWHM compatible with the simulated one, but the up conversion efficiency does not drop at zero as soon as the wavelength does not satisfy the phasematching condition of the process. This may be due to fabrication errors of the poling.

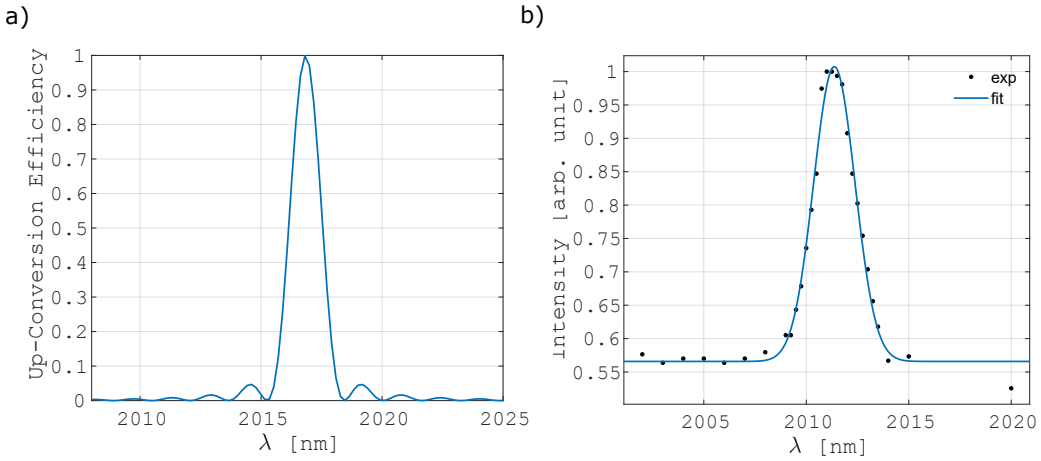

FIGURE 4.23: a) Simulated phase matching spectrum of the SFG process. b) Experimental measurement and gaussian fit of the SFG spectrum.

Since idler and signal photons are emitted in pairs, it is possible to extract the whole detection efficiency of the up-converter coupled to the SPAD by comparing the measured counts for the signal and idler beams. Knowing the idler counts and the losses of the idler beam, it is possible to calculate the pair generation rate on-chip. By rescaling the generated photon pair for the coupling loss of the signal fiber (-6.2(5) dB) the resulting detection efficiency of the whole signal detection stage is about 1%, with the cavity operating at about 70 W of internal circulating power. The problem

of the signal detection stage is the presence of noise due to the up-conversion itself. In fact, depending on the quality of the PPLN crystal and the working temperature of the cavity, several unwanted generation processes may occur [160]. First of all, if the PPLN has a low quality poling it is possible that other nonlinear processes are phase matched, giving rise to unwanted photons collinear with the up-converted signal. Because of this a long-pass filter to eliminate the SHG of the crystal has been placed at the output of the up-converter. Another source of noise is constituted by the thermal radiation of the cavity itself. In fact, the cavity behaves as a black body, whose radiated power scales with the operation temperature. If this radiation respects the phasematching condition for the up-conversion, it will be up-converted exactly like the target signal photon. Since the up-conversion spectrum is not a well defined sinc function, as shown in Fig. 4.23b, the larger effective bandwidth of the process may contribute to an increased amount of converted black body radiation photons. Because of this, the noise superimposed to the signal is even more important. Such a broad band noise spectrum propagates differently with respect to the SFWM photon, therefore it is possible to improve the signal-to-noise ratio (SNR) by using a pin-hole placed in front of the Si-SPAD. A detail of the measurement setup which shows the up-converter module interfaced to the SPADs is reported in Fig. 4.24. In particular, we chose the aperture of the pin-hole in order to maximize the SNR, resulting in about 2000 Hz of dark counts on each SPAD.

Details on the signal detection line

In Fig. 4.24 the detection stage for the signal is described in detail. The signal is sent into the up-converter through an optical system composed by a collimator (a), a diverging lens (b) with 7 cm focal length and a converging lens (c) with 15 cm focal length. The distances between these three elements and the cavity are chosen in order to have the minimum waist of the signal beam in the middle of the PPLN crystal. The minimum waist has been calculated to be around 250 μm. Before entering the up-converter, the signal field is filtered through a germanium long pass filter (e) ($\lambda > 1.9\,\mu m$). The up-converted light, after being filtered with a band pass filter (f) in order to eliminate the SHG of the pump and the pump itself, is splitted through a 50/50 beam splitter. Each beam is then focused through a 4 cm focal length convergent lens (g) into the active area of the SPAD. The SPAD active area is 175(5) μm in diameter, therefore we modified the position of the lens relative to the up-converter and the SPAD such that the signal spot was smaller (about 70 μm diameter). In order to filter out part of the collinear noise, a pin-hole (h) is placed in front of the SPAD.

4.5.3 Idler and signal characterization

On the same chip, several devices with different waveguide widths have been fabricated. In this way it was possible to control the wavelength of the generated pair. In Fig. 4.25 the spectra for the generated idler are reported for different waveguide widths. For the heralding experiment we chose the waveguide with 1.95 μm width, in order to use a lower temperature of the up-converter crystal, thus reducing the up-converted black body radiation (the temperature used is 63°C). In particular, from the simulations it is found that the simulated idler wavelength is close to the measured one if instead of the nominal waveguide height h_s of 190 nm it is used 180 nm, and a 5 nm wider waveguide. This correction allows to match better also the experimental idler positions of the other waveguides shown in Fig. 4.25. In Fig. 4.25

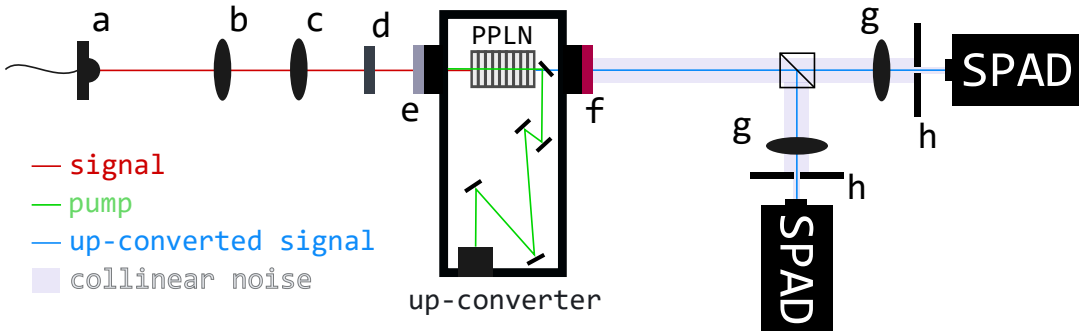

FIGURE 4.24: A detail of the whole heralding setup showing the signal detection stage. The 2μm signal photon is coupled into the collimator (a) through an optical fiber. The signal photon is then focused in the PPLN crystal passing through a divergent (b) and convergent (c) pair of lenses, and after being TM-polarized with a $\lambda/2$ waveplate (d) and filtered with a germanium long-pass filter (e). The up-converted photon is filtered with a band-pass filter (f), divided by a 50/50 beam splitter and focused in the active area of the SPADs through a pair of convergent lenses (g). The collinear noise photons are partially filtered by means of a pin-hole (h) in front of each SPAD.

also the Raman noise contribution is visible at 1434.5 nm, due to crystalline silicon. The broad band extending from 1400 to 1500 nm is the contribution coming from the Raman in the fiber and the leakage of the pump laser.

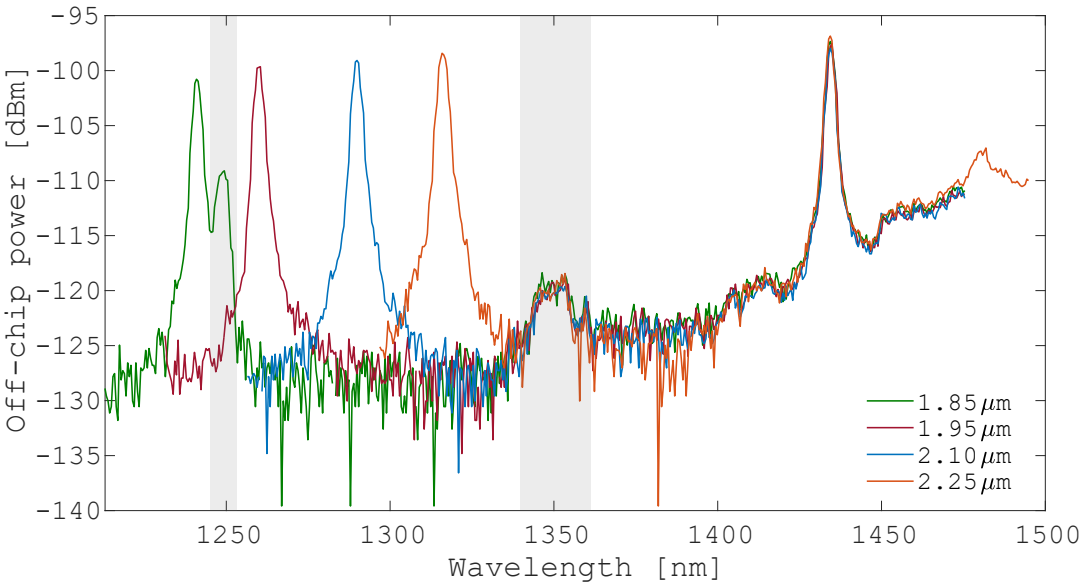

FIGURE 4.25: Spectra of the idler photon generated through 1221TE intermodal FWM for different waveguides. The peak at 1434.5 nm is the anti-stokes Raman peak of crystalline silicon. The shaded gray boxes indicate spurious peaks due to the monochromator. In legend there are the nominal widths of the different waveguides.

The first characterization of the signal and idler photons is the measurement of their quadratic dependence with the pump power, as explained in Section 3.4.1. In Fig. 4.26 are reported the on-chip pair generation rate (a), the measured idler counts (b) and the measured signal counts (c) as a function of the on-chip pump peak power. All these measurements have been fitted with a quadratic function

$(y = ax^2)$, with a good agreement up to 1 W peak power. For higher power, in fact, TPA limits the available pump power, therefore leading to the saturation of the generated photons [149]. The quadratic coefficients for the three fitting functions are $a = 4.93\,(4.46, 5.40)$ MHz W^{-2} (pairs), $a = 69.61\,(63.00, 76.22)$ kHz W^{-2} (idler) and $a = 1.82\,(1.71, 1.93)$ kHz W^{-2} (signal). The fit bounds are the 95% confidence bounds.

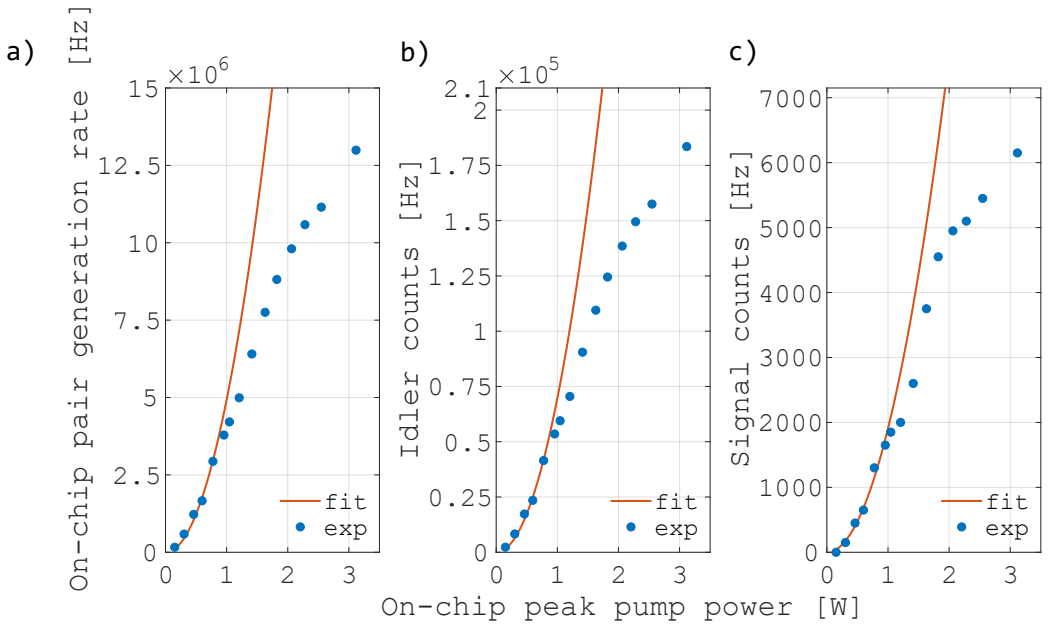

FIGURE 4.26: Measurements performed on the waveguide with 1.95 μm nominal width. (a) On-chip pair generation rate. (b) Idler detected counts. (c) Signal detected counts. All the measurements are shown as a function of the on-chip peak pump power. All the measurements have been fitted with a quadratic power function.

CAR

We measured the CAR for various input powers, as shown in Fig. 4.27a. Each CAR value has been measured integrating the counts under a bin width of 1 ns, in order to be sure to integrate all the signal counts, that spread in time due to the jitter of detectors and electronics. Each measurement lasted till the saturation of the statistics, with at least 1 hour integration time. Since the noise due to the up-converter was significant, we decided to give both a raw CAR value (blue in plot) and a noise corrected CAR (orange in plot). The noise correction is performed evaluating the average noise counts falling in the bin width, and by subtracting this value to all the bins containing the signal photons. In Fig. 4.27b is reported, as an example, the measured histogram for 0.5 W power; the bars are centered at the pump period. In the inset of Fig. 4.27b, an example of the data with the minimum bin width is reported, where the shaded bars represent the 1 ns integration bin. As expected, as the power is reduced, the CAR increases due to the reduced multipair generation probability. We obtained a maximum not corrected CAR of 11.0(4) and a maximum corrected CAR of 58(16).

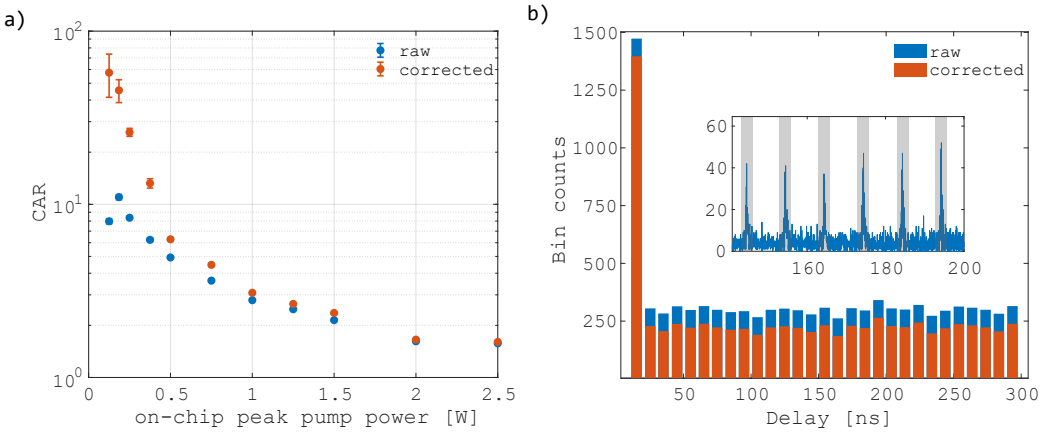

FIGURE 4.27: a) CAR as a function of the input peak power. In blue the raw values and in orange the noise corrected values. b) Measured coincidence as a function of the delay for 0.5 W input pump power. The ratio between the highest bar (the zero-peak) and the average of the side bars gives the CAR. The bins have 1 ns width (see inset, where the shaded bars represent the bin integration). The bins are centered at multiple pump periods. In blue the raw counts and in orange the noise corrected counts.

Unheralded $g^{(2)}$

The unheralded $g^{(2)}$ has been carried out on the signal beam, to show the purity of the single photon beyond 2 μm. It has been measured exactly like the CAR, thus by integrating over a defined bin width, with and without noise correction. For the $g^{(2)}$ measurement we took a bin width of 2 ns, due to the larger counts spreading, due to the larger jitter arising from the use of two Si-SPAD, which exhibit individually a larger jitter. Moreover, this measurement, with respect to the CAR one, is affected by a larger noise, due to the use of free running detection; in the CAR measurement the idler was affected by less noise due to the external gating of the pump. Due to the worse SNR, it was possible to measure the $g^{(2)}(0)$ only for input pump powers larger than 1 W, as shown in Fig. 4.28a. Moreover, the larger noise results in a larger difference between the raw and corrected $g^{(2)}(0)$ values. As the power increases, the $g^{(2)}$ gets lower due to a larger multipair generation probability. The integration time in this case was about 2 hours.

From the $g^{(2)}(0)$ it is possible to evaluate the purity of the state as $P = 1 - g^{(2)}(0)$, as explained in Section 4.3.2. Therefore, in our measurements we get a maximum purity of the single photon state of 0.54(3), which corrected becomes 0.76(4). From simulated values of the purity, that we simulated by calculating the JSI as in Section 4.1.7, it is evident the role of the up-converter in filtering the signal photon. This filtering, with a bandwidth of 2 nm as measured in Fig. 4.23b, results in an increased purity of the state, as can be seen by comparing Fig. 4.29a and b, where by considering such filter the purity is increased from 0.16 to 0.47. However, this is not enough to justify the measured purity. Therefore the measured pump lineshape was considered. This is shown in Fig. 4.29c. By considering the pump lineshape, which exhibits a dual peak profile, the JSI in Fig. 4.29d is obtained. The purity now is 0.59. This purity is much closer to the experimental one, but still far from the noise corrected value. A possible explanation is that the measured purity is overestimated and longer acquisition times are required, or other effects that have not been considered play a role in improving the purity, like a broadening of the pump pulse

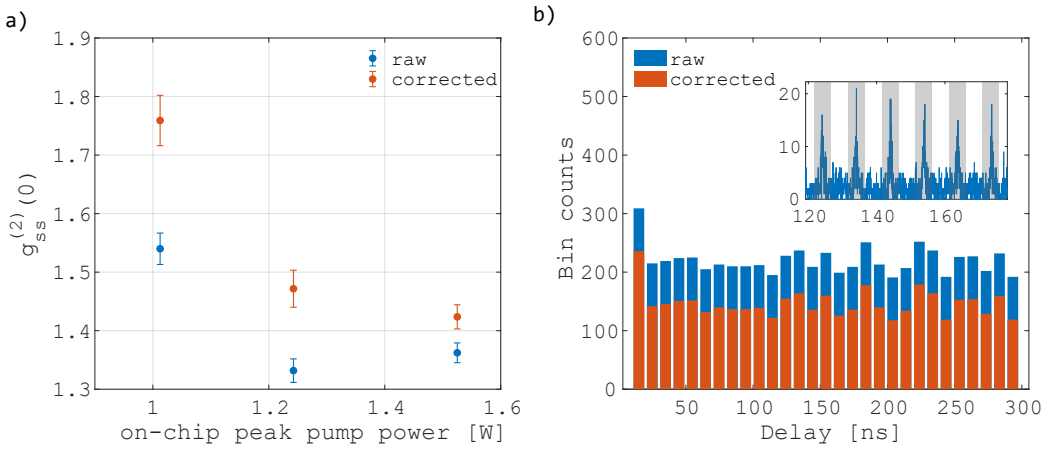

FIGURE 4.28: a) $g^{(2)}(0)$ for the signal beam as a function of the input peak power. In blue the raw values and in orange the noise corrected values. b) Measured coincidence as a function of the delay for 1.01 W input pump power. The ratio between the highest bar (the zero-peak) and the average of the side bars gives the $g^{(2)}(0)$. The bins have 2 ns width (see inset, where the shaded bars represent the bin integration). The bins are centered at multiple pump periods. In blue the raw counts and in orange the noise corrected counts.

bandwidth due to SPM. In any case, the dual peak profile of the pump contributes importantly to the rising of the purity value, due to the larger effective bandwidth involved.

Heralded $g^{(2)}$

The measurement of the heralded $g^{(2)}$ has been performed for two pump powers, 0.75 W and 1.5 W, using the scheme introduced in Fig. 4.21b. These measurements do not give an evidence of the antibunching, since the acquisition time required is prohibitive with our setup. In fact, the rate of measured three-fold coincidences was 0.00012 Hz (70.5 hours acquisition) and 0.0014 Hz (14.3 hours acquisition) for the 0.75 W and 1.5 W measurements respectively. In Fig. 4.30 are reported the counts integrated over a bin of 2 ns relative to the triple coincidence idler-signal-signal. It is clear that the integration time is not enough, since the side peaks are all different. In any case, $g^{(2)}_H(0)$ has been calculated, both raw and noise corrected, as in Eq. (4.78), i.e. the ratio between the normalized three-fold counts and the CAR at the same input power. The resulting $g^{(2)}_H(0)$ are reported in Fig. 4.31. Only for 0.75 W power $g^{(2)}_H(0) < 1$, but it is still larger than 0.5, that is the threshold to claim a single photon behaviour [59].

4.5.4 Conclusions

With the experiment in this section, I reported the first coincidence detection and characterization of pairs of photons with one photon in the NIR and the other in the MIR, coming from a spontaneous process in silicon. In particular, a maximum CAR of 11.0(4) and 58(16), respectively without and with noise correction, was measured. The maximum purity, measured on the signal photons, has been quantified in 0.54(3) and 0.76(4), respectively without and with noise correction. These values for purity and CAR are lower than those of state of the art sources at telecom wavelengths

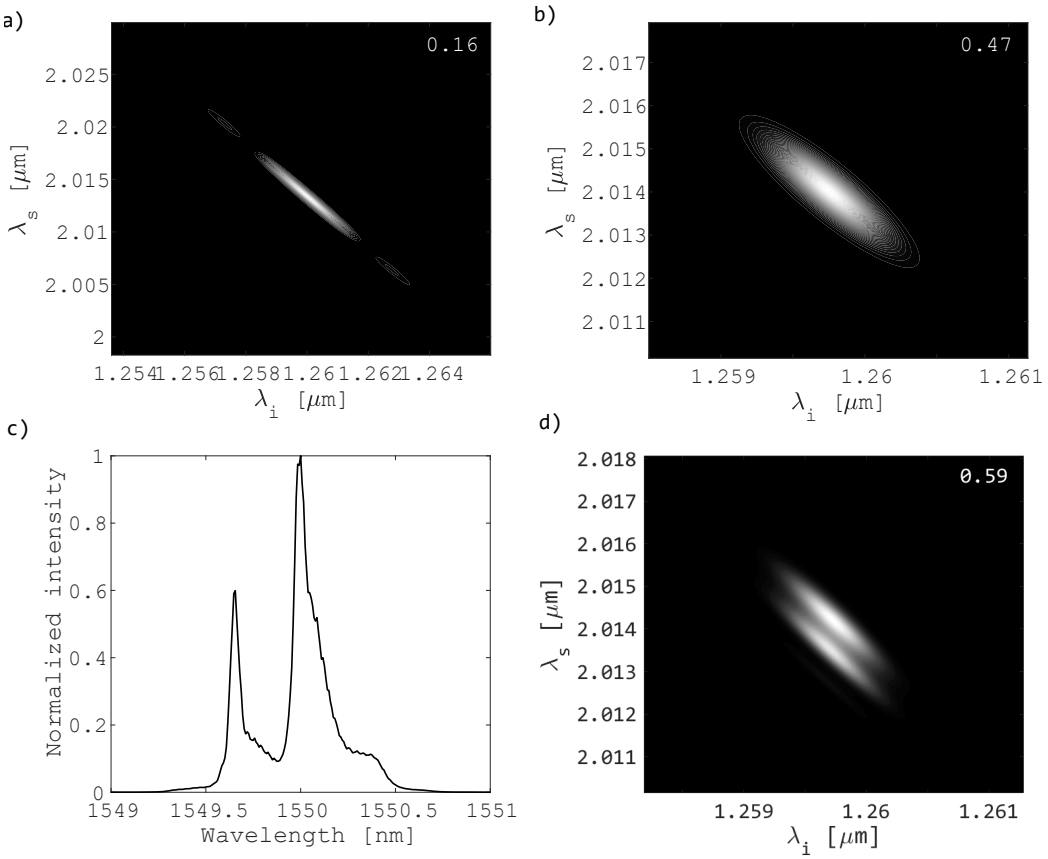

FIGURE 4.29: Simulated JSI for the 1.95 μm wide waveguide a) without any spectral filtering and with a 0.1 nm bandwidth gaussian beam and b) with 2 nm filter on the signal beam and a 0.1 nm bandwidth gaussian beam. c) Measured pump spectrum. d) Simulated JSI with 2 nm filter on the signal and the measured pump spectrum in c). In a), b), d) the purity is reported at the right-top of the figure.

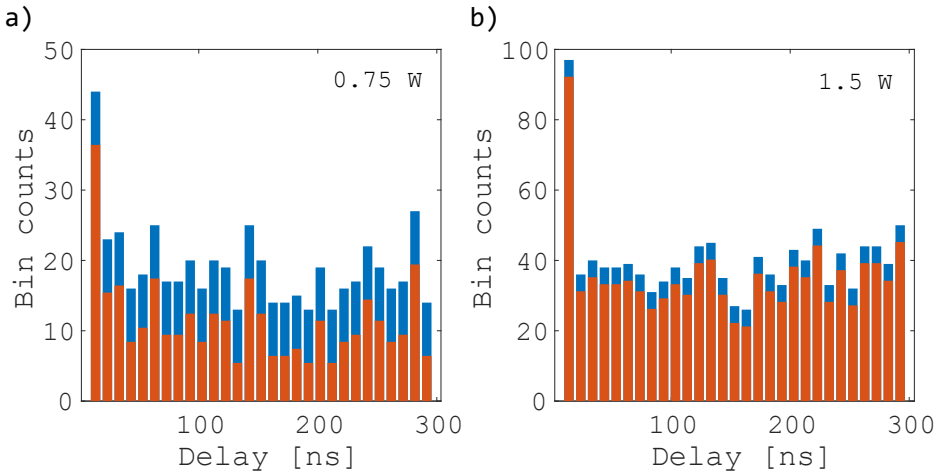

FIGURE 4.30: Counts for the three-fold coincidence between the two signal detectors and the idler. Measurements with a) 0.75 W and b) 1.5 W input powers. In blue the raw counts, while in orange are the noise corrected counts.

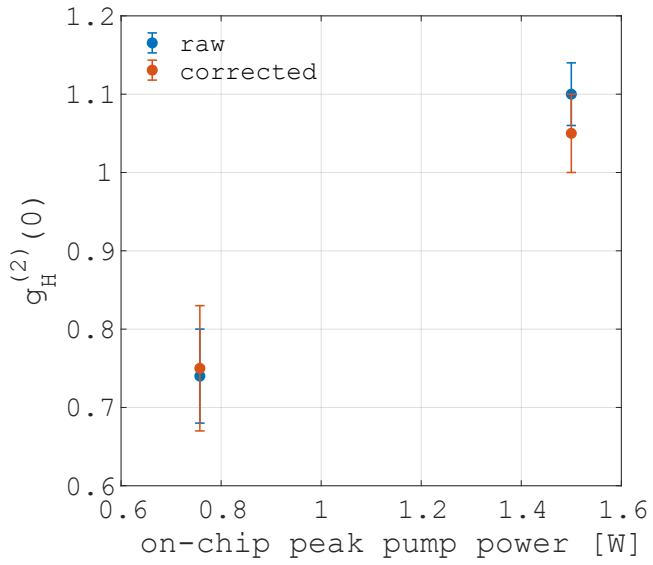

FIGURE 4.31: Measured $g_H^{(2)}(0)$ as from the definition in Eq. (4.78). In blue the raw results, in orange the noise corrected measurements.

[161]. This can be ascribed to the high value of losses due to the measurement of the 2 μm photon. We also measured the heralded $g^{(2)}(0)$, which displays a moderate antibunching with $g_H^{(2)}(0) = 0.74(6)$ and 0.75(8), respectively without and with noise correction. With these results it can be stated that a SOI integrated source of photon pairs with one photon at NIR wavelengths and the other beyond 2 μm has been demonstrated. Coincidence and purity measurements have been successfully performed. The purity has not a record value, but the target of this experiment was to show the possibility to have a broadband source of pairs rather than the demonstration of a high purity source. In order to demonstrate a clear antibunching, as the one needed for the unambiguously demonstration of a single photon source, much lower losses are required in the detection stage. As far as I know, the source of photons that we demonstrated is the first experimental demonstration of a 2 μm on-chip heralded photon source and can find application particularly in quantum gas sensing. In addition, we also demonstrated that it is possible to perform coincidence measurements without relying on strong pump and Raman spectral filtering.

4.6 Improved purity with moderate spectral filtering

This experiment was carried out at the QET Labs of Bristol (UK) in collaboration with Dr. Massimo Borghi. The samples used have been fabricated by the Centre for Materials and Microsystems of Bruno Kessler Foundation (Trento, Italy).

Intermodal FWM allows to achieve discrete band generation of photon pairs. As introduced in Section 4.4.2, via intermodal FWM it is possible to achieve state purification through a dual pump approach. However, this is possible only when the two pump photons are distinguishable at least in one degree of freedom, so that their different group velocities can be used. When the intermodal FWM combination is of the type (a,a,b,b), i.e. with the two input pump photons on the same waveguide mode, they cannot be separated through the different group velocities. Therefore, the JSI exhibits sinc lobes, with reduced purity, as in Fig. 4.32a. However, it is still possible to use the discrete band of the intermodal process. In fact, by introducing a

proper spectral filtering, sinc lobes can be eliminated, improving the purity without reducing significantly the brightness, as shown in Fig. 4.32b. The intermodal FWM therefore allows to improve the filtering of the single photon state by generating the photons far from the Raman and pump noise and providing an initial filtering with discrete band. In this section it is described the experiment carried out on the intermodal FWM combination 1122TE, with 6 μm wide waveguide and far detuning between signal (2.014 μm) and idler (1.274 μm) with 1.561 μm pump, showing an increased photon purity thanks to the moderate filtering (1.8 nm filter) operated on the idler photon.

4.6.1 Setup and chip design

The chip design for this experiment is shown in Fig. 4.32c. The chip has the rib cross section of Fig. 4.18, with 6 μm width and 1.6 cm length. From the input of the device (left) the pump is coupled into the multimode waveguide where FWM occurs by means of a tapering. Then, to extract separately the idler and signal, which propagate on higher order modes, ADCs are used. The spectrum of the generated idler is shown in Fig. 4.32d, a 1.55 μm pump was used. The idler wavelength was at 1.269 μm, close to the simulated one at 1.263 μm.

The purity measurement has been carried out in a different setup. The pump laser was a pulsed laser at 1.561 μm, with 207 MHz repetition rate and a tunable bandwidth. The outcoupled light is firstly filtered with a 1.8 nm bandwidth double monochromator and then sent into a HBT interferometer composed by a 3-dB fiber connected to two SNSPDs.

4.6.2 Results

The average power was about 100 μW, with a maximum detected pair generation rate of 50 kHz (with 2.3 nm pump bandwidth). The purity of the state has been measured as a function of the pump bandwidth. The results are shown in Fig. 4.32e. The purity has been calculated by measuring the $g^{(2)}(0)$ of the idler photon. As the pump bandwidth increases, the state becomes more and more indistinguishable, resulting in an increased purity. The maximum purity achieved was 0.90(2), with 2.27(3) nm pump bandwidth. The measured purity follows the same behaviour of the simulated one (blue line in 4.32e), calculated as in Eq. (4.51). The simulated purity is higher than the measured one. This can be due to a larger filter bandwidth on the idler; in fact, the experimental points are in between the simulation with the 1.8 nm filter (blue) and the simulation without the filter (orange). In order to have the simulated purity maximized at the same pump bandwidth of the experiment, it is used 1 cm waveguide length instead of the experimental 1.6 cm. This is due to the walk off occurring between the generated photons and the pump, which limits the interaction length of the process; by changing the pump bandwidth, also the coherence length of the pulse is changed, resulting in a different effective interaction length. This is shown in the simulation in Fig. 4.33, where the peak of the purity is obtained at different pump bandwidths depending on the waveguide length. In fact, the purity calculated as in Eq. (4.51), takes into account the walk off between the pumps, but does not consider the generated photons walk off from the pumps; therefore, to compare the experimental results with the simulated ones the reduced interaction length has to be taken into account by reducing the length of the sample in the simulation.

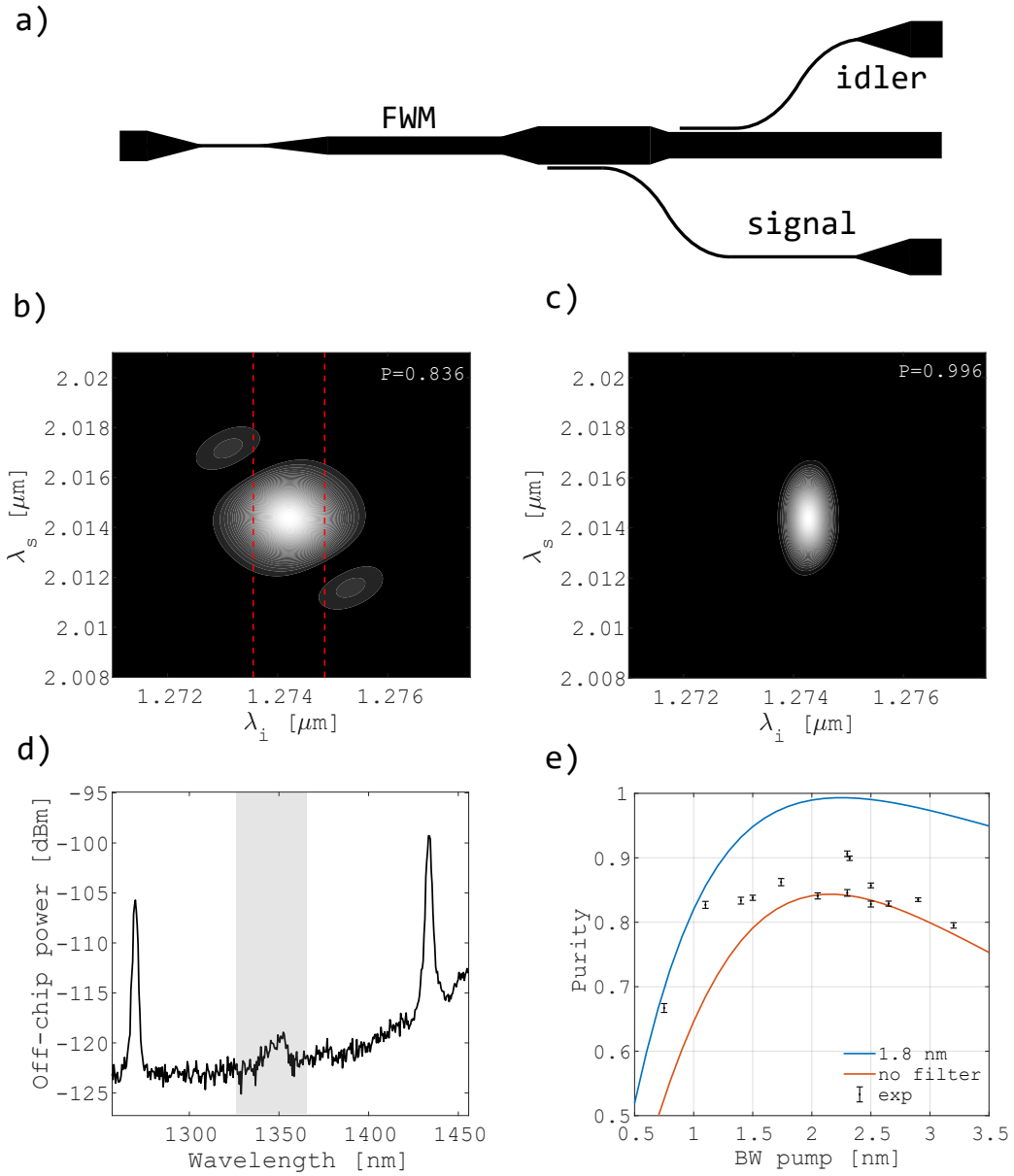

FIGURE 4.32: a) Scheme of the chip for the excitation and collection of the 1122TE intermodal FWM combination. b) Simulated JSI of the 1122TE intermodal FWM in a 6 μm wide waveguide. The dashed red lines refer to the 3-dB bandwidth of the spectral filter (1.8 nm) that is used in the setup to filter the idler photon. c) Same JSI of b) but with the 1.8 nm filter applied on the idler. The purity is now increased to 0.996. d) Measured spectrum of the 1122TE combination in the 6 μm waveguide measured with 1.55 μm pump. In shaded gray a spurious peak. The peak at 1434 nm is the Raman of silicon. e) Purity as a function of the pump bandwidth. The experimental points (black dots) follow approximately the same behaviour of the simulated curves calculated for a 1 cm long waveguide. The purity has been simulated with 1.8 nm filter (blue) and without any filter (orange) on the idler.

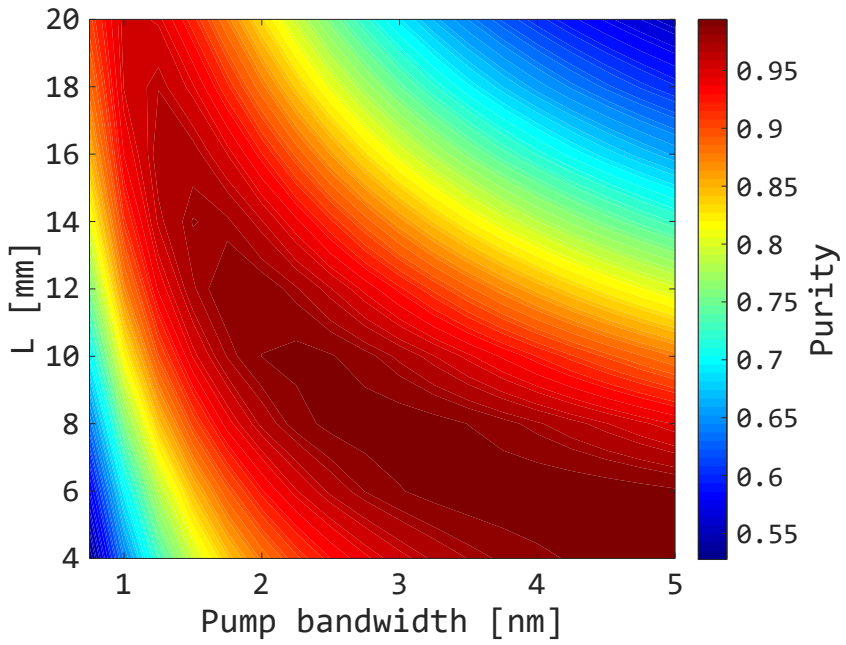

FIGURE 4.33: Simulated purity as a function of the waveguide length and pump bandwidth.

4.6.3 Conclusions

With this experiment it was demonstrated the possibility to achieve high purity single photon states with far detuning from the pump via on-chip intermodal FWM. Also in this case the signal is at a wavelength beyond 2 μm, thus completing the work already begun with the experiment in Section 4.5. A moderate filtering of the idler photon allows to achieve a large purity of 0.90(2), essentially related to the elimination of the sinc side lobes in the JSI. The discrete band of the intermodal FWM combined with a proper pump engineering allows to achieve on-chip high purity states with flexible spectral properties and broadband generation. This kind of source, with high purity single photons and such large detuning, has no counterpart in the literature of heralded single photon sources.

4.7 99% purity with dual-pump delay intermodal four wave mixing

In this section I report some simulations and the proposal of the chip design for the generation of extremely high purity states based on the dual pump delay approach described in Section 4.4.2. The idea of applying the dual pump method to the intermodal FWM has been developed together with Dr. Massimo Borghi, former member of QET Labs in Bristol (UK)

In order to apply the dual pump delay scheme, it is required that the two pump photons involved in the FWM process have different group velocities. With the intermodal FWM, it is possible to find modal combinations such that the two pump photons excite two different waveguide modes, which propagate with different group velocities. We chose the 1221TM intermodal combination for our simulation. We studied a SOI channel waveguide, with 2 μm width and 220 nm height. In Fig. 4.34, we show the JSIs and the relative purities when the FWM is excited by a 5 nm wide

pump at 1.55 μm and the waveguide has 1 cm length. In a), the case without any delay is reported, while in b) a delay of 1.838 ps is applied between the pump pulses. Through the delay, the purity improves from 0.72 (a) to $\sim$1 (b). The purity is here calculated directly from the JSA given by Eq. (4.89), thus without any approximation.

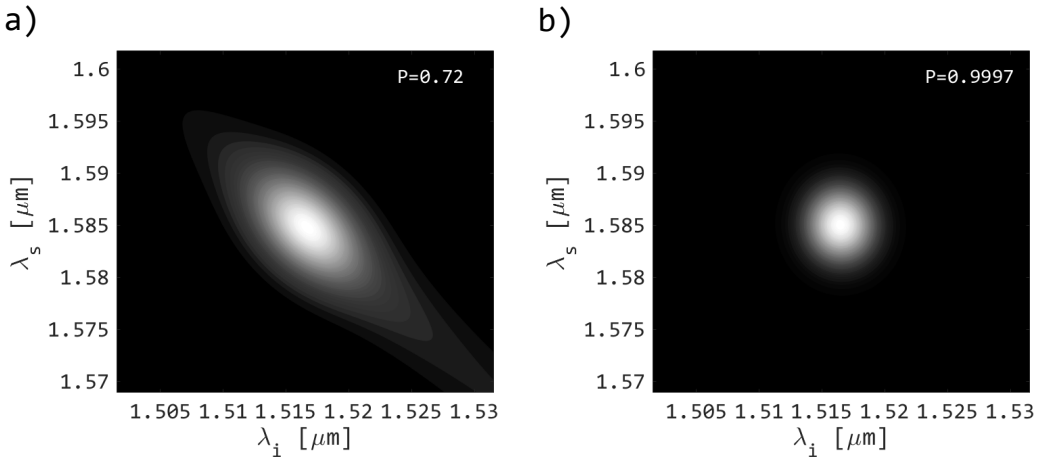

FIGURE 4.34: JSI from intermodal FWM with 1221TM combination for 2 cm long and 2 μm wide waveguide. a) Without the delay between the pumps purity is limited to 0.72. b) With the optimal delay between the pumps (1.838 ps) the purity exceeds 0.99.

To apply on-chip the delay required, it is necessary to know the group velocities of the different optical modes: in our case, the 1TM mode has a group velocity of 75.213 $\mu m\, ps^{-1}$ and the 2TM mode has group velocity 73.190 $\mu m\, ps^{-1}$, at 1.55 μm. For example, considering the case of 1 cm length waveguide, the optimal delay is 1.838 ps. Such a delay is added as shown in the device design in Fig. 4.35. The intermodal combination involves both the first and the second mode for the pump, so the input part of the chip is constituted by the pump 3dB splitting and mode coupling though ADC, exactly like the chip in Section 4.5; however, in the design here presented also the delay line is introduced, on the pump exciting the first order mode, since it is the faster one. The generated signal and idler are outcoupled as usual via ADCs or directly from the multimode waveguide.

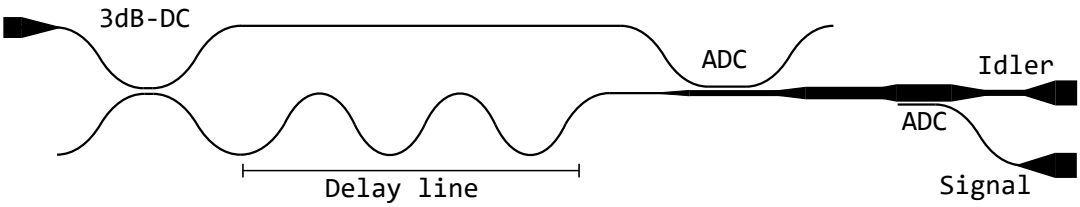

FIGURE 4.35: Chip design for the experimental investigation of the dual pump delay approach to the generation of pure single photon states in a waveguide.

With the proposed design, very high purities are expected, as shown in Fig. 4.36. Here, we show the simulated purities as a function of the pump bandwidth and of the length of the device, for a 1.55 μm pump and for the idler and the signal generated at 1.517 μm and 1.585 μm. This figure shows also that it is possible to optimize the purity of the state by varying the waveguide length and the pump bandwidth. From Fig. 4.36 is evident the saturation of the purity at almost unit value

(0.9997), which means that the constraints on the pump and waveguide length can be also relaxed to smaller values while keeping high values of purity.

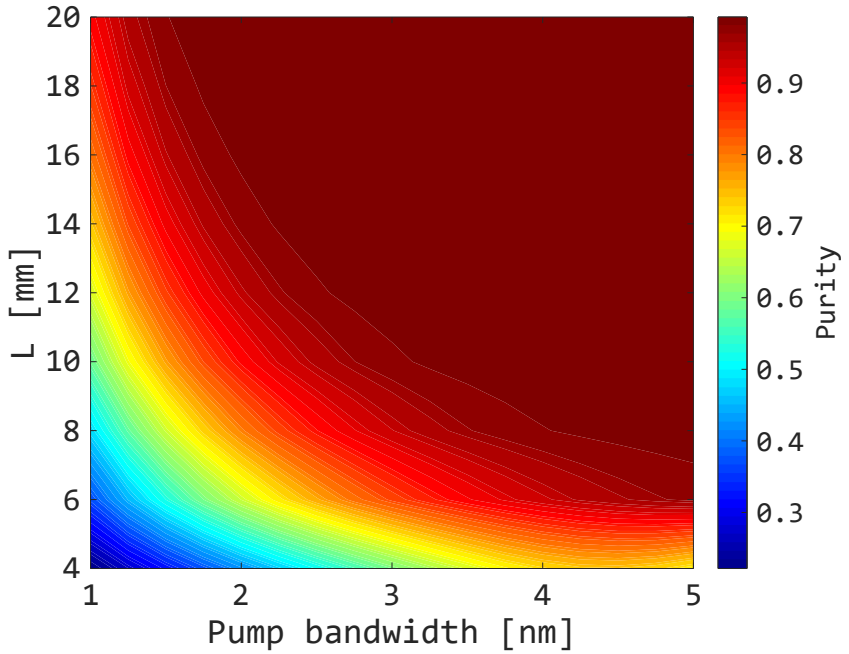

FIGURE 4.36: Simulated purity as a function of the waveguide length and pump bandwidth in the case of optimal delay included.

4.7.1 Conclusions

In this section it has been proposed a design for the generation of pure single photon states through intermodal FWM in SOI waveguides. The simulations suggest purities exceeding 0.99 with photon pairs generated in the telecom band, thus of interest for quantum computation. This approach can be applied also for far spectral detunings between idler and signal, with purities still larger than 0.98, thus of great interest for quantum sensing and free-space quantum communications.

Chapter 5

Conclusions

This thesis explored different topics from classical linear devices, to novel nonlinear processes, to new sources of quantum states of light. The common thread is the use of higher order modes in waveguides, and the main result I got is that they can be enabler of new optical processes and devices.

In chapter 2, I addressed the problem of a new compact mode coupler which can be used as an alternative to current devices for mode multiplexing. I investigated a method to use the interference pattern arising when two coherent tilted beams superimpose. Such device has been theoretically described and simulated in its integrated form. I have also experimentally validated the underlying mechanism. Simulations of the integrated implementation show very compact footprint and very low crosstalk between even and odd modes, that are peculiar of this approach to mode coupling. The integrated interferometer is compared with the state of the art devices in Table 2.3. In terms of minimum cross-talk, the integrated interferometer competes with the other devices (27 dB vs. 25-40 dB), with much larger bandwidth (> 200 nm vs. 100 nm). These values make the device compatible with DWDM and wavelength conversion processing, where broadband signals are involved. The device has a length of 200 μm, which can be reduced to tens of microns if heaters are not included; heaters are required only to face the fabrication imperfections. Nonetheless, the proposed interferometer design is highly fabrication tolerant, thus the perspective is to avoid the heaters after the experimental validation of the integrated chip design. With respect to the state of the art (Table 2.3), the device shows high excess losses (2.85-4 dB vs. 0.2-1 dB). Excess losses are the main drawback of the proposed device, which hinders its application in large scale optical networks. Moreover, further analysis have to be done in order to verify the number of possible channels (N_{ch} in Table 2.3), which is potentially larger than 2. In conclusion, the compactness, broadband and fabrication tolerance of the proposed device suggest its adoption as a robust coupling technique for signal processing and data routing, particularly in applications where parity mode selection is needed.

In chapter 3, I discussed a novel nonlinear optical process in waveguide: the intermodal FWM. Its experimental demonstration in waveguides has been performed for the first time in this thesis. The main advantage of intermodal FWM is the increased flexibility due to the extra degree of freedom of the spatial waveguide mode. In particular, it allows the generation of broad band and tunable new frequencies within a discrete band. This allows to perform selective wavelength conversion and light generation compatible with multimode operation. The wavelength conversion can be easily controlled via the waveguide geometry. This functionality is particularly useful for the mode division multiplexing technology, that needs mode selective wavelength conversion [78]. Moreover, intermodal FWM exhibits the unique property of achieving a very large spectral detuning between the signal and idler photons, accessing the MIR part of the spectrum with C-band pump photons. This

is an interesting possibility for integrated MIR photonics, which opens the way to on-chip gas sensing and free-space communications. The measured conversion efficiency is -15 dB, with signal and idler respectively at 1640 nm and 1469 nm. This is lower than what achieved with intramodal FWM, which exhibits -10 dB efficiency within a conversion band of 150 nm [7]. However, intramodal FWM is based on dispersion engineering and therefore is limited to convert wavelengths close to the pump spectral position. With intermodal FWM, I demonstrated a spectral conversion between signal and idler that ranges from 180 nm up to 980 nm. To get such a wide spectral conversion, intramodal FWM needs the engineering of the β_4 dispersion term. A detuning of 820 nm between signal and idler has been demonstrated, where to reach a 19 dB conversion gain it was needed a pump above 1.9 μm, thus not affected by TPA [48]. Thus, also intramodal FWM gives raise to discrete band phasematching and large spectral generation, but only the intermodal FWM allows controlling the generation of the signal and idler waves over all the telecom band, even near the pump wavelength. In my work, I mainly investigated the 1221TE intermodal combination, but also 1122TE, 1331TE, 1221TM and 1331TM combinations have been experimentally demonstrated. The large and tunable wavelength conversion/generation, the flexibility offered by the spatial modes and the discrete band phase matching make the intermodal FWM a solution for on-chip optical processing and sensing, with perspectives that interest the emerging fields of classical multimode processing and integrated quantum optics.

Actually, the peculiar properties of intermodal FWM impact quantum photonics. This was the topic of chapter 4, which discusses how integrated quantum optics can benefit of this nonlinear process. Exploiting the broad band and tunable intermodal phasematching, the generation of heralded single photons in the MIR has been demonstrated in this thesis. This is motivated by the huge interest of MIR light sources, also at the single photon level. The idea was to generate pairs with one photon at standard NIR wavelengths which could be used as an efficient herald for the other 2 μm photon. It has been here demonstrated the possibility to perform coincidences between such photons, with the signal at 2011 nm and the idler at 1260 nm. In this way, the first source of pairs bridging the MIR and NIR spectral windows on a silicon chip, using a C-band pump, has been demonstrated. The experimental results show a maximum CAR of 54 after noise correction, with purity larger than 0.75 and on-chip pair production rate of about 0.1 MHz. The heralded $g^{(2)}(0)$ was 0.75, that is a good indication of the heralding occurrence but it is still to high to claim the single photon operation of this source. However, the measurements are largely affected by the losses experienced by the signal detection setup. With respect to the state of the art, the CAR is comparable to other heralded sources in SOI waveguides [112, 162], but it is much lower with respect to ring resonators, with CAR > 12000 [161]. Moreover, the heralded $g^{(2)}(0)$ for ring resonators is less than 0.0006 [161], or below 0.2 for waveguides [112, 162]. When comparing the state of the art with our heralded source, it has to be considered that in this experiment the herald and the heralded are far apart by about 750 nm. Moreover, the purity of the state can be easily increased with a larger pump bandwidth. In addition, I exploited the discrete band of the intermodal phase matching to achieve high purities for broad band photons, with 0.90 purity for a photon at 1.28 μm. The filtering only eliminates the sinc side lobes, thus with limited brightness reduction. Such high purity has no counterpart in the quantum silicon photonics literature, where purities larger than 0.90 have been achieved but with small detuning and relying on narrow spectral filtering [111] or ring resonances [98]. Nonetheless, I have shown that the higher order modes characterizing intermodal FWM enable new solutions

to get high purity single photon states without any filtering. This is the case of the dual pump delay approach to purification, proposed in this thesis. The higher order modes involved in the intermodal FWM allows to exploit and engineer the different group velocities of the waveguide modes, achieving near unit purity states. This is a completely new solution for silicon quantum photonics, which here I demonstrated theoretically. Therefore, the perspectives for intermodal FWM in quantum photonics is to enable near unit purity single photon sources operating at both telecom and MIR wavelengths, providing a new tool for the implementation of quantum sensing and processing on-chip.

Appendix A

Formation of waveguide modes

Optical waveguides, in general, are micron sized structures used to confine light along a certain path. Waveguides on a photonic chip can be considered as "optical wires", in analogy with the electrical wires of the well developed micro electronics platform. In the optical waveguide the light is confined in the higher refractive index core, while the surroundings (cladding and substrate) are fabricated with a lower refractive index. Thanks to this refractive index contrast the light is confined due to the total internal reflection at the borders of the core region, propagating through the waveguide; as a consequence, the waveguide is associated with a critical angle θ_c and all the waveguide modes propagating with an angle lower than this critical angle will be confined, while the others will be radiated outside the core region. The intensity of the light trapped in the core material exhibits a particular spatial profile, depending on the excited waveguide mode, with evanescent field tails in the surrounding regions, as shown in the waveguide modes in Fig. 1.1d. The evanescent field is crucial for a number of applications exploiting the opportunity to interact with the surroundings through this exponential decaying field, for example for sensing [163] or light coupling with directional couplers [25]. The evanescent field is also at the basis of the principal loss mechanism affecting waveguide propagation, which is the scattering at the core borders. In fact, the propagation losses are due to material absorption and scattering; since the material used is usually transparent at the working wavelength, the main contribution to losses comes from the scattering due to the core roughness introduced by the fabrication process. The evanescent tail interact with the rough core borders, and the less confined the optical mode, the higher the evanescent field intensity and so also the scattered intensity will be higher. Also the waveguide effective index is related to the evanescent field, such that as the tails of the field increase the effective index decreases due to the larger probing of the lower refractive index surroundings [21]. This mechanism allows to engineer the propagating properties of the guided light by perturbing the vicinity of the optical waveguide introducing other integrated devices or materials.
The field profile of the waveguide modes can be calculated by solving the Maxwell's equations. Unfortunately, only for planar waveguides (Fig. 1.1a) analytical solutions are present, while for channel waveguide it is necessary to use numerical simulation softwares which extract the field profiles by means of the beam envelop method or the finite elements method. Despite it is not possible to access analytically the channel waveguide field profiles, a deep insight into the modes distribution can be achieved by studying the solutions for the planar waveguide. Considering the scheme in Fig. A.1, the slab extends indefinitely on the (x,z)-plane, while the light is confined along the y direction. According to the ray optics interpretation of waveguiding [5], the ray of light propagating inside the dielectric waveguide experiences total internal reflection at the core boundaries, with θ_m angle between the ray and the z direction, with m the mode order. The higher the order mode, the higher the

θ_m [5].

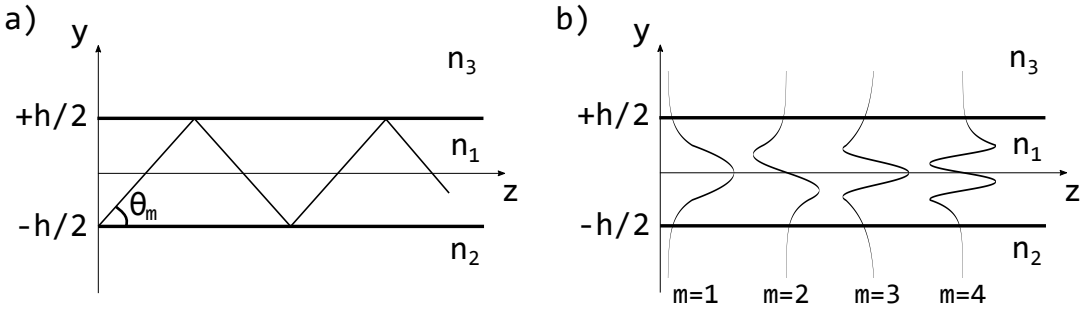

FIGURE A.1: a) Scheme of the planar waveguide with the confinement along the y direction and the slab along the x direction. b) First four modal profiles (u_m) in the slab waveguide with the confinement along the y direction.

The scalar wavevector components for the propagating wave are

$$(0, n_1 k_0 \sin\theta_m, n_1 k_0 \cos\theta_m), \tag{A.1}$$

with $k_0 = 2\pi/\lambda$ the wavevector in free space. The electric field for TE polarization can be written as $e_{x,m}(y,z) = a_m u_m(y)\exp(-i\beta_m z)$, with a_m a constant, the propagation constant $\beta_m = n_1 k_0 \cos\theta_m$, and the y-field profile inside the waveguide can be written as

$$u_m(y) \propto \begin{cases} \cos\left(n1\, k_0 \sin\theta_m\, y\right), & m = 1,3,5,... \\ \sin\left(n1\, k_0 \sin\theta_m\, y\right), & m = 2,4,6,... \end{cases} \quad \text{with } -\frac{h}{2} \leq y \leq \frac{h}{2}, \tag{A.2}$$

where the proportionality constants come from the normalization condition

$$\int_{-\infty}^{\infty} u_m^2(y)dy = 1. \tag{A.3}$$

From eq. (A.2) it is clear that the higher the θ_m, the larger the variation of the field profile along y, such that the higher order modes have a faster oscillating profile with respect to lower order modes. The field extending outside the core region must match the field inside the core at the boundaries ($y = \pm h/2$), and therefore should propagate along z as $\exp(-i\beta_m z)$; for $|y| > h/2$, the field has thus the form $e_{x,m} = a_m u_m(y)\exp(-i\beta_m z)$ and, by plugging it into the usual Helmholtz equation $(\nabla^2 + n_2^2 k_0^2)e_{x,m}(y,z) = 0$, it is obtained

$$\frac{d^2\, u_m}{dy^2} - \eta_m^2 u_m = 0, \tag{A.4}$$

where $\eta_m^2 = \beta_m^2 - n_2^2 k_0$, that is a non-zero positive quantity for guided modes. As a result, eq. (A.4) is satisfied by

$$u_m(y) \propto \begin{cases} \exp\left(-\eta_m\, y\right), & y > \frac{h}{2} \\ \exp\left(+\eta_m\, y\right), & y < -\frac{h}{2} \end{cases} \quad \text{with } -\frac{h}{2} \leq y \leq \frac{h}{2}. \tag{A.5}$$

This solution defines the evanescent wave, with η_m the extinction coefficient, that can be expressed as

$$\eta_m = n_2 k_0 \sqrt{\frac{\cos^2\theta_m}{\cos^2\bar{\theta}_c} - 1}, \tag{A.6}$$

with $\bar{\theta}_c = \cos^{-1}(n_2/n_1)$ the complement of the critical angle. From eq. (A.6), as the order mode increases, θ_m becomes larger and η_m decreases, suggesting that for higher order modes the evanescent field penetrates deeper into the surrounding media. The first four modal profiles in the slab waveguide along the y direction have been calculated as in eq. (A.2) and (A.5) and are reported in Fig. A.1b. Analogous derivation can be done also for confinement along the x direction and with TM waves [5]. The field profiles for a channel or rib waveguide resemble the same result obtained for the planar waveguide, with the only difference that the confinement is present on both the x and y direction: the resulting mode profiles have the same profile of the planar modes along the width of the waveguide, while along the height only one mode is typically possible due to its typical lower size with respect to the width. As a result, the modes of a channel/rib waveguide have the profiles shown in Fig. 1.1.

Bibliography

[1] Zhou Fang and Ce Zhou Zhao. "Recent progress in silicon photonics: a review". In: *ISRN Optics* 2012 (2012).

[2] RA Soref and JP Lorenzo. "Single-crystal silicon: a new material for 1.3 and 1.6 μm integrated-optical components". In: *Electronics Letters* 21.21 (1985), pp. 953–954.

[3] David J Lockwood and Lorenzo Pavesi. *Silicon photonics II: Components and integration*. Vol. 119. Springer Science & Business Media, 2010.

[4] Dan-Xia Xu et al. "Silicon photonic integration platform—Have we found the sweet spot?" In: *IEEE Journal of Selected Topics in Quantum Electronics* 20.4 (2014), pp. 189–205.

[5] BEA Saleh and MC Teich. *Fundamentals of photonics, ch 14*. 1991.

[6] Fengnian Xia et al. "Ultra-compact high order ring resonator filters using submicron silicon photonic wires for on-chip optical interconnects". In: *Optics express* 15.19 (2007), pp. 11934–11941.

[7] Mark A Foster et al. "Broad-band continuous-wave parametric wavelength conversion in silicon nanowaveguides". In: *Optics Express* 15.20 (2007), pp. 12949–12958.

[8] Vilson R Almeida et al. "All-optical control of light on a silicon chip". In: *Nature* 431.7012 (2004), p. 1081.

[9] Graham T Reed and Andrew P Knights. *Silicon photonics: an introduction*. John Wiley & Sons, 2004.

[10] Simeon Bogdanov et al. "Material platforms for integrated quantum photonics". In: *Optical Materials Express* 7.1 (2017), pp. 111–132.

[11] Ting Hu et al. "Silicon photonic platforms for mid-infrared applications". In: *Photonics Research* 5.5 (2017), pp. 417–430.

[12] Hongtao Lin et al. "Mid-infrared integrated photonics on silicon: a perspective". In: *Nanophotonics* 7.2 (2017), pp. 393–420.

[13] GZ Mashanovich et al. "Group IV mid-infrared photonics". In: *Optical Materials Express* 8.8 (2018), pp. 2276–2286.

[14] Jeremy L O'brien, Akira Furusawa, and Jelena Vučković. "Photonic quantum technologies". In: *Nature Photonics* 3.12 (2009), p. 687.

[15] Joshua W Silverstone et al. "Silicon quantum photonics". In: *IEEE Journal of Selected Topics in Quantum Electronics* 22.6 (2016), pp. 390–402.

[16] Faraz Najafi et al. "On-chip detection of non-classical light by scalable integration of single-photon detectors". In: *Nature communications* 6 (2015), p. 5873.

[17] Svetlana Khasminskaya et al. "Fully integrated quantum photonic circuit with an electrically driven light source". In: *Nature Photonics* 10.11 (2016), p. 727.

[18] Lucia Caspani et al. "Chip-based photon quantum state sources using nonlinear optics". In: *arXiv preprint arXiv:1706.04300* (2017).

[19] Justin B Spring et al. "On-chip low loss heralded source of pure single photons". In: *Optics express* 21.11 (2013), pp. 13522–13532.

[20] M Borghi et al. "Nonlinear silicon photonics". In: *Journal of Optics* 19.9 (2017), p. 093002.

[21] William SC Chang. *Fundamentals of guided-wave optoelectronic devices*. Cambridge University Press, 2009.

[22] John David Jackson. *Classical electrodynamics*. John Wiley & Sons, 2012.

[23] Thomas Feuchter and Carsten Thirstrup. "High precision planar waveguide propagation loss measurement technique using a Fabry-Perot cavity". In: *IEEE photonics technology letters* 6.10 (1994), pp. 1244–1247.

[24] Alfredo De Rossi et al. "Measuring propagation loss in a multimode semiconductor waveguide". In: *Journal of applied physics* 97.7 (2005), p. 073105.

[25] Daoxin Dai and Shipeng Wang. "Asymmetric directional couplers based on silicon nanophotonic waveguides and applications". In: *Frontiers of Optoelectronics* 9.3 (2016), pp. 450–465.

[26] Stefano Signorini et al. "Oblique beams interference for mode selection in multimode silicon waveguides". In: *Journal of Applied Physics* 122.11 (2017), p. 113106.

[27] Chenlei Li, Dajian Liu, and Daoxin Dai. "Multimode silicon photonics". In: *Nanophotonics* 8.2 (2018), pp. 227–247.

[28] Lucas B Soldano and Erik CM Pennings. "Optical multi-mode interference devices based on self-imaging: principles and applications". In: *Journal of lightwave technology* 13.4 (1995), pp. 615–627.

[29] Fei Guo et al. "A two-mode (de) multiplexer based on multimode interferometer coupler and y-junction on inp substrate". In: *IEEE Photon. J.* 8.1 (2016).

[30] RWC Vance and JD Love. "Asymmetric adiabatic multiprong for mode-multiplexed systems". In: *Electronics Letters* 29.24 (1993), pp. 2134–2136.

[31] Chunlei Sun et al. "An ultra-low crosstalk and broadband two-mode (de) multiplexer based on adiabatic couplers". In: *Scientific reports* 6 (2016), p. 38494.

[32] Jian Wang, Sailing He, and Daoxin Dai. "On-chip silicon 8-channel hybrid (de) multiplexer enabling simultaneous mode-and polarization-division-multiplexing". In: *Laser & Photonics Reviews* 8.2 (2014), pp. L18–L22.

[33] Yan-Si Le et al. "Three-mode all-optical (de) multiplexing on a SOI chip". In: *Optics Communications* 406 (2018), pp. 173–176.

[34] Daoxin Dai, Jian Wang, and Sailing He. "Silicon multimode photonic integrated devices for on-chip mode-division-multiplexed optical interconnects". In: *Prog. Electromagn. Res.* 143 (2013), pp. 773–819.

[35] Yuchan Luo et al. "Integrated dual-mode 3 dB power coupler based on tapered directional coupler". In: *Scientific reports* 6 (2016).

[36] Takui Uematsu et al. "Design of a compact two-mode multi/demultiplexer consisting of multimode interference waveguides and a wavelength-insensitive phase shifter for mode-division multiplexing transmission". In: *Journal of Lightwave Technology* 30.15 (2012), pp. 2421–2426.

[37] Jian Wang et al. "Improved 8-channel silicon mode demultiplexer with grating polarizers". In: *Optics express* 22.11 (2014), pp. 12799–12807.

[38] Daoxin Dai et al. "10-Channel Mode (de) multiplexer with Dual Polarizations". In: *Laser & Photonics Reviews* 12.1 (2018), p. 1700109.

[39] Weijie Chang et al. "Ultra-compact mode (de) multiplexer based on subwavelength asymmetric Y-junction". In: *Optics express* 26.7 (2018), pp. 8162–8170.

[40] Kangmei Li and Amy C Foster. "Parametric Nonlinear Silicon-Based Photonics". In: *Proceedings of the IEEE* 106.12 (2018), pp. 2196–2208.

[41] Robert W Boyd. *Nonlinear optics*. Elsevier, 2003.

[42] Juerg Leuthold, C Koos, and W Freude. "Nonlinear silicon photonics". In: *Nature photonics* 4.8 (2010), p. 535.

[43] RICHARDA Soref and BRIANR Bennett. "Electrooptical effects in silicon". In: *IEEE journal of quantum electronics* 23.1 (1987), pp. 123–129.

[44] Eric Dulkeith et al. "Self-phase-modulation in submicron silicon-on-insulator photonic wires". In: *Optics express* 14.12 (2006), pp. 5524–5534.

[45] Faisal R Ahmad et al. "Energy limits imposed by two-photon absorption for pulse amplification in high-power semiconductor optical amplifiers". In: *Optics letters* 33.10 (2008), pp. 1041–1043.

[46] Bahram Jalali et al. "Raman-based silicon photonics". In: *IEEE Journal of Selected Topics in Quantum Electronics* 12.3 (2006), pp. 412–421.

[47] RM Osgood et al. "Engineering nonlinearities in nanoscale optical systems: physics and applications in dispersion-engineered silicon nanophotonic wires". In: *Advances in Optics and Photonics* 1.1 (2009), pp. 162–235.

[48] Xiaoping Liu et al. "Bridging the mid-infrared-to-telecom gap with silicon nanophotonic spectral translation". In: *Nature Photonics* 6.10 (2012), p. 667.

[49] Bart Kuyken et al. "Generation of 3.6 μm radiation and telecom-band amplification by four-wave mixing in a silicon waveguide with normal group velocity dispersion". In: *Optics letters* 39.6 (2014), pp. 1349–1352.

[50] Bart Kuyken et al. "50 dB parametric on-chip gain in silicon photonic wires". In: *Optics letters* 36.22 (2011), pp. 4401–4403.

[51] Xiaoping Liu et al. "Mid-infrared optical parametric amplifier using silicon nanophotonic waveguides". In: *Nature Photonics* 4.8 (2010), p. 557.

[52] Ke-Yao Wang, Mark A Foster, and Amy C Foster. "Wavelength-agile near-IR optical parametric oscillator using a deposited silicon waveguide". In: *Optics express* 23.12 (2015), pp. 15431–15439.

[53] PD Maker and RW Terhune. "Study of optical effects due to an induced polarization third order in the electric field strength". In: *Physical Review* 137.3A (1965), A801.

[54] RL Carman, RY Chiao, and PL Kelley. "Observation of degenerate stimulated four-photon interaction and four-wave parametric amplification". In: *Physical Review Letters* 17.26 (1966), p. 1281.

[55] RH Stolen, JE Bjorkholm, and A Ashkin. "Phase-matched three-wave mixing in silica fiber optical waveguides". In: *Applied Physics Letters* 24.7 (1974), pp. 308–310.

[56] Hiroshi Fukuda et al. "Four-wave mixing in silicon wire waveguides". In: *Optics Express* 13.12 (2005), pp. 4629–4637.

[57] Joshua W Silverstone et al. "Qubit entanglement between ring-resonator photon-pair sources on a silicon chip". In: *Nature communications* 6 (2015), p. 7948.

[58] Govind P Agrawal. "Nonlinear fiber optics". In: *Nonlinear Science at the Dawn of the 21st Century*. Springer, 2000, pp. 195–211.

[59] Lucia Caspani et al. "Integrated sources of photon quantum states based on nonlinear optics". In: *Light: Science & Applications* 6.11 (2017), e17100.

[60] Leonard Mandel and Emil Wolf. *Optical coherence and quantum optics*. Cambridge university press, 1995.

[61] Massimo Borghi. "Linear, nonlinear and quantum optics in Silicon Photonics". PhD thesis. University of Trento, 2016.

[62] Joshua W Silverstone et al. "On-chip quantum interference between silicon photon-pair sources". In: *Nature Photonics* 8.2 (2014), p. 104.

[63] Albert Messiah. "Quantum mechanics, volume II". In: *Appedix C (Section IV)(North-Holland Publishing Company, Amsterdam, 1969)* (1962).

[64] Yi Zhan et al. "Generation of anti-Stokes pulses through phase-matched four wave mixing in birefringent photonic crystal fibers". In: *Optical and Quantum Electronics* 47.7 (2015), pp. 2065–2074.

[65] Christoph Krüger et al. "Birefringence measurements on crystalline silicon". In: *Classical and Quantum Gravity* 33.1 (2015), p. 015012.

[66] Toshiaki Suhara and Masatoshi Fujimura. *Waveguide nonlinear-optic devices*. Vol. 11. Springer Science & Business Media, 2013.

[67] Jeffrey B Driscoll et al. "Width-modulation of Si photonic wires for quasi-phase-matching of four-wave-mixing: experimental and theoretical demonstration". In: *Optics express* 20.8 (2012), pp. 9227–9242.

[68] Bart Kuyken et al. "Nonlinear optical interactions in silicon waveguides". In: *Nanophotonics* 6.2 (2017), pp. 377–392.

[69] Ji Cheng et al. "Intermodal four-wave mixing in a higher-order-mode fiber". In: *Applied physics letters* 101.16 (2012), p. 161106.

[70] Rene-Jean Essiambre et al. "Experimental investigation of inter-modal four-wave mixing in few-mode fibers". In: *IEEE Photonics Technology Letters* 25.6 (2013), pp. 539–542.

[71] H Tu et al. "Intermodal four-wave mixing from femtosecond pulse-pumped photonic crystal fiber". In: *Applied physics letters* 94.10 (2009), p. 101109.

[72] Eric A Kittlaus, Nils T Otterstrom, and Peter T Rakich. "On-chip inter-modal Brillouin scattering". In: *Nature communications* 8 (2017), p. 15819.

[73] Stefano Signorini et al. "Intermodal four-wave mixing in silicon waveguides". In: *Photonics Research* 6.8 (2018), pp. 805–814.

[74] Cosimo Lacava et al. "Intermodal Bragg-Scattering Four Wave Mixing in Silicon Waveguides". In: *Journal of Lightwave Technology* (2019).

[75] C Lacava et al. "Ultra-Broadband Bragg Scattering Four Wave Mixing in Silicon Rich Silicon Nitride Waveguides". In: *Optical Fiber Communication Conference*. Optical Society of America. 2019, W1C–5.

[76] Lan-Tian Feng et al. "On-chip transverse-mode entangled photon pair source". In: *npj Quantum Information* 5.1 (2019), p. 2.

[77] Jianhao Zhang et al. "Self-adaptive waveguide boundary for wideband multimode four-wave mixing". In: *arXiv preprint arXiv:1902.06170* (2019).

[78] Yunhong Ding et al. "Mode-selective wavelength conversion based on four-wave mixing in a multimode silicon waveguide". In: *Optics express* 22.1 (2014), pp. 127–135.

[79] Ming Ma and Lawrence R Chen. "On-chip silicon mode-selective broadband wavelength conversion based on cross-phase modulation". In: *CLEO: Science and Innovations*. Optical Society of America. 2016, STh3E–3.

[80] Ying Qiu et al. "Mode-selective wavelength conversion of OFDM-QPSK signals in a multimode silicon waveguide". In: *Optics express* 25.4 (2017), pp. 4493–4499.

[81] Mark A Foster et al. "Broad-band optical parametric gain on a silicon photonic chip". In: *Nature* 441.7096 (2006), p. 960.

[82] Kai Guo et al. "Broadband wavelength conversion in a silicon vertical-dual-slot waveguide". In: *Optics Express* 25.26 (2017), pp. 32964–32971.

[83] JG Crowder et al. "Infrared methods for gas detection". In: *Mid-Infrared Semiconductor Optoelectronics*. Springer, 2006, pp. 595–613.

[84] M Mancinelli et al. "Mid-infrared coincidence measurements on twin photons at room temperature". In: *Nature communications* 8 (2017), p. 15184.

[85] Alex S Clark et al. "Raman scattering effects on correlated photon-pair generation in chalcogenide". In: *Optics Express* 20.15 (2012), pp. 16807–16814.

[86] Amy C Turner et al. "Tailored anomalous group-velocity dispersion in silicon channel waveguides". In: *Optics express* 14.10 (2006), pp. 4357–4362.

[87] Wei Pan et al. "All-optical wavelength conversion for mode-division multiplexing signals using four-wave mixing in a dual-mode fiber". In: *JOSA B* 32.12 (2015), pp. 2417–2424.

[88] Yuzhe Xiao et al. "Theory of intermodal four-wave mixing with random linear mode coupling in few-mode fibers". In: *Optics express* 22.26 (2014), pp. 32039–32059.

[89] Qiang Lin et al. "Ultrabroadband parametric generation and wavelength conversion in silicon waveguides". In: *Optics Express* 14.11 (2006), pp. 4786–4799.

[90] Fulvio Flamini, Nicolò Spagnolo, and Fabio Sciarrino. "Photonic quantum information processing: a review". In: *Reports on Progress in Physics* 82.1 (2018), p. 016001.

[91] Matthew D Eisaman et al. "Invited review article: Single-photon sources and detectors". In: *Review of scientific instruments* 82.7 (2011), p. 071101.

[92] Nicholas C Harris et al. "Large-scale quantum photonic circuits in silicon". In: *Nanophotonics* 5.3 (2016), pp. 456–468.

[93] Mario Krenn et al. "Quantum communication with photons". In: *Optics in Our Time* 18 (2016), p. 455.

[94] SA Castelletto and RE Scholten. "Heralded single photon sources: a route towards quantum communication technology and photon standards". In: *The European Physical Journal-Applied Physics* 41.3 (2008), pp. 181–194.

[95] Alan Migdall et al. *Single-photon generation and detection: physics and applications*. Vol. 45. Academic Press, 2013.

[96] Xiao-Liu Chu, Stephan Götzinger, and Vahid Sandoghdar. "A single molecule as a high-fidelity photon gun for producing intensity-squeezed light". In: *Nature Photonics* 11.1 (2017), p. 58.

[97] ZY Ou, J-K Rhee, and LJ Wang. "Photon bunching and multiphoton interference in parametric down-conversion". In: *Physical Review A* 60.1 (1999), p. 593.

[98] Imad I Faruque et al. "On-chip quantum interference with heralded photons from two independent micro-ring resonator sources in silicon photonics". In: *Optics express* 26.16 (2018), pp. 20379–20395.

[99] Daniel Huber et al. "Highly indistinguishable and strongly entangled photons from symmetric GaAs quantum dots". In: *Nature communications* 8 (2017), p. 15506.

[100] Feng Liu et al. "High Purcell factor generation of indistinguishable on-chip single photons". In: *Nature nanotechnology* 13.9 (2018), p. 835.

[101] Igor Aharonovich, Dirk Englund, and Milos Toth. "Solid-state single-photon emitters". In: *Nature Photonics* 10.10 (2016), p. 631.

[102] Yuya Yonezu et al. "Efficient Single-Photon Coupling from a Nitrogen-Vacancy Center Embedded in a Diamond Nanowire Utilizing an Optical Nanofiber". In: *Scientific reports* 7.1 (2017), p. 12985.

[103] Pascale Senellart, Glenn Solomon, and Andrew White. "High-performance semiconductor quantum-dot single-photon sources". In: *Nature nanotechnology* 12.11 (2017), p. 1026.

[104] CI Osorio, N Sangouard, and Robert Thomas Thew. "On the purity and indistinguishability of down-converted photons". In: *Journal of Physics B: Atomic, Molecular and Optical Physics* 46.5 (2013), p. 055501.

[105] Ken-ichi Harada et al. "Indistinguishable photon pair generation using two independent silicon wire waveguides". In: *New Journal of Physics* 13.6 (2011), p. 065005.

[106] Stephan Krapick et al. "An efficient integrated two-color source for heralded single photons". In: *New Journal of Physics* 15.3 (2013), p. 033010.

[107] Kevin Zielnicki et al. "Engineering of near-IR photon pairs to be factorable in space-time and entangled in polarization". In: *Optics Express* 23.6 (2015), pp. 7894–7907.

[108] Matthias Bock et al. "Highly efficient heralded single-photon source for telecom wavelengths based on a PPLN waveguide". In: *Optics express* 24.21 (2016), pp. 23992–24001.

[109] Chaitali Joshi et al. "Frequency multiplexing for quasi-deterministic heralded single-photon sources". In: *Nature communications* 9.1 (2018), p. 847.

[110] Justin B Spring et al. "Chip-based array of near-identical, pure, heralded single-photon sources". In: *Optica* 4.1 (2017), pp. 90–96.

[111] Evan Meyer-Scott et al. "Limits on the heralding efficiencies and spectral purities of spectrally filtered single photons from photon-pair sources". In: *Physical Review A* 95.6 (2017), p. 061803.

[112] Marcelo Davanco et al. "Telecommunications-band heralded single photons from a silicon nanophotonic chip". In: *Applied Physics Letters* 100.26 (2012), p. 261104.

[113] Stefano Signorini et al. "Are on-chip heralded single photon sources possible by intermodal four wave mixing in silicon waveguides?" In: *Quantum Photonic Devices 2018*. Vol. 10733. International Society for Optics and Photonics. 2018, 107330G.

[114] Jacob G Koefoed et al. "Spectrally pure heralded single photons by spontaneous four-wave mixing in a fiber: reducing impact of dispersion fluctuations". In: *Optics express* 25.17 (2017), pp. 20835–20849.

[115] Majid Ebrahim-Zadeh and Irina T Sorokina. *Mid-infrared coherent sources and applications*. Springer, 2007.

[116] Richard A McCracken, Francesco Graffitti, and Alessandro Fedrizzi. "Numerical investigation of mid-infrared single-photon generation". In: *JOSA B* 35.12 (2018), pp. C38–C48.

[117] Daniel C Fernandez et al. "Infrared spectroscopic imaging for histopathologic recognition". In: *Nature biotechnology* 23.4 (2005), p. 469.

[118] Guilherme Temporao et al. "Feasibility study of free-space quantum key distribution in the mid-infrared". In: *Quantum Information & Computation* 8.1 (2008), pp. 1–11.

[119] Paul-Antoine Moreau et al. "Demonstrating an absolute quantum advantage in direct absorption measurement". In: *Scientific reports* 7.1 (2017), p. 6256.

[120] Qiang Wang et al. "Super-resolving quantum lidar: entangled coherent-state sources with binary-outcome photon counting measurement suffice to beat the shot-noise limit". In: *Optics express* 24.5 (2016), pp. 5045–5056.

[121] Bin Fang et al. "State engineering of photon pairs produced through dual-pump spontaneous four-wave mixing". In: *Optics express* 21.3 (2013), pp. 2707–2717.

[122] Rodney Loudon. *The quantum theory of light*. OUP Oxford, 2000.

[123] Michael A Nielsen and Isaac Chuang. *Quantum computation and quantum information*. 2002.

[124] F Mintert, C Viviescas, and A Buchleitner. "Basic concepts of entangled states". In: *Entanglement and Decoherence*. Springer, 2009, pp. 61–86.

[125] Peter J Mosley et al. "Conditional preparation of single photons using parametric downconversion: a recipe for purity". In: *New Journal of Physics* 10.9 (2008), p. 093011.

[126] Artur Ekert and Peter L Knight. "Entangled quantum systems and the Schmidt decomposition". In: *American Journal of Physics* 63.5 (1995), pp. 415–423.

[127] Kevin Zielnicki et al. "Joint spectral characterization of photon-pair sources". In: *Journal of Modern Optics* 65.10 (2018), pp. 1141–1160.

[128] AK Ekert and PL Knight. "Correlations and squeezing of two-mode oscillations". In: *American Journal of Physics* 57.8 (1989), pp. 692–697.

[129] Claude Cohen-Tannoudji, Bernard Diu, and Frank Laloe. "Quantum Mechanics, Volume 2". In: *Quantum Mechanics, Volume 2, by Claude Cohen-Tannoudji, Bernard Diu, Frank Laloe, pp. 626. ISBN 0-471-16435-6. Wiley-VCH, June 1986.* (1986), p. 626.

[130] Andreas Christ et al. "Probing multimode squeezing with correlation functions". In: *New Journal of Physics* 13.3 (2011), p. 033027.

[131] CK Law, Ian A Walmsley, and JH Eberly. "Continuous frequency entanglement: effective finite Hilbert space and entropy control". In: *Physical Review Letters* 84.23 (2000), p. 5304.

[132] Stephen Barnett and Paul M Radmore. *Methods in theoretical quantum optics*. Vol. 15. Oxford University Press, 2002.

[133] Wolfgang Mauerer et al. "How colors influence numbers: Photon statistics of parametric down-conversion". In: *Physical Review A* 80.5 (2009), p. 053815.

[134] Peter P Rohde, Wolfgang Mauerer, and Christine Silberhorn. "Spectral structure and decompositions of optical states, and their applications". In: *New Journal of Physics* 9.4 (2007), p. 91.

[135] Iman Jizan et al. "Bi-photon spectral correlation measurements from a silicon nanowire in the quantum and classical regimes". In: *Scientific reports* 5 (2015), p. 12557.

[136] K Garay-Palmett et al. "Photon pair-state preparation with tailored spectral properties by spontaneous four-wave mixing in photonic-crystal fiber". In: *Optics express* 15.22 (2007), pp. 14870–14886.

[137] Georg Harder et al. "An optimized photon pair source for quantum circuits". In: *Optics express* 21.12 (2013), pp. 13975–13985.

[138] Luis Edgar Vicent et al. "Design of bright, fiber-coupled and fully factorable photon pair sources". In: *New Journal of Physics* 12.9 (2010), p. 093027.

[139] Z Vernon et al. "Truly unentangled photon pairs without spectral filtering". In: *Optics letters* 42.18 (2017), pp. 3638–3641.

[140] Aaron J Miller et al. "Demonstration of a low-noise near-infrared photon counter with multiphoton discrimination". In: *Applied Physics Letters* 83.4 (2003), pp. 791–793.

[141] JS Lundeen et al. "Tomography of quantum detectors". In: *Nature Physics* 5.1 (2009), p. 27.

[142] Shin Arahira et al. "Generation of polarization entangled photon pairs at telecommunication wavelength using cascaded χ (2) processes in a periodically poled LiNbO 3 ridge waveguide". In: *Optics express* 19.17 (2011), pp. 16032–16043.

[143] Marco Liscidini and JE Sipe. "Stimulated emission tomography". In: *Physical review letters* 111.19 (2013), p. 193602.

[144] Fumihiro Kaneda et al. "Heralded single-photon source utilizing highly nondegenerate, spectrally factorable spontaneous parametric downconversion". In: *Optics express* 24.10 (2016), pp. 10733–10747.

[145] Chong-Ki Hong, Zhe-Yu Ou, and Leonard Mandel. "Measurement of subpicosecond time intervals between two photons by interference". In: *Physical review letters* 59.18 (1987), p. 2044.

[146] M Razavi et al. "Characterizing heralded single-photon sources with imperfect measurement devices". In: *Journal of Physics B: Atomic, Molecular and Optical Physics* 42.11 (2009), p. 114013.

[147] E Bocquillon et al. "Coherence measures for heralded single-photon sources". In: *Physical Review A* 79.3 (2009), p. 035801.

[148] Mark Bashkansky et al. "Significance of heralding in spontaneous parametric down-conversion". In: *Physical Review A* 90.5 (2014), p. 053825.

[149] Chad A Husko et al. "Multi-photon absorption limits to heralded single photon sources". In: *Scientific reports* 3 (2013), p. 3087.

[150] Ian A Walmsley and Michael G Raymer. "Toward quantum-information processing with photons". In: *Science* 307.5716 (2005), pp. 1733–1734.

[151] TB Pittman et al. "Experimental controlled-NOT logic gate for single photons in the coincidence basis". In: *Physical Review A* 68.3 (2003), p. 032316.

[152] Justin B Spring et al. "Boson sampling on a photonic chip". In: *Science* 339.6121 (2013), pp. 798–801.

[153] Brian J Smith et al. "Photon pair generation in birefringent optical fibers". In: *Optics express* 17.26 (2009), pp. 23589–23602.

[154] Matthaeus Halder et al. "Nonclassical 2-photon interference with separate intrinsically narrowband fibre sources". In: *Optics express* 17.6 (2009), pp. 4670–4676.

[155] Karsten Rottwitt, Jacob Koefoed, and Erik Christensen. "Photon-pair sources based on intermodal four-wave mixing in few-mode fibers". In: *Fibers* 6.2 (2018), p. 32.

[156] Lijian Zhang et al. "Heralded generation of single photons in pure quantum states". In: *Journal of Modern Optics* 59.17 (2012), pp. 1525–1537.

[157] Michael G Tanner et al. "Enhanced telecom wavelength single-photon detection with NbTiN superconducting nanowires on oxidized silicon". In: *Applied Physics Letters* 96.22 (2010), p. 221109.

[158] Francesco Marsili et al. "Efficient single photon detection from 500 nm to 5 μm wavelength". In: *Nano letters* 12.9 (2012), pp. 4799–4804.

[159] Jeppe Seidelin Dam, Peter Tidemand-Lichtenberg, and Christian Pedersen. "Room-temperature mid-infrared single-photon spectral imaging". In: *Nature photonics* 6.11 (2012), p. 788.

[160] Ajanta Barh, Peter Tidemand-Lichtenberg, and Christian Pedersen. "Thermal noise in mid-infrared broadband upconversion detectors". In: *Optics express* 26.3 (2018), pp. 3249–3259.

[161] Chaoxuan Ma et al. "Silicon photonic entangled photon-pair and heralded single photon generation with CAR> 12,000 and g (2)(0)< 0.006". In: *Optics Express* 25.26 (2017), pp. 32995–33006.

[162] Matthew J Collins et al. "Integrated spatial multiplexing of heralded single-photon sources". In: *Nature communications* 4 (2013), p. 2582.

[163] S Janz et al. "Silicon photonic wire evanescent field sensors: From sensor to biochip array". In: *Group IV Photonics, 2009. GFP'09. 6th IEEE International Conference on*. IEEE. 2009, pp. 89–91.

Publications

- **Signorini, S.**, Borghi, M., Mancinelli, M., Bernard, M., Ghulinyan, M., Pucker, G., & Pavesi, L. (2017). *Oblique beams interference for mode selection in multimode silicon waveguides.* Journal of Applied Physics, 122(11), 113106.
- **Signorini, S.**, Mancinelli, M., Borghi, M., Bernard, M., Ghulinyan, M., Pucker, G., & Pavesi, L. (2018). *Intermodal four-wave mixing in silicon waveguides.* Photonics Research, 6(8), 805-814.
- Borghi, M., Castellan, C., **Signorini, S.**, Trenti, A., & Pavesi, L. (2017). *Nonlinear silicon photonics.* Journal of Optics, 19(9), 093002.
- **Signorini, S.**, Mancinelli, M., Bernard, M., Ghulinyan, M., Pucker, G., & Pavesi, L. (2017, August). *Broad wavelength generation and conversion with multi modal Four Wave Mixing in silicon waveguides.* In Group IV Photonics (GFP), 2017 IEEE 14th International Conference on (pp. 59-60). IEEE.
- **Signorini, S.**, Piccione, S., Ghulinyan, M., Pucker, G., & Pavesi, L. (2018, September). *Are on-chip heralded single photon sources possible by intermodal four wave mixing in silicon waveguides?.* In Quantum Photonic Devices 2018 (Vol. 10733, p. 107330G). International Society for Optics and Photonics.
- **Signorini S.**, Piccione S., Ghulinyan M., Pucker G., & Pavesi L. (2018). *Heralded single photon source of 2 micron photons in silicon waveguides.* In ECIO 2018 Conference proceedings, ISBN: 978-84-09-20653-1.
- **Signorini, S.**, Piccione, S., Fontana, G., Pavesi, L., Ghulinyan, M., & Pucker, G. (2019, April). *Towards MIR heralded photons via intermodal four wave mixing in silicon waveguides.* In Quantum Information and Measurement (pp. T5A-11). Optical Society of America.
- M. Biesuz , P. Bettotti , **S. Signorini** , M. Bortolotti, R. Campostrini, M. Bahri, O. Ersen, G. Speranza, A. Lale, S. Bernard & G. D. Sorarù., *First synthesis of silicon nanoscrystals in amorphous silicon nitride from a preceramic polymer*, Nanotechnology (2019).

Conferences

- IEEE 14th International Conference on Group IV Photonics, GFP 2017 - Berlin, Germany - *Poster presentation*
- SPIE 5th International Symposium on Optics and its applications, OPTICS 2017 - Wroclaw, Poland - *Oral presentation*
- 103rd National Congress of the Italian Physical Society, 2017 - Trento, Italy - *Oral presentation*
- SPIE 6th International Symposium on Optics and its applications, OPTICS 2018 - Trento, Italy - *Oral presentation*
- SPIE Photonics Europe, 2018 - Strasbourg, France - *Oral presentation*
- 20th Fotonica AEIT Italian conference on photonics technologies, 2018 - Lecce, Italy - *Oral presentation*
- 20th European Conference on Integrated Optics, ECIO 2018 - Valencia, Spain - *Poster presentation*
- SPIE Optics + Photonics, 2018 - San Diego, USA - *Oral presentation*
- OSA 5th Quantum information and measurement: quantum technologies, 2019 - Rome, Italy - *Poster presentation*